When dynamic cracks meet disorder: A journey along the fracture process zone

THÈSE N^{O} 8956 (2018)

PRÉSENTÉE LE 23 NOVEMBRE 2018
À LA FACULTÉ DE L'ENVIRONNEMENT NATUREL, ARCHITECTURAL ET CONSTRUIT
LABORATOIRE DE SIMULATION EN MÉCANIQUE DES SOLIDES
PROGRAMME DOCTORAL EN GÉNIE CIVIL ET ENVIRONNEMENT

ÉCOLE POLYTECHNIQUE FÉDÉRALE DE LAUSANNE

POUR L'OBTENTION DU GRADE DE DOCTEUR ÈS SCIENCES

PAR

Fabian BARRAS

acceptée sur proposition du jury:

Prof. B. T. A. Lecampion, président du jury
Prof. J.-F. Molinari, directeur de thèse
Prof. E. Bouchbinder, rapporteur
Prof. J.-P. Ampuero, rapporteur
Prof. M. Violay, rapporteuse

ÉCOLE POLYTECHNIQUE
FÉDÉRALE DE LAUSANNE

Suisse
2018

There is a crack in everything;
That’s how the light gets in.
— Leonard Cohen, *Anthem*

Acknowledgements

This long and exciting journey (along the fracture process zone) would not have been possible without the help and support of many people. First and foremost, I want to sincerely thank Jean-François Molinari, my thesis director, for offering me the opportunity of conducting this Ph.D. research. Jean-François welcomed me in his team already during my undergraduate studies, which was eight years ago. This particularly long collaboration expresses certainly better than any words my immense gratitude and the great pleasure I had to work under his supervision. I am particularly grateful for his guidance and the confidence he always gave to my suggestions and ideas during this research. His permanent trust and enthusiasm regarding my work have been a strong support and motivation to give my best during this thesis.

I was also privileged to work in direct collaboration with world experts of the field. I want to acknowledge Philippe Geubelle who hosted me in his lab during my master thesis and shared his expertise on the spectral boundary integral method. I really enjoyed our collaboration, which helped me exploring three-dimensional aspects of fracture, notably during the co-supervision of the theses of Damien Spielmann and René Carpaij. I am also thankful to Daniel Bonamy and Alizée Dubois for the enthralling discussions on statistical aspects of dynamic fracture during my visits in Paris. I also enjoyed working with Eran Bouchbinder, Efim Brener and Michael Aldam who introduced me to the instable dynamics of rate-and-state friction laws. I was glad to have Eran in my thesis committee. I want to sincerely thank him and the other committee members Marie Violay, Brice Lecampion and Jean-Paul Ampuero for their precious time and the warm and encouraging comments on my work.

I was particularly lucky to know several generations of the "LSMS family". I feel privileged to be part of this fantastic, multicultural and lively working environment and, therefore, I want to sincerely thank all of my past colleagues. I will keep fantastic memories of the various lab outings, squash games, hike in Champsaur, Star Wars evenings, Frühlingsfest and, not forgetting, the long and glorious Advent periods. I want to particularly thank Guillaume Anciaux for his priceless help and advices throughout the thesis, notably for proofreading this manuscript. I was lucky to work with David Kammer who introduced me to the art of LEFM during my master thesis and gave me precious advices all along my Ph.D. thesis. I am also grateful to Nicolas Richart who helped me for the coding aspects and, more importantly, to give a name to my library *cRacklet*. I was also fortunate to work with Ramin Aghababaei to discover the slippery and tough aspects of friction and wear at small scales. During the last months of my thesis, I enjoyed collaborating with Fatima Fekak and Thibault Roch on heterogeneous dynamic fracture. I am happy that cRacklet will grow up in good hands with both of them. I was also lucky to count on the great help of Emma Sorrentino and Birgitte Seem to balance my natural laziness regarding the administrative tasks. Before switching to French, I also want to sincerely thank Anastasia Ford for removing the remaining Frenglish aspects from this manuscript.

Je voudrais spécialement remercier l'ensemble de ma famille pour leur soutien permanent durant ces cinq dernières années, tout particulièrement ma sœur Laure et mes parents Patricia et Jean-Victor. Je suis très chanceux et reconnaissant d'avoir toujours pu compter sur leur présence et leur confiance en mes choix.

Ces années de thèse auraient été un long fleuve trop tranquille sans la présence et l'amitié de nombreuses personnes. Un grand merci aux loups du Vanex pour les bed, les einfach et surtout les nombreux quadraat, aux ducs de Bussigny qui m'ont appris que tout succès se bâtit brique après brique, au visionnaire de Sensine pour me rappeler constamment qu'il n'y a plus de petite thèse, à la famille Marchand pour son accueil chaleureux et les après-midis jeux de société, à toute l'équipe sociale et politique de l'ENAC/EDCE pour l'aide et le fun dans l'organisation de multiples apéros, aux présidents d'Instituts pour m'avoir fait découvrir le Caire, aux parents d'Aslan pour le tango, les bières et les châtaignes, aux BCBG pour Stuttgart, Glaris et Bruxelles.

Enfin, ce travail de thèse n'aurait pas été possible sans toi, Cynthia. Merci pour ton amour, ton soutien et ton immense patience au quotidien. Durant les derniers mois, tu m'as aidé avec une énergie exceptionnelle pour que je puisse me consacrer pleinement à la rédaction de ce manuscrit. Cette thèse est un peu la tienne. Si notre rencontre a coïncidé avec ses débuts, j'ai hâte de planifier les futures étapes avec toi.

Lausanne, October 2018 Fabian Barras

Abstract

The onset of earthquakes along crustal faults, the triggering of slab avalanches or the break of a wine glass are all serious problems driven by the propagation of a dynamic rupture front. Our physical understanding of this ubiquitous phenomenon is however still far from being well-established. While Linear Elastic Fracture Mechanics (LEFM) became a successful theoretical framework to describe the stability and the slow growth of flaws within materials, it still fails at describing the dynamics of fast and sudden rupture fronts. Several experimental studies recorded the propagation of dynamic crack fronts and revealed the origin of this discrepancy. As the rupture speed approaches the one of the elastic waves, the crack stops being the simple planar object pictured by the theory. Indeed, dynamic instabilities start interfering with the crack propagation, while the fracture surface roughens and reveals the permanent interplay between the rupture front and the heterogeneities emerging from the material microstructure.

In this context, the objective of the present Ph.D. work is precisely to bring novel insights in these complex and unstable dynamics using the great potential of modern computational methods. The originality of its approach consists in looking at the scale of the intimate interaction existing between the rupture front and material heterogeneities, where the crack tip spreads over some distance called the *fracture process zone*. To this aim, it relies on two "homemade" implementations of the elastodynamic equations running on modern computing cluster facilities.

This Ph.D. work consists mainly in two parts. The first one presents a fundamental study of the interplay between a crack front and microscopic heterogeneities. This work reveals the direct impact of the heterogeneities on the local speed of the rupture front, which can even exceed the admissible values predicted for homogeneous conditions. The simulations further allow to connect the progressive roughening of the fracture surface to the "relativistic" contraction of the process zone observed when the crack speed approaches the speed of elastic waves. In the second part of the manuscript, the same formalism is applied to the study of frictional interfaces, for which the microscopic heterogeneities correspond to the scattered topography emerging from the contact between two rough surfaces. This study notably proposes a new estimation of the part of fracture energy entering the seismic energy budget.

In spite of being a rather fundamental study of heterogeneous crack dynamics, this Ph.D. work finds direct implications in a large range of domains, from earthquake science to the design of more resilient materials.

Keywords: Linear Elastic Fracture Mechanics, fracture process zone, heterogeneous microstructure, elastodynamic, shock waves, friction, multicontact interface, rate-and-state laws, earthquake, boundary integral method, finite-element method, cohesive laws, high performance computing

Résumé

L'initiation d'un séisme le long de failles tectoniques, le déclenchement d'une avalanche de plaque ou la fracture d'un verre à vin sont autant de situations catastrophiques causées par la propagation dynamique d'un front de rupture. Notre compréhension physique de ce phénomène omniprésent est cependant loin d'être complètement acquise. Si la Mécanique Linéaire Élastique de la Rupture (MLER) est devenu un cadre théorique reconnu et unanimement appliqué pour étudier la stabilité et la propagation lente de défauts présents dans les matériaux, elle reste néanmoins insuffisante pour décrire la dynamique des ruptures soudaines et rapides. L'origine de cette divergence a été révélée au travers de plusieurs études expérimentales ayant observé la propagation rapide de fissures dans les matériaux. Lorsque la vitesse de fissuration se rapproche de celle des ondes élastiques, la pointe de fissure cesse de correspondre à la représentation simple et planaire supposée dans la théorie. En effet, des instabilités dynamiques se manifestent à haute vitesse et interfèrent avec l'avancée de la fissure. Le profil des surfaces ainsi créées par la rupture devient rugueux et trahit l'interaction permanente entre le front de rupture et les hétérogénéités existantes dans la microstructure du matériau.

Dans ce contexte, ce travail de doctorat repose sur des approches numériques qui représentent une alternative prometteuse pour faire la lumière sur ces dynamiques complexes et instables. L'originalité de l'approche consiste à étudier l'interaction avec les hétérogénéités du matériau existant au plus près de la pointe de fissure, à une échelle où elle ne correspond plus à un point singulier, mais s'étale sur une région communément appelée *la zone d'endommagement*. A cet effet, ce travail de recherche s'appuie sur deux implémentations numériques de l'élastodynamique déployées sur des supercalculateurs modernes, spécialement taillés pour le calcul scientifique.

Ce travail de doctorat se divise principalement en deux parties. La première consiste en l'étude fondamentale de l'interaction entre une fissure dynamique et des hétérogénéités microscopiques. Cette étude révèle l'impact direct de ces dernières sur la vitesse locale du front de rupture qui peut même dépasser les valeurs théoriquement admises par la MLER pour une interface homogène. De plus, ce travail permet d'associer l'augmentation des rugosités de surfaces de rupture à la contraction "relativiste" de la zone d'endommagement lorsque la vitesse de fissuration se rapproche de celle des ondes élastiques. Dans la deuxième partie du manuscrit, le même formalisme est appliqué à l'étude d'interfaces de frottement, pour lesquelles les hétérogénéités microscopiques naissent du profil éparse des points de contact existants entre deux surfaces rugueuses. Cette étude propose notamment une nouvelle estimation de la part

d'énergie de rupture participant au budget énergétique d'un séisme.
Bien qu'étant une étude plutôt fondamentale de la dynamique de rupture en milieux hétérogènes, ce travail de doctorat trouve des applications dans divers domaines, allant de la dynamique des séismes à la conception de matériaux plus résistants.

Mots clefs : Mécanique Linéaire Élastique de la Rupture, zone d'endommagement, microstructure hétérogènes, élasto-dynamique, ondes de choc, frottement, interface multi-contact, loi de frottement rate-and-state, séisme, méthode des intégrales de frontière, méthode des éléments finis, lois cohésives, calcul scientifique à haute performance

Contents

Acknowledgements **i**

Abstract (English) **iii**

Résumé (Français) **v**

List of figures **xi**

List of tables **xxi**

1 Introduction **1**

1.1 Motivation 1
1.2 Objectives 3
1.3 Approach 4
1.4 Outline of chapters 5

2 State of the art **7**

2.1 Continuum solid mechanics 7
  2.1.1 Conservation laws 8
  2.1.2 Kinematics 9
  2.1.3 Constitutive law 11
  2.1.4 Elastodynamics 12
  2.1.5 Boundary and initial value problems 13
2.2 Fracture mechanics 15
  2.2.1 On the elastodynamics of moving cracks 21
  2.2.2 Relativistic effects in dynamic fracture 25
  2.2.3 Dynamic fracture experiments 27
  2.2.4 Heterogeneous fracture mechanics 28
  2.2.5 Dynamic rupture of weak interfaces 29
2.3 Solid friction of multi-contact interfaces 31
  2.3.1 Laboratory-derived interface models 31
  2.3.2 The elastodynamic approach 36

3 Numerical framework **39**
3.1 Spectral boundary integral formulation 40
3.2 Finite-element method 44
3.2.1 Standard bulk element 44
3.2.2 Cohesive element 46

4 Dynamic fracture along bimaterial interfaces **49**
4.1 Introduction 50
4.2 Problem description 52
4.2.1 Geometry and elastodynamics 52
4.2.2 Interface laws 53
4.2.3 Material properties 54
4.3 Numerical method 54
4.4 Reference case ($\psi = 75°$) 56
4.4.1 Evolution of cohesive and contact zones 56
4.4.2 Failure process 57
4.4.3 Energetics 58
4.5 Influence of loading angle ψ 59
4.5.1 Evolution of cohesive and contact zones 59
4.5.2 Impact of ψ on the failure process 62
4.6 Effect of material mismatch 65
4.7 Conclusion 66

5 Interplay between process zone and material heterogeneities **69**
5.1 Introduction 70
5.2 Problem Description 71
5.2.1 Geometry and elastodynamics 71
5.2.2 Numerical scheme 71
5.2.3 Fracture initiation 72
5.3 The effect of heterogeneous microstructure 73
5.4 Transition from homogeneous to heterogeneous fracture 75
5.5 Process zone size in dynamic fracture 76
5.6 Discussion 78
5.7 Supplemental material 78
5.7.1 Material properties 78
5.7.2 Effect of heterogeneous microstructure 78
5.7.3 Transition from homogeneous to heterogeneous fracture 80
5.7.4 Process zone size in dynamic fracture 80

6 Supershear bursts in the propagation of tensile crack **81**
6.1 Introduction 83
6.2 Set-up 83
6.3 Material properties 85

6.4 Methodology 85
6.5 Supershear bursts 86
6.6 Geometrical model 88
6.7 Parametric study 90
6.8 Shock waves 92
6.9 Conclusion 93

7 Onset of sliding across scales 95
7.1 Introduction 96
7.2 Problem description 98
7.2.1 Numerical method 99
7.2.2 Material properties 100
7.3 A characteristic length scale controlling the brittle-to-ductile transition 101
7.4 Effect of l_{pz} at the scale of the heterogeneous microcontacts 104
7.5 Discussion 106

8 The rupture dynamics of interfaces obeying laboratory-derived friction laws 109
8.1 Introduction 110
8.2 Geometry and elastodynamic formulation 111
8.3 Numerical method 112
8.3.1 Cohesive formulation 113
8.3.2 Rate-and-state formulation 113
8.3.3 Bulk and interface properties 114
8.4 Crack tip equation of motion 114
8.5 Rupture dynamics with rate-and-state friction laws 119
8.6 Application to other rate-and-state formulations 128
8.6.1 The original velocity-weakening formulation 128
8.6.2 Velocity-strengthening and slow earthquakes 130
8.6.3 Nucleation from sticking conditions 130
8.6.4 Aging versus slip law 131
8.6.5 Magnitudes of the equivalent fracture energy 131
8.7 Conclusion 133
8.8 Supplementary materials 136

9 Conclusion 139
9.1 Summary 139
9.2 Outlook and perspectives 141

Bibliography 159

Curriculum Vitae 161

List of Figures

1.1 The fast rupture of a brittle material creates particularly rough fracture surfaces. Microscope image (millimeter scale) of the fracture surface created by a fast dynamic crack in PMMA (acrylic glass). **(Inset)** Zoom (hundreds of micrometers) in the fracture surface using scanning electron microscopy revealing the onset of an out-of-plane microbranch appearing in the middle of in-plane conic marks. Courtesy of Alizée Dubois. 2

2.1 Stresses existing at the surfaces of an elementary block of matter of size $dx\,dy\,dz$. This concept is only valid for a large scale description of solids, far from the discrete nature of matter existing at the atomistic length scales. 8

2.2 Kinematics of a deformable solid from its original Ω to its deformed $\mathit{\Omega}$ configuration. 9

2.3 The typical axes convention used in this thesis and its three associated modes of fracture. 15

2.4 Stress concentration at the vicinity of a sharp crack existing within a semi-infinite plate and its evolution along $y = 0$. 16

2.5 Comparison between the exact stress field and the singular approximation along $y = 0$. The asymptotic stress field is only accurate in the close neighborhood of the crack tip. 17

2.6 The two configurations used by Irwin [1] to compute the change of potential energy observed as crack grows of Δa. The blue arrows represent the surface tractions required to close the crack between a and $a + \Delta a$. 19

2.7 Schematic evolution of the stress at the vicinity of a crack and its approximation following LEFM theoretical framework (dashed black line). See the main text for a detailed description of the three regions (A-B-C). 21

2.8 Asymptotic evolution along the crack plane $y = 0$ of the velocity (left) and shear stress (right) at the vicinity of a mode III crack moving at any subsonic speed along an interface characterized by a given fracture energy G_c. 24

2.9 Asymptotic hoop stress profiles predicted at the vicinity of a tensile crack moving at different speeds along an interface characterized by G_c and $c_R = 0.93c_s$. . . . 25

2.10 Analogy between the relativistic effects existing for a particle of mass m_e moving at speed c (**Right**) and the one computed for a dynamic crack (**Left**). 26

2.11 Schematic evolution of the post-mortem appearance of the fracture surface as function of the crack propagation speed. 27

2.12 Interaction of a dynamic crack with heterogeneities at two different scales. (**Left**) If the process zone size is much smaller than the heterogeneities, the crack is viewed as a line and studied using Rice's first-order perturbation analysis [2]. (**Right**) At the scale of the fracture process zone, the crack advances through the nucleation, growth and coalescence of pre-existing microcracks. This dynamics is typically studied using damage models [3]. 28

2.13 Two interacting scales control the onset of sliding of a frictional interface. (**Left**) Bulk elastodynamics driving the propagation of slip fronts. (**Right**) The complex micromechanical response of the rough surfaces in contact. 31

2.14 The frictional strength emerges from the micromechanical interlocking of asperities along the rough surfaces. Three behaviors were suggested in the literature: a) Coulomb's geometrical interpretation: Rigid uplifting along the contacting plane forming at an angle θ_s. b) Brittle fracture of the contacting apexes predicted by Byerlee [4]. c) Gradual plastic smoothing of the microcontact junction pictured by Bowden and Tabor [5]. 33

2.15 The different kinds of friction laws existing in the literature. a) Amontons-Coulomb friction law (Equation 2.84). b) The slip-weakening law (Equation 2.93). c) The rate-and-state friction law (Equation 2.87). 35

3.1 The exponential (**Left**) and linear-decreasing (**Right**) cohesive laws adopted in this manuscript. In the cohesive approaches of fracture, the amplitude of the tractions carried across the interface progressively drops to zero (i.e. free surface conditions) as a function of crack opening displacement δ. Consequently, the crack tip is not singular but smeared over a finite distance, the fracture process zone l_{pz}. Throughout the manuscript, this framework is equivalently applied to study each fracture mode, as well as mixed mode conditions. 40

3.2 Convolution kernels entering the spectral formulation $H_{ij}(T)$ for $\nu = 0.35$. . . . 43

3.3 Typical elastodynamic boundary value problem solved following a finite-element method. The continuum contains a crack surface Ω_c (in red), whose discretization and representation using a cohesive element is detailed. 46

4.1 Geometry of the dynamic fracture problem. 52

4.2 Space-time diagram of a dynamic debonding between Aluminum and Homalite for $\psi = 75°$. The black regions correspond to intact portions of the interface, the red areas indicate the cohesive zones, the yellow regions are traction-free and the white regions correspond to the contact zones. Squares highlight measurement points for which the propagation speed is reported in Figure 4.8. 57

4.3 Evolution over time of the propagation speed of the cohesive and contact zones for the left (a) and right (b) debonding path under $\psi = 75°$. 58

4.4 Evolution of the cohesive strength, normal and shear tractions and displacement jumps at $x/X = 0.25$ (a) and at $x/X = 0.75$ (b) with $\psi = 75°$. 58

4.5 Evolution of the effective fracture energy and its different components, i.e. the dissipation by friction Γ_f and by tensile Γ_n and shear Γ_s debonding, for the left (dashed lines) and right (full lines) paths with $\psi = 75°$. 60

4.6 Space-time diagram of dynamic debonding between Aluminum and Homalite for $\psi = 50°$ illustrating subsonic/intersonic transition for both directions. (Colour code as in Figure 4.2). 60

4.7 Evolution of the propagation speed of the cohesive and contact zones for the left (a) and right (b) debonding path under $\psi = 50°$. 61

4.8 Influence of ψ on the propagation speed v. As illustrated in Figure 4.2, red squares show the propagation velocities reached at the end of the simulation, blue squares the speeds when a contact area appears behind the crack tip and green squares the speeds when the contact zone detaches from the crack tip. The vertical gray bars highlight crack velocities where the contact zone is trailing the crack tip. The vertical dashed line represents the abscissa of Figure 4.9. . . . 62

4.9 Histogram of the crack velocities as function of the distance traveled for $\psi = 50°$ on the left side showing the existence of a forbidden velocity regime between c_R^H and $\sqrt{2}c_s^H$. The abscissa of the histogram corresponds to the dashed line in Figure 4.8. 62

4.10 Normal and shear stress profiles at $t = 0.48\ c_s^{Al}\, t/X$ along the interface for $\psi = 0°$ and $\psi = 90°$. Along bimaterial interfaces, mixed-mode stress fields at the crack tip are observed even under pure tensile and shear far-field loadings. 63

4.11 Normal and shear stress profiles along the interface for subsonic ($t = 0.07\ c_s^{Al}\, t/X$) and intersonic ($t = 0.62\ c_s^{Al}\, t/X$) crack growth under $\psi = 50°$. 64

4.12 Evolution of the ratio of energy dissipated by mode I failure over the total energy dissipated in cohesive zones as function of the crack velocity for different values of ψ, at the left (green) and right (red) crack fronts. 64

4.13 Evolution of the propagation speed of the cohesive and contact zones of the right front at a bimaterial interface with (a) $E^+/E^H = 1.5$ and (b) $E^+/E^H = 4$. . . 66

4.14 Space-time diagram of dynamic debonding along a $E^+/E^H = 2.5$ interface under $\psi = 75°$ showing contact behavior related to the top and bottom wave speeds. (Colour code as in Figure 4.2). 67

5.1 Geometry of the in-plane heterogeneous fracture problem. A crack of length L is inserted along an interface with constant macroscopic fracture energy G_c^H at rest under an uniform shear loading τ^0. The interface is made of a homogeneous portion L_{hom} and a region with a heterogeneous fracture energy L_{het} in form of alternately weaker (yellow)/tougher (orange) stripes of constant width w. . . . 72

5.2 Space-time diagrams of two macroscopically equivalent dynamic fracture events where the normalized slip velocity $\dot{\delta}_x/c_s$ is shown using the same color scale while the crack tip position at $L_1 = 5L_c$ and $L_2 = 20L_c$ is highlighted with cyan stars. In (a) the crack grows on a perfectly homogeneous interface, while in (b) the rupture front interacts with smaller-scale heterogeneities. 73

5.3 Effect of heterogeneities on the supershear transition. Color curves trace the observed boundary between sub-Rayleigh and supershear regimes for different loading conditions (seismic ratio) and toughness distribution. The dashed arrow draws the trajectory of ruptures of Fig. 5.2 where the crack is initially in the sub-Rayleigh regime (cyan star at $L_1 = 5L_c$) and grows toward a size (cyan star at $L_2 = 20L_c$) where it either crosses the boundary toward supershear regime (as in the interface of Fig. 5.2b with $w = 0.6L_c$), or not (as in the homogeneous interface of Fig. 5.2a). The dark blue star shows the maximum seismic ratio allowing supershear crack in homogeneous plane strains interface [6, 7]. 74

5.4 The process zone size is the length scale controlling crack front interaction with heterogeneities. For $v = 0.5c_s$ and a fracture energy ratio of 3.5, colors in plots (b-d) divide broken surface (sky-blue), cohesive zone (blue) and intact interface which is either dark blue (average properties), yellow (weaker properties) or orange (tougher properties).(a) Normalized increase of slip velocity as function of interface heterogeneity, namely asperity size and fracture energy ratio for $v = 0.5c_s$. (b) Asperities are much smaller than l_{pz} leading to quasi-homogeneous dynamics. (c) Collective interaction between depinning events when w is in the range of l_{pz} leading to a significant impact on rupture dynamics. (d) When the asperities are much larger than l_{pz}, the material is macroscopically heterogeneous. 76

5.5 Faster crack fronts interact with smaller heterogeneities. The main plot details how the process zone size contracts as the crack accelerates toward c_R. Cyan dots show simulation data compared with the theoretical prediction in yellow (details are provided in Section 5.7). The inset shows the increase of slip velocity as function of asperity size for $G_c^{\text{strong}}/G_c^{\text{weak}} = 3.5$ and different crack speeds using $l_{pz}(v)$ for normalization to collapse data. 77

5.6 Space-time diagrams of the two macroscopically equivalent dynamic fracture events described in Figures 5.2a-b. The color code is the same as in Figures 5.4b-d. 79

5.7 Increase in slip velocity associated with the interaction of a dynamic crack growing at $v = 0.5c_s$ with a heterogeneous microstructure of a given asperity size and fracture energy ratio. Figure 5.4a presents the same data after normalization by the process zone size. 79

6.1 A supershear burst occurs at the cusp located at the center of the crack front line $z = 1.25L_c$. a) Evolution of the crack front line (in red) captured at regular time interval. b) Space-time diagram of the rupture event along $z = 1.25L_c$. Colors divide broken surface (yellow), cohesive zone (red) and intact interface which is either black (homogeneous properties) or white (tougher asperity). c) Evolution of crack front velocity along $z = 1.25L_c$. The dashed black line depicts the Rayleigh wave speed. 84

6.2 Typical crack tip dynamics observed along a homogeneous fracture plane. The dashed line highlights the Rayleigh wave speed. 86

6.3 The supershear burst arises exclusively at the cusp emerging along the front at $z = Z/2$. Evolution of the crack front velocity v_x/c_s in the x-direction (a) and in the direction normal to the crack front v_n/c_s (b) computed along the interface for $z < Z/2$ and $z > Z/2$. The color map is scaled between the minimum and maximum values verifying the supershear range of the apparent forward velocity v_x and the sub-Rayleigh range of the normal crack speed v_n ($c_R \cong 0.934c_s$) predicted by LEFM for smooth crack front. 87

6.4 Schematic representation of a kinked crack front, with $\boldsymbol{n}$ denoting the unit normal at (z, t). 88

6.5 Amplitude of the front perturbation required to observe $v_x > c_R$ at the center point as function of the incident crack speed v. The dashed lines highlight the required amplitude for each of the three different crack speeds considered in the parametric study presented in Figure 6.6. 89

6.6 Maximum crack front deflection a_0 observed for various asperity toughnesses and three different values of the incident crack speed v/c_s. The deflection of the crack front interacting with the tougher asperity either creates a supershear burst (star symbols) or not (round symbols). From the geometrical model (cf. Equation 6.7 and Figure 6.5), this observed transition is predicted to occur at a given crack front deflection, which depends on the incident crack speed and is depicted by the horizontal dashed lines. 90

6.7 Portion of the crack front moving with a forward velocity $v_x > c_R$. The dashed blue line emphasizes the expected portion for the reference case presented in Figure 6.3, while the value $a_0/Z = 0.371$ is read from Figure 6.6 ($v = 0.6c_s$ and $\zeta = 3$). 91

6.8 The supershear burst creates shock waves driving energy far from the asperity site. a) Snapshot of crack opening velocity field $\dot{\delta}_n$ following the failure of the asperity whose position is highlighted by the white dashed circle. The colored stars denote the positions at which the time-evolution of $\dot{\delta}_n$ is computed and presented in (b) and (c). b) Evolution of $\dot{\delta}_n$ observed at the different positions highlighted in (a). The strong surface waves caused by the rupture of the asperity are visible after the initial peak characteristic of the rupture front. c) Zoom in $\dot{\delta}_n$ history (dotted rectangle in (b)) emphasizing first the trace leaved by the persistent “triangular” shock wave, sharply followed by the decaying “circular” front. The black curves correspond to additional sampling points located between the red and cyan positions. 92

7.1 Geometry of the studied problem. The inset presents the schematic shear stress σ_{xy} profile predicted by LEFM at a distance r from the crack tip. Dissipative zone (I) at the immediate vicinity of the tip. Far from the dissipative zone (II), σ_{xy} is dominated by the square root singularity. Further away from the tip (III), the non-singular contributions dominate the profile of σ_{xy} which converges toward the far-field stress conditions. Our work aims at describing how tiny perturbations only visible at the scale of (I) have a direct impact on the onset of rupture fronts. 97

7.2 Elastodynamic solution under intact interface conditions. The dynamic fields are mediated by the vertical propagation of a shear wave front. $t^* = h/c_s$ is the time needed by the front to travel between the top and bottom surfaces and $n \in \mathbb{N}$ is the total number of reflections observed at the top boundary. 99

7.3 Exponential cohesive law given in Equation 7.4 and derived from a Rose-Ferrante-Smith [8] type of universal binding potential. 100

7.4 The ratio of the process zone size to the length of the resisting junction mediates the work required to initiate sliding. (a) and (b) present two typical time evolutions of the energetic quantities prior to the rupture onsets, which occur, respectively, at $t = 92t^*$ and $t = 35t^*$. The two events shared the same elastic properties and $G_c = 4\langle G_c \rangle$, but their respective interface cohesive laws lead to $l_{pz}/(l - w_0) = 3.5 \cdot 10^{-2}$ and $l_{pz}/(l - w_0) = 3.5$. The latter are highlighted on the associated shear stress profiles presented for the two interfaces before the onset of sliding (the colors of each stress profile are scaled between zero and the respective values of τ_c). The dashed lines in (a) and (b) describe the theoretical build-up of elastic strain energy expected for intact interface conditions according to the dynamics presented in Figure 7.2. (c) Normalized external work required to initiate sliding between the two bodies as function of the ratio between the process zone size l_{pz} and the resisting junction size $(l - w_0)$ for different types of interface properties and geometries. 103

7.5 Process zones smaller than w magnify the properties of the heterogeneous microcontacts, which are averaged in the case of larger process zone sizes. The colored circles present the results of two types of interfaces characterized by the same average rupture energy $\langle G_c \rangle$. Since $l_{pz}^{A,B} << l - w_0$, the two interfaces require a similar amount of work to start sliding when the strength is homogeneously distributed along the interface (blue circles). However, the two values of W_Δ^* significantly diverge in presence of heterogeneous microcontacts with a characteristic size w standing in between l_{pz}^A and l_{pz}^B (red circles). The grey circles recall the data presented in Figure 7.4c. 104

7.6 Zooms at the tip of the critical junction ($x = w_0$) revealing the shear stress profile existing just before the onset of sliding for interfaces A and B. An artificial vertical displacement $\left(u_y(x, y) = u_x(x, y)\right)$ is applied to help visualizing the slip profile along the interface. The cohesive strength existing between the top and bottom surfaces is depicted with a gradation from black ($\tau^{\text{str}} = \tau_c$) to white ($\tau^{\text{str}} = 0$). (**Left**) For interface A, the shear stress and slip localize at the edge of the critical junction, magnifying its toughness. (**Right**) Along interface B, several microcontact junctions start slipping and damaging within the larger process zone. The sketches located in the top right of the plots associate these two distinct situations to the typical failure behaviors of microcontact junctions discussed in Figure 2.14. 105

7.7 At a distance from the interface the evolutions of the dynamic stress fields observed macroscopically during the rupture of the heterogeneous interfaces A (top) and B (bottom) comply with LEFM predictions for an interface fracture energy corresponding to $\langle G_c \rangle$. On the left panels, shear stress at the vicinity of the propagating slip front is mapped using the same color scale. To mimic the experimental measurements, the white lines highlight the position along which the components of the Cauchy stress tensor are presented on the right panels in red. LEFM stress fields, which are presented in Section 2.2, are plotted in blue for a fracture energy equal to $\langle G_c \rangle$. Note that the "bump" visible in the simulation profiles of σ_{xy} is expected and is caused by a shear wave propagating ahead of accelerating shear cracks. This phenomenon is discussed in details in [9]. . . . 106

8.1 Space-time diagram of the dynamic mode III rupture event whose colors divide broken surface (yellow), fracture process zone (red) and intact interface (black). The blue line highlights the instant at which snapshots of the stress and sliding velocity are presented in Figure 8.2. (**Inset**) Evolution of the rupture speed as function of the crack size. 116

8.2 Stress and velocity concentration observed in the neighborhood of the left-propagating crack tip at $t = 2c_s/L_c$ (corresponding to the cyan line in Figure 8.1). The red area highlights the fracture process zone. 117

8.3 (**Left**) Asymptotic contribution mapping the stress and velocity fields presented in Figure 8.2. (**Right**) Dynamic energy balance computed during crack propagation from the fracture energy $\dot{E}_{\text{diss}}/v_c$ (Equation 8.18), whose value G_c is prescribed in the slip-weakening model, and the energy release rate G (Equation 8.22). See the main text for an explanation of the differences between G, G^v and G^τ. The dashed gray lines are guide to the eyes highlighting the ±25% precision. 119

8.4 Evolution of the friction coefficient observed under homogeneous steady-state sliding conditions. For a given loading ratio $\tau^0/\sigma^0 = 0.36$ (dashed black line), two equilibrium states exist, one at low slip rate on the velocity-weakening branch v_w and one at high slip rate on the velocity-strengthening branch v_s. The dashed blue line and its associated green star highlight the evolution of $c_f(v^{\mathrm{ss}})$ accounting for inertial effects (see the main text for the detailed explanation). . 120

8.5 Evolution of the maximum sliding velocity observed during the destabilization of an interface initially sliding uniformly at v_w. $t < t_1$: the perturbation grows following a linear instability regime (cf. Equation 8.28). $t_1 < t < t_2$: two rupture fronts are propagating along the contact plane. $t > t_2$: rupture fronts have broken the entire interface which progressively converges toward a new steady-state at v_s.121

8.6 Typical profiles of interface fields (v,τ_z,ϕ) observed during the three stages of the onset of sliding discussed in Figure 8.5, respectively in blue for $t < t_1$, in red for $t_1 < t < t_2$ and in green for $t > t_2$. 123

8.7 (**Left**) Zoom into the stress and velocity profiles observed at the vicinity of the leftward propagating rupture front.(**Right**) Evolution of the propagation speed. 124

8.8 (**Left**) Shear stress and velocity drops observed at the vicinity of a slip front are mapped by the asymptotic contribution described in Equations 8.29 and 8.30. (**Right**). The stress intensity factor emerging from this mapping is used to compute the elastic energy released rate, similarly as in Figure 8.3. However, the vertical axes are conversely displayed with units to emphasize that no intrinsic value of interface strength τ_c or energy G_c are prescribed with the rate-and-state formulation. 125

8.9 (**Left**) Archetype evolution of the sliding velocity tailored to illustrate the frictional response of the rate-and-state interface at the vicinity of a rupture front. (**Right**) Evolution of the real contact area computed from Equation 8.33 with the evolution law described in Equations 8.13 and 8.38. The red area corresponds to the direct effect, during which the total contact area is reduced by the slip acceleration. At the end of this phase, the real contact area reaches a minimum value and starts to progressively rebuild over a longer time scale highlighted by the yellow area. 126

8.10 (**Left**) The equivalent process zone described by the red area is outlined by the evolution of $v\phi/D$ which indicates the portion of the interface where the rupture is currently reducing the real contact area. (**Right**). Validation of the energy balance resulting from the mapping of the asymptotic fields presented in Figure 8.8 and the integration of the equivalent fracture energy from Equation 8.32. . . 127

8.11 (**Left**) Equivalent fracture energy measured for slip fronts moving under different interface conditions. The rate-and-state parameters are unchanged, while we investigate different bulk properties (dashed lines represent setups with μ being 10 times smaller), various far-field loadings (τ^0), including a mode II setup ($\tau^0 = 1.015\tau_{\min}$). $\tau_{\min}$ represents the minimum loading for which a steady-state sliding solution exists (i.e. the minimum of the steady-state curve of Figure 8.4.) (**Right**). Verification of the energy balance for the different setups presented in the left plot using the same color code. 128

8.12 Steady-state evolution of the friction coefficient observed for four different types of rate-and-state formulations. The blue curve represents the standard formulation used in this work (Equation 8.12). The same formulation is used with the parameters given in Table 8.2 (yellow curve). The green curve is the original Dieterich-Ruina formulation (Equation 8.35) and the red curve describes the "N-shaped" formulation given by Equation 8.37. 129

8.13 Equivalent fracture energy versus rupture speed (**Left**) and energy balance (**Right**) computed for a large variety of slip fronts, emerging from different rate-and-state formulations, whose steady-state behaviors can be visualized in Figure 8.12. The standard formulation used in this manuscript is shown in blue for the aging evolution law and in cyan for the slip law. A slow rupture front (yellow) is simulated and studied using the set of parameters given in Table 8.2, while the behavior of interfaces following the original Dieterich-Ruina formulation is depicted in green. Unstable slip pulses nucleated from the N-shaped formulation of Equation 8.37 is plotted in red. The upside-down triangles in the inset of the right plot highlight the analytical predictions of G_c discussed in the main text. (Note that the vertical coordinate of these triangles is meaningless and arbitrarily chosen for the visualization.) 133

8.14 Traction versus slip evolution observed along the interface at the position $x/X = 0.4$ during the rupture event detailed in Figure 8.6. The red area corresponds to the equivalent fracture energy driving the slip front propagation. (**Left inset**) Zoom in the traction versus slip evolution. (**Right inset**) Evolution of the breakdown and equivalent fracture energy computed at four different interface locations. The latter is dissipated during shorter time scales, concurrent to the arrival of the rupture front and, therefore, represents a small portion of the total breakdown energy. 135

8.15 A shear front traveling ahead of an accelerating mode II crack creates a "bump" in the shear stress profile, which slightly impacts the mapping of the stress intensity factors and, therefore, the value of G and G^{τ}. The plots are the mode II equivalent of Figure 8.10. 137

9.1 Simulations snapshots of the propagation of a tensile crack along a heterogeneous rupture plane made of circular asperities of different radius (blue being weaker and red tougher heterogeneities). Two regimes exist as a function of the ratio of the asperity radius to the process zone size. (**Left**) Asperities much larger than the process zone distort the front line in agreement with the predictions of line tension models. (**Right**) At the scale of the fracture process zone, crack growth occurs through the nucleation and coalescence of microcracks from the locations of weaker asperities. The front is moving rightward, with colors dividing broken surface (cyan), cohesive zone (blue), and intact portion of the interface (dark blue). 141

List of Tables

2.1 Summary of the admissible crack speeds predicted by LEFM. 27

4.1 Material properties. 54

8.1 Typical PMMA material parameters used in the simulations. 115
8.2 Interface parameters leading to the steady-state behavior depicted by the yellow curve in Figure 8.12. 130

1 Introduction

1.1 Motivation

Stephen Hawking (1942-2018) once stated that “one of the basic rules of the universe is that nothing is perfect. Perfection simply doesn’t exist. Without imperfection, neither you nor I would exist”. In the context of materials and structures, defects are indeed ubiquitous and fracture mechanics can hence be understood as the science of dealing with flaws.

About a century ago, Griffith [10] studied how the apparent strength of materials is mediated by the inherent presence of microscopic flaws. Stresses concentrate around flaws, which start growing, merging and finally lead to premature material failure, for loadings significantly lower than the theoretical strength of a perfectly sane material. He further proposed a thermodynamic criterion to predict the stability of flaws: a crack grows if the energy released by its advance is sufficient to balance the cost of the resulting surfaces creation. Later, Irwin [1] derived a relation for estimating the release of elastic energy for any crack geometry using the universal asymptotic stress fields existing at the immediate vicinity of a crack tip.

The works of Griffith and Irwin became the keystones of Linear Elastic Fracture Mechanics (LEFM). The power of LEFM relies on the *autonomy principle*, according to which the crack growth is entirely controlled by the linear elastic stress singularity, as long as every nonlinear dissipative process associated to fracture is confined within a region of negligible size. The diverse and complex phenomena involved in fracture are hence buried within this so-called *fracture process zone* and characterized by a constant value, the *fracture energy*, which can be determined through standardized experiments. As a result, LEFM became a well-established theory, successfully applied to predict the stability of flaws in materials and structures.

Consequently, the LEFM approach was extended to the description of cracks out of equilibrium, i.e. to dynamic fracture. While LEFM is used to predict if an existing crack will grow, the dynamic fracture theory aims at describing how a crack is propagating, at which speed, with which energy budget. The subsequent dynamic fracture experiments confirmed the predictions of this dynamic theory for slowly propagating cracks. However, they revealed how the dynamics of fast ruptures (with crack speeds exceeding a few tenths of the material shear wave speed) diverges from the theoretical predictions.

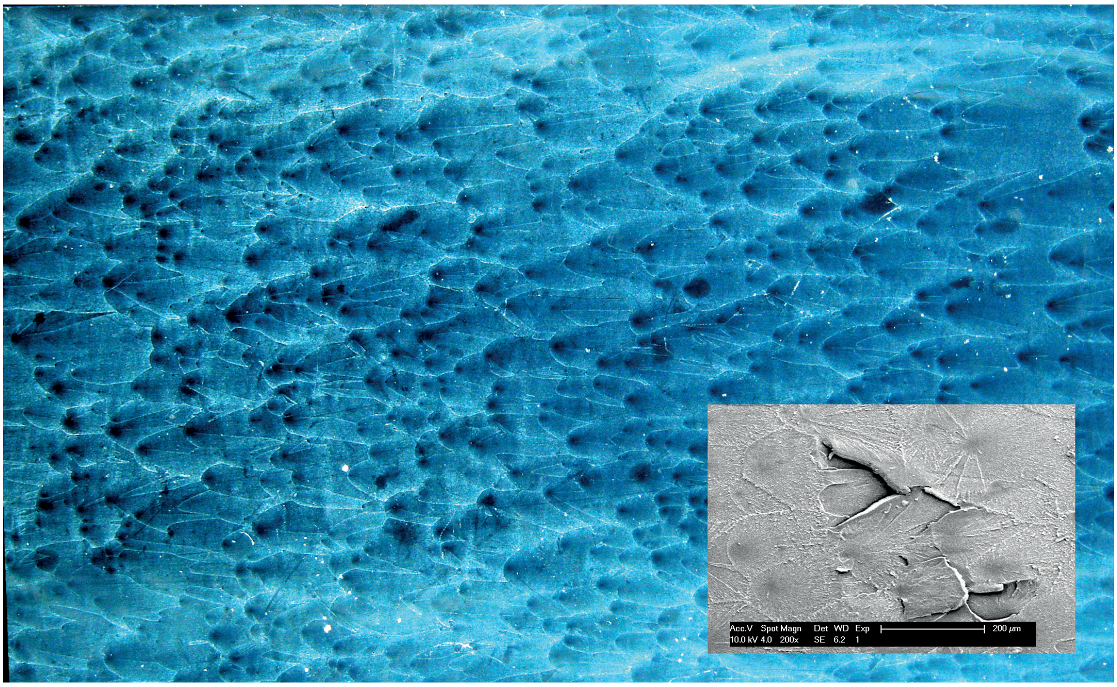

Figure 1.1 – The fast rupture of a brittle material creates particularly rough fracture surfaces. Microscope image (millimeter scale) of the fracture surface created by a fast dynamic crack in PMMA (acrylic glass). **(Inset)** Zoom (hundreds of micrometers) in the fracture surface using scanning electron microscopy revealing the onset of an out-of-plane microbranch appearing in the middle of in-plane conic marks. Courtesy of Alizée Dubois.

The observed divergence between theory and experiments coincides with the onset of microscopic instabilities occurring at the crack tip. Indeed, visualizations of the crack surface after failure (*post-mortem*) revealed the appearance of microscopic surface marks as the rupture speed exceeds a characteristic velocity (cf. Figure 1.1). Therefore, a fast crack propagating within a nominally brittle material stops having a simple sharp tip but becomes a smeared rupture front interplaying with material heterogeneities. As the crack speed keeps increasing, microbranches start to grow out of the rupture plane before a macroscopic branching event arises and splits the rupture front into two or several sub-branches. In this context, understanding the interplay between a dynamic crack front and heterogeneities is paramount to gain insights on the origin of these dynamic instabilities reported along various brittle materials. In addition, several recent studies revealed how a significant gain in fracture toughness can be achieved using a heterogeneous microstructure [11]. A fascinating biological example of this toughening mechanism was found in the nacre of mollusks shell, whose fracture energy is 3000 times higher than the raw material it is made of [12]. In the recent context of micro-architected metamaterials [13, 14], a deeper understanding of the interplay between cracks and heterogeneous microstructures will open new prospects in the design of materials capable of impeding dynamic crack growth.

Crack propagation along a heterogeneous rupture plane is typically studied following Rice's perturbation analysis [2]. In this first-order approach, a crack is viewed as an elastic line whose distortion by asperities locally increases the stress intensity factor up to values sufficiently large to overpass them. This so-called *line tension* approach, whose dynamic extension was derived by Willis and Movchan [15], was built on two restrictive hypotheses: A crack front is described as a line (i.e. infinitesimal fracture process zone), whose distortions should remain small (first-order approximation). The dynamic interactions, arising during a fast crack propagation, occur however at scales, where the fracture process zone is smeared over a finite length. In this context, modern numerical approaches offer a great alternative to bypass the limitations of line tension models and bring new insights on the interactions existing at the scale of the fracture process zone. However, capturing the fine spatio-temporal scales characterizing these microscopic heterogeneous processes requires an exceptionally fine description of the rupture plane, unattainable with conventional numerical approaches.

Finally, several mechanical systems are controlled by a similar interplay between the long-range elastodynamics driving a rupture front and the local heterogeneous microstructure. Examples of such systems include landslides, snow avalanches or crustal earthquakes. In the latter, the resistance to shear results from the scattered contact profile emerging when two rough surfaces are brought into contact. In this context, the computational framework developed and implemented in the context of dynamic fracture can equivalently be applied to the problem of frictional interfaces, for which the macro- and microscopic aspects of friction were typically described in the literature following two distinct and complementary approaches.

1.2 Objectives

The main objective of this work consists in systematically investigating the effect of heterogeneities on dynamic crack propagation, from the macroscopic scale down to the fracture process zone scale. This thesis particularly aims at probing crack dynamics beyond the assumptions of the standard LEFM solutions. Therefore, this work relies on the implementation of efficient numerical methods. In light of these global objectives, below is a set of important questions that this thesis addresses:

- **Homogenization**/ Which conditions legitimate the homogenization of microscopic properties? What are the characteristic scales controlling the transition from quasi-homogeneous to heterogeneous rupture dynamics?
- **Elastic radiation**/ How does the presence of heterogeneities affect the radiation of elastic waves by the propagating rupture?
- **Rupture speed**/ Why do dynamic instabilities/surface marks reported in experiments

initiate at precise velocities and progressively increase with crack speed? What is the effect of heterogeneities on the crack propagation speed?

- **Large front distortions**/ What is the outcome of a large distortion of the crack front in presence of heterogeneities?

- **Multicontact interfaces**/ How does the heterogeneous topography existing for two rough surfaces in contact interplay with the macroscopic propagation of slip fronts along frictional interfaces?

The leitmotiv of this work is therefore the investigation of systems governed by the permanent competition between the long-range elastodynamics and the heterogeneous strength profile existing locally at the microscopic scale.

1.3 Approach

The objectives stated above require an efficient elastodynamic model providing a particularly fine description of the rupture plane. Therefore, the present work relies on a boundary integral formulation [16, 17] of elastodynamics, for which the numerical discretization is concentrated along the interface bonding two semi-infinite half spaces. Moreover, this particular setup eases the comparison with the standard LEFM solutions derived under the same infinite boundary conditions. The finite-element method [18, 19] is also occasionally used in this work to account for finite size boundary conditions.

A non-singular description of fracture is needed in order to study the impact of the fracture process zone. To this aim, a cohesive zone model [20, 21] is adopted in this work together with the elastodynamic models. In this well-established approach, the material strength takes a finite value which progressively drops as the crack opens, which leads to a finite process zone size. Moreover, the cohesive approach corresponds to a local description of fracture, easily tunable to account for heterogeneous interface properties. In the final part of this manuscript, the standard cohesive law will be replaced by rate-and-state formulations [22, 23] describing the complex frictional response of multicontact interfaces existing between two rough surfaces.

In this manuscript, the description of different kinds of heterogeneities possibly existing along rupture planes are systematically investigated. This includes the mismatch of elastic properties across the rupture plane, the local variations of the fracture toughness and the pinning of the crack front by a tougher asperity. Finally the impact of a rough contact profile on the nucleation and propagation of slip fronts at the onset of frictional slip will be studied using different approaches.

The simulations reported in this manuscript rely on my own parallel implementation of the numerical method deployed on the high performance computing infrastructure of EPFL[1].

1.4 Outline of chapters

This Ph.D. dissertation is structured in nine different chapters which are briefly presented below:

- **Chapter 2 - State of the art**
  This chapter introduces the key concepts and derivations of continuum solid mechanics and dynamic fracture mechanics, which define the theoretical framework supporting this research. Their implications as well as the open challenges in the context of rapid failure of brittle materials and of the onset of sliding along frictional interfaces are then reviewed and discussed.

- **Chapter 3 - Numerical framework**
  This thesis uses two “homemade” implementations solving the elastodynamic fracture problems, whose main concepts and formulations are introduced in this chapter. The boundary integral formulation provides an unprecedented level of discretization along the rupture plane, essential to describe phenomena at the scale of the process zone. The finite-element method allows to represent the realistic finite-size geometry of the problem, but at a larger cost. Finally, in these two elastodynamic models, the interface behavior is represented following a cohesive description of fracture.

- **Chapter 4 - Dynamic fracture along bimaterial interfaces**
  The elastic mismatch across the fracture plane is the first kind of heterogeneity studied in this thesis. The resulting bimaterial interfaces are frequently encountered in composite and laminate materials as well as along geological layers. It will be shown that these inhomogeneous interface conditions lead to dynamic instabilities. In the case of mixed shear and tensile fracture, these instabilities take the form of large scale contact zones emerging in the wake of the rupture front. The theoretical range of admissible crack speeds is extended and generalized to the case of bimaterial interfaces, which is then directly used to rationalize the origins of these observed instabilities.

- **Chapter 5 - Interplay between process zone and material heterogeneities**
  This chapter studies the impact of heterogeneities in terms of fracture energy. A two-dimensional plane strain setup is assumed and prevents any crack front distortion. Local variations of the fracture energy around its mean value are described in the form of alternate weaker and stronger patches. This study reveals how these local variations can have a strong impact on rupture dynamics. In the context of shear cracks, these heterogeneities significantly promote crack front propagation at a speed faster than the shear waves (supershear rupture fronts), which finds direct implications in the context

---

[1] https://scitas.epfl.ch/

of earthquakes dynamics. This study further emphasizes how the fracture process zone is the characteristic length scale controlling the transition from quasi-homogeneous to heterogeneous fracture. Finally, this chapter discusses how the observed relativistic process zone contraction brings faster crack fronts to interact with smaller details of the microstructure.

- **Chapter 6 - Supershear bursts in the propagation of tensile crack**
  This chapter investigates the distortion of a rupture front in the presence of a circular asperity, beyond the small distortions assumed in first-order models. For the first time, this study reveals how supershear bursts can also arise during tensile failure and how they are triggered by heterogeneities. These supershear episodes emerge at discontinuities resulting from strong crack front distortions, which are assumed to frequently occur during dynamic instabilities due to the interaction with the microstructure or the formation of microbranches. Finally, this work shows how these short-lived events create persistent shock waves capable of perturbing the front dynamics far from the asperity site.

- **Chapter 7 - Onset of sliding across scales**
  This chapter investigates the effect of the scattered contact profile existing at the scale of surface roughness on the onset of frictional sliding. The complex contact topography existing at smaller scales is explicitly modeled as an idealized array of junctions and valleys. The resulting microcontact junctions typically break via two distinct mechanisms: the yielding of the contact junction or via brittle crack-like rupture. This study presents how a cohesive law representative of the micro-mechanical response of contact junctions is able to account for these two failure mechanisms and how the observed transition is controlled by the process zone. Furthermore, this chapter studies the direct impacts of these different microscopic mechanisms on the macroscopic strength of the interface measured at the onset of sliding. This work finally discusses the implications of this transition arising at the scale of the surface roughness in relation with the unexpected response of some lubricated interfaces presenting a tougher behavior than equivalent interfaces but dry [24].

- **Chapter 8 - On the rupture dynamics of laboratory-derived friction laws**
  In this second chapter about frictional interfaces, the complex behavior of the underlying microcontacts is implicitly represented by a constitutive friction law derived from laboratory experiments, also known as a *rate-and-state* friction law. Grounded on the formalism of dynamic fracture, this chapter presents the energy balance driving the rupture fronts nucleating and propagating along interfaces described by rate-and-state formulations. This work culminates in a discussion of the equivalent fracture energy and its actual contribution in the energetic budget of earthquakes.

- **Chapter 9 - Conclusion**
  This manuscript concludes with a summary of the main results and a discussion about the future prospects it opens.

2 State of the art

Materials break as a result of different processes arising across several length scales, from the rupture of the atomic bonds toward cracks propagation within the macroscopic structures. As a result, fracture mechanics was studied in the literature using various modeling approaches grounded on different descriptions of solid matter. This thesis focuses on fracture aspects at large scales (micro- to macroscale), where the long range elastodynamics is the main carrier of crack propagation. Other kinds of models exist at much smaller scales (nanoscale) and account for the discrete nature of matter. These *atomistic* aspects of fracture will not be discussed in this manuscript, but the reader is redirected to [25] for a broad presentation of this topic. The bulk behavior is hence described within the framework of *continuum solid mechanics*. After presenting some key concepts of continuum mechanics and elastodynamics, the LEFM theory and its dynamic extension are introduced. Heterogeneous fracture models are then discussed in light of the experimental validations of the dynamic fracture theory. The macroscopic description of solid friction is finally presented and linked to the framework of the dynamic rupture of heterogeneous interfaces.

2.1 Continuum solid mechanics

Continuum solid mechanics represents a well-established theoretical framework mainly developed during the 19th century and describing the displacement of a macroscopic deformable solid under the action of forces. The fundamentals of this broad topic will be introduced in this chapter, inspired from the detailed description existing in reference textbooks [26–28].

Depending on the problem of interest (small versus large deformations, linear versus nonlinear material behaviors, etc.), different formulations were proposed in the literature, but rest upon the same three ingredients:

1. Conservation principles controlling the balance of momentum through the solid.

2. The kinematics describing the geometric changes of a deformable solid.

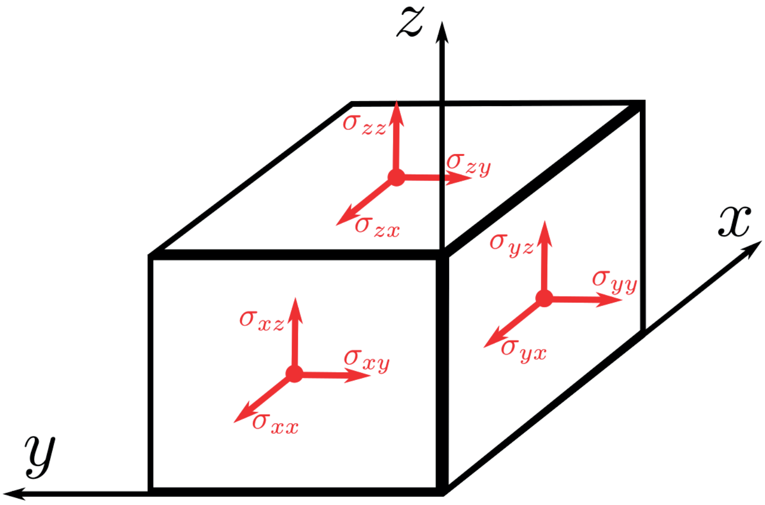

Figure 2.1 – Stresses existing at the surfaces of an elementary block of matter of size $dx\,dy\,dz$. This concept is only valid for a large scale description of solids, far from the discrete nature of matter existing at the atomistic length scales.

3. The constitutive laws characterizing the material behavior and bridging the two first work-conjugated ingredients.

2.1.1 Conservation laws

Conservation laws are typically derived on an elementary block of matter studied within a Cartesian frame of reference as presented in Figure 2.1. The sum of forces $\boldsymbol{P}^{\text{ext}}$ acting at its surfaces should obey Newton's[1] second law:

$$\sum \boldsymbol{P}^{\text{ext}}(t) = \rho \ddot{\boldsymbol{u}}(t)\; dx\; dy\; dz, \tag{2.1}$$

with $\ddot{\boldsymbol{u}}$ being the acceleration vector and ρ the volumetric solid mass density. In this context, the concepts of *stress* and *traction* are introduced and represent the transmitted forces $\Delta\boldsymbol{P}$ across a sufficiently small surface area ΔA:

$$\boldsymbol{\tau} = \lim_{\Delta A \to 0} \frac{\Delta \boldsymbol{P}}{\Delta A}. \tag{2.2}$$

The term *traction* is often associated to an external force acting at the solid surface, while *stress* refers to the transmission of an inner force. From the action-reaction principle (Newton's third law), Cauchy[2] stated that the stresses/tractions acting on the two sides of a surface are equal and opposite. The tractions and stresses acting on a surface defined by the normal vector $\boldsymbol{n}$

---

[1] Isaac Newton (1642-1727)

[2] Augustin-Louis Cauchy (1789-1857)

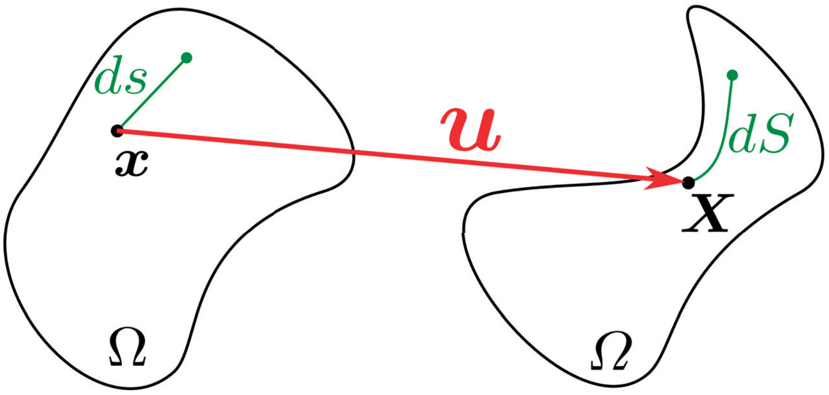

Figure 2.2 – Kinematics of a deformable solid from its original Ω to its deformed $\mathit{\Omega}$ configuration.

are related according to

$$\boldsymbol{\tau} = \underline{\boldsymbol{\sigma}}\,\boldsymbol{n}. \tag{2.3}$$

The second-order tensor $\underline{\boldsymbol{\sigma}}$ is named *Cauchy stress tensor* and is defined such that its component σ_{ij} corresponds to the stress acting in the j direction through a surface normal to the i direction (cf. Figure 2.1).

In this framework, the conservation of momentum (in absence of body force) of an elementary block of solid matter is written in the three directions as:

$$\begin{aligned}
&\frac{\partial \sigma_{xx}}{\partial x} + \frac{\partial \sigma_{yx}}{\partial y} + \frac{\partial \sigma_{zx}}{\partial z} = \rho \ddot{u}_x \\
&\frac{\partial \sigma_{xy}}{\partial x} + \frac{\partial \sigma_{yy}}{\partial y} + \frac{\partial \sigma_{zy}}{\partial z} = \rho \ddot{u}_y \\
&\frac{\partial \sigma_{xz}}{\partial x} + \frac{\partial \sigma_{yz}}{\partial y} + \frac{\partial \sigma_{zz}}{\partial z} = \rho \ddot{u}_z.
\end{aligned} \tag{2.4}$$

The relations above, also known as *Cauchy's equations of motion*, can be expressed in a compact form using the divergence operator ∇:

$$\nabla \cdot \underline{\boldsymbol{\sigma}}(t) = \rho \ddot{\boldsymbol{u}}(t). \tag{2.5}$$

2.1.2 Kinematics

The kinematic study of a deformable solid consists in quantifying the deformation of a body between the current time t and a reference time t^0, as illustrated in Figure 2.2. In this context, the *displacement field* $\boldsymbol{u}(\boldsymbol{x}, t)$ is the function mapping points between the current $\boldsymbol{X}(\boldsymbol{x}, t)$ and the reference configuration $\boldsymbol{x}$:

$$\boldsymbol{X}(\boldsymbol{x}, t) = \boldsymbol{x} + \boldsymbol{u}(\boldsymbol{x}, t). \tag{2.6}$$

The length of an infinitesimal segment $d\boldsymbol{s}$ in the original configuration is defined as

$$ds^2 = dx^2 + dy^2 + dz^2 = d\boldsymbol{x}^\top d\boldsymbol{x}, \tag{2.7}$$

while its length in the deformed configuration dS is given by:

$$dS^2 = dX^2 + dY^2 + dZ^2 = d\boldsymbol{X}^\top d\boldsymbol{X}. \tag{2.8}$$

The differentiation of Equation 2.6 gives

$$\begin{aligned} dX &= dx + \frac{\partial u_x}{\partial x}dx + \frac{\partial u_x}{\partial y}dy + \frac{\partial u_x}{\partial z}dz \\ dY &= dy + \frac{\partial u_y}{\partial x}dx + \frac{\partial u_y}{\partial y}dy + \frac{\partial u_y}{\partial z}dz \\ dZ &= dy + \frac{\partial u_z}{\partial x}dx + \frac{\partial u_z}{\partial y}dy + \frac{\partial u_z}{\partial z}dz, \end{aligned} \tag{2.9}$$

which corresponds to

$$d\boldsymbol{X} = (\underline{\boldsymbol{I}} + \nabla\boldsymbol{u})d\boldsymbol{x} = \underline{\boldsymbol{F}}d\boldsymbol{x}. \tag{2.10}$$

In the equation above, $\underline{\boldsymbol{I}}$ is the identity matrix and $\underline{\boldsymbol{F}}$ is known as the *deformation gradient tensor* and includes both the rigid body translation and its deformations. The former is removed when expressing the extension of the infinitesimal segment:

$$dS^2 - ds^2 = d\boldsymbol{x}^\top \underline{\boldsymbol{F}}^\top \underline{\boldsymbol{F}} d\boldsymbol{x} - d\boldsymbol{x}^\top d\boldsymbol{x} = d\boldsymbol{x}^\top (\underline{\boldsymbol{F}}^\top \underline{\boldsymbol{F}} - \underline{\boldsymbol{I}}) d\boldsymbol{x} = d\boldsymbol{x}^\top (2\underline{\boldsymbol{E}}) d\boldsymbol{x}. \tag{2.11}$$

$\underline{\boldsymbol{E}}$ is called the Green[3]-Lagrange[4] *strain* tensor:

$$\underline{\boldsymbol{E}} = \frac{1}{2}(\underline{\boldsymbol{F}}^\top \underline{\boldsymbol{F}} - \underline{\boldsymbol{I}}) = \frac{1}{2}\Big((\nabla\boldsymbol{u})^\top + \nabla\boldsymbol{u} + (\nabla\boldsymbol{u})^\top \nabla\boldsymbol{u}\Big). \tag{2.12}$$

This thesis investigates the dynamic rupture of nominally brittle materials, for which strains during the rupture are very small $\partial u_i / \partial x_j \ll 1$. The *infinitesimal strain tensor* is hence used:

$$\underline{\boldsymbol{\varepsilon}} = \frac{1}{2}\Big((\nabla\boldsymbol{u})^\top + \nabla\boldsymbol{u}\Big), \tag{2.13}$$

which represents a small-strain approximation of $\underline{\boldsymbol{E}}$ owning the convenient property of being a linear operator.

---

[3] George Green (1793-1841)

[4] Joseph-Louis Lagrange (1736-1813)

2.1.3 Constitutive law

The constitutive law relates the stress and strain tensors defined above and represents the material behavior. The latter is often characterized through material experiments, rarely from first-principles, and can be generically written as

$$\underline{\boldsymbol{\sigma}} = \mathscr{C}(\underline{\boldsymbol{\varepsilon}}, t, T, \boldsymbol{\phi}, \ldots). \tag{2.14}$$

In the relation above, $\mathscr{C}$ represents a function of the strains, as well as other variables such as time t, temperature T , and a collection of internal variables $\boldsymbol{\phi}$ accounting for material history. A linear elastic materials obeying Hooke's[5] law is assumed in the context of this thesis. Similar to a spring whose force-extension ratio is described by a unique constant (i.e. its stiffness), the *stiffness* tensor $\underline{\underline{\boldsymbol{C}}}$ relates stresses to strains as

$$\underline{\boldsymbol{\sigma}} = \underline{\underline{\boldsymbol{C}}} : \underline{\boldsymbol{\varepsilon}}, \tag{2.15}$$

where the operator ":" corresponds to the tensor contraction. $\underline{\underline{\boldsymbol{C}}}$ is a fourth-order tensor containing 81 components, which can be reduced to 21 by taking advantage of the symmetries of $\underline{\boldsymbol{\sigma}}$ and $\underline{\boldsymbol{\varepsilon}}$. For a homogeneous, isotropic, linearly elastic material, the constitutive law further simplifies into:

$$\underline{\boldsymbol{\sigma}} = \lambda \mathrm{Tr}(\underline{\boldsymbol{\varepsilon}})\underline{\boldsymbol{I}} + 2\mu\underline{\boldsymbol{\varepsilon}}, \tag{2.16}$$

with $\mathrm{Tr}(\underline{\boldsymbol{\varepsilon}})$ being the trace of $\underline{\boldsymbol{\varepsilon}}$ and (λ, μ) the Lamé[6] coefficients. The latter are directly related to engineering elastic properties, such as Young's[7] modulus E and Poisson's [8] ratio ν, which are respectively the material stiffness and the ratio of lateral to longitudinal strain observed during uniaxial loading:

$$\lambda = \frac{\nu E}{(1+\nu)(1-2\nu)} \tag{2.17}$$

and

$$\mu = \frac{E}{2(1+\nu)}. \tag{2.18}$$

Different definitions of stresses and strains, associated to a large variety of constitutive laws exist in the literature. For a detailed presentation of the different approaches existing in continuum mechanics, the reader is redirected to [28].

---

[5] Robert Hooke (1635-1703)

[6] Gabriel Lamé (1795-1870)

[7] Thomas Young (1773-1829)

[8] Siméon Denis Poisson (1781-1840)

2.1.4 Elastodynamics

The equation of motion of a continuum solid is obtained by combining the three ingredients defined above, i.e. the conservation law (Equation 2.5), the kinematics (Equation 2.13) and the constitutive law (Equation 2.16):

$$(\lambda+\mu)\nabla(\nabla\cdot\boldsymbol{u})+\mu\nabla^2\boldsymbol{u}=\rho\frac{\partial^2\boldsymbol{u}}{\partial t^2}. \tag{2.19}$$

Using the vector identity ($\nabla(\nabla\cdot\boldsymbol{u})-\nabla^2\boldsymbol{u}=\nabla\times(\nabla\times\boldsymbol{u})$), the partial differential equation (PDE) above, also known as Lamé-Navier[9] equation of motion, can be rewritten as:

$$\frac{\lambda+2\mu}{\rho}\nabla(\nabla\cdot\boldsymbol{u})-\frac{\mu}{\rho}\nabla\times(\nabla\times\boldsymbol{u})=\frac{\partial^2\boldsymbol{u}}{\partial t^2}. \tag{2.20}$$

Following Helmholtz's [10] decomposition, any vectorial field can be represented in terms of a scalar potential Φ and a vector potential $\boldsymbol{\Psi}$ such that:

$$\boldsymbol{u}=\nabla\Phi+\nabla\times\boldsymbol{\Psi}. \tag{2.21}$$

Using the properties of the curl and divergence operators ($\nabla\times(\nabla\Phi)=\nabla\cdot(\nabla\times\boldsymbol{\Psi})=0$), Equation 2.20 can be decomposed into two wave equations:

$$\frac{\lambda+2\mu}{\rho}\nabla^2(\nabla\Phi)=\frac{\partial^2(\nabla\Phi)}{\partial t^2}, \tag{2.22}$$

$$\frac{\mu}{\rho}\nabla^2(\nabla\times\boldsymbol{\Psi})=\frac{\partial^2(\nabla\times\boldsymbol{\Psi})}{\partial t^2}. \tag{2.23}$$

Equation 2.20 is hence a second order differential equation describing solid elastodynamics, which is characterized by the propagation of two types of waves traveling at different speeds:

- The longitudinal component $\nabla\Phi$ is associated to volumetric strains and propagates at a speed

  $$c_d=\sqrt{\frac{\lambda+2\mu}{\rho}}, \tag{2.24}$$

  referred to as the *dilatational wave speed.*

- The transverse component $\nabla\times\boldsymbol{\Psi}$ corresponds to deviatoric strains and moves with a speed

  $$c_s=\sqrt{\frac{\mu}{\rho}}, \tag{2.25}$$

---

[9] Claude-Louis Navier (1785-1836)

[10] Hermann Ludwig Ferdinand von Helmholtz (1821-1894)

which is known as the *shear wave speed.*

c_d and c_s are connected by Poisson's ratio as

$$c_d = \sqrt{\frac{2(1-\nu)}{1-2\nu}}\, c_s = \eta\, c_s. \tag{2.26}$$

In addition to these two waves, elastic waves can also travel along the surface of isotropic linearly elastic solids in the form of *Rayleigh waves* [29], whose propagation speed can be estimated as

$$c_R \cong \frac{0.862 + 1.14\nu}{1+\nu} c_s. \tag{2.27}$$

For the typical values of Poisson's ratio, the Rayleigh wave speed corresponds to $0.86 < c_R / c_s < 0.96$.

2.1.5 Boundary and initial value problems

The elastodynamic *boundary value problem* is defined by associating some constraints existing at the solid boundaries $\partial\Omega$ to the continuum region Ω governed by the PDE. The latter are referred to as *boundary conditions* and mainly exist within two forms:

1. Dirichlet[11] boundary conditions imposing the value of $\boldsymbol{u} = \overline{\boldsymbol{u}}$ over the surface $\partial\Omega_u$.
2. Neumann[12] boundary conditions imposing the value of the surface tractions $\underline{\boldsymbol{\sigma}}\boldsymbol{n} = \overline{\boldsymbol{\tau}}$ acting along the surface $\partial\Omega_\tau$.

These boundary conditions are completed by a set of initial conditions defining the specific value of the elastic fields at the initial time $t = t^0$.

In this context, the *virtual work principle* is an important method to solve boundary value problems. It states that if the following integral equation is satisfied for any arbitrary kinematically admissible [13] virtual displacement field $\hat{\boldsymbol{u}}$:

$$\int_\Omega \underline{\boldsymbol{\sigma}} : \hat{\underline{\boldsymbol{\varepsilon}}} dV + \int_\Omega \rho \ddot{\boldsymbol{u}} \cdot \hat{\boldsymbol{u}} dV - \int_{\partial\Omega_\tau} \overline{\boldsymbol{\tau}} \cdot \hat{\boldsymbol{u}} dA = 0, \tag{2.28}$$

then the stress field $\underline{\boldsymbol{\sigma}}$ is a solution of the boundary value problem. For a static problem,

---

[11] Peter Gustave Lejeune Dirichlet (1805-1859)

[12] Carl Gottfried Neumann (1832-1925)

[13] A displacement field is *kinematically admissible* if it is continuous, differentiable and if it satisfies the Dirichelet boundary conditions on Ω_u.

Equation 2.28 is equivalently written as

$$\int_{\Omega} \underline{\boldsymbol{\sigma}} : \underline{\hat{\boldsymbol{\varepsilon}}} dV - \int_{\partial\Omega_\tau} \overline{\boldsymbol{\tau}} \cdot \hat{\boldsymbol{u}} dA = 0. \tag{2.29}$$

In particular for $\hat{\boldsymbol{u}} = \boldsymbol{u}$, Equation 2.29 states that

$$\int_{\Omega} \underline{\boldsymbol{\sigma}} : \underline{\boldsymbol{\varepsilon}} dV = \int_{\partial\Omega_\tau} \overline{\boldsymbol{\tau}} \cdot \boldsymbol{u} dA. \tag{2.30}$$

From classical mechanics, the potential energy of the system is defined as

$$E_{\text{pot}} = E_{\text{el}} - W_{\text{ext}} = \frac{1}{2} \int_{\Omega} \underline{\boldsymbol{\sigma}} : \underline{\boldsymbol{\varepsilon}} dV - \int_{\partial\Omega_\tau} \overline{\boldsymbol{\tau}} \cdot \boldsymbol{u} dA, \tag{2.31}$$

with E_{el} and W_{ext} being, respectively, the elastic strain energy and the work of external forces. Moreover, the kinetic energy of continuum solids can be written as:

$$E_{\text{kin}} = \frac{1}{2} \int_{\Omega} \rho \dot{\boldsymbol{u}} \cdot \dot{\boldsymbol{u}} dV. \tag{2.32}$$

In the next section, the description of crack within the continuum mechanics framework will be presented. Therefore, a crack is introduced within the Cartesian frame of reference $x - y - z$, such that its propagation is contained within the plane $y = 0$ and occurs in the x-direction. Within this convention, one can define three possible modes of fracture, as illustrated in Figure 2.3:

1. Tensile loading (mode I), where the loading is applied normally to the crack plane (σ_{yy}).

2. In-plane shear loading (mode II), where the loading is applied in the same direction as the crack propagation (σ_{xy}).

3. Anti-plane shear loading (mode III), where the loading is applied perpendicular to both the normal of the crack plane and the direction of crack propagation (σ_{yz}).

A particularly convenient setup to simplify the vectorial elastodynamic equation is the z-invariant ($\frac{\partial}{\partial z} = 0$) anti-plane displacement field ($u_x = u_y = 0$) corresponding to a mode III fracture problem. In this setup, the elastodynamic Equation 2.20 becomes scalar and involves a unique characteristic speed:

$$c_s^2 \nabla^2 u_z = c_s^2 (u_{z,xx} + u_{z,yy}) = u_{z,tt}. \tag{2.33}$$

In the following sections, a few key fracture mechanics results will be demonstrated within this anti-plane setup to keep their proof concise.

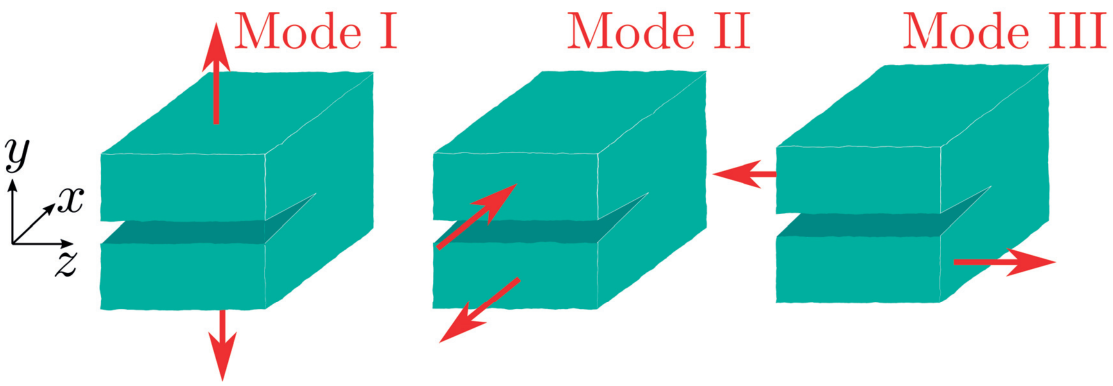

Figure 2.3 – The typical axes convention used in this thesis and its three associated modes of fracture.

2.2 Fracture mechanics

Fracture mechanics is a rather young discipline of physical science and engineering, whose origin coincides with the advent of large-scale modern steel production. In the wake of the Industrial Revolution, many technological innovations relied on the design of lighter and thinner structural components working in tension. Subsequently, several unexpected, often spectacular, failures of components and structures caused by brittle fracture were reported between the 19th and 20th centuries and motivated the advent of a rigorous understanding of fracture mechanics. For a complete presentation of the historical aspects of fracture mechanics, the reader is redirected to the reference text books [30, 31], which inspired this chapter.

Griffith [10] was the first to quantitatively describe how the presence of inherent flaws within materials directly control their tensile strength, which is several order of magnitude lower than the theoretical strength of their atomic bonds. Relying on the stress concentration predicted by Inglis [32] at the vicinity of an elliptic flaw, Griffith studied how the stress concentration caused by the existence of flaws explains the premature rupture of materials. However, the definition of a stress criterion of fracture was complicated by the "unphysical" infinite stress concentration predicted at the vicinity of sharp cracks. Hence, Griffith proposed an energy-based criterion, stating that a crack will expend if and only if the associated change in potential energy E_{pot} compensates the energy required to create new surfaces. The so-called *Griffith energy balance*, grounded on the first law of thermodynamics, can be expressed for an infinitesimal crack advance dA as:

$$G = -\frac{dE_{\text{pot}}}{dA} = 2\gamma_s, \tag{2.34}$$

with γ_s being the surface energy and G being defined as the *energy release rate*. The energy balance in Equation 2.34 leads to Griffith's stability criterion for existing flaws: $G \leq 2\gamma_s$. The success of this approach was however limited to perfectly brittle materials, e.g. glass. For other kinds of materials, such as metals, the fracture resistance is significantly underestimated.

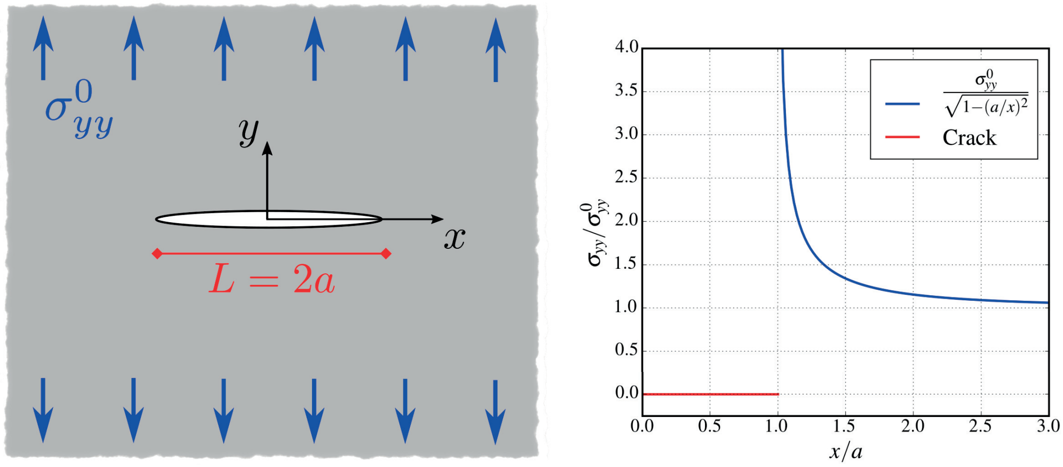

Figure 2.4 – Stress concentration at the vicinity of a sharp crack existing within a semi-infinite plate and its evolution along $y = 0$.

Moreover, it was not clear how to compute the energy release rate for any arbitrary crack geometry.

In 1939, Westergaard [33] published the elastostatic solution of several interface problems implying singular stress fields. Among them, the evolution of the stress field in the neighborhood of a crack of size $2a$ located in the middle of an infinite plate loaded by a far-field tensile loading σ^0_{yy}:

$$\sigma_{yy} = \begin{cases} \frac{\sigma^0_{yy}}{\sqrt{1-(a/x)^2}}, \ ||x|| > a, \\ 0, \ ||x|| \leq a, \end{cases} \tag{2.35}$$

This remarkably compact expression, whose evolution along the mid-plane $y = 0$ is presented in Figure 2.4, uncovers the evolution of stresses at the vicinity of cracks and inspired the subsequent investigations on the stress singularity [1,34,35]. Among them, Williams [35,36] derived the asymptotic elastic fields existing within any crack configuration, independently of the boundary conditions. For the sake of simplicity, Williams' solution is briefly presented hereafter for the convenient anti-plane shearing geometry.

From Equation 2.33, the equilibrium relation ($u_{,tt} = 0$) can be expressed within the polar system of coordinates (r, θ) presented in Figure 2.5:

$$\frac{1}{r}\frac{\partial}{\partial r}\left(r\frac{\partial u_z}{\partial r}\right) + \frac{1}{r^2}\frac{\partial^2 u_z}{\partial \theta^2} = \frac{\partial^2 u_z}{\partial r^2} + \frac{1}{r}\frac{\partial u_z}{\partial r} + \frac{1}{r^2}\frac{\partial^2 u_z}{\partial \theta^2} = 0. \tag{2.36}$$

In this new frame of coordinates centered at the crack tip, Williams postulated a solution of the form:

$$u_z(r,\theta) = r^{\lambda} f(\theta, \lambda). \tag{2.37}$$

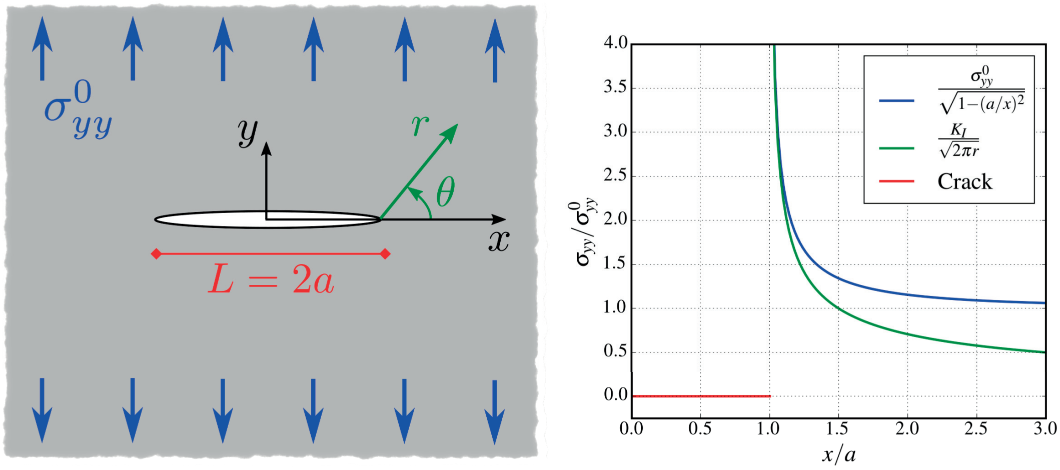

Figure 2.5 – Comparison between the exact stress field and the singular approximation along $y = 0$. The asymptotic stress field is only accurate in the close neighborhood of the crack tip.

Combining Equations 2.36 and 2.37, the following second order ordinary differential equation (ODE) is obtained:

$$f''(\theta,\lambda) + \lambda^2 f(\theta,\lambda) = 0, \tag{2.38}$$

leading to a general solution of the form:

$$u_z(r,\theta) = r^\lambda (A\cos\lambda\theta + B\sin\lambda\theta). \tag{2.39}$$

The anti-symmetry of the problem implies that $A = 0$, such that the shear stresses are written as:

$$\sigma_{xz} = \mu\frac{\partial u_z}{\partial x} = \mu\left[\frac{\partial u_z}{\partial r}\frac{\partial r}{\partial x} + \frac{\partial u_z}{\partial \theta}\frac{\partial \theta}{\partial x}\right] = -\mu\lambda B r^{\lambda-1}\sin\Big\{\theta(\lambda-1)\Big\}, \tag{2.40}$$

$$\sigma_{yz} = \mu\frac{\partial u_z}{\partial y} = \mu\left[\frac{\partial u_z}{\partial r}\frac{\partial r}{\partial y} + \frac{\partial u_z}{\partial \theta}\frac{\partial \theta}{\partial y}\right] = \mu\lambda B r^{\lambda-1}\cos\Big\{\theta(\lambda-1)\Big\}. \tag{2.41}$$

A generic crack boundary condition implies that the surface lying at $(r,\theta = \pm\pi)$ is free of stress:

$$\sigma_{yz} = \mu\lambda B r^{\lambda-1}\cos\Big\{\pi(\lambda-1)\Big\} = 0, \tag{2.42}$$

which leads to

$$\lambda = \frac{n}{2}, \quad n = \pm1, \pm3, \pm5, \ldots \tag{2.43}$$

Moreover, unbounded displacements as $r \to 0$ are unphysical and, hence, the singular terms

($\lambda < 0$) can be removed, leading to the following solution:

$$u_z(r,\theta) = \sum_{n=1,3,5,...} B_n r^{\frac{n}{2}} \sin\left(\frac{n\theta}{2}\right), \tag{2.44}$$

with its associated shear stresses:

$$\sigma_{xz}(r,\theta) = -\mu \sum_{n=1,3,5,...} B_n \frac{n}{2} r^{\frac{n}{2}-1} \sin\left(\theta \frac{n-2}{2}\right), \tag{2.45}$$

$$\sigma_{yz}(r,\theta) = \mu \sum_{n=1,3,5,...} B_n \frac{n}{2} r^{\frac{n}{2}-1} \cos\left(\theta \frac{n-2}{2}\right). \tag{2.46}$$

Equations 2.44, 2.45 and 2.46, are often referred to as *Williams series* and assume no specific crack geometry and correspond hence to a very generic description of the elastic fields existing around a crack tip. In particular, very close from the tip, the stress fields are dominated by a unique singular contribution ($n = 1$) and hence follow a *universal square root singularity*:

$$\lim_{r\to 0} \sigma_{xz}(r,\theta) = -\frac{\mu B_1}{2} r^{-\frac{1}{2}} \sin\left(\frac{\theta}{2}\right), \tag{2.47}$$

$$\lim_{r\to 0} \sigma_{yz}(r,\theta) = \frac{\mu B_1}{2} r^{-\frac{1}{2}} \cos\left(\frac{\theta}{2}\right). \tag{2.48}$$

During the same year than Williams' publication, Irwin [1] reached similar conclusions by conducting a limit analysis of Westergaard's solution. He used a slightly different notation, which introduced the notion of stress intensity factors K, and expressed the asymptotic elastic fields as

$$\sigma_{xz}(r,\theta) = -\frac{K_{III}}{\sqrt{2\pi r}} \sin\left(\frac{\theta}{2}\right), \tag{2.49}$$

$$\sigma_{yz}(r,\theta) = \frac{K_{III}}{\sqrt{2\pi r}} \cos\left(\frac{\theta}{2}\right), \tag{2.50}$$

$$u_z(r,\theta) = \frac{2K_{III}}{\mu} \sqrt{\frac{r}{2\pi}} \sin\left(\frac{\theta}{2}\right). \tag{2.51}$$

The subscript of K refers to each fracture mode, for which the associated stress intensity factors are defined as

$$\left\{ \begin{array}{c} K_I \\ K_{II} \\ K_{III} \end{array} \right\} = \chi\sqrt{\pi a} \left\{ \begin{array}{c} \sigma^0_{yy} \\ \sigma^0_{xy} \\ \sigma^0_{yz} \end{array} \right\}, \tag{2.52}$$

where χ represents a dimensionless scalar accounting for the geometry of the problem and typically equals to one within an infinite domain. Asymptotic solutions equivalent to Equations 2.49, 2.50 and 2.51 exist for mode I and mode II and their expressions can be found in the reference textbooks [31, 37]. Figure 2.5 compares the exact solution derived by Westergaard with the singular approximation, which is only accurate at the immediate vicinity of the crack tip.

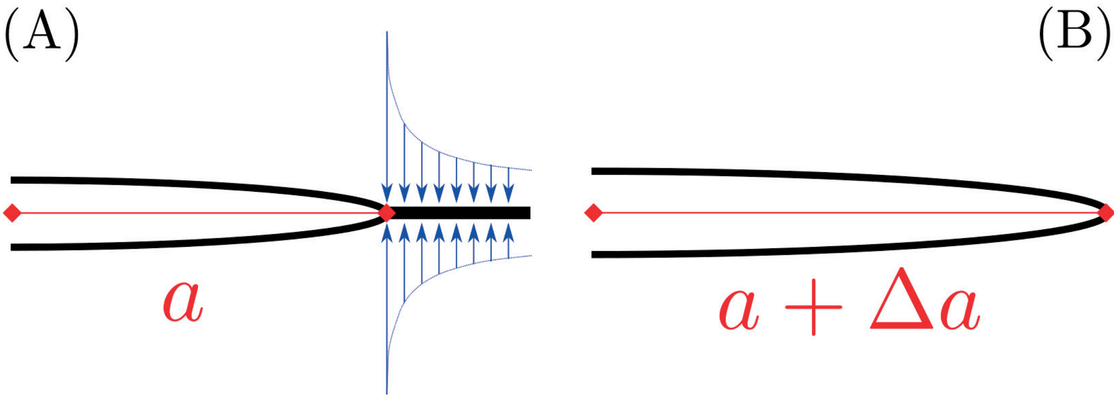

Figure 2.6 – The two configurations used by Irwin [1] to compute the change of potential energy observed as crack grows of Δa. The blue arrows represent the surface tractions required to close the crack between a and $a + \Delta a$.

In this context, Irwin's major contribution consisted to show that the energy release rate is entirely mediated by the near-tip field and, therefore, by the asymptotic approximation.

Figure 2.6 presents the two configurations considered by Irwin for his demonstration: a crack with size a (configuration A) and a crack with size $a + \Delta a$ (configuration B). Moreover, the potential energy can be written in terms of the work done at the boundary surfaces by combining Equations 2.31 and 2.30:

$$E_{\text{pot}} = -\frac{1}{2}\int_{\partial\Omega_\tau} \overline{\boldsymbol{\tau}} \cdot \boldsymbol{u} \, dA. \tag{2.53}$$

In an infinite solid, $\partial\Omega_\tau$ corresponds solely to the crack surfaces[14], which is growing as the rupture propagates of Δa. Irwin tackled this problem by assuming an equivalent configuration A, for which the surface extension Δa already exists but is kept closed by a pair of opposite tractions acting between a and $a + \Delta a$ (depicted in blue in Figure 2.6).
Applying the same strategy to the mode III configuration of interest, Equation 2.53 becomes per a unit crack width:

$$\Delta E_{\text{pot}}(\Delta a) = -\frac{1}{2}\int_0^{\Delta a} \sigma_{yz}^A(x)\, u_z^B(x)\, dx, \tag{2.54}$$

where the superscript denotes the configuration considered. If Δa is taken sufficiently small, σ_{yz}^A and u_z^B are dominated by the singular contribution for, respectively, a crack of size a and a crack of size $a + \Delta a$. The previous integral can hence be written using Equations 2.50 and

---

[14] For finite size systems, this postulate is extended by assuming that the crack is far enough from the solid boundaries, such that changes in $\boldsymbol{u}$ and $\overline{\boldsymbol{\tau}}$ mostly arise along the crack plane.

2.51 as:

$$\begin{aligned}
\Delta E_{\text{pot}}(\Delta a) &= -\frac{1}{2}\int_0^{\Delta a} \sigma_{yz}(\theta=0, r=x)\, u_z(\theta=\pi, r=\Delta a - x)\, dx \\
&= -\frac{1}{2}\int_0^{\Delta a} \frac{K_{III}(a)}{\sqrt{2\pi x}} \frac{2K_{III}(a+\Delta a)}{\mu}\sqrt{\frac{\Delta a - x}{2\pi}}\, dx \\
&= -\frac{K_{III}(a)K_{III}(a+\Delta a)}{\mu\pi}\int_0^{\Delta a}\sqrt{\frac{\Delta a - x}{x}}\, dx \\
&= -\frac{\Delta a K_{III}(a)K_{III}(a+\Delta a)}{2\mu}.
\end{aligned} \tag{2.55}$$

Finally, using Griffith definition of the energy release rate (Equation 2.34), one obtains:

$$G = -\frac{dE_{\text{pot}}}{da} = \lim_{\Delta a \to 0}\left\{-\frac{\Delta E_{\text{pot}}(\Delta a)}{\Delta a}\right\} = \frac{1}{2\mu}K_{III}^2. \tag{2.56}$$

The equation above can be similarly derived for the three modes of fracture and is generically written as:

$$G = \frac{1-\nu^2}{E}\left(K_I^2 + K_{II}^2\right) + \frac{1}{2\mu}K_{III}^2. \tag{2.57}$$

Equation 2.57 remarkably connects Griffith energy criterion to the universal square-root singular stress fields existing at the tip of a crack in a linearly elastic material.
Finally, Irwin replaced the energy required by surface creation $2\gamma_s$ by a generalized concept of *fracture energy* G_c. This new definition allowed to extend the applicability of the energy balance beyond the scope of perfectly brittle fracture, to materials for which $2\gamma_s$ only represents a small amount of the total fracture energy. In this context, Equation 2.34 is rewritten as

$$G = G_c. \tag{2.58}$$

Griffith energy balance and Irwin asymptotic analysis, embodied in Equations 2.57 and 2.58, represent the core of our modern understanding of fracture, often referred to as *Linear Elastic Fracture Mechanics* (LEFM). Figure 2.7 summarizes the main assumptions and results of LEFM. The neighborhood of a crack can be decomposed in three different regions:

- (A) Immediately ahead of the tip, stresses reach extremely high magnitudes that no real material can withstand. A tiny region, often referred to as *fracture process zone*, develops over the width l_{pz} containing all the dissipative processes involved within G_c.
- (B) Right behind the process zone, the linear elastic behavior is dominated by the universal square-root singular contribution.
- (C) Further away from the tip, higher-order terms of Williams series (cf. Equations 2.44, 2.45 and 2.46) are required to describe the elastic fields, which converge toward their far-field values.

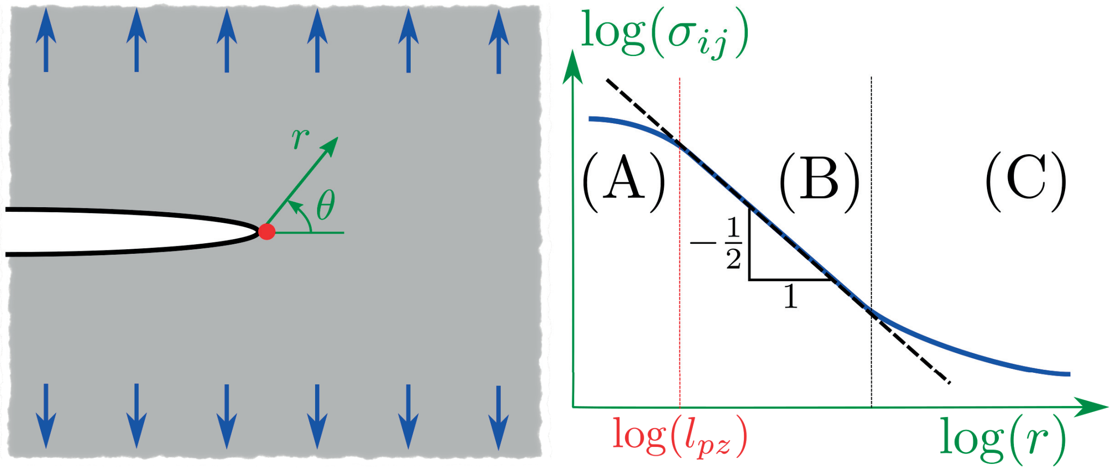

Figure 2.7 – Schematic evolution of the stress at the vicinity of a crack and its approximation following LEFM theoretical framework (dashed black line). See the main text for a detailed description of the three regions (A-B-C).

LEFM theory applies to predict crack stability as long as a well-defined region (B) dominated by the singular contribution exists. This implies that the size of the process zone is small enough compared to other representative length scales ($l_{\text{pz}} << a$) and that the crack stands at a sufficient distance from the far-field boundary conditions. When these conditions are verified, the energy release rate is entirely contained in Equation 2.57, a situation which is often referred to as *K-controlled fracture*.

In the past fifty years LEFM became a well-established theory applied in many engineering and physical applications to predict the stability of defects and flaws in materials and structures. LEFM framework was successfully extended to broader kinds of phenomena; among others plastic and ductile fracture [38], fatigue of materials [39], landslides [40], snow avalanches [41] and earthquake science (extensively discussed in Section 2.3).

Because of these successes, it was natural to try extending LEFM concepts to the description of cracks far from equilibrium, i.e. to dynamic fracture mechanics. In the next section, the main concepts of the dynamic fracture theory are introduced for the convenient anti-plane mode III setup. For a complete description of dynamic fracture, the reader is redirected to the reference textbooks [37, 42, 43].

2.2.1 On the elastodynamics of moving cracks

Let us once more consider the mode III or tearing fracture conditions, for which a z-invariant ($\frac{\partial}{\partial z} = {}_{,z} = 0$) out-of-plane displacement field ($u_x = u_y = 0$) is assumed, such that the elastodynamic wave equation becomes scalar with a unique characteristic wave speed c_s (cf. Equation

2.33):

$$u_{z,xx} + u_{z,yy} = \frac{1}{c_s^2} u_{z,tt}. \tag{2.59}$$

The common strategy behind dynamic fracture theory is to solve the elastodynamic relations within a moving system of coordinates, whose origin follows the crack tip moving with a steady velocity v_c. Assuming a subsonic rupture speed ($v_c < c_s$), this moving system of coordinates can be conveniently defined in the framework of Lorentz[15] transforms:

$$x_1 = \frac{x - v_c t}{\sqrt{1 - v_c^2/c_s^2}},\ x_2 = y, x_3 = z,\ t' = \frac{t - (v_c x/c^2)}{\sqrt{1 - v_c^2/c_s^2}}, \tag{2.60}$$

which has the great advantage of preserving the shape of the wave equation:

$$u_{3,11} + u_{3,22} = \frac{1}{c^2} u_{3,t't'}. \tag{2.61}$$

Under the steady-state postulate ($\frac{\partial}{\partial t'} = 0$), the relation 2.61 becomes a Laplace's equation

$$u_{3,11} + u_{3,22} = 0, \tag{2.62}$$

similar to the elastostatic equation written in the mode III setup of interest as

$$\nabla \boldsymbol{\sigma} = 0 \Leftrightarrow \mu(u_{z,xx} + u_{z,yy}) = 0. \tag{2.63}$$

Hence, Williams series can be equivalently used to describe the asymptotic stresses at the vicinity of a crack existing within a continuum governed either by the Laplace's equation 2.62 or 2.63. Let us recall, the asymptotic elastic field predicted for a static crack ahead of the crack ($x = r, \theta = 0$):

$$\sigma_{yz} = \frac{K_{III}^s}{\sqrt{2\pi x}}, \tag{2.64}$$

and in the wake of the crack ($x = r, \theta = \pi$):

$$u_z = 2\frac{K_{III}^s}{\mu}\sqrt{\frac{x}{2\pi}}. \tag{2.65}$$

By analogy, the asymptotic fields at the tip of a crack existing within a continuum governed by Equation 2.62 are written as

$$\sigma_{23} = \frac{\overline{K}_{III}}{\sqrt{2\pi x_1}} \tag{2.66}$$

---

[15] Hendrick Antoon Lorentz (1853-1928)

ahead of the crack and

$$u_3 = 2\frac{\overline{K}_{III}}{\mu}\sqrt{\frac{x_1}{2\pi}} \tag{2.67}$$

in the wake of the crack. K^s_{III} denotes the stress intensity factor in the case of a static crack, while $\overline{K}_{III}$ is the stress intensity factor existing in the Lorentz frame of coordinates. Moreover, Irwin's analysis presented above (cf. Equation 2.56) similarly applies to compute the crack energy release rate:

$$-\frac{dE_{\text{pot}}}{da} = G = \frac{\overline{K}^2_{III}}{2\mu}. \tag{2.68}$$

Relations 2.66, 2.67 and 2.68 are derived in the Lorentz frame of coordinates such that $\overline{K}_{III}$ is different from the stress intensity factor K_{III} measured in the lab. Since $\partial u_z/\partial y = \partial u_3/\partial x_2$ and $r = x - v_c t$, one can express the stress intensity factor observable from the lab K_{III}

$$\sigma_{yz} = \sigma_{23} = \frac{\overline{K}_{III}}{\sqrt{2\pi\frac{x-v_c t}{\sqrt{1-v_c^2/c_s^2}}}} = \frac{\overline{K}_{III}}{\sqrt{2\pi\frac{r}{\sqrt{1-v_c^2/c_s^2}}}} = \frac{K_{III}}{\sqrt{2\pi r}}. \tag{2.69}$$

K_{III} corresponds hence to the stress intensity factor that can be directly measured from the stress profile observed experimentally or from numerical simulations. It is often referred to as the *dynamic stress intensity factor*. Conversely, $\overline{K}_{III}$ is the stress intensity factor measured in the relativistic space, contracted by the Lorentz transform:

$$K_{III} = \overline{K}_{III}\left(1 - v_c^2/c_s^2\right)^{\frac{1}{4}}. \tag{2.70}$$

Similarly, material point velocity can be computed as

$$\dot{u}_z = \frac{\partial u_3}{\partial t} = \frac{\partial u_3}{\partial x_1}\frac{\partial x_1}{\partial t} = -\frac{\partial u_3}{\partial x_1}\frac{v_c}{\sqrt{1-v_c^2/c_s^2}} = \frac{\overline{K}_{III}}{\mu\sqrt{2\pi\frac{x-v_c t}{\sqrt{1-v_c^2/c_s^2}}}}\frac{v_c}{\sqrt{1-v_c^2/c_s^2}}, \tag{2.71}$$

which becomes, using the definition of the dynamic stress intensity factor,

$$\dot{u}_z = \frac{K_{III}}{\mu\sqrt{2\pi r}}\frac{v_c}{\sqrt{1-v_c^2/c_s^2}}. \tag{2.72}$$

Moreover, the systems of coordinates (x, y, z) and (x_1, x_2, x_3) are two inertial frames of reference and therefore the laws of physics are invariant, and in particular the energy balance $G = G_c$ of Equation 2.58, which becomes in the fixed system of coordinates:

$$G_c = G = \frac{\overline{K}^2_{III}}{2\mu} = \frac{K^2_{III}}{2\mu}\frac{1}{\sqrt{1-v_c^2/c_s^2}} = \frac{K^2_{III}}{2\mu}A_{III}(v_c). \tag{2.73}$$

A_{III} is a universal function of the crack speed, which allows to generalize the concepts of LEFM to dynamic crack. In this context, Figure 2.8 presents the asymptotic stress and velocity profiles, invariant with the rupture speed.

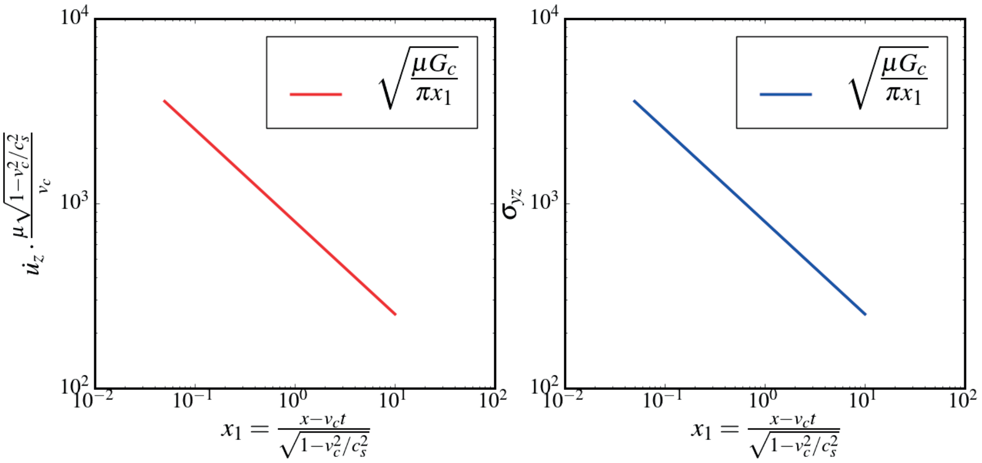

Figure 2.8 – Asymptotic evolution along the crack plane $y = 0$ of the velocity (left) and shear stress (right) at the vicinity of a mode III crack moving at any subsonic speed along an interface characterized by a given fracture energy G_c.

The derivations above can be generalized to any mode of fracture, for which, however, several characteristic wave speeds (c_R,c_s,c_d) come into play and prevent the direct use of Lorentz transform. The generalized asymptotic fields are therefore computed following the Galilean transform ($x_1 = x - v_c t, x_2 = y, x_3 = z, t' = t$), leading to more complex derivations which can be found for the different modes of fracture in reference textbooks [42, 43]. As example, Figure 2.9 presents the singular profile of the hoop stress predicted at the vicinity of a tensile crack growing at different speeds along an interface characterized by a constant fracture energy G_c. The generalization of crack energy balance for any arbitrary dynamic fracture setups is then written as:

$$G_c = G = \frac{E}{(1-\nu^2)}\left(A_I K_I^2 + A_{II} K_{II}^2\right) + \frac{1}{2\mu} A_{III} K_{III}^2, \tag{2.74}$$

with

$$A_I(v_c) = \frac{\alpha_d v_c^2}{(1-\nu) D c_s^2}, \tag{2.75}$$

and

$$A_{II}(v_c) = \frac{\alpha_s v_c^2}{(1-\nu) D c_s^2}, \tag{2.76}$$

where $\alpha_{s,d}^2 = 1 - v^2/c_{s,d}^2$, and $D = 4\alpha_d \alpha_s - (1+\alpha_s^2)^2$.

The universal function

$$A_{III}(v_c) = \frac{1}{\alpha_s} \tag{2.77}$$

is recalled from Equation 2.73.

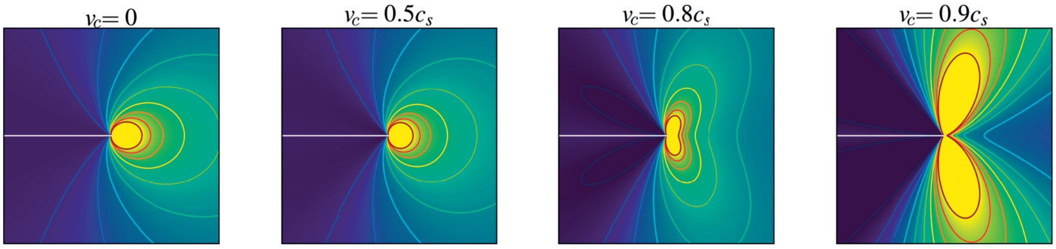

Figure 2.9 – Asymptotic hoop stress profiles predicted at the vicinity of a tensile crack moving at different speeds along an interface characterized by G_c and $c_R = 0.93c_s$.

2.2.2 Relativistic effects in dynamic fracture

The title of Section 2.2.1 was humbly inspired from Einstein's paper *On the electrodynamics of moving bodies* [44]. Indeed, as particles in an electrodynamic field, the propagation of a crack within a linearly elastic solid is entirely driven and characterized by the elastodynamics, for which information travels at characteristic wave speeds. As a result, several relativistic effects arise as a crack moves with velocities approaching the range of elastic wave speeds. For example, let us express the evolution of the kinetic energy released by the rupture. Using the asymptotic fields derived for mode III crack, the elastic strain energy at the vicinity of a dynamic crack scales as [42]

$$E_{\mathrm{el}} = \frac{1}{2}\int \sigma_{yz}\varepsilon_{yz}\, r dr d\theta = \int \frac{1}{2\mu}\sigma_{yz}^2 \sim \frac{1}{2\mu}K_{III}^2, \tag{2.78}$$

while the kinetic energy is scaling according to

$$E_{\mathrm{kin}} = \frac{1}{2}\int \rho \dot{u}_z^2\, r dr d\theta \sim \frac{1}{2}\frac{\rho}{\mu^2}K_{III}^2\frac{v_c^2}{1 - v_c^2/c_s^2}. \tag{2.79}$$

The ratio of the kinetic energy over the strain energy is therefore expected to evolve with the propagation speed as

$$\frac{E_{\mathrm{kin}}}{E_{\mathrm{el}}} \sim \frac{\rho}{\mu}\frac{v_c^2}{1 - v_c^2/c_s^2} = \frac{v_c^2}{c_s^2}A_{III}^2 = \frac{v_c^2}{c_s^2 - v_c^2}. \tag{2.80}$$

Figure 2.10(**Left**) presents the resulting evolution of $E_{\mathrm{kin}}/E_{\mathrm{el}}$ with the crack propagation speed, compared to the scaling $E_{\mathrm{kin}}/E_{\mathrm{el}} \sim v_c^2/c_s^2$ proposed by Freund [42] under a quasi-static assumption. An interesting analogy can be made by comparing the relativistic kinetic energy of a particle with mass m_e and speed v_e [44]

$$E_{\text{kin}} = \frac{m_e c^2}{\sqrt{1 - \frac{v_e^2}{c^2}}} - m_e c^2 \tag{2.81}$$

to its classical expression $E_{\text{kin}} = 1/2 m_e v_e^2$, which is valid at velocities smaller than the light speed c. The two expressions are normalized by $E_{\text{pot}} = m_e c^2$ and plotted in Figure 2.10(**Right**). Similarly to a particle accelerating toward c, the rupture speed of a mode III crack is bounded by c_s as its kinetic energy diverges when $v_c \rightarrow c_s$. Another relativistic effect arising in dynamic fracture and its impact in the rupture of heterogeneous planes is presented in Chapter 5.

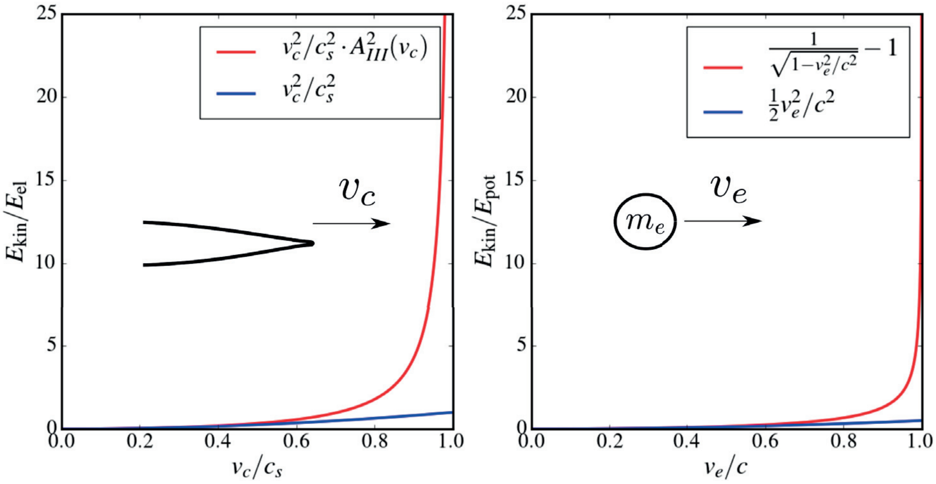

Figure 2.10 – Analogy between the relativistic effects existing for a particle of mass m_e moving at speed c (**Right**) and the one computed for a dynamic crack (**Left**).

From the evolution of the universal functions A_I and A_{II} defined in Equations 2.75 and 2.76, the energy release rate becomes negative for rupture speeds between c_R and c_s. The velocity range $c_R < v_c < c_s$ is hence a thermodynamically forbidden range of velocity for mode I and mode II cracks. With *intersonic/supershear* crack speeds, i.e. $c_s < v_c < c_d$, the structure of the partial differential equation changes (i.e. the equation derived from the vectorial shear potential becomes hyperbolic). In this context, Freund [45] obtained the energy released rate of a supershear mode II crack, which is precisely zero for every speed except $\sqrt{2}c_s$. The admissibility of intersonic shear cracks was further proven using non-singular approaches, for which a strictly positive energy release rate is predicted for every $c_s < v < c_d$ [46–48]. The energy release rate of an intersonic tensile crack is however predicted to be strictly negative, forbidding therefore mode I cracks to propagate faster than c_R. In a nutshell, the admissible crack speeds predicted by LEFM are presented in Table 2.1. For a complete review on the topic, the reader can refer to [49].

Table 2.1 – Summary of the admissible crack speeds predicted by LEFM.

	$0 < v_c < c_R$	$c_R \leq v_c < c_s$	$c_s < v_c < c_d$
Mode I	✓	✗	✗
Mode II	✓	✗	✓
Mode III	✓	✓	✗

2.2.3 Dynamic fracture experiments

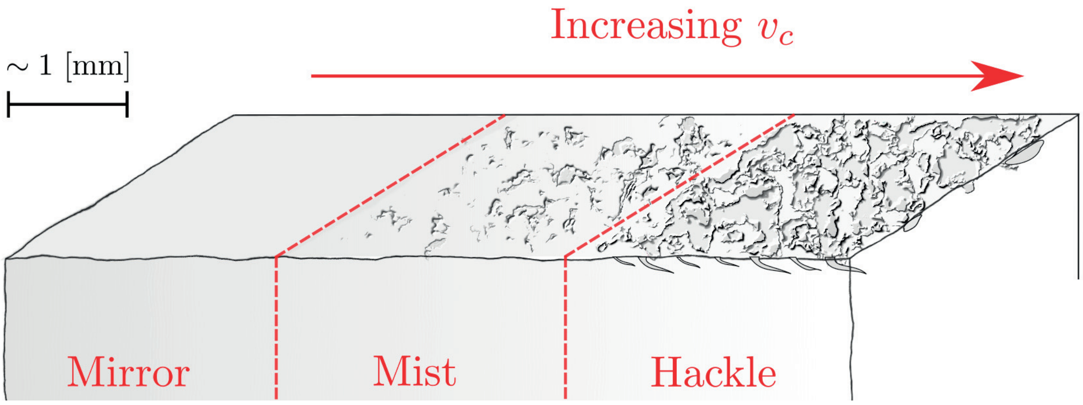

Figure 2.11 – Schematic evolution of the post-mortem appearance of the fracture surface as function of the crack propagation speed.

The experimental validation of this dynamic theory of fracture lead to rather mitigated results. While a good agreement is observed for slow crack propagation speeds, the dynamics of tensile ruptures exceeding a few tenths of c_s significantly diverge from the theoretical predictions. In particular, the theory underestimates the dissipated energy and overestimates the crack propagation speed, which barely exceeds $0.65c_R$ in the experiments. As the rupture speed increases, the crack experiences three different dynamic phases sketched in Figure 2.11 and usually referred to as “mirror”, “mist”, and “hackle” in reference to the postmortem appearance of the fracture surfaces.

- Mirror: For slow crack front speeds, an in-plane crack growth arises and leads to two very smooth surfaces.
- Mist: As the speed increases, the fracture surfaces roughen and reveal the systematic interplay between a crack front and the material microstructure.
- Hackle: If the crack speed keeps increasing, microcracks start growing out of the main rupture plane leading to the so-called *microbranching instability*.

This three-phase transition, which was reported for different types of brittle materials [50–52] and at different scales [53, 54], explains how the dynamic fracture theory breaks down as the

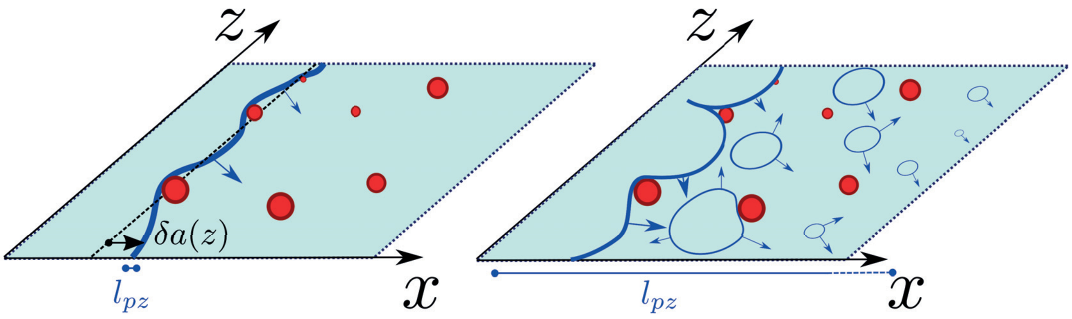

Figure 2.12 – Interaction of a dynamic crack with heterogeneities at two different scales. (**Left**) If the process zone size is much smaller than the heterogeneities, the crack is viewed as a line and studied using Rice's first-order perturbation analysis [2]. (**Right**) At the scale of the fracture process zone, the crack advances through the nucleation, growth and coalescence of pre-existing microcracks. This dynamics is typically studied using damage models [3].

crack dynamics stops being simple and becomes a heterogeneous dynamic fracture problem. A complete review of the dynamic fracture experiments and discussions about their inherent instabilities can be found in [50, 55–59]. Significant advances have been made in the past years in the description of these complex crack dynamics. However, a clear understanding of their origin and their evolution intimately mediated by the rupture speed is still missing. These complex crack patterns are supposedly emerging from the combination of two effects: the evolution of the elastic asymptotic fields presented in Section 2.2.1 and the presence of material heterogeneities discussed in the next section.

2.2.4 Heterogeneous fracture mechanics

The heterogeneities discussed in this section correspond to local variations of the fracture energy. The latter stops being a constant over the rupture plane and is now defined with some local variations $G_c(x,z)$.

For two-dimensional setups, no distortion of the front is possible and therefore v_c is the only variable of Equation 2.74. Therefore, a crack growing along a heterogeneous interface is predicted to instantaneously adapt its speed as a function of the value of G_c at the crack tip. Hence, the dynamic rupture keeps no memory from past events. This observation mostly relies on the assumption of a singular crack tip. Chapter 5 investigates in details how this predicted behavior evolves as the fracture process zone approaches the size of the heterogeneities.

In three-dimensional setups, rupture fronts are however distorted by the presence of heterogeneities along the fracture plane. v_c stops being the unique variable of Equation 2.74 as distortions of the crack front induce local perturbations of the stress intensity factor. For a semi-infinite crack front, Rice [2] derived the first-order perturbation ΔK_I of the stress intensity factor associated to slight distortions of the crack front δa illustrated in Figure 2.12:

$$\Delta K_I(z) = \frac{1}{2\pi}\mathrm{PV}\int_{-\infty}^{\infty}\frac{K_I^0\delta a(z')}{(z-z')^2}dz' + O(\delta a^2). \tag{2.82}$$

Under the assumption of small front distortions, this perturbation analysis can be successfully applied to study the interaction of quasi-static [60] and dynamic [15] crack fronts with material heterogeneities. In this approach, the crack front is viewed as an elastic line pinned by the heterogeneities until ΔK_I is large enough to rupture them. This first-order approach was extensively used to describe the statistical morphologies of crack fronts within disordered materials, both for in-plane [61–63] and out-of-plane roughness [64, 65]. These models shared LEFM assumptions, i.e. the crack front is described as a line whose process zone is much smaller than the characteristic size of the heterogeneities. However, the dynamic instabilities observed during fast rupture events arise at much smaller length scales, where fracture processes develop over a finite length comparable with the size of the heterogeneities.

At smaller scales, close to the size of the fracture process zone, the crack propagation evolves toward a new mechanism, characterized by the nucleation, the growth and the coalescence of microcracks ahead of the main rupture front [51, 66]. This transition in the rupture mechanism is also revealed by a significant change in the self-affine properties of the out-of-plane roughness [67, 68]. This mechanism at smaller scales is typically studied with damage models, for which the fracture process is modeled as successive ruptures of individual fibers or fuses with individual random strengths [3]. While these damage models successfully reproduced the statistical and intermittent properties of fracture, they derive from a simplified description of the continuum elastodynamics.

The readers interested by the statistical aspects of fracture in heterogeneous materials can refer to these recent reviews [69, 70].

Figure 2.12 compares the two different dynamics existing at scale larger or comparable to the size of the process zone. The changes in the rupture dynamics caused by heterogeneities larger and smaller than the fracture process zone will be specifically investigated in Chapter 5 and 7.

2.2.5 Dynamic rupture of weak interfaces

The dynamic rupture of weak planes received an increasing attention in the recent advent of composite and laminate materials, which have several preferential weak rupture planes that localize crack propagation [71]. It also applies to the context of frictional interfaces and geological layers.

Prescribing a crack growth along a weaker interface allows for the experimental confirmation of the admissible range of speed theoretically predicted by dynamic fracture theory (cf. Table 2.1) for both mode I [72] and mode II [73]. The weak planes usually consist of bonding two plates together, therefore creating a preferential path of lower fracture energy. Hence, the experiments of Rosakis *et al.* [73] along two plates of Homalite became the first experimental evidence of intersonic crack front between similar materials. The so-called *supershear* crack fronts received a particular echo in the context of earthquakes, for which supershear ruptures have been measured along some portions of crustal faults [74, 75]. Similar to the Mach cone observed in the wake of supersonic aircrafts, a supershear earthquake creates shock waves, causing very large ground motion at the surface and, hence, significantly increasing the seismic hazards for the built environment and population [9, 76–79]. As a result, the mechanism predicted by Burridge [46] and Andrews [47] (more than twenty years before the experiments of Rosakis *et al.* [73]) became a reference to rationalize under which conditions a crack transitions to the supershear regime. Crustal faults correspond to a highly heterogeneous contact region between two tectonic plates. However, the criterion currently used to predict the supershear transition relies on the assumption of homogeneous fault conditions. Hence, several numerical works recently studied how the presence of heterogeneous interface conditions can trigger premature supershear transitions [80–85]. In this context, Chapter 5 presents and studies the evolution of the supershear criterion in the presence of microscopic heterogeneities.

Finally, rupture along bimaterial interfaces was studied by bonding two plates made of dissimilar material with strong elastic contrast. Several experiments revealed the presence of large scale contact zones in the wake of the propagating crack despite far-field tensile loading conditions [86–88]. In the context of bimaterial interfaces, Chapter 4 generalizes the admissible range of ruptures to the case of bimaterial interfaces and rationalizes the origin of these large scale contact zones observed experimentally.

2.3 Solid friction of multi-contact interfaces

Understanding how sliding initiates between two nominally flat solids brought into contact is paramount in the description of various engineering and physical systems including the seismic cycles. Those systems are typically characterized by (long) silent periods during which shear stress progressively builds up in the surrounding continua, followed by (short) periods of slip releasing the accumulated strain energy [89, 90]. *Stick-slip* dynamics emerges from processes existing at different scales. At smaller scales, surfaces are rough and contact only exists between the peaks of the surface forming the *microcontacts*. This heterogeneous topography, whose evolution was directly observed in the experiments of Dieterich and Kilgore [91] and more recently by Weber *et al.* [92], explains the highly non-linear response of frictional interfaces. At a larger scale, long-range elasticity mediates the release of the strain energy accumulated in the surrounding bulks. Slipping motion nucleates somewhere along the interface and progressively invades the rest of the contact plane. These *slip fronts*, whose propagations were experimentally observed through different "laboratory-earthquake" experiments [76, 77, 93], are driven by a similar release of elastic energy as shear cracks. Therefore, frictional interfaces were typically studied and described in the literature from these two perspectives sketched in Figure 2.13; A first approach described the complex interface response to friction, while a second focused on the elastodynamics of the surrounding solids.

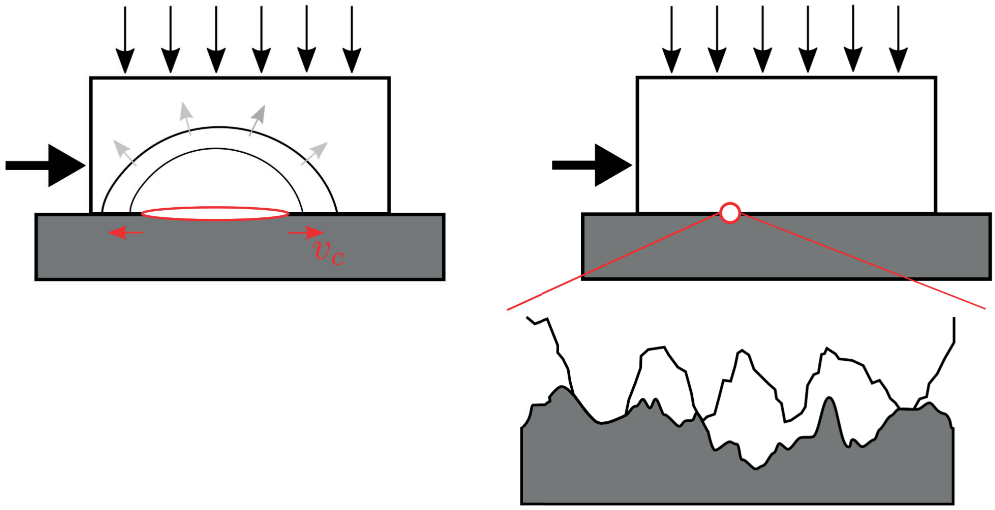

Figure 2.13 – Two interacting scales control the onset of sliding of a frictional interface. (**Left**) Bulk elastodynamics driving the propagation of slip fronts. (**Right**) The complex micromechanical response of the rough surfaces in contact.

2.3.1 Laboratory-derived interface models

There are many fascinating evidences that friction has challenged men throughout history, whose testimonies include Leonardo Da Vinci notebooks [94] or Egyptian wall paintings depicting the transport of heavy stones or colossus [95]. In this sense, tribology received an earlier scientific/engineering interest than fracture mechanics. The reader wishing to learn more about the history of friction can refer to [96]. Our modern understanding of the physics of friction arises from the experiments of Amontons [97] and Coulomb [98] who observed how friction increases proportionally with normal pressure and only weakly depends on other parameters such as the sliding velocity. At first order, the frictional strength can hence be written as a function of the normal pressure σ^0:

$$\tau^{\text{str}} = c_f \sigma^0. \tag{2.83}$$

The friction between two surfaces is therefore characterized by a unique number c_f, *the friction coefficient*. As long as the shear traction $\tau_s < c_f \sigma^0$, the interface is sticking. When this condition stops being satisfied, sliding initiates and a dynamic motion arises under a constant frictional shear stress corresponding to:

$$\tau_s = \tau^{\text{str}} = c_f \sigma^0. \tag{2.84}$$

Coulomb already interpreted the origin of c_f from the tangential force required to slip two rigid corrugated surfaces in contact [99, 100]. As illustrated in the left of Figure 2.14, the friction coefficient can therefore be connected to the surface topography as $c_f = \tan\theta_s$, with θ_s characterizing the maximum slope of the surface. More than a century after Coulomb's experiments, Bowden and Tabor [101] measured the evolution of the electric conductance across two blocks in contact and drew two landmark conclusions:

1. The real area of contact A_r between two nominally flat surfaces represents a tiny portion ($< 1\%$) of the apparent area of contact A.
2. A_r is progressively increasing with normal pressure.

In light of these observations, they proposed a novel interpretation of Amontons-Coulomb law: Two rough surfaces only come in contact at their surface peaks. The entire normal pressure is carried through these scattered contact points, such that the local normal pressure reaches very high values sufficient to yield the material. The normal far-field pressure can hence be written as

$$\sigma^0 = \frac{A_r}{A} \sigma^{\text{Y}}, \tag{2.85}$$

with σ^{Y} corresponding to the material yield stress. These *microcontacts junctions* represent highly confined regions, where the shear stress will also localize. Similarly, if one defines the shear strength of the junction τ_c, the macroscopic shear stress can be written as

$$\tau_s = \frac{A_r}{A} \tau_c. \tag{2.86}$$

Combining Equations 2.85 and 2.86 leads to $c_f = \tau_c / \sigma^Y$, which explains the independence of the friction coefficient to the apparent contact area A or the normal pressure. Moreover,

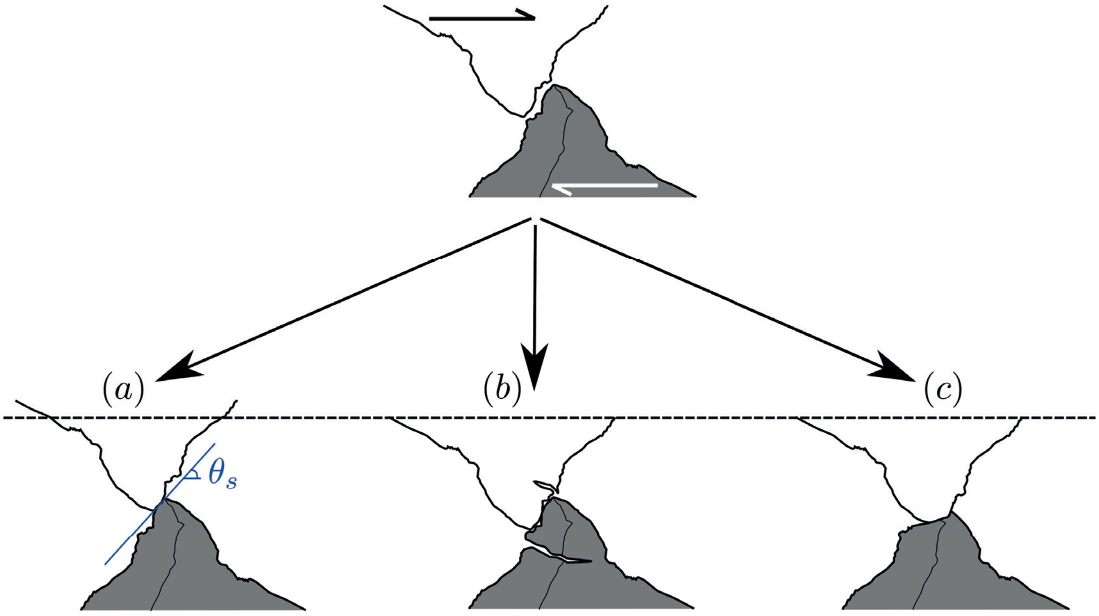

Figure 2.14 – The frictional strength emerges from the micromechanical interlocking of asperities along the rough surfaces. Three behaviors were suggested in the literature: a) Coulomb's geometrical interpretation: Rigid uplifting along the contacting plane forming at an angle θ_s. b) Brittle fracture of the contacting apexes predicted by Byerlee [4]. c) Gradual plastic smoothing of the microcontact junction pictured by Bowden and Tabor [5].

the ratio τ_c/σ^Y is consistent with the value of the friction coefficient measured for metals $0.6 < c_f < 1.2$ [5]. The linear dependency between the real contact area and the normal pressure predicted in Equation 2.85 was later verified using a more rigorous resolution of the contact problem [102] or realistic self-affine rough surfaces [103, 104]. For brittle materials, Byerlee [4] revised the Equation 2.86 by assuming that slipping does not occur through the plastic shearing of junctions but rather by fracturing the microcontacts, which leads to a smaller value of the friction coefficient ($c_f \sim 0.1$) in agreement with the ones measured for rock interfaces. Recently Aghababaei *et al.* [105, 106] defined a characteristic microcontact junction size d^* allowing to predict the observed transition between these two mechanisms illustrated in Figure 2.14. Microcontacts smaller than d^* rupture following the plastic shearing of the junction suggested by Bowden and Tabor [5]. Conversely, microcontact junctions larger than d^* break through the brittle failure of their apexes according to Byerlee's picture [4]. Along self-affine rough surfaces, these two rupture mechanisms co-exist at the onset of sliding [107] but their respective impact on the slip front dynamics is still overlooked and will be investigated in Chapter 7.

The Amontons-Coulomb friction model represents a remarkably simple first-order approximation, widely used in many physical and engineering applications. However it is insufficient to describe systems, for which friction is the core driving mechanism. In particular, it cannot predict stick-slip dynamics, which arise from the weakening of friction as the interface transitions from static c_f^{stat} to dynamic c_f^{dyn} sliding conditions [90, 108]. Rabinowicz's experiments [109] described how frictional interfaces require to slip over a characteristic distance δ_c for the friction coefficient to drop from its static to its dynamic value. This behavior inspires the first slip-weakening models proposed by Ida [110] and later adapted by Andrews [6, 47]. These friction laws received a significant interest for their direct analogy with cohesive models of fracture and will be discussed with more details in Section 2.3.2.

However, several frictional experiments [22, 111] reported how c_d^f is not a constant value and depends on the sliding rate v [112] and the contact time [109, 113]. In order to approach this experimental evolution of c_f, Dieterich [22] and later Ruina [23] proposed a generic empirical law:

$$c_f(v,\phi) = c_f^0 + a\ln\left(\frac{v}{v^*}\right) + bc_f^0\ln\left(\frac{\phi v^*}{D}\right). \tag{2.87}$$

The relation above introduces then a rate-dependency as well as a dependency to a state variable ϕ, which is often interpreted as the average microcontacts lifetime. In Equation 2.87, c_f^0, a, b, v^*, are several empirical parameters derived from laboratory experiments and were successfully used to reproduce the frictional response universally observed along different kinds of interfaces (polymer, glass, rock, wood, paper) [91, 114]. Figure 2.15c illustrates the typical response predicted by rate-and-state formulations to a sudden change in sliding velocity.

Furthermore, the logarithmic increase of c_f with contact time is typically accounted within rate-and-state formulations by the following *evolution law* proposed by Dieterich [22]:

$$\dot{\phi} = 1 - \frac{v\phi}{D}. \tag{2.88}$$

Taking advantage of the transmission of light across microcontact junctions and its reflection in absence of contact, Dieterich and Kilgore [91] directly observed the map of microcontacts by projecting a beam of light through two transparent blocks of PMMA pressed in contact. Their experiments allowed to confirm how the real area of contact increases by the creep of microcontacts. The evolution law further describes the *rejuvenation* of microcontact populations during frictional sliding. In particular, for steady-state sliding at v^{ss}, the existing microcontacts are destroyed at the same rate that new ones are created such that ϕ reaches a constant value:

$$\phi^{\text{ss}} = \frac{D}{v^{\text{ss}}}. \tag{2.89}$$

Hence, D represents a characteristic size of the microcontact junctions, typically in the micrometer range for laboratory experiments. Combining Equations 2.87 and 2.89, this rate-and-state constitutive law predicts velocity-weakening friction for

$$\frac{dc_f^{\text{ss}}}{d(\ln v^{\text{ss}})} = a - bc_f^0 < 0. \tag{2.90}$$

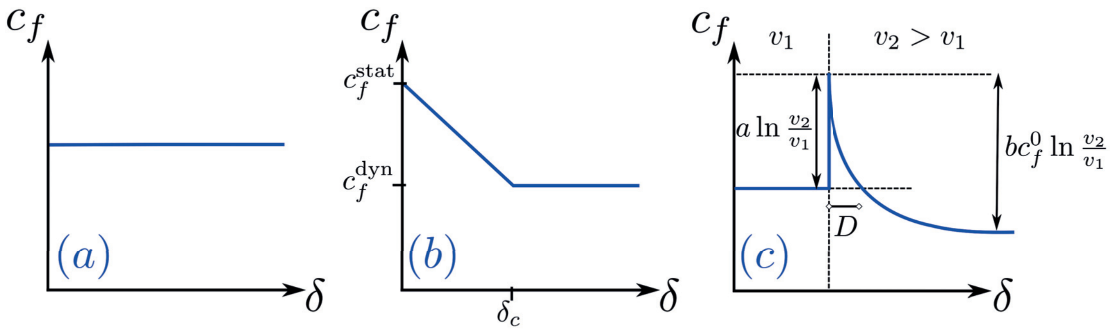

Figure 2.15 – The different kinds of friction laws existing in the literature. a) Amontons-Coulomb friction law (Equation 2.84). b) The slip-weakening law (Equation 2.93). c) The rate-and-state friction law (Equation 2.87).

Velocity-weakening has been widely observed for the ranges of sliding velocity typically studied in experiments [114] and its origin is associated to a faster renewal of microcontacts with larger sliding velocities. The intrinsic instability of velocity-weakening friction has been suggested as a potential mechanism for earthquake nucleation [23, 108, 115–117]. However, several works discussed how the velocity-weakening regime breaks down at much smaller or much larger sliding velocities [114, 118, 119].

Following the original works of Dieterich [22] and Ruina [23], many different rate-and-state formulations have been proposed in the literature and the reader is redirected to [120] for a detailed review. However, many questions remain open about their physical impact on the dynamics of rupture events and motivate for physics-based interpretations of rate-and-state formulations. For example, Baumberger *et al.* [121] connected them to the microcontacts picture proposed by Bowden and Tabor [101]. Therefore, they rewrote Equation 2.86 after assuming that v mainly affects the local strength of the junction, while ϕ controls the real contact area:

$$\tau_s = \sigma^0 c_f(v, \phi) = \frac{A_r(\phi)}{A} \tau_c(v). \tag{2.91}$$

In particular, they suggested that the real contact area scales as

$$A_r(\phi) \sim 1 + b \ln\left(\frac{\phi v^*}{D}\right). \tag{2.92}$$

Inspired from this interpretation, Chapter 8 presents an approach to rationalize the dynamics of slip fronts in the framework of rate-and-state friction laws.

2.3.2 The elastodynamic approach

In parallel to the laboratory studies of friction presented above, another category of works focused on the macroscopic behavior of frictional systems at the onset of sliding, using the elastodynamic wave equation to study the energy budget of slip fronts. In this context, the propagation of a slip front along a frictional interface or a crustal fault was rationalized as a dynamic shear crack driven by the release of strain energy accumulated around the fault [122]. This elastodynamic approach of friction is therefore grounded on the same dynamic fracture concepts introduced previously in Section 2.2. Similarly, cohesive models were developed to regularize the infinite shear stress theoretically predicted at the tip of a singular shear crack [47, 110]. These models assumed that the friction coefficient drops from a static c_f^{stat} to a dynamic c_f^{dyn}, once the frictional slip δ_s reaches a characteristic distance δ_c. The resulting *slip-weakening* law illustrated in Figure 2.15b is equivalent to the cohesive model of fracture proposed by Dugdale [20] and Barenblatt [21], such that the frictional strength can be written as

$$\tau^{\text{str}}(x,z,t)/\sigma^0 = c_f^{\text{stat}} - (c_f^{\text{stat}} - c_f^{\text{dyn}})\min\Big\{\delta_s(x,z,t)/\delta_c; 1\Big\}. \tag{2.93}$$

Taking advantage of the linear elasticity of the surrounding bulk, Palmer and Rice [40] demonstrated how this formulation can be directly mapped on the dynamic fracture mechanics description after subtracting the residual shear stress τ^r. Using,once more, the mode III shear crack solution given in Equation 2.69, such decomposition can be written as

$$\sigma_{yz} = \Delta\tau + \tau^r = \frac{K_{III}}{\sqrt{2\pi x}} + \sigma^0 c_f^{\text{dyn}}, \tag{2.94}$$

while the integral of the dissipated energy is therefore given by

$$G_c = \int_0^{\delta_c} \Delta\tau \, d\delta_s = \int_0^{\delta_c} \Big(\tau(\delta_s) - \tau^r\Big) d\delta_s = \frac{1}{2}\sigma^0 (c_f^{\text{stat}} - c_f^{\text{dyn}})\delta_c. \tag{2.95}$$

G_c corresponds then to an equivalent fracture energy of the frictional interface. The remaining energy is interpreted as heat dissipation [6]. The slip-weakening laws, for which both τ^r and G_c are prescribed, share a direct analogy with the cohesive formulation of fracture (cf. Section 3) and have therefore been extensively used to study the rupture dynamics of seismic events including the speed of the front [47, 123, 124] and its interplay with fault heterogeneities [80–83, 85, 125] already discussed in the previous section.

Recent frictional experiments [126–129] measured the strains evolution near the interface during the onset of slip. Using Palmer and Rice decomposition, they quantitatively demonstrated how dynamic fracture mechanics perfectly describes the slip fronts propagation and arrest along dry and lubricated interfaces. However, they revealed how the nucleation of slip fronts still eludes the classical fracture mechanics models [24]. An illustrative situation arises after the lubrication of the interface which increases its measured fracture energy, but reduces, at the same time, the required force to initiate sliding. This “slippery but tough” paradox was presumed to emerge from the microscopic nature of contact and will be discussed in Chapter 7.

The estimation of the energy budget/partition of earthquakes also inherits from the slip-weakening description of friction. Abercombie and Rice [130] proposed a generalization of Equation 2.95 to integrate the equivalent fracture energy of earthquakes as function of the post-seismic slip distance δ_p:

$$G_c(\delta_p) = \int_0^{\delta_p} \Big(\tau(\delta_s) - \tau(\delta_p)\Big) d\delta_s. \tag{2.96}$$

However the estimation of the equivalent fracture energy of large earthquakes systematically overestimates the value measured experimentally, and shaping a precise partition of the seismic energy budget, still represents a major challenge in geophysics [131–134]. In this context, Chapter 8 discusses the equivalent fracture energy predicted from rate-and-state formulations and its divergences with the predictions from slip-weakening models.

In light of the two approaches presented above, the onset of slip along frictional interfaces is a fascinating example of a heterogeneous dynamic rupture, as it results from the interplay of the crack-like elastodynamics with the local heterogeneous topography of frictional interfaces. For a detailed presentation of this wide topic, the reader is referred to textbooks [90, 122].

3 Numerical framework

Cracks represent discontinuities existing within solids, at the tip of which stresses are singular. Their modeling within numerical models is hence particularly challenging. However, no material is able to withstand the stress singularity theoretically existing at the tips of crack, which implies the existence of a process zone where material-dependent dissipative processes are regularizing the singularity (cf. Figure 2.7). In this context, Dugdale [20] and Barenblatt [21] proposed an elegant way of modeling these nonlinear processes without loosing the universality of the LEFM theory. In their model, referred to as the *cohesive approach* of fracture, the crack tip is smeared over space and time by the progressive reduction of interface strength τ^{str} (i.e. its ability to transfer tractions across the rupture plane) from τ_c to zero as crack is opening:

$$\frac{\tau^{\text{str}}}{\tau_c} = \mathscr{F}(\boldsymbol{\delta}). \tag{3.1}$$

$\boldsymbol{\delta}$ represents the crack opening displacement vector while τ_c can be understood as the maximal material strength. $\mathscr{F}(\boldsymbol{\delta})$ is known as the *cohesive law* and Figure 3.1 gives two examples of cohesive laws used later in this thesis. Moreover, the value of the fracture energy can be prescribed locally in cohesive models and corresponds to:

$$G_c = \int \tau_c \mathscr{F}(\boldsymbol{\delta})\, d\boldsymbol{\delta}. \tag{3.2}$$

Apart from regularizing the stress singularity, the other great advantage of cohesive approaches is to assume that every dissipative process is contained within the fracture plane and described by the cohesive law. Hence, the rest of the continuum can still be studied within the conventional frameworks of continuum mechanics, and classical constitutive laws such as linear elasticity. This thesis focuses on perturbations occurring at the scale of the fracture process zone of dynamic cracks and requires, therefore, a particularly fine discretization of the rupture plane. The formulation adopted in the major part of this manuscript relies on a boundary integral formulation of the elastodynamic equation, for which all the numerical effort is invested along the rupture plane.

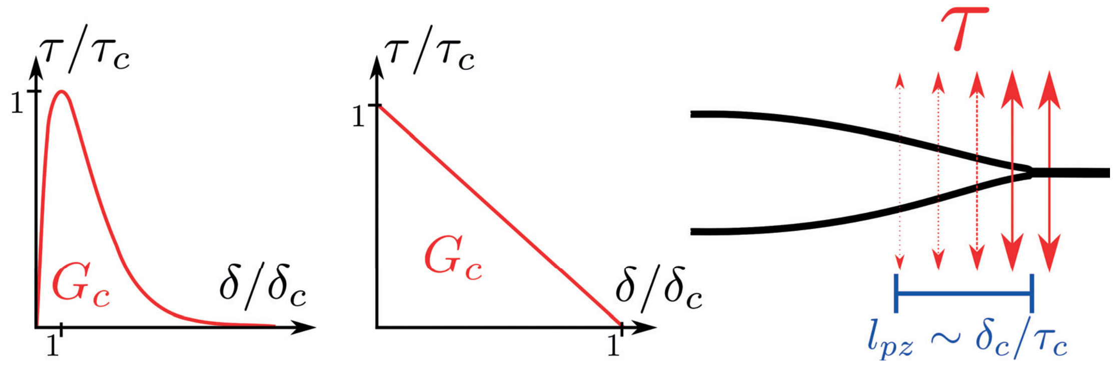

Figure 3.1 – The exponential (**Left**) and linear-decreasing (**Right**) cohesive laws adopted in this manuscript. In the cohesive approaches of fracture, the amplitude of the tractions carried across the interface progressively drops to zero (i.e. free surface conditions) as a function of crack opening displacement δ. Consequently, the crack tip is not singular but smeared over a finite distance, the fracture process zone l_{pz}. Throughout the manuscript, this framework is equivalently applied to study each fracture mode, as well as mixed mode conditions.

3.1 Spectral boundary integral formulation

The boundary integral formulation solves the tractions and displacements existing at the surface lying between two semi-infinite continua. Two formulations were proposed in the literature, the *combined formulation* [16,135], which solves simultaneously the top and bottom half-spaces and the *independent formulation*, which considers the top and bottom solids separately [17]. This thesis relies on the independent formulation which is more stable and allows for describing bimaterial interfaces.

To illustrate the derivation of the spectral boundary integral formulation, let us consider only the bottom half-space with the convenient anti-plane shear setup (Equations 2.33). $u_z(x, y, t)$ is first expressed in spatial Fourier[1] $U(k, y, t)$ and then in the combined Fourier (spatial) and Laplace[2] (temporal) space $\tilde{U}(k, y, p)$. In this $k-y-p$ space, the wave equation becomes

$$c_s^2(-k^2\tilde{U} + \tilde{U}_{,yy}) = p^2\tilde{U} - pU_{t_0} - \dot{U}_{t_0}. \tag{3.3}$$

The solid is assumed to be initially at rest such that (i.e. $U_{t_0} = U(k, y, 0) = 0$, $\dot{U}_{t_0} = \dot{U}(k, y, 0) = 0$) and

$$c_s^2\tilde{U}_{,yy} = (p^2 + c_s^2k^2)\tilde{U} \tag{3.4}$$

$$\tilde{U}_{,yy} = k^2\beta_s^2\tilde{U}, \tag{3.5}$$

---

[1] Joseph Fourier (1768-1830)

[2] Pierre-Simon Laplace (1749-1827)

with $\beta_s = \sqrt{1+\frac{p^2}{k^2 c_s^2}}$. The general solution of this ODE has the form

$$\tilde{U}(k,y,p) = Ae^{|k|\beta_s y} + Be^{-|k|\beta_s y}. \tag{3.6}$$

Semi-infinite boundary conditions $\tilde{U}(k,\infty,p)=0$ and $\tilde{U}(k,0,p)=\tilde{U}_0(k,p)$ lead to

$$\tilde{U}(k,y,p) = \tilde{U}_0(k,p)e^{-|k|\beta_s y}. \tag{3.7}$$

The functional $\tilde{U}_0(p,k)$ represents the displacement field at the interface which should be related to its associated interface tractions $\boldsymbol{\tau}$. The projection of Cauchy stress tensor at the interface of normal $\boldsymbol{n} = (0,1,0)^\top$ is a three-component vector $\boldsymbol{\tau} = \underline{\boldsymbol{\sigma}} \cdot \boldsymbol{n} = (\sigma_{xy}, \sigma_{yy}, \sigma_{yz})^\top$. In our mode III setup of interest ($\frac{\partial}{\partial z} = 0$ and $u_x = u_y = 0$), the only non-zero component is the out-of-plane shear stress $\sigma_{yz} = \tau_z$. The constitutive law writes

$$\tau_z(x,t) = \mu \frac{\partial u_z(x,y=0,t)}{\partial y}, \tag{3.8}$$

which becomes in the $k-y-p$ space

$$\tilde{T}(k,p) = \mu \frac{\partial \tilde{U}(k,y=0,p)}{\partial y} = -\mu|k|\beta_s \tilde{U}_0(k,p). \tag{3.9}$$

The final step consists in decomposing $\tilde{U}_0(k,p)$ in an instantaneous part and a part depending on the history:

$$\tilde{T}(k,p) = -\frac{\mu}{c_s} p\tilde{U}_0(k,p) - \mu|k|\left(\beta_s - \frac{p}{|k|c_s}\right)\tilde{U}_0(k,p), \tag{3.10}$$

whose formulation in the $k-y-t$ space is then

$$T(k,t) = -\frac{\mu}{c_s}\frac{\partial}{\partial t}U_0(k,t) + F_z(k,t). \tag{3.11}$$

In the equation above, F_z is then expressed as a convolution over the displacement history:

$$F_z(k,t) = -\mu|k|\int_0^t K(t-t')U_0(k,t')dt', \tag{3.12}$$

with the convolution kernel $K(t)$ computed through an inverse Laplace transform $\mathscr{L}_p^{-1}$ as

$$K(t) = \mathscr{L}_p^{-1}\left\{\sqrt{1+\frac{p^2}{k^2 c_s^2}} - \frac{p}{|k|c_s}\right\}. \tag{3.13}$$

Let us define $w = |k|c_s > 0$ and rewrite this kernel

$$\begin{aligned}
K(t) &= \mathscr{L}_p^{-1}\left\{\sqrt{1+\frac{p^2}{w^2}}-\frac{p}{w}\right\} = \mathscr{L}_p^{-1}\left\{\frac{\sqrt{w^2+p^2}-p}{w}\right\} = \mathscr{L}_p^{-1}\left\{\frac{w^2+p^2-p\sqrt{w^2+p^2}}{w\sqrt{w^2+p^2}}\right\}\\
&= \frac{w}{2}\mathscr{L}_p^{-1}\left\{\frac{w^2+(\sqrt{w^2+p^2}-p)^2}{w^2\sqrt{w^2+p^2}}\right\} = \frac{w}{2}\left[\mathscr{L}_p^{-1}\left\{\frac{1}{\sqrt{w^2+p^2}}\right\}+\mathscr{L}_p^{-1}\left\{\frac{(\sqrt{w^2+p^2}-p)^2}{w^2\sqrt{w^2+p^2}}\right\}\right]\\
&= \frac{w}{2}\left[J_0(wt)\mathscr{H}(t)+J_2(wt)\mathscr{H}(t)\right] = w\mathscr{H}(t)\frac{J_1(wt)}{wt}.
\end{aligned} \tag{3.14}$$

The heaviside function $\mathscr{H}(t) = 1$ since $t > 0$ and one obtains therefore

$$F_z(k,t) = -\mu|k|\int_0^t H_{zz}\Big(|k|c_s(t-t')\Big)U_0(k,t')|k|c_s\,dt'\,;\;\; H_{zz}(\gamma) = \frac{J_1(\gamma)}{\gamma}. \tag{3.15}$$

After transforming Equation 3.11 back in real space and adding the contribution of the far-field initial stress τ_z^0, the equation of motion at the interface of a semi-infinite solid is then written as:

$$\tau_z(x,t) = \tau_z^0(x,t) - \frac{\mu}{c_s}\dot{u}_z(x,t) + f_z(x,t). \tag{3.16}$$

The equation above corresponds to the boundary integral formulation of the elastodynamic problem. The first right hand side (RHS) term corresponds to the far-field initial loading conditions, the last RHS term f_z accounts for the history of displacements along the interface, while the second RHS term represents the instantaneous stress response to a change in sliding velocity. This term can be understood as the damping of interface energy caused by elastic waves leaving in the infinite domain. Hence, it is sometimes referred to as the *radiation damping term*. Equation 3.16 can be generalized for the 3D elastodynamics of an interface bounding two dissimilar solids as:

$$\boldsymbol{\tau}^{\pm}(x,z,t) = \boldsymbol{\tau}^{\mathbf{0}\pm}(x,z,t) - \underline{\boldsymbol{V}}^{\pm}\frac{\partial \boldsymbol{u}^{\pm}}{\partial t}(x,z,t) + \boldsymbol{f}_j^{\pm}(x,z,t), \tag{3.17}$$

with

$$\underline{\boldsymbol{V}}^{\pm} = \frac{\mu^{\pm}}{c_s^{\pm}}\begin{bmatrix} 1 & 0 & 0\\ 0 & \eta^{\pm} & 0\\ 0 & 0 & 1\end{bmatrix}. \tag{3.18}$$

In this three-dimensional problem, the convolution terms become:

$$\begin{aligned} \begin{Bmatrix} F_x^\pm(k,m,t)\\ F_y^\pm(k,m,t)\\ F_z^\pm(k,m,t)\end{Bmatrix} &= -i\mu^\pm(2-\eta^\pm)\begin{pmatrix}0&-k&0\\k&0&m\\0&-m&0\end{pmatrix}\begin{Bmatrix} U_x^\pm(k,m,t)\\ U_y^\pm(k,m,t)\\ U_z^\pm(k,m,t)\end{Bmatrix}\\ &-\mu^\pm q\int_0^t\left[i\frac{H_{xy}^\pm(qc_s^\pm t')}{|q|}\begin{pmatrix}0&-k&0\\k&0&m\\0&-m&0\end{pmatrix} \pm H_{yy}^\pm(qc_s^\pm t')\begin{pmatrix}0&0&0\\0&1&0\\0&0&0\end{pmatrix}\right.\\ &\left.\pm\frac{H_{xx}^\pm(qc_s^\pm t')}{q^2}\begin{pmatrix}k^2&0&km\\0&1&0\\km&0&m^2\end{pmatrix} \pm\frac{H_{zz}^\pm(qc_s^\pm t')}{q^2}\begin{pmatrix}m^2&0&-km\\0&1&0\\-km&0&k^2\end{pmatrix}\right]\begin{Bmatrix} U_x^\pm(k,m,t-t')\\ U_y^\pm(k,m,t-t')\\ U_z^\pm(k,m,t-t')\end{Bmatrix}|q|c_s^\pm dt' \end{aligned} \tag{3.19}$$

These convolutions are connecting in the Fourier domain the displacements $\boldsymbol{u}^\pm$ and associated tractions $\boldsymbol{f}^\pm$:

$$\begin{Bmatrix} \boldsymbol{f}^\pm(x,z,t)\\ \boldsymbol{u}^\pm(x,z,t)\end{Bmatrix} = e^{i(kx+mz)}\begin{Bmatrix} \boldsymbol{F}^\pm(k,m,t)\\ \boldsymbol{U}^\pm(k,m,t)\end{Bmatrix}, \tag{3.20}$$

with $q=\sqrt{k^2+m^2}$. Unlike their mode III counterpart, the convolution kernels $H_{xx}^\pm$, $H_{xy}^\pm$ and $H_{yy}^\pm$ do not have closed-form expressions and their inverse Laplace transforms are precomputed numerically. Their full expression can be found in [17] and their evolution is presented in Figure 3.2 for $\nu=0.35$.

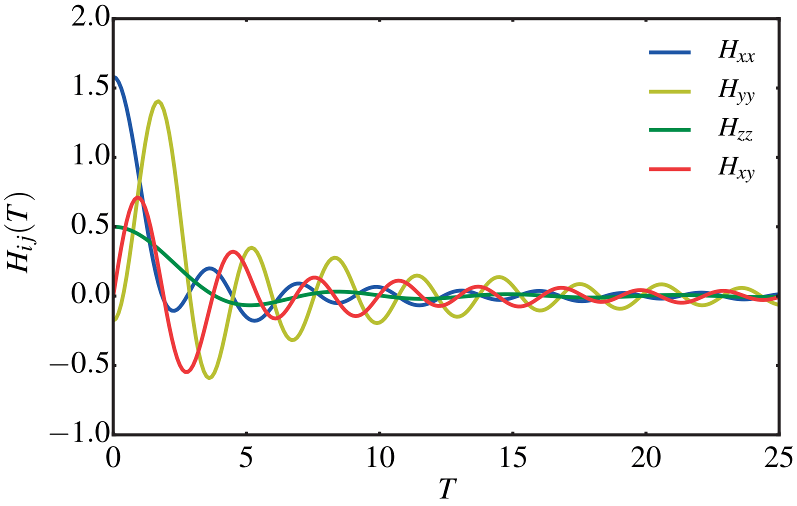

Figure 3.2 – Convolution kernels entering the spectral formulation $H_{ij}(T)$ for $\nu=0.35$.

At each time t, two unknowns per side exist in Equation 3.17, namely $\boldsymbol{\tau}^\pm$ and $\partial\boldsymbol{u}^\pm/\partial t$, which are solved using interface conditions. Several interface conditions are considered in this thesis (bimaterial, mode I and II, rate-and-state friction) and will be presented later on a case-to-case basis. Finally time is integrated using an explicit time stepping scheme such that

$$\boldsymbol{u}^{\pm}(x,z,t+\Delta t) = \boldsymbol{u}^{\pm}(x,z,t) + \frac{\partial \boldsymbol{u}^{\pm}}{\partial t}(x,z,t)\Delta t, \tag{3.21}$$

with Δt being the time step defined through a Courant-Friedrichs-Lewy (CFL) conditions [136] of the kind

$$\max(c_s^+; c_s^-)\Delta t = \beta \Delta x, \tag{3.22}$$

with $0.2 \leq \beta \leq 0.4$ as a function of the studied problem [17]. Due to the spectral nature of the scheme, the spatial discretization consists in a periodic grid of spacing $\Delta x = \Delta z$.

My own parallel implementation[3] of the algorithm is used behind the simulations reported in this thesis. The convolution operations reported in Equation 3.19 are computed within a shared-memory parallel framework, while the computational cost is further reduced by introducing a kernel cut ($100 \geq \gamma = q c_s^{\pm} t$) as discussed in [137].

3.2 Finite-element method

The finite-element method is one of the most popular numerical approaches existing to solve boundary value problems in science and engineering. This success is explained by its great versatility to compute any kinds of geometries at the cost of a full discretization of the continuum. This section aims at giving a general picture of the method, but for a complete presentation of the finite-element approach and its application in continuum solid mechanics, the reader is referred to reference textbooks [18, 19].

3.2.1 Standard bulk element

As illustrated in Figure 3.3, the continuum is divided into smaller units (the elements) over which the weak formulation of the problem (cf. Equation 2.28) is solved:

$$\int_{\Omega^e} \underline{\boldsymbol{\sigma}} : \underline{\hat{\boldsymbol{\varepsilon}}} dV + \int_{\Omega^e} \rho \ddot{\boldsymbol{u}} \cdot \hat{\boldsymbol{u}} dV - \int_{\partial\Omega^e_\tau} \overline{\boldsymbol{\tau}} \cdot \hat{\boldsymbol{u}} dA = 0 \tag{3.23}$$

Following the works of Ritz [138] and Galerkin [139], the displacement and virtual displacement fields are approximated by

$$\begin{aligned} \boldsymbol{u}(\boldsymbol{x},t) &= \underline{\boldsymbol{N}}\boldsymbol{u}, \\ \hat{\boldsymbol{u}}(\boldsymbol{x},t) &= \sum_{i=1}^{n} N_i(\boldsymbol{x})\hat{\boldsymbol{u}}_i(t) = \underline{\boldsymbol{N}}\hat{\boldsymbol{u}}, \end{aligned} \tag{3.24}$$

---

[3] *cRacklet*: https://c4science.ch/project/view/701/

with N_i being piecewise interpolation functions across the elements also known as *shape functions*. i represents discretization points referred to as the *nodes* of the finite-element mesh. Defining $\underline{\boldsymbol{B}}$ as the derivatives of the shape functions, such that $\underline{\boldsymbol{B}}(\boldsymbol{x})\boldsymbol{u} = \underline{\boldsymbol{\varepsilon}}$, Equation 3.23 is evaluated over the volume of each element Ω_e as:

$$\hat{\boldsymbol{u}}^\top \int_{\Omega^e} \underline{\boldsymbol{B}}^\top \underline{\underline{\boldsymbol{C}}}\,\underline{\boldsymbol{B}}\boldsymbol{u}\,dV + \hat{\boldsymbol{u}}^\top \int_{\Omega^e} \underline{\boldsymbol{N}}^\top \rho \underline{\boldsymbol{N}}\ddot{\boldsymbol{u}}\,dV - \hat{\boldsymbol{u}}^\top \int_{\partial\Omega^e_\tau} \underline{\boldsymbol{N}}^\top \bar{\boldsymbol{\tau}}\,dA = 0. \tag{3.25}$$

These integrals are then evaluated over each element to build the local matrices

$$\underline{\boldsymbol{K}}_e = \int_{\Omega^e} \underline{\boldsymbol{B}}^\top \underline{\underline{\boldsymbol{C}}}\,\underline{\boldsymbol{B}}\,dV,\ \underline{\boldsymbol{M}}_e = \int_{\Omega^e} \underline{\boldsymbol{N}}^\top \rho \underline{\boldsymbol{N}}\,dV,\ \boldsymbol{F}_e^{\text{ext}} = \int_{\partial\Omega^e_\tau} \underline{\boldsymbol{N}}^\top \bar{\boldsymbol{\tau}}\,dA, \tag{3.26}$$

which are then assembled into a global system of equations (in absence of any damping term):

$$\sum_e \left(\underline{\boldsymbol{K}}_e\right)\boldsymbol{u} + \sum_e \left(\underline{\boldsymbol{M}}_e\right)\ddot{\boldsymbol{u}} - \sum_e \left(\boldsymbol{F}_e^{\text{ext}}\right) = \underline{\boldsymbol{K}}\boldsymbol{u} + \underline{\boldsymbol{M}}\ddot{\boldsymbol{u}} - \boldsymbol{F}^{\text{ext}} = 0. \tag{3.27}$$

For the simulations reported in this manuscript, the resulting elastodynamic system is integrated using an explicit time integration scheme based on a Newmark-β method [140], which is particularly well-suited for transient elastodynamic problems such as dynamic ruptures or impacts:

$$\begin{cases} \boldsymbol{u}(x, y, t+\Delta t) = \boldsymbol{u}(x, y, t) + \Delta t\,\dot{\boldsymbol{u}}(x, y, t) + \dfrac{1}{2}(\Delta t)^2 \ddot{\boldsymbol{u}}(x, y, t) \\ \dot{\boldsymbol{u}}(x, y, t+\Delta t) = \dot{\boldsymbol{u}}(x, y, t) + \dfrac{\Delta t}{2}\left(\ddot{\boldsymbol{u}}(x, y, t) + \ddot{\boldsymbol{u}}(x, y, t+\Delta t)\right). \end{cases} \tag{3.28}$$

The kinematic unknowns $\boldsymbol{u}$, $\dot{\boldsymbol{u}}$ and $\ddot{\boldsymbol{u}}$ are hence solved at the time $t+\Delta t$ according to the following scheme:

1. Prediction

$$\begin{aligned} \boldsymbol{u}(t+\Delta t) &= \boldsymbol{u}(t) + \Delta t\,\dot{\boldsymbol{u}}(t) + \frac{\Delta t^2}{2}\ddot{\boldsymbol{u}}(t) \\ \dot{\boldsymbol{u}}(t+\Delta t) &= \dot{\boldsymbol{u}}(t) + \frac{\Delta t}{2}\ddot{\boldsymbol{u}}(t) \end{aligned} \tag{3.29}$$

2. Assemble and solve

$$\delta\ddot{\boldsymbol{u}} = \underline{\boldsymbol{M}}^{-1}\left(\boldsymbol{F}^{\text{ext}}(t) - \underline{\boldsymbol{K}}\dot{\boldsymbol{u}}(t+\Delta t) - \underline{\boldsymbol{M}}\ddot{\boldsymbol{u}}(t)\right) \tag{3.30}$$

3. Update

$$\begin{aligned} \dot{\boldsymbol{u}}(t+\Delta t) &= \dot{\boldsymbol{u}}(t+\Delta t) + \frac{\Delta t}{2}\delta\ddot{\boldsymbol{u}}, \\ \ddot{\boldsymbol{u}}(t+\Delta t) &= \ddot{\boldsymbol{u}}(t+\Delta t) + \delta\ddot{\boldsymbol{u}}. \end{aligned} \tag{3.31}$$

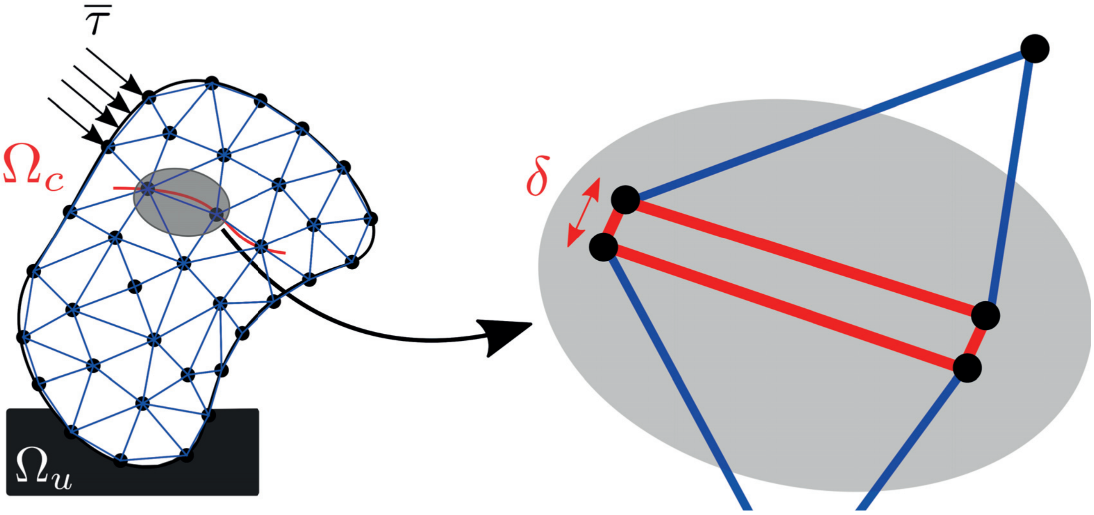

Figure 3.3 – Typical elastodynamic boundary value problem solved following a finite-element method. The continuum contains a crack surface Ω_c (in red), whose discretization and representation using a cohesive element is detailed.

This explicit scheme described by 3.29, 3.30 and 3.31 is however conditionally stable and the following CFL condition is typically ensured in the simulations reported in this manuscript

$$\Delta t = 0.7\frac{\Delta s}{c_d}, \tag{3.32}$$

with Δs being the smallest element size of the finite-element mesh.

Several well-established approaches exist nowadays to integrate crack and their propagation within finite-element models, such as the phase field [141, 142] or the extended finite-element approaches [143]. A cohesive approach is adopted, for the problems of interface rupture studied in this thesis.

3.2.2 Cohesive element

Figure 3.3 presents a finite-element domain containing a crack along the surface Ω_c. Following the hypothesis of the cohesive approach, every dissipative process arises within Ω_c such that the surrounding continuum still follows the linear elastic behavior. More details about the cohesive approach within finite-element model can be found in [144, 145].

The virtual work contribution of the cracked surface can be written as:

$$\int_{\Omega_c} \boldsymbol{\tau}(x,t)\cdot\hat{\boldsymbol{\delta}}\,dA. \tag{3.33}$$

A *cohesive element* is hence introduced along Ω_c and bridges nodes from the top and bottom surfaces as illustrated in Figure 3.3. The interpolation function of the cohesive element $\underline{\boldsymbol{P}}$ can hence be constructed using the one of the standard elements according to:

$$\boldsymbol{\delta} = \boldsymbol{u}^+ - \boldsymbol{u}^- = \sum_{i^+=1}^{n} N_{i^+}(\boldsymbol{x})\boldsymbol{u}_{i^+}(t) - \sum_{i^-=1}^{n} N_{i^-}(\boldsymbol{x})\boldsymbol{u}_{i^-}(t) = \sum_{i=1}^{2n} P_i(\boldsymbol{x})\boldsymbol{u}_i(t). \tag{3.34}$$

From the cohesive formulation (Equations 3.2) together with Equations 3.33 and 3.34, the vector of external forces in presence of cohesive elements e' can then be computed and assembled as

$$\boldsymbol{F}^{\text{ext}} = \sum_e \left(\boldsymbol{F}_e^{\text{ext}}\right) + \sum_{e'} \left(\int_{\partial\Omega_c^e} \underline{\boldsymbol{P}}^\top \boldsymbol{\tau}\, dA\right) = \sum_e \left(\boldsymbol{F}_e^{\text{ext}}\right) + \sum_{e'} \left(\int_{\partial\Omega_c^e} \underline{\boldsymbol{P}}^\top \tau_c \mathscr{F}(\boldsymbol{\delta})\, dA\right). \tag{3.35}$$

To comply with the requirement of a very fine discretization of the rupture plane, the simulations reported in this thesis rely on a scalable parallel finite-element implementation developed within our laboratory and capable of computing several millions of nodes on high performance computing clusters. This open source finite-element library named *Akantu* is freely available online[4], while its technical description is given in [146, 147].

---

[4] https://c4science.ch/project/view/34/

4 Dynamic fracture along bimaterial interfaces

This chapter studies a first type of heterogeneous interfaces existing between two solids made of different elastic properties. Such interfaces became prominent within lightweight composite materials or along geological layers and represent weak rupture planes channeling the crack propagation and leading to much faster ruptures than within an isotropic material. Moreover, the elastic mismatch across the rupture plane makes it an intrinsically mixed mode fracture problem and leads to little-understood dynamic instabilities visible in tensile experiments as large scale contact zones traveling in the wake of the crack front. This chapter presents the simulations and descriptions of the different phenomena observed experimentally (distinct natures of contact zones, unfavorable velocity range, asymmetric crack propagation). It shows that different behaviors are observed as a function of the crack propagation direction, i.e., with respect to the particle displacements of the compliant material. When the crack propagates in the same direction, the propagation velocities between c_R and c_s are forbidden and the subsonic/intersonic transition occurs with the nucleation of a daughter crack in front of the main rupture. The intersonic stress field at the crack front is compressive due to the material mismatch and a contact zone appears behind the tip. In the opposite direction, a smooth subsonic/intersonic transition occurs although a crack face closure (in the normal direction) is observed for speeds between c_s and $\sqrt{2}c_s$. In this regime, a Rayleigh disturbance is generated at the crack surface causing a contact zone which detaches from the tip. Using a contact model governed by a regularized Coulomb law, this work provides a quantitative evaluation of the influence of friction on the effective fracture energy. Finally, the applicability of our analysis to the description of different bimaterial situations as well as the single-material set-up is demonstrated.

This chapter is a modified version of a scientific article published by Elsevier:

F. Barras, D. S. Kammer, P. H. Geubelle, and J.-F. Molinari, “A study of frictional contact in dynamic fracture along bimaterial interfaces,” *International Journal of Fracture*, vol. 189, no. 2, pp. 149–162, 2014

4.1 Introduction

Intersonic debonding, for which the speed of the front exceeds the shear wave speed of the material, has received increasing attention over the past two decades. Although intersonic crack growth was thought to be unattainable for a while, it is now acknowledged that it plays an important role in interface failure of multi-phase materials, composites or geophysical layers.

Experiments of crack propagation in homogeneous brittle solids measured crack propagations always slower than 65 percent of the material's Rayleigh wave speed c_R [49]. Observed cracks were purely mode-I and their propagation speeds were often limited by branching. Singular dynamic fracture models (i.e. in which there is a stress singularity at the sharp crack tip) also showed that super-Rayleigh crack growth is unreachable in homogeneous elastic solids. For instance, Freund [42] showed that the energy flux into the tip of a remotely loaded crack decreases as the crack accelerates, and vanishes at a velocity equal to c_R.

However, these limitations are removed by reducing the specimen thickness up to plane stress conditions [149–151] or when crack branching and kinking is prevented by the existence of a weak plane of propagation where the fracture toughness is lower than in the surrounding solids [72, 73]. When the crack is trapped into a plane of propagation, it is usually mixed mode, which allows for a higher propagation speed. Freund [45] studied the dynamic propagation of sharp mode-II cracks at weak interfaces. His analytical work demonstrates that the energy release rate is nonzero only at speed $\sqrt{2}c_s$ or sub-Rayleigh regimes for which the stress field is square root singular at the crack tip. Other intersonic speeds present a zero energy release rate which was not a sufficient proof of their existence. However when the rupture is not considered to be singular but smeared out in space and time within a cohesive zone, both analytical (Broberg [48]) and numerical (Andrews [47]) models showed that every intersonic mode-II crack speed is physically admissible.

The first experimental evidence of an intersonic crack propagation in a homogeneous material was provided by Rosakis *et al.* [73]. To avoid energetic dissipation by branching or micro-cracking, a weak plane of propagation was created by bonding two plates of Homalite together. A pre-notch crack at the edge of the interface was loaded by a lateral impact, while crack propagation was monitored using high speed photoelasticity. Coker and Rosakis [152] also studied crack propagation in unidirectional graphite-epoxy composite plates. If under mode-I loading the recorded speeds were bounded at c_R, the authors observed intersonic crack propagations for mode-II loading conditions. The role of crack velocity on the cohesive failure along a single-material interface was studied by Kubair *et al.* [153]. Their analytical work showed that the cohesive damage is purely shear when the crack is intersonic, even for mixed-mode loadings. In parallel to steady-state models, numerical simulations provided the opportunity to study the transition from subsonic to intersonic speeds. Needleman *et al.* [124] observed that the crack speed jumps from values close to c_R up to a regime between $\sqrt{2}c_s$ and the P-wave speed c_p.

Before these observations at single-material interfaces, it was already known that between dissimilar materials, crack can propagate intersonically with respect to the compliant medium. Lambros and Rosakis [154] showed the first experimental proof of an intersonic crack propagation along a straight-line weak interface between PMMA and steel plates. Moreover, between two dissimilar materials, the presence of large scale contact zones after failure is a new feature of intersonic crack growth. Liu *et al.* [155] derived the asymptotic solution for intersonic crack growth at the interface between an elastic solid and a rigid substrate. The asymptotic model shows that when the crack speed is between the shear wave speed of the elastic medium c_s and $\sqrt{2}c_s$, the normal stress ahead of the crack front has the opposite sign of the normal displacement behind it, i.e., with a tensile loading, a face closure is predicted behind the crack tip. The authors concluded that this regime might cause the presence of large scale contact during intersonic debonding and is unfavorable for stable crack growth.

Beside this theoretical work, several experiments [86–88] were conduced along interfaces bonding a very stiff body (Steel or Aluminium) to a more compliant material (PMMA or Homalite) revealing the presence of large scale contact zones behind intersonic ruptures. By adding a trailing contact zone of finite length to Liu's asymptotic solution, Huang *et al.* [156] were able to reproduce the main experimental observations. Moreover, the presence of compressive normal stress along part of the interface associated with intersonic crack growth is also observed in numerical simulations of bimaterial debonding [123, 157, 158]. Even though these numerical models did not account for real contact conditions between crack faces, the presence of this compressive stress field confirms the ability of large scale contact zones to develop along bimaterial interfaces. If the presence of contact is now obvious in intersonic crack propagation, its effect on the fracture process and the crack propagation is still overlooked. Subsequent experiments confirmed that the behavior of those large scale contact zones is little understood. Between a polymer and a very stiff body, Samudrala and Rosakis [88] observed two distinct contact behaviors. Depending on the applied loading, the contact zone either trailed the crack tip or detached from the front and had its own leading and trailing edges. Along composite-Homalite interfaces, Coker *et al.* [71] showed experimentally and numerically that the crack speed regime also varies as a function of crack growth direction with respect to particle displacement. The effect of the propagation direction was also observed numerically at frictional interfaces [159].

In this context, the purpose of this work is the numerical study of the behavior and the role of large scale contact zones appearing at intersonic debonding. The effect of the applied loading and the material mismatch are also analyzed. The spectral method is chosen for its ability to describe interface phenomenon with a very fine level of discretization. Interpenetration is prevented at the interface by a contact model with friction being governed by a regularized Coulomb law. The geometry of our dynamic fracture problem is described in Section 4.2, while the numerical method is presented in Section 4.3. The failure event is studied in Section 4.4 along an Aluminum-Homalite interface through space-time diagrams, the evolution of damage parameters at discrete positions in the path of the crack, energetic arguments, and the evolution of the speed of the leading and trailing edges of the cohesive and contact zones. The influence of the loading conditions in Section 4.5, as well as the material mismatch in Section 4.6, are discussed with the intention to define criteria describing the behavior of different bimaterial situations.

4.2 Problem description

4.2.1 Geometry and elastodynamics

The problem geometry is described by two semi-infinite bodies bonded together along a planar interface. Each body is made of a linear isotropic elastic material characterized by the elastic modulus E, the Poisson's ratio ν, the shear wave speed c_s and the dilatational wave speed c_p. By convention, the top material is defined as the stiffer material. The indices $+/-$ differentiate respectively the top and bottom materials. The bonds at the interface are defined by a fracture energy G_c. Let a Cartesian system be defined such as y is the normal to the fracture plane. The interface is pre-stressed with a load τ^0 applied in the $x - y$ plane with an angle ψ with respect to the y axis. At time $t = 0$, a crack of initial length L_0 is introduced and starts to propagate along the interface. Figure 4.1 illustrates the geometry of the problem.

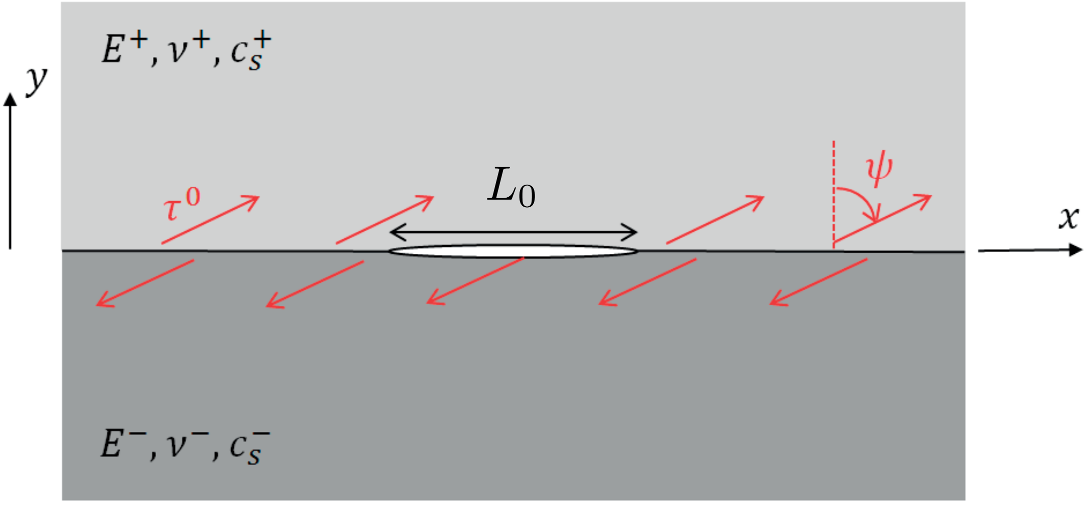

Figure 4.1 – Geometry of the dynamic fracture problem.

This fracture problem is described by the elastodynamics wave equations with the two in-plane components of the displacement field u_i defined as

$$u_x(\alpha, t) = \phi_{,x} + \vartheta_{,y}\,, \quad u_y(\alpha, t) = \phi_{,y} - \vartheta_{,x}\,, \tag{4.1}$$

where $()_{,\kappa}$ is defined as ∂/κ. ϕ and ϑ are potentials satisfying

$$c_p^2\phi_{,\alpha\alpha} = \phi_{,tt}, \quad c_s^2\vartheta_{,\alpha\alpha} = \vartheta_{,tt}. \tag{4.2}$$

4.2.2 Interface laws

In addition to the continuum model, the problem is described by two interface laws. First, the failure of the interface bonds is described by a rate-independent model which couples normal and shear decohesion. The normal/shear strength of the bonds $\tau_{n,s}^{\mathrm{str}}$ is related to the associated normal/shear opening of the interface $\delta_{n,s}$ as

$$\tau_{n,s}^{\mathrm{str}} = \tau_c \left\{1 - \sqrt{(\delta_n/\delta_c)^2 + (\delta_s/\delta_c)^2}\right\}, \tag{4.3}$$

with $\{\kappa\} = \kappa$ if $\kappa > 0$ and 0 otherwise and where the opening at the interface is defined by the displacement discontinuities,

$$\delta_j(x,t) \equiv u_j(x,0^+,t) - u_j(x,0^-,t)\,. \tag{4.4}$$

In this study, the shear and normal directions are respectively associated to the x and y components, such that $\delta_s = \delta_x$ and $\delta_n = \delta_y$. In Equation (4.3), τ_c and δ_c describe the parameters of this cohesive model reducing for a pure mode I or mode II failure to a linear law with fracture energy $G_c = 0.5\,\tau_c\,\delta_c$. In perfect mixed-mode failure, the fracture energy increases to $\sqrt{2}G_c$. After failure, the faces of the interface may come in contact again with a local compressive stress at the interface $\sigma_{yy}(x,0,t) < 0$. In this case, a shear strength due to friction is observed. A Coulomb friction law is used hereafter as

$$\tau_s^{\mathrm{str}} = c_f|\tilde{\sigma}_{yy}|\,, \tag{4.5}$$

where $\tilde{\sigma}_{yy}$ corresponds to the regularized contact pressure and c_f is the coefficient of friction. To avoid ill-posedness of the friction problem, a simplified Prakash regularization is considered [160]. Since the regularizing effect is directly related to the contact pressure, Rubin and Ampuero [161] suggested to regularize directly the later instead of the shear strength. Similarly to this approach, we applied the following simplified regularization to the contact pressure:

$$\frac{d\tilde{\sigma}_{yy}}{dt} = -\frac{1}{t^*}(\tilde{\sigma}_{yy} - \sigma_{yy})\,, \tag{4.6}$$

where t^* is the regularization parameter set as $t^* = 10 \cdot \Delta t$ to satisfy the convergence criteria. More details about the convergence of regularized friction are given in [162].

4.2.3 Material properties

We study dynamic fracture problems along an interface between two materials with an important mismatch. The Aluminum-Homalite interface is chosen to match the experiments of Samudrala and Rosakis [88]. The material properties used in our simulations are presented in Table 4.1.

Table 4.1 – Material properties.

	Aluminum	Homalite
Young's modulus E [GPa]	71	5.3
Poisson's ratio ν [-]	0.33	0.35
Shear wave speed c_s [m/s]	3100	1263

Note that index '+/-' can be interchanged hereafter with 'Al' or 'H', the two components of the bimaterial system. The interface is described by $\tau_c = 5$ [MPa] and $\delta_c = 0.02$ [mm], which yields an interface fracture energy of $G_c = 50$ [J/m^2]. After failure, the coefficient of friction of the interface is set as $c_f = 0.25$.

4.3 Numerical method

The dynamic fracture problem is solved with a spectral formulation of the elastodynamic equations. A detailed presentation of this boundary integral formulation is given in Section 3.1. For the two-dimensional problem of interest, only one spectral component is examined such that

$$[f_j^{\pm}(x,t), u_j^{\pm}(x,t)] = e^{iqx}[F_j^{\pm}(q,t), U_j^{\pm}(q,t)], \tag{4.7}$$

while the convolution integrals are expressed for a given time t and spectral mode q as

$$
\begin{aligned}
F_x^{\pm}(t;q) = {} & \mp \mu^{\pm}|q| \int_0^t H_{xx}^{\pm}(|q|c_s^{\pm}t')U_x^{\pm}(t-t';q)|q|c_s^{\pm}dt' \\
& + i\mu^{\pm}q \int_0^t H_{xy}^{\pm}(|q|c_s^{\pm}t')U_y^{\pm}(t-t';q)|q|c_s^{\pm}dt' \\
& + i(2-\eta^{\pm})\mu^{\pm}qU_y^{\pm}(t;q)\,, \\
F_y^{\pm}(t;q) = {} & \mp \mu^{\pm}|q| \int_0^t H_{yy}^{\pm}(|q|c_s^{\pm}t')U_y^{\pm}(t-t';q)|q|c_s^{\pm}dt' \\
& - i\mu^{\pm}q \int_0^t H_{xy}^{\pm}(|q|c_s^{\pm}t')U_x^{\pm}(t-t';q)|q|c_s^{\pm}dt' \\
& - i(2-\eta^{\pm})\mu^{\pm}qU_x^{\pm}(t;q)\,.
\end{aligned}
\tag{4.8}
$$

An illustration of the different convolution kernels is presented in Figure 3.2 for $\nu = 0.35$. Finally, the interface relations (cf. Equation 3.17) are completed by the continuity of displacements and tractions through the interface yielding the interface velocities $\dot{u}_j^{\pm}$:

$$
(\tau_{n,s}^{\text{str}} > \tau_{2,1})
\begin{cases}
\dot{u}_x^+ = \dot{u}_x^- & = \frac{c_s^+}{\mu^+}\left(\frac{f_x^+ - f_x^-}{1+\frac{\xi}{\zeta}}\right) \\
\dot{u}_y^+ = \dot{u}_y^- & = \frac{c_s^+}{\mu^+}\left(\frac{f_y^+ - f_y^-}{\eta^+ + \frac{\xi}{\zeta}\eta^-}\right)
\end{cases}
\,,
\tag{4.9}
$$

$$
(\tau_{n,s}^{\text{str}} \le \tau_{2,1})
\begin{cases}
\dot{u}_x^{\pm} & = c_s^{\pm}\left(\frac{\tau_x^0 + f_x^{\pm} - \tau_s^{\text{str}}}{\mu^{\pm}}\right) \\
\dot{u}_y^{\pm} & = c_s^{\pm}\left(\frac{\tau_y^0 + f_y^{\pm} - \tau_n^{\text{str}}}{\mu^{\pm}\eta^{\pm}}\right)
\end{cases}
\,,
\tag{4.10}
$$

where $\xi = c_s^+ / c_s^-$ and $\zeta = \mu^+ / \mu^-$.

In the case of possible overlapping of the crack faces, relations (4.10) are adapted to ensure the vanishing of the normal displacement. The normal motion is modified as

$$
\begin{aligned}
\dot{u}_y^+ & = \frac{c_s^+}{\eta^+ + \frac{\xi\eta^-}{\zeta}}\left[\frac{\tau_y^+ - \tau_y^-}{\mu^+} - \frac{\xi\eta^-}{\zeta}\left(\frac{u_y^+ - u_y^-}{c_s^+\Delta t}\right)\right], \\
\dot{u}_y^- & = \dot{u}_y^+ + \frac{u_y^+ - u_y^-}{\Delta t}\,.
\end{aligned}
\tag{4.11}
$$

This modification generates a compressive stress at the interface,

$$
\sigma_{yy} = \tau_y^+ - \eta^+\mu^+\frac{\dot{u}_y^+}{c_s^+}\,.
\tag{4.12}
$$

The shear motion is still governed by (4.10), with the associated strength τ_s^{str} due to friction at the interface given by the chosen friction model (cf. Equations 4.5 and 4.6).

4.4 Reference case ($\psi = 75°$)

The dynamic debonding along an Aluminum-Homalite interface obtained for a shear-dominated loading is described in detail in this section. The material properties of each medium and the interface were defined in Section 4.2.3. Since it is based on a Fourier series representation of the solution, the spectral scheme introduces a spatial period X. A $X = 1$ [m] domain prestressed with an in-plane uniform load of $\tau^0/\tau_c = 0.6$ is investigated. The in-plane loading angle is set at $\psi = 75°$.

At time $t = 0$, an initial crack of size $L_0/X = 0.05$ is introduced at the center of the domain and starts to propagate in both directions. For simplicity and efficiency of the Fourier transform between spatial and spectral domains, the number of grid points is usually chosen as a power of 2. The interface is discretized with 4096 elements, resulting in an element size of $\Delta x = 0.24$ [mm]. The time step is set by the parameter β corresponding to the fraction of one grid spacing traveled by a shear wave in the stiffer material,

$$\Delta t = \beta \frac{\Delta x}{c_s^+}. \tag{4.13}$$

Breitenfeld and Geubelle [17] showed that a value of $\beta = 0.4$ guarantees a good stability of the solution. This value is therefore adopted in the simulations presented hereafter. A convergence study validates the choice of the grid spacing and time step values.

4.4.1 Evolution of cohesive and contact zones

Figure 4.2 shows a space-time representation of the crack propagation. The mismatch between the top and bottom materials causes different failure behaviors for the two directions of propagation. Asymmetry in the crack growth was also recorded experimentally for a centered crack growing under a mixed-mode loading (Xia *et al.* [163]). On the left side, a contact area appears and directly trails the crack tip throughout the simulation. On the right side, a friction zone also trails the crack tip for a while but quickly detaches. As the simulation goes on, the size of this frictional contact area decreases before the contact zone completely vanishes. Those two distinct behaviors are in good agreement with the different types of contact zones assessed in the experimental work of Samudrala and Rosakis [88]. To confirm that the two behaviors are clearly different, the simulation duration was extended showing that the left friction area does not detach from the crack tip. The study of the crack and contact zone velocity profiles (Figure 4.3) also highlights two different regimes.

In the left direction (Figure 4.3a), friction appears at intersonic propagation speed, around $0.75 c_s^{Al} \simeq 1.84 c_s^H$. At the end of the simulation, the crack propagation reaches a quasi steady

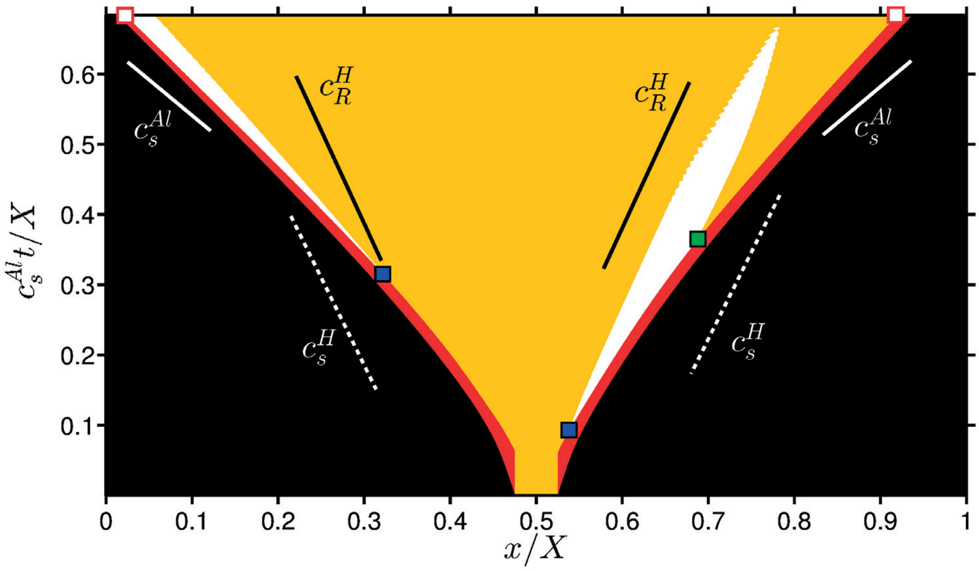

Figure 4.2 – Space-time diagram of a dynamic debonding between Aluminum and Homalite for $\psi = 75°$. The black regions correspond to intact portions of the interface, the red areas indicate the cohesive zones, the yellow regions are traction-free and the white regions correspond to the contact zones. Squares highlight measurement points for which the propagation speed is reported in Figure 4.8.

state and the friction zone continues to grow.

On the right side (Figure 4.3b), the contact zone appears when the crack propagates in the unfavorable speed range as defined by Liu *et al.* [155], i.e., between c_s^H and $\sqrt{2}c_s^H$. As the propagation speed continues to increase and leaves the unstable range, the contact area decreases in size and eventually vanishes completely. This observation is in agreement with the asymptotic model derived by Liu *et al.* [155], which predicts a crack face closure only at this unfavorable velocity regime.

4.4.2 Failure process

Figure 4.4 compares the history of interface points located in the path of the left-propagating and right-propagating debonding fronts.

As the crack tip approaches the point of observation, a stress concentration is observed in the shear and normal directions. On both sides, failure is initiated in shear due to the shear-dominated nature of the loading. The key difference is the traction behavior in the normal direction. For the left side, the normal traction is in compression. Thereby, the failure is in pure shear. The concentration in compression explains that the two faces are in contact just after failure. Inversely, the concentration of normal stress comes up in tension for the right side. In this case, the normal stress curve also intercepts the strength curve and the

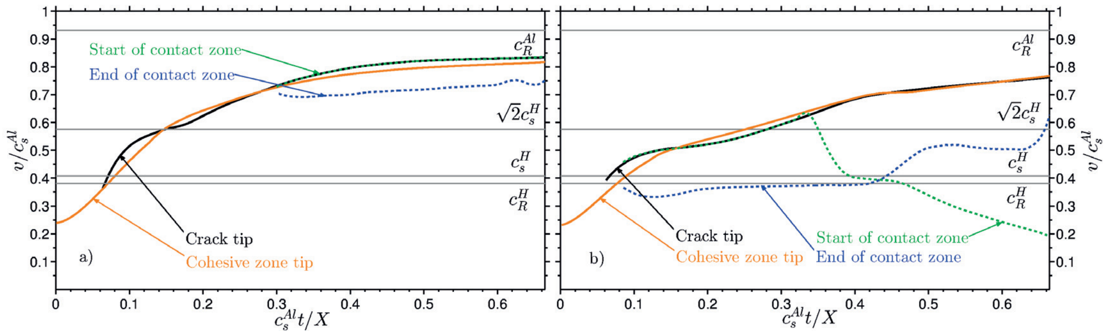

Figure 4.3 – Evolution over time of the propagation speed of the cohesive and contact zones for the left (a) and right (b) debonding path under $\psi = 75°$.

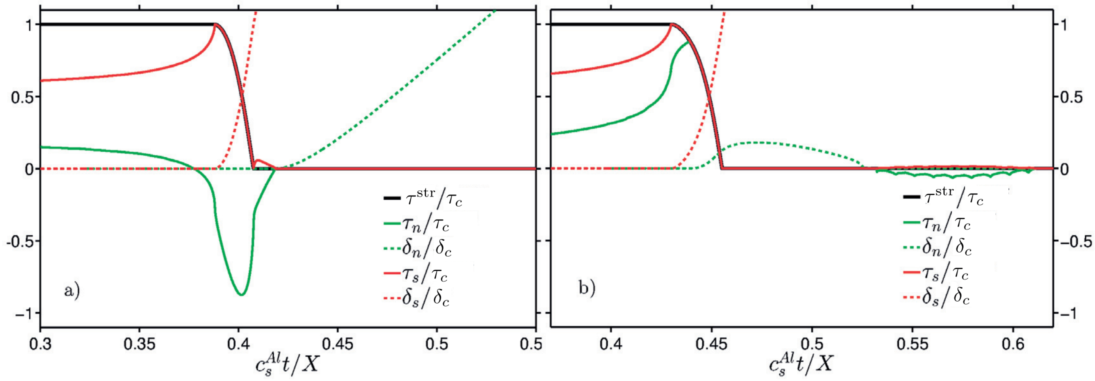

Figure 4.4 – Evolution of the cohesive strength, normal and shear tractions and displacement jumps at $x/X = 0.25$ (a) and at $x/X = 0.75$ (b) with $\psi = 75°$.

debonding is a mixed-mode failure. Because the interface is under tension, the crack face opens after failure. However, after a certain amount of time, a closure motion brings both faces in contact. This delayed contact corresponds to the region with a detached friction area in Figure 4.2. This particular effect indicates that a closure wave propagating at the Homalite surface causes this detached friction area. The propagation speed of the trailing end of the detached contact zone is close to c_R^H as shown in Figure 4.3b and sustains the assumption of a surface-level perturbation. A similar disturbance traveling at the Rayleigh wave velocity of the more compliant material is described in the experiments of Singh and Shukla (cf. Figure 4.3b compared to Figure 12 in [164]).

4.4.3 Energetics

Finally, the evolution of the effective fracture energy dE/dA is computed during the simulation, where E denotes the energy and A represents the debonded area. The effective fracture energy is then directly related to v, the crack propagation speed as

$$\Gamma = \frac{dE}{dA} = \frac{dE}{dt}\frac{1}{v} = \frac{\dot{E}}{v}\,. \tag{4.14}$$

During the failure process, energy is dissipated in the cohesive zone by debonding and in the contact zone by friction as

$$\begin{aligned}
\dot{E}_n(t) &= \int_{\text{cohesive zone}(t)} \tau_n^{\text{str}}(x,t)\,\dot{\delta}_n(x,t)\,dx\,,\\
\dot{E}_s(t) &= \int_{\text{cohesive zone}(t)} \tau_s^{\text{str}}(x,t)\,\dot{\delta}_s(x,t)\,dx\,,\\
\dot{E}_f(t) &= \int_{\text{contact zone}(t)} c_f|\tilde{\tau}_y|\,\dot{\delta}_x(x,t)\,dx\,.
\end{aligned} \tag{4.15}$$

Figure 4.5 presents the evolution of the fracture energy normalized by the reference fracture energy G_c, which is the energy dissipated in a pure mode (I or II) failure. Shear failure process is predominant (see Figure 4.5b), as expected for this intersonic crack. With the same numerical method, Geubelle and Kubair [165] showed that intersonic debonding along a single-material interface is purely driven by shear. Nevertheless, two additional features are observed with this bimaterial situation. First, the effective fracture energy is significantly higher than G_c because of the friction-induced dissipation. Figure 4.5a presents values of Γ_f up to $0.4\,G_c$. It might even exceeds $0.7\,G_c$ by increasing the coefficient of friction up to $c_f = 0.8$. Therefore the presence of a contact zone along the interface plays an important role in failure energetics. Second, in bimaterial set-ups, mixed mode failure occurs also for intersonic cracks, which was shown to be impossible along single-material interfaces [48, 165]. In Figure 4.5b, mode-I failure process is observed at $c_s^{Al}t/X = 0.36$ as soon as the contact zone detaches from the right tip.

4.5 Influence of loading angle ψ

In this section, we investigate the effect of the loading condition by reproducing the reference set-up with different values of ψ between 0° and 90°.

4.5.1 Evolution of cohesive and contact zones

For a pure far field tensile loading, i.e $\psi = 0°$, the crack propagation is perfectly symmetric and no contact area is observed in both directions of propagation. Each crack tip propagates at a subsonic speed close to c_R^H, as a sufficient amount of shear is needed to allow intersonic propagations [165]. Adding shear to the far field loading ($\psi > 0°$) has two effects. First, the shear stress becomes more prominent and results in higher crack speeds. Secondly, the

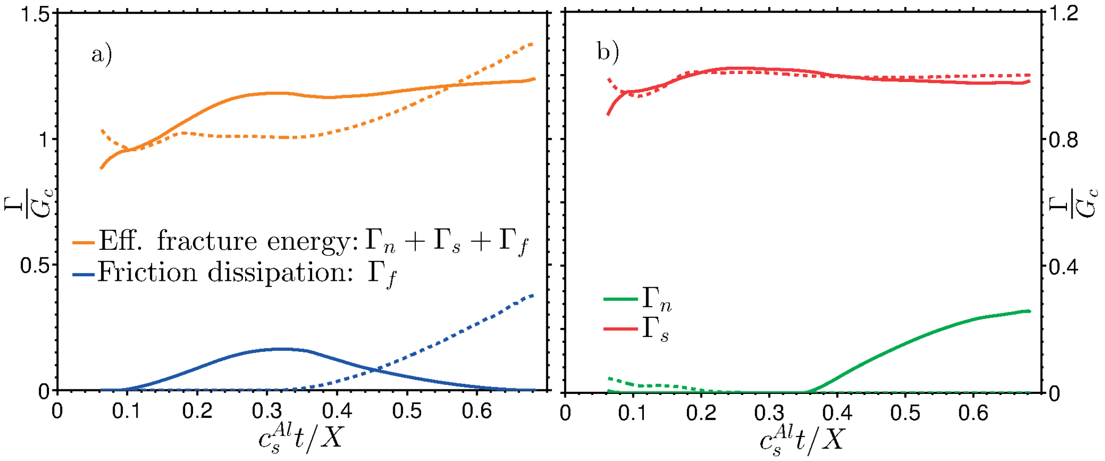

Figure 4.5 – Evolution of the effective fracture energy and its different components, i.e. the dissipation by friction Γ_f and by tensile Γ_n and shear Γ_s debonding, for the left (dashed lines) and right (full lines) paths with $\psi = 75°$.

symmetry is broken and the two propagation paths present different behaviors, as shown in Figure 4.6 for $\psi = 50°$. On the right path, the crack accelerates progressively, while the left tip stays almost at a constant speed close to c_R^H before jumping suddenly to intersonic velocities.

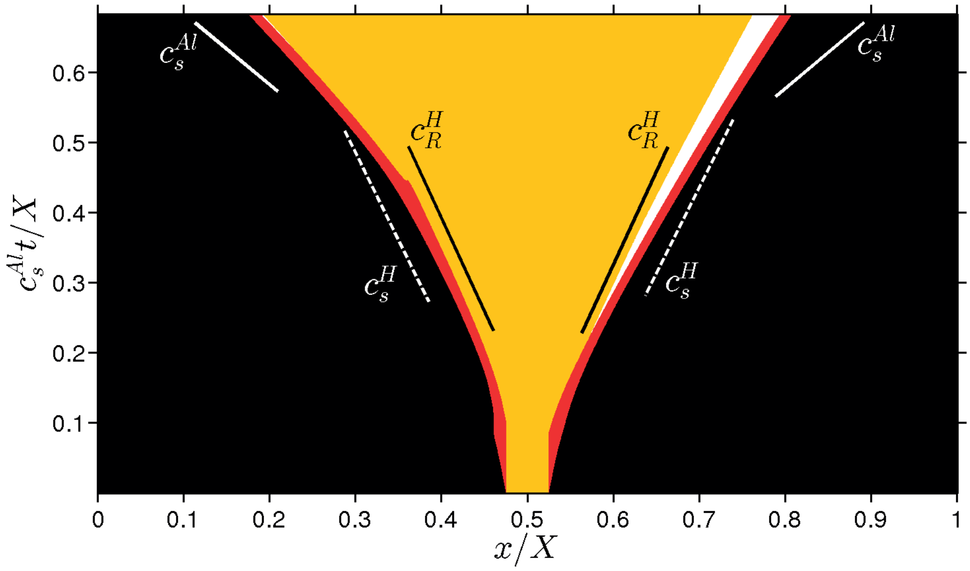

Figure 4.6 – Space-time diagram of dynamic debonding between Aluminum and Homalite for $\psi = 50°$ illustrating subsonic/intersonic transition for both directions. (Colour code as in Figure 4.2).

This sharp transition is also observable on the velocity profile at about $c_s^{Al}t/X = 0.45$ in Figure 4.7a, where the left tip jumps directly from c_R^H to a speed above $\sqrt{2}c_s^H$. This sharp behavior causes the singularity observed in Figure 4.7a. At the end of the simulation, a thin contact zone appears directly behind the left tip. The right crack tip accelerates continuously up to the intersonic regime and a contact zone develops as soon as it exceeds c_s^H (see Figure 4.7b). Unlike the $\psi = 75°$ configuration (Figure 4.3b), the right tip never exceeds $\sqrt{2}c_s^H$ and the contact zone does not detach from the tip.

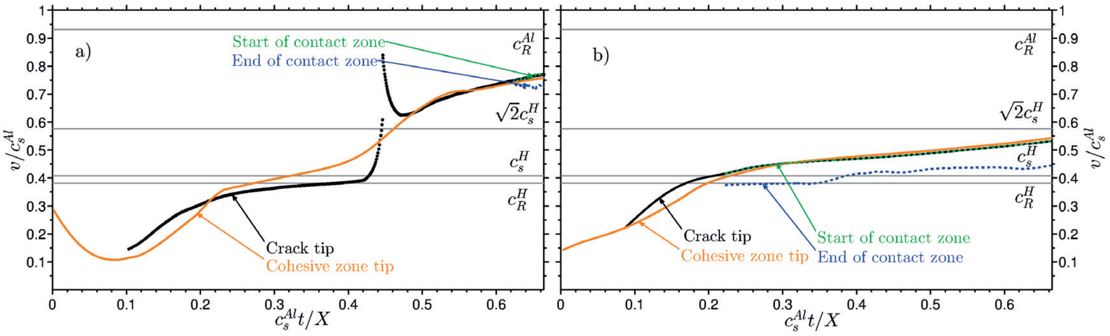

Figure 4.7 – Evolution of the propagation speed of the cohesive and contact zones for the left (a) and right (b) debonding path under $\psi = 50°$.

We have considered different values of ψ between 0° and 90°. A summary of the velocity profiles (i.e. the crack speed when contact appears behind the tip, as the contact zone detaches and at the end of the simulation) is presented in Figure 4.8. As observed before, with normal-dominated loading conditions, the crack propagates at sub-Rayleigh speed and no contact is observed at the interface. As the loading conditions go from pure tensile ($\psi = 0°$) to pure shear ($\psi = 90°$), the propagation speed and the asymmetry increase. The difference between each side of propagation can be characterized in two distinct ways. First, the subsonic/intersonic transition is clearly different. In the left direction, the crack has only two regimes of propagation: a subsonic steady state close to c_R^H for $\psi \leq 40°$ and an intersonic at about 0.8 c_s^{Al} for higher ψ. Between these velocities, the transition is sharp and sudden. The unfavorable range is a forbidden region of propagation, as illustrated in Figure 4.9 which presents the histogram of left crack speeds recorded with $\psi = 50°$. Similar behavior were observed in the experiments of Lambros and Rosakis [154] where the crack stayed at a speed just below c_s^H for a while before accelerating rapidly above $\sqrt{2}c_s^H$. On the right side of the domain, the subsonic/intersonic transition is smooth and progressive.

The behavior of contact is the second clear difference between left and right crack propagation directions. In the left direction, contact zones appear with intersonic propagation speed, around 0.75 c_s^{Al}. The emergence of this friction zone coincides with the end of crack acceleration. In the right direction, Figure 4.8 confirms that contact areas are directly related to a propagation at unfavorable speeds. As the crack moves faster than $\sqrt{2}c_s^H$, the contact zone detaches from the crack tip and eventually fully vanishes. Before detaching, the trailing end of this contact zone is propagating at the Rayleigh wave speed of Homalite (cf Figure 4.3b).

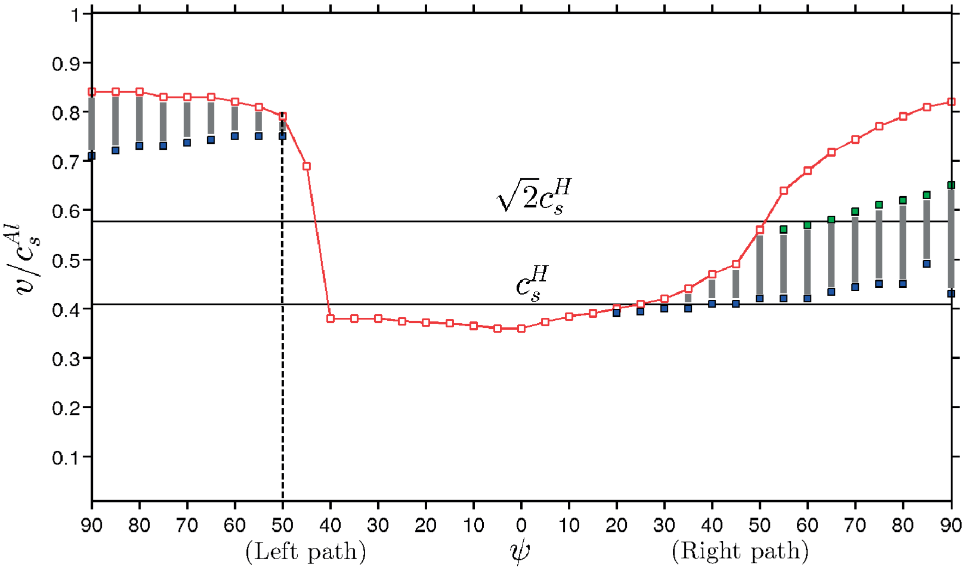

Figure 4.8 – Influence of ψ on the propagation speed v. As illustrated in Figure 4.2, red squares show the propagation velocities reached at the end of the simulation, blue squares the speeds when a contact area appears behind the crack tip and green squares the speeds when the contact zone detaches from the crack tip. The vertical gray bars highlight crack velocities where the contact zone is trailing the crack tip. The vertical dashed line represents the abscissa of Figure 4.9.

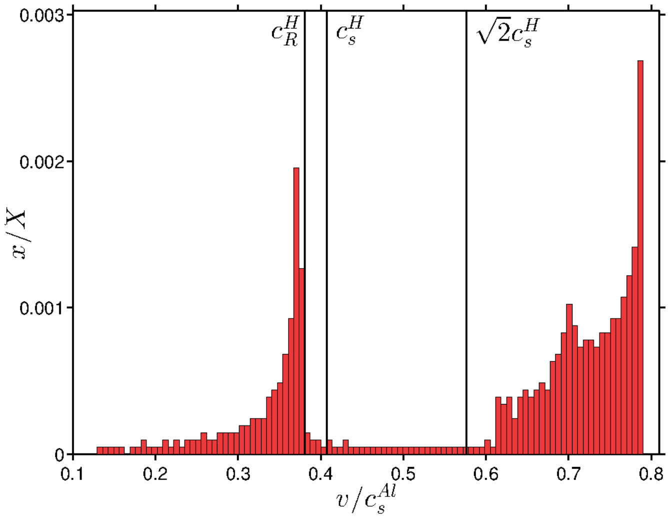

Figure 4.9 – Histogram of the crack velocities as function of the distance traveled for $\psi = 50°$ on the left side showing the existence of a forbidden velocity regime between c_R^H and $\sqrt{2}c_s^H$. The abscissa of the histogram corresponds to the dashed line in Figure 4.8.

4.5.2 Impact of ψ on the failure process

A characteristic feature of bimaterial interface failure is the inherent mode mixity of the failure process, even under pure far-field loading conditions ($\psi = 0°$ or $\psi = 90°$). Bimaterial conditions break the symmetry at the interface and the direction of principal stresses are not perpendicular anymore to the interface. The presence of both shear and normal stresses at crack tips of pure tensile and shear loadings is shown in Figure 4.10.

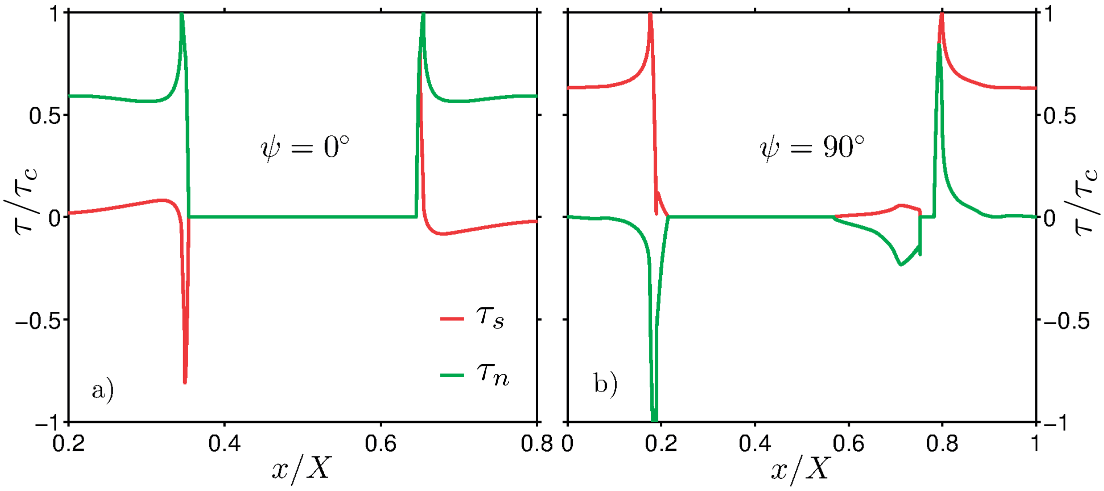

Figure 4.10 – Normal and shear stress profiles at $t = 0.48\, c_s^{Al}\, t/X$ along the interface for $\psi = 0°$ and $\psi = 90°$. Along bimaterial interfaces, mixed-mode stress fields at the crack tip are observed even under pure tensile and shear far-field loadings.

The comparison of failure processes between shear and tensile loading conditions explains the asymmetric behavior observed in Figure 4.8 between left and right propagating fronts. The stress field at the right tip has similar patterns under $\psi = 0°$ and $\psi = 90°$, i.e positive values for normal and shear stresses. In the left direction, the stress field presents a different pattern between $\psi = 0°$ and $\psi = 90°$, with both components changing sign. The sharp transition observed in Figure 4.8 is therefore explained by the fact that the crack changes its regime of propagation as the loading condition goes from tensile to shear.

The same analysis explains the subsonic/intersonic transition under a fixed value of ψ. Figure 4.11 compares the stress profiles measured for a subsonic and an intersonic crack propagation under $\psi = 50°$. At subsonic speeds, the normal stress close to the tips is tensile and contributes to the cohesive failure. At intersonic speeds, the normal stress at the left tip changes sign and is now compressive. This drastic change in the failure pattern associated to the sharp jump in the velocity profile corresponds to a subsonic/intersonic transition similar to the Burridge-Andrews mechanism [46, 47]. This transition, initially described for shear cracks along frictional interfaces, occurs through the nucleation of an intersonic daughter crack in front of the main rupture. Coker *et al.* [71] gave the first experimental observation of this transition mechanism along a composite-Homalite interface. Geubelle and Kubair [165] as well as Liu and Lapusta [80] observed similar intersonic daughter cracks with the spectral boundary integral method. The Figure 4.12 presents the evolution of mode mixity evaluated through the energy dissipated during bonds failure as function of the propagation speed. In the left direction (Figure 4.12a), the existence of two distinct regimes of propagation are

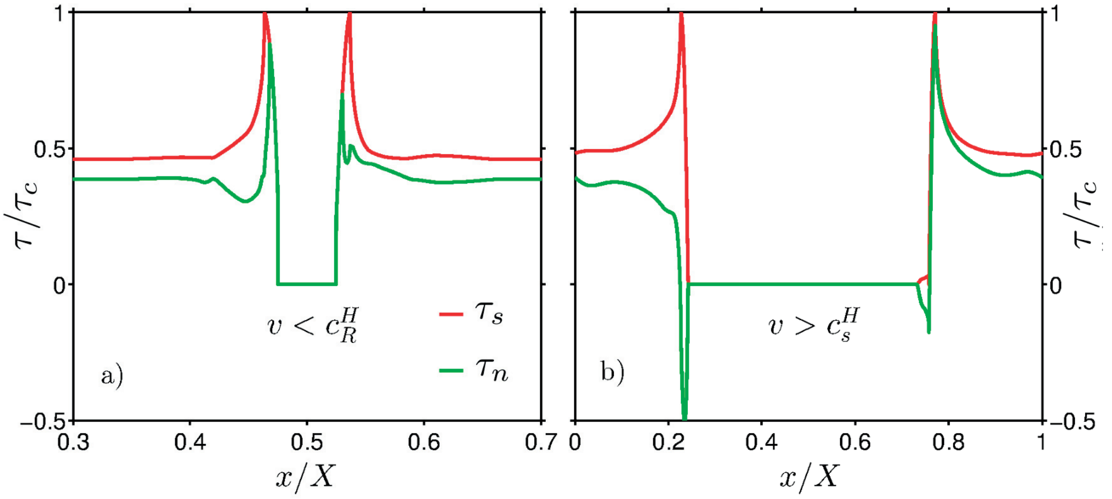

Figure 4.11 – Normal and shear stress profiles along the interface for subsonic ($t = 0.07\, c_s^{Al}\, t/X$) and intersonic ($t = 0.62\, c_s^{Al}\, t/X$) crack growth under $\psi = 50°$.

identified between sub-Rayleigh and intersonic speeds separated by spaced out dots at forbidden velocities (also observed at the singularity in Figure 4.7a). While mixed mode failure is observed in the subsonic regime, intersonic cracks are purely driven by shear and the normal opening only occurs after complete failure of the interface. In the right direction, the subsonic/intersonic transition is smoother (Figure 4.12b). As crack closure (in normal direction) is predicted for crack speeds between c_s^H and $\sqrt{2}c_s^H$ [155], the energy dissipation by mode I failure tends to zero when the right front propagates in this regime where a contact zone appears directly behind the tip (Figure 4.11b at $x/X = 0.75$). However, once the propagation speed exceeds $\sqrt{2}c_s^H$, mixed-mode failure is possible in the right direction. Intersonic cracks driven by both tension and shear are the results of the bimaterial nature of this system and were not observed along single-material interfaces [48, 165].

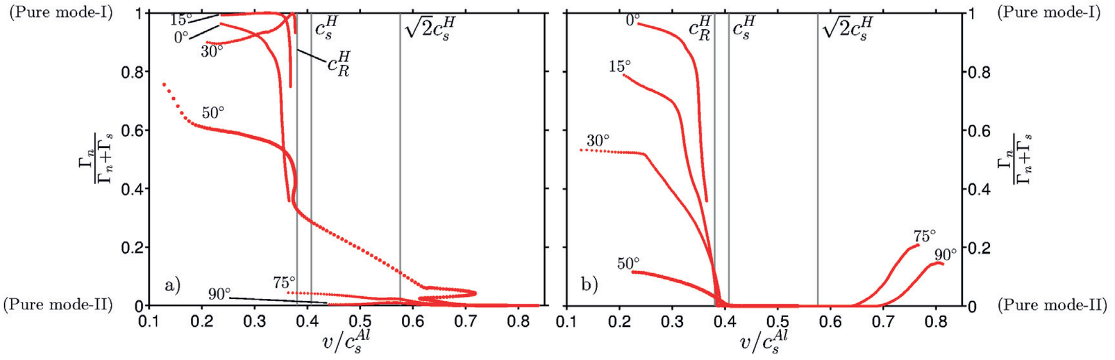

Figure 4.12 – Evolution of the ratio of energy dissipated by mode I failure over the total energy dissipated in cohesive zones as function of the crack velocity for different values of ψ, at the left (green) and right (red) crack fronts.

4.6 Effect of material mismatch

The observed mechanisms of the Aluminium-Homalite problem studied before could be described only by wave speeds of the compliant material (c_s^H, c_R^H) since Aluminium wave speeds are much higher than the crack propagation velocity. In this section, the effect of the material mismatch on the crack behavior is evaluated. Homalite is kept as bottom material, with the properties defined in Section 4.1. The top material is only defined by the Young's modulus mismatch E^+/E^H. To simplify the analysis, the Poisson's ratio and the density of the top material are always the same as Homalite. Thereby, the shear wave speed of the top material can directly be computed as

$$c_s^+ = \sqrt{\frac{E^+}{E^H}}\, c_s^H \, . \tag{4.16}$$

The fracture energy of the interface remains the same as in the previous simulations and reference case loading conditions are applied ($\psi = 75°$). With lower mismatch values, the speeds of crack fronts are in the range of top material wave speeds (c_s^+, c_R^+) and crack propagation is described by material properties of both medium. The single-material problem $E^+/E^H = 1$ corresponds to an intersonic pure shear failure without contact along the interface. Under this shear-dominant loading, the crack propagation is characterized by a rapid acceleration up to the steady state velocity close to $v = 1.87 c_s^H$. This behavior is consistent with both experimental [73] and numerical [165] observations of intersonic crack growth along homogeneous interfaces. Similar to the description made on the left region of propagation for the Aluminium-Homalite system, the crack front needs a sufficient amount of energy to become intersonic, otherwise it continues propagating at a sub-Rayleigh velocity. For small values of mismatch, the crack has sufficient energy to accelerate up to intersonic speeds with respect to both materials as illustrated in Figure 4.13a. As the mismatch increases, the top material intersonic regime distances itself from the crack velocity range, up to levels unreachable by the crack front. Figure 4.13b presents this situation for $E^+/E^H = 4$ where the right tip velocity is bonded at $v \leq c_R^+$. It is interesting to note that this behavior related to the left propagation path during Aluminium-Homalite simulations is observed in the right direction while related to top material wave speeds. More generally, this behavior is observed in relation with the material whose particle displacements are in the direction of failure propagation. In their experimental and numerical work, Coker *et al.* [71] also showed different crack speed regimes as a function of the direction of relative sliding. This observation is also verified in the left path of propagation influenced by top material wave speeds for small mismatches. Indeed, the detached contact zone, observed exclusively in the right direction with an Aluminium-Homalite interface is inverted when it is related to top material wave speeds. As the mismatch increases, the left front propagates through the speed range between c_s^+ and $\sqrt{2}c_s^+$ and a detaching contact zone appears in addition to the trailing contact zone (cf. Figure 4.14). Thus, a detached contact zone is caused by a Rayleigh disturbance emerging up at the surface of the material whose

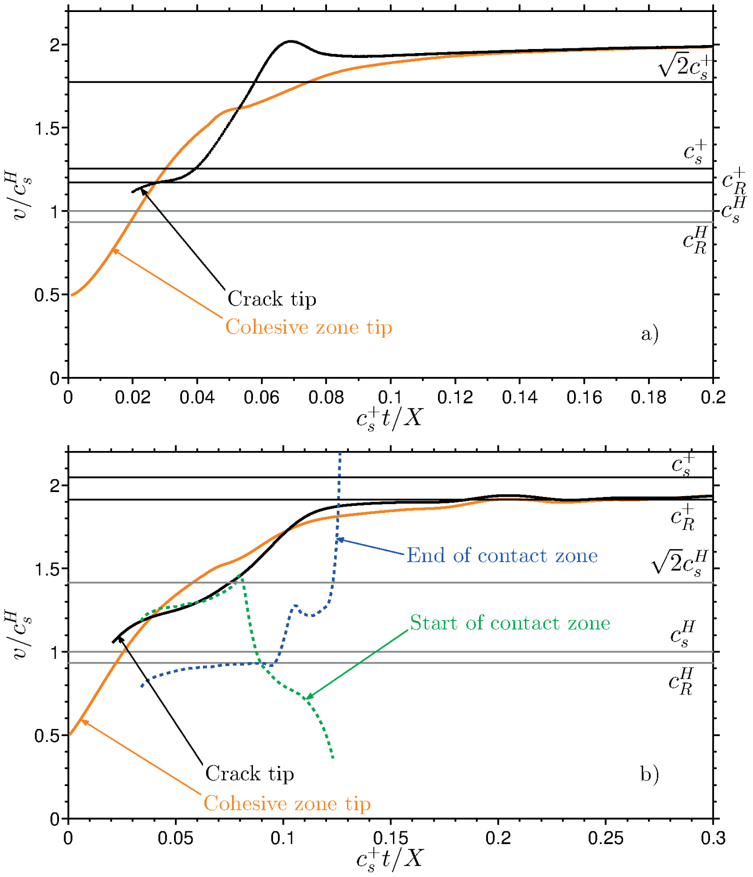

Figure 4.13 – Evolution of the propagation speed of the cohesive and contact zones of the right front at a bimaterial interface with (a) $E^+/E^H = 1.5$ and (b) $E^+/E^H = 4$.

particle displacements are in the opposite direction compared to the front propagation. This statement is confirmed by the propagation speed of the trailing end of the detached contact zones in Figure 4.14 which are c_R^+ in the left direction and c_R^H in the right direction.

4.7 Conclusion

Bimaterial interface fracture has been investigated numerically between two linearly elastic semi-infinite media. The analysis has been conducted using a spectral scheme, which allows for a fine spatial and temporal discretization of the failure process. The objective was to study the subsonic/intersonic transition and to provide a better description of the role of frictional contact in this process.

Compared to the single-material system, the bimaterial set-up breaks the symmetry at the interface causing two effects. First, an inherent mode mixity participates in the failure, even with purely tensile or shear far field loading conditions. Secondly, we observed different crack behaviors at the left and the right tips as function of compliant material wave speeds . By

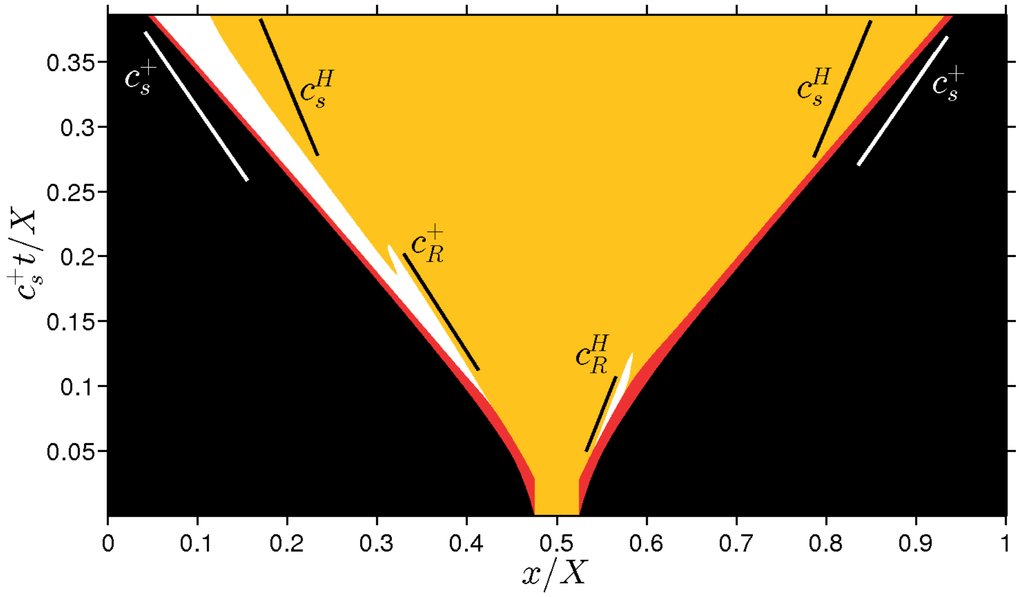

Figure 4.14 – Space-time diagram of dynamic debonding along a $E^+/E^H = 2.5$ interface under $\psi = 75°$ showing contact behavior related to the top and bottom wave speeds. (Colour code as in Figure 4.2).

reducing the material mismatch, we showed that the description of the different crack speed regimes is also valid when related to the wave speeds of the stiffer material. Therefore, the crack behavior can be described as function of the front propagation direction with respect to the slip direction of material particles. If the front has the same direction than the particle displacements of the material, a forbidden speed range was observed between c_R and c_s, forcing the crack to have two distinct regimes of propagation. Either it moves at a sub-Rayleigh speed or, when sufficient energy is available, it jumps to an intersonic regime. This sharp jump and a complete change in the failure stress pattern is caused by the nucleation of a daughter crack in front of the main rupture, similar to the Burridge-Andrews mechanism [46, 47]. When the front propagates in a direction opposite to particle displacements of the material, the subsonic/intersonic acceleration is smooth and any speed is admissible in the transition. Nevertheless, in the velocity range $c_s < v < \sqrt{2}c_s$, mode I failure is forbidden and the faces stay in contact after decohesion. This behavior is consistent with the asymptotic solution of Liu *et al.* [155] predicting crack face closure when the crack propagates at these unfavorable velocities.

Particular attention was given to the behavior and the role of frictional contact in bimaterial failures. For this purpose, contact conditions were implemented in the model associated with a regularized Coulomb friction law. Similar to the experiments [88], two distinct contact behaviors were observed along the interface. At the left tip of cracks subjected to a shear-dominated loading (with stiffer material on top), the material mismatch causes a normal compressive stress leading to a contact zone trailing the crack front. Another type of contact zone was observed as the front propagates with $c_s < v < \sqrt{2}c_s$ with respect to the material whose particle displacements are opposite to the front. Subsequent to face closure behind the crack tip, a Rayleigh disturbance propagating at the surface of the material causes a contact zone detached from the propagation front. The energetic study provided a quantitative description of the effect of friction increasing the effective fracture energy of the interface, even for small coefficients of friction ($c_f = 0.25$).

To conclude, with a single set-up our study allows for the simulations and the descriptions of many different behaviors observed experimentally (distinct natures of contact zones, unfavorable velocity range, asymmetric crack propagation). Our analysis was verified by changing the loading conditions as well as the material mismatch at the interface confirming the applicability of the proposed criteria to the description of different bimaterial situations as well as the single-material set-up.

5 Interplay between process zone and material heterogeneities

In this chapter, the effects of local variations of the fracture toughness are investigated. The impact of heterogeneities on dynamic rupture fronts is studied within a 2D in-plane system preventing any distortion of the front. The effects associated with crack front distortions in presence of heterogeneities are discussed later in Chapter 6. This study shows how microscopic variations of fracture toughness change the macroscopic rupture dynamics because of the elastic waves radiated during front accelerations. As a result, this work demonstrates how small-scale heterogeneities facilitate the supershear transition of a mode II crack. Perturbations of dynamic fronts are then systematically studied with different microstructures and loading conditions. The process zone size is the intrinsic length scale controlling heterogeneous dynamic rupture. The ratio of this length scale to asperity size is proposed as an indicator to transition from quasi-homogeneous to heterogeneous fracture. Moreover, this chapter discusses how the shortening of the process zone size with increasing crack speed brings the front to interact with smaller details of the microstructure. This study shines new light on recent experiments reporting perturbations of dynamic rupture fronts, which intensify with crack propagation speed.

This chapter is a modified version of a scientific article published by the American Physical Society (APS):

F. Barras, P. H. Geubelle, and J.-F. Molinari, “Interplay between Process Zone and Material Heterogeneities for Dynamic Cracks,” *Physical Review Letters*, vol. 119, no. 14, 2017

5.1 Introduction

Our modern understanding of fracture arose from Griffith [10] and Irwin [1] who viewed crack propagation as a thermodynamic process where, at equilibrium, the energetic cost of creating new surfaces in the material is balanced by the release of strain energy subsequent to crack advance. This theoretical framework (LEFM) has been successfully used over the last fifty years to predict the stability of flaws in engineering materials. Consequently LEFM was extended to cracked bodies far from equilibrium, i.e., to dynamic fracture mechanics [42, 43].

Experiments on brittle solids showed that this dynamic theory of fracture gives good prediction for slow crack propagation, but is unsuitable to describe fast rupture events where the crack front speed is a significant fraction of material shear wave speed c_s and the propagation dynamics is perturbed by dynamic instabilities. In particular, linear elastic theory overestimates the propagation speed and significantly underestimates the dissipated energy. For a review of dynamic fracture experiments, the reader is referred to [50, 55–58]. A three-stage transition is universally observed within brittle materials, usually referred as “mirror”, “mist” and “hackle” in reference to the post-mortem appearance of fracture surface. At low rupture velocity, fracture surfaces are planar and smooth (mirror) and crack dynamics is thereby well predicted by LEFM theory. As crack speed increases, the rupture remains in-plane but the fracture surface roughens (mist), followed by a stage characterized by the formation of out-of-plane microbranches (hackle) and finally the onset of macroscopic branching. This transition observed in various brittle materials [50, 51] and at different scales [53, 54] explains how linear elasticity fails at describing fast rupture events where the front starts to interplay with the microstructure and/or dynamic instabilities and becomes a heterogeneous fracture problem [166–169].

An extension of LEFM to heterogeneous problems was proposed by Rice [2] and Gao and Rice [60] who gave a first-order estimation of the stress intensity perturbation caused by crack front distortion in presence of tougher asperities. Recently, Ponson [70] reviewed how this approach can successfully predict the roughness of slow rupture front in brittle disordered material as long as crack front can be viewed as a unique elastic line. The complex mechanisms driving fast crack propagation occur however at a smaller scale where fracture develops along a finite length. In this context, numerical models have a great potential to bring new insights on the interaction of a dynamic front with material heterogeneities. However, the small spatio-temporal scales characterizing this process require a very fine discretization of the fracture plane and explain why dynamic heterogeneous fracture remains overlooked.
This chapter investigates the interaction of a dynamic rupture front with small-scale heterogeneities. The objective is to understand how rupture dynamics is perturbed when the average fracture properties are identical but their statistical distribution changes. The rupture is assumed to propagate along a weak interface under mode II plane strain conditions. This heterogeneous fracture problem is solved using a boundary integral formulation of the elastodynamics equation proposed by Breitenfeld and Geubelle [17].

5.2 Problem Description

5.2.1 Geometry and elastodynamics

Let us consider two semi-infinite linearly elastic solids under plane strain conditions with the top $(y > 0)$ and bottom $(y < 0)$ displacements fields respectively denoted by $\boldsymbol{u}^+(x,y,t)$ and $\boldsymbol{u}^-(x,y,t)$. Along the interface $(y = 0)$, the two half spaces are initially bounded in static equilibrium under a uniform in-plane shear (mode II) loading τ^0. The initial conditions can then be summarized as:

$$\begin{aligned}&\dot{\boldsymbol{u}}^+(x,y,t=0) = \dot{\boldsymbol{u}}^-(x,y,t=0) = 0\\&\underline{\boldsymbol{\sigma}}^+_{xy}(x,y,t=0) = \underline{\boldsymbol{\sigma}}^-_{xy}(x,y,t=0) = \tau^0\end{aligned} \tag{5.1}$$

with $\dot{\boldsymbol{u}} = \frac{\partial \boldsymbol{u}}{\partial t}$ and $\underline{\boldsymbol{\sigma}}$ the Cauchy stress tensor. Due to the spectral nature of the numerical scheme, which is based on a Fourier series representation of the interface quantities, the domain of interest is periodic with period X, i.e, $\boldsymbol{u}(0,y,t) = \boldsymbol{u}(X,y,t)$. At time $t = 0$, a crack of length L is inserted at the left corner of the domain and starts to grow dynamically in the right direction while left tip propagation is prevented. Crack propagation is studied while $L < 2X/3$ to neglect the effect of periodic boundary conditions. Figure 5.1 illustrates the studied brittle fracture process, which is constrained to the interface $(y = 0)$. Across the interface, the displacement discontinuity is defined as

$$\boldsymbol{\delta}(x,t) = \boldsymbol{u}^+(x,y=0^+,t) - \boldsymbol{u}^-(x,y=0^-,t). \tag{5.2}$$

The interface resists crack motion with G_c^H, which corresponds to twice the material surface energy for brittle materials. Far from initiation site $(x > L_{\text{hom}})$, the fracture energy presents dispersion in the idealized form of constant width w stripes alternately weaker $(G_c^{\text{weak}} < G_c^H)$ and tougher $(G_c^{\text{strong}} > G_c^H)$. This arrangement of asperities is designed to keep the macroscopic fracture energy unchanged; $\langle G_c \rangle = 0.5(G_c^{\text{weak}} + G_c^{\text{strong}}) = G_c^H$. Plane strain conditions prevent any crack front distortions during failure and the straight crack front successively breaks this array of asperities.

5.2.2 Numerical scheme

The dynamic fracture problem is solved, once more, with the aid of the spectral scheme [16,17], a spectral form of the elastodynamic boundary integral relations between the displacements $\boldsymbol{u}^\pm$ along the fracture plane and the corresponding traction stress $\boldsymbol{\tau}(x,t)$. The numerical method allows for a detailed description of the evolution of the displacements, velocities and traction stresses along the interface, especially in the failure zone captured with the aid of a cohesive failure model relating the displacement jump in the slip direction, δ_x, and the interface strength

$$\tau^{\text{str}}(x,t) = \tau_c(x)\,\{1 - \delta_x(x,t)/\delta_c(x)\}\,. \tag{5.3}$$

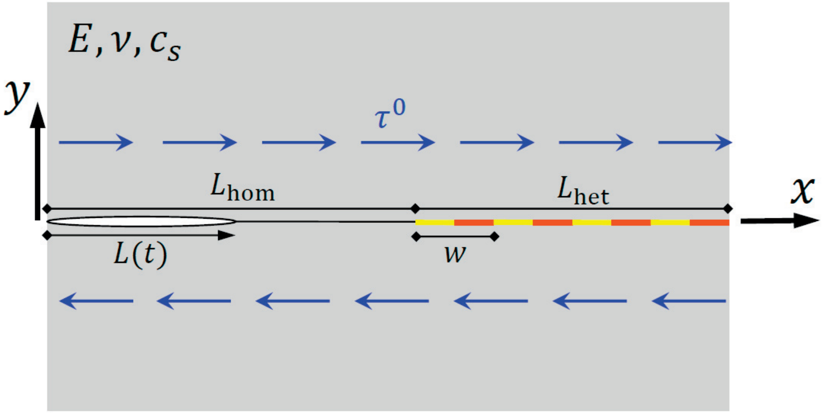

Figure 5.1 – Geometry of the in-plane heterogeneous fracture problem. A crack of length L is inserted along an interface with constant macroscopic fracture energy G_c^H at rest under an uniform shear loading τ^0. The interface is made of a homogeneous portion L_{hom} and a region with a heterogeneous fracture energy L_{het} in form of alternately weaker (yellow)/tougher (orange) stripes of constant width w.

In (5.3), τ_c and δ_c respectively denote the failure strength and critical slip, and $\{\xi\} = \xi$ if $\xi > 0$ and 0 otherwise. The corresponding value of the fracture energy is $G_c(x) = \frac{1}{2}\tau_c(x)\delta_c(x)$. The interface is typically discretized with 65,536 nodes in the simulations presented hereafter. Details about the numerical method are provided to the reader in Chapter 3 and, for the two-dimensional formulation, in Chapter 4. For the mode II slip-weakening interface problems of interest, the interface relations (cf. Equation 3.17) are completed by interface conditions implying the continuity of tractions and displacements along the interface as long as the shear traction τ_x is lower than the interface strength τ^{str} defined in Equation 5.3. Otherwise, the fracture process breaks the continuity of displacements and the velocity $\partial u_j^{\pm}/\partial t$ of the crack faces are computed such that $\tau_x^+ = \tau_x^- = \tau^{\text{str}}$, with the value of the interface strength being related to the displacement jump δ_x through the cohesive failure model described by Equation 5.3.

5.2.3 Fracture initiation

The material and failure properties are given to the reader in Section 5.7 for the sake of reproducibility, but the conclusion drawn in the chapter are independent from this choice and results are hereafter presented in adimensional scales. Based on the expression of the stress intensity factor $K_{II} = \tau^0\sqrt{\pi L/2}$ for a static shear-loaded crack in an infinite medium [1,31], we compute the critical crack size L_c satisfying Griffith's failure criterion:

$$L_c = \frac{2K_{II}^2}{\pi(\tau^0)^2} = \frac{2G_c^H}{\pi(\tau^0)^2}\frac{E}{(1-\nu^2)} = \frac{\tau_c^H\delta_c}{\pi(\tau^0)^2}\frac{E}{(1-\nu^2)}, \tag{5.4}$$

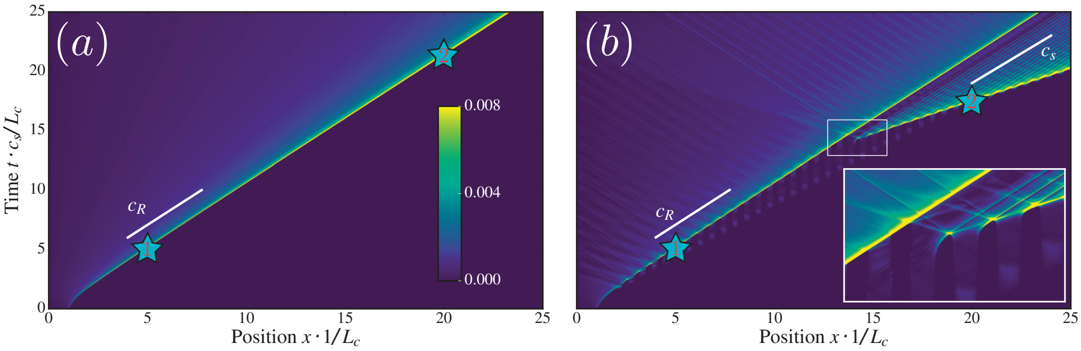

Figure 5.2 – Space-time diagrams of two macroscopically equivalent dynamic fracture events where the normalized slip velocity $\dot{\delta}_x/c_s$ is shown using the same color scale while the crack tip position at $L_1 = 5L_c$ and $L_2 = 20L_c$ is highlighted with cyan stars. In (a) the crack grows on a perfectly homogeneous interface, while in (b) the rupture front interacts with smaller-scale heterogeneities.

often referred as *Griffith crack length* [6]. Rupture is initiated in this work by slowly growing an infinitesimal crack to its critical length $L \simeq L_c$ and dynamic rupture begins ($t = 0$) when it starts to grow spontaneously.

5.3 The effect of heterogeneous microstructure

We start our study with the rupture of a perfectly homogeneous interface ($L_{\text{het}} = 0$) initially at rest with $\tau^0 = 0.22\,\tau_c$. As predicted by the crack tip equation of motion [42], the constant loading makes the crack continuously accelerate up to the upper limit represented by the Rayleigh wave speed c_R (Figure 5.2a). While keeping the same system on average, we increase its statistical dispersion after $L_{\text{hom}} = 2L_c$ by introducing stripes of weaker ($\tau_c^{\text{weak}} = \frac{1}{3}\tau_c^H$) and stronger ($\tau_c^{\text{strong}} = \frac{5}{3}\tau_c^H$) heterogeneities of width $w = 0.6L_c$ according to Figure 5.1. This heterogeneous microstructure leads, however, to a dramatic change in rupture dynamics, which is presented in Figure 5.2b. After a first propagation phase at a sub-Rayleigh regime $x/L_c < 15$, the rupture front is able to exceed the Rayleigh wave speed and c_s (see Section 5.7 for additional representations of these rupture events). The supershear transition of mode II crack is fundamental in the understanding of earthquake dynamics [73, 74, 170] and several works [6, 9, 46, 82, 171, 172] studied how a propagating front may eventually get supershear; the time-growing pulse radiated ahead of an accelerating shear crack causes the nucleation of a secondary supershear front if its maximum amplitude exceeds interface strength. For a rupture growing from $L = L_c$, Andrews [6] was the first to report how this transition occurs at a specific crack size, which depends on the initial ratio between interface strength and pre-stress, the so-called seismic ratio $S = (\tau_c^H - \tau^0)/\tau^0$. Following the same formalism, Figure 5.3 summarizes our quantitative study of this supershear criterion for different loading conditions and toughness distributions. With a plane strain homogeneous setup, we meet the transition dynamics reported in the literature [6, 7]. The comparison

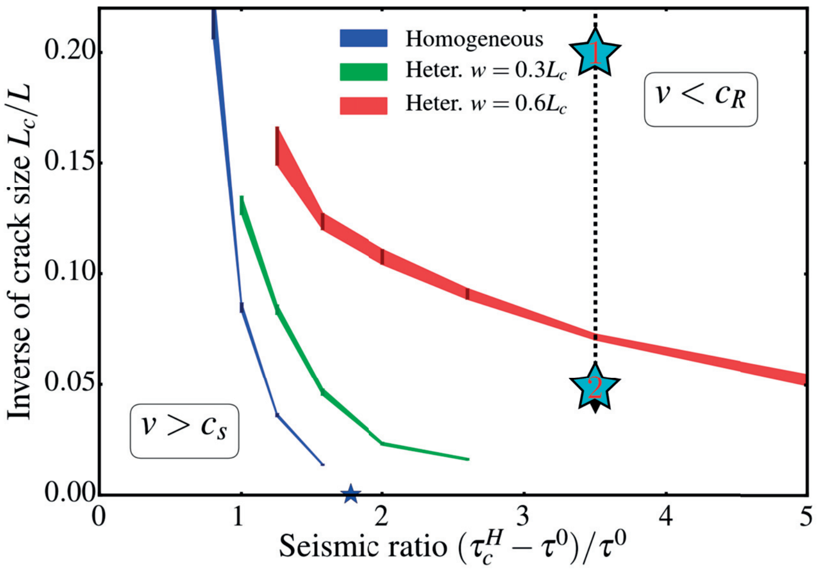

Figure 5.3 – Effect of heterogeneities on the supershear transition. Color curves trace the observed boundary between sub-Rayleigh and supershear regimes for different loading conditions (seismic ratio) and toughness distribution. The dashed arrow draws the trajectory of ruptures of Fig. 5.2 where the crack is initially in the sub-Rayleigh regime (cyan star at $L_1 = 5L_c$) and grows toward a size (cyan star at $L_2 = 20L_c$) where it either crosses the boundary toward supershear regime (as in the interface of Fig. 5.2b with $w = 0.6L_c$), or not (as in the homogeneous interface of Fig. 5.2a). The dark blue star shows the maximum seismic ratio allowing supershear crack in homogeneous plane strains interface [6, 7].

with the heterogeneous set-up reveals how increasing the microscopic toughness dispersion facilitates the supershear transition by both extending the limiting seismic ratio and reducing the required transition length. The explanation is found in the increase of elastic radiations caused by the heterogeneous microstructure. During homogeneous rupture, the slip velocities profile is smooth and high velocities are concentrated within the process zone. In presence of heterogeneities, elastic waves are continuously emitted from the propagating tip resulting in a succession of pulses visible in the slip velocity profile. The inset of Figure 5.2b presents a collective mechanism where the rupture of tougher asperities creates waves which are later helping the rupture of the neighboring asperities. Super-shear transition caused by a favorable heterogeneity has been reported in several works in the context of earthquake dynamics in the presence of heterogeneous pre-stress or toughness along the slip plane [80–82, 84] or with off-fault elastic heterogeneity [83, 85]. Following this benchmark problem of dynamic fracture, our study reveals how a collective mechanism occurring at the smaller scale of a heterogeneous interface can deeply impact the macroscopic rupture dynamics. Moreover, Figure 5.3 emphasizes the importance of the details of microscale properties which are systematically discussed in the next section.

5.4 Transition from homogeneous to heterogeneous fracture

In the system considered, two parameters characterize the heterogeneity of the interface: the size w of the asperities and the fracture energy contrast $G_c^{\text{strong}}/G_c^{\text{weak}}$. The rupture speed is another important parameter, which constantly increases in the preceding simulations because of the load-controlled setup. After an identical smooth initiation, a progressively decaying loading $\tau^0(L)$ allows for crack growth at a constant speed along a perfectly homogeneous interface (K-controlled set-up). The same loading conditions are further replicated to rupture fronts meeting a heterogeneous region far from the initiation site ($L_{\text{hom}} = L_{\text{het}} = 5L_c$). As described in the previous section (see Figure 5.2b), one signature of the interplay of dynamic crack front with heterogeneities is the slip pulses emitted during the successive front accelerations. We measure and compare then the maximum slip velocity $\max\{\dot{\delta}_x\}$ observed when the front breaks the heterogeneous region and compare it to the value measured when the interface is perfectly homogeneous $\max\{\dot{\delta}_x^H\}$. The normalized increase in slip velocity

$$\Phi(w, \frac{G_c^{\text{strong}}}{G_c^{\text{weak}}}) = \frac{\max\{\dot{\delta}_x\} - \max\{\dot{\delta}_x^H\}}{\max\{\dot{\delta}_x^H\}} \tag{5.5}$$

is then used as an indicator of crack front perturbation for a given heterogeneous microstructure. A progressive increase of slip velocities is observed when increasing the fracture energy ratio between weaker and stronger asperities. However, when changing the size of the asperities, the evolution of Φ is not monotonic and depends on a critical asperity size. The width of the process zone, l_{pz}, namely the distance over which the interface evolves from intact to broken, is the characteristic length scale emerging from this K-controlled setup. Figure 5.4a presents how the increase in slip velocity measured with different asperity sizes and fracture energy ratios collapses after being normalized by the size of the process zone (data before normalization are available in Section 5.7). Three characteristic behaviors emerge from this normalization. When $w \sim l_{pz}$ (Figure 5.4c), the heterogeneous interface develops a collective mechanism similar to the one discussed in Figure 5.2b and leads to a significant perturbation of the rupture dynamics. The effect of heterogeneities quickly decays as $w < l_{pz}$. When several weaker and stronger heterogeneities are contained within the process zone (Figure 5.4b), their fracture properties are averaged and homogenized resulting in a rupture dynamics identical to the perfectly homogeneous set-up. Finally when $w \gg l_{pz}$, the collective interaction between asperities ceases as the elastic waves have time to dissipate within the bulk between two depinning events. In this macroscopically heterogeneous interface, l_{pz} stops characterizing the rupture dynamics which meets the predictions of the singular fracture theory according to which the crack speed instantaneously adapts to a change in fracture toughness (Figure 5.4d). These characteristic behaviors controlled by the process zone size are universally observed with different types of heterogeneity $G_c^{\text{strong}}/G_c^{\text{weak}}$ (Figure 5.4a) as well as different crack front speeds (inset of Figure 5.5).

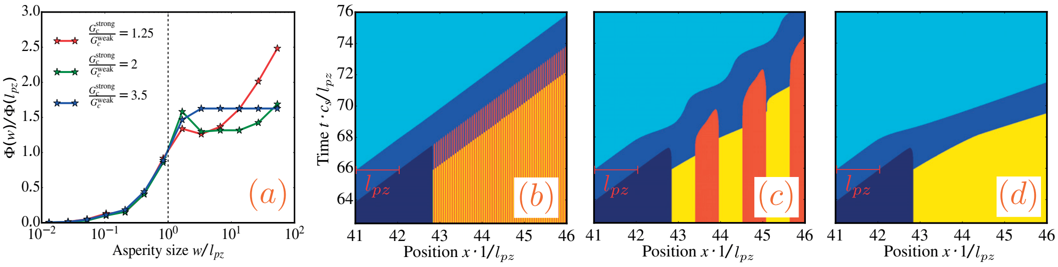

Figure 5.4 – The process zone size is the length scale controlling crack front interaction with heterogeneities. For $v = 0.5c_s$ and a fracture energy ratio of 3.5, colors in plots (b-d) divide broken surface (sky-blue), cohesive zone (blue) and intact interface which is either dark blue (average properties), yellow (weaker properties) or orange (tougher properties).(a) Normalized increase of slip velocity as function of interface heterogeneity, namely asperity size and fracture energy ratio for $v = 0.5c_s$. (b) Asperities are much smaller than l_{pz} leading to quasi-homogeneous dynamics. (c) Collective interaction between depinning events when w is in the range of l_{pz} leading to a significant impact on rupture dynamics. (d) When the asperities are much larger than l_{pz}, the material is macroscopically heterogeneous.

5.5 Process zone size in dynamic fracture

At the very vicinity of crack tip, one should admit a region, the process zone, where nonlinear dissipative processes are regularizing the square root singularity. The nature of these nonlinear processes is far from being understood and should certainly be highly dependent on the material. Cohesive models arose from Dugdale [20] and Barenblatt [21] approaches which propose an elegant way of modeling these processes without losing the universality of LEFM theory. In this non-singular framework, l_{pz} scales as:

$$\left(\frac{K_{II}}{\tau_c^H}\right)^2 \sim l_{coh}^* = \frac{G_c^H}{(\tau_c^H)^2}\frac{E}{(1-\nu^2)} = \frac{1}{2}\frac{\delta_c}{\tau_c^H}\frac{E}{(1-\nu^2)}, \tag{5.6}$$

for a crack at equilibrium with the linear slip-weakening law of Equation (5.3). Within the K-controlled set-up, the process zone has then a constant size along the homogeneous portion of the interface as highlighted in Figures 5.4b, 5.4c and 5.4d. We thereby measured its length at different rupture speeds in Figure 5.5 and observe a shrinkage of l_{pz} as v increases. This relativistic process zone contraction as v approaches the information speed is indeed predicted theoretically [153, 173, 174] and was recently measured in experiments [126]. l_{pz} is even expected to be infinitely small when v approaches c_R. The fine level of discretization provided by the boundary element model enables us to capture this process zone contraction. Since l_{pz} is the characteristic length governing the interaction of crack front with material heterogeneities, its contraction implies that faster cracks are perturbed by smaller heterogeneities/defects along their path.

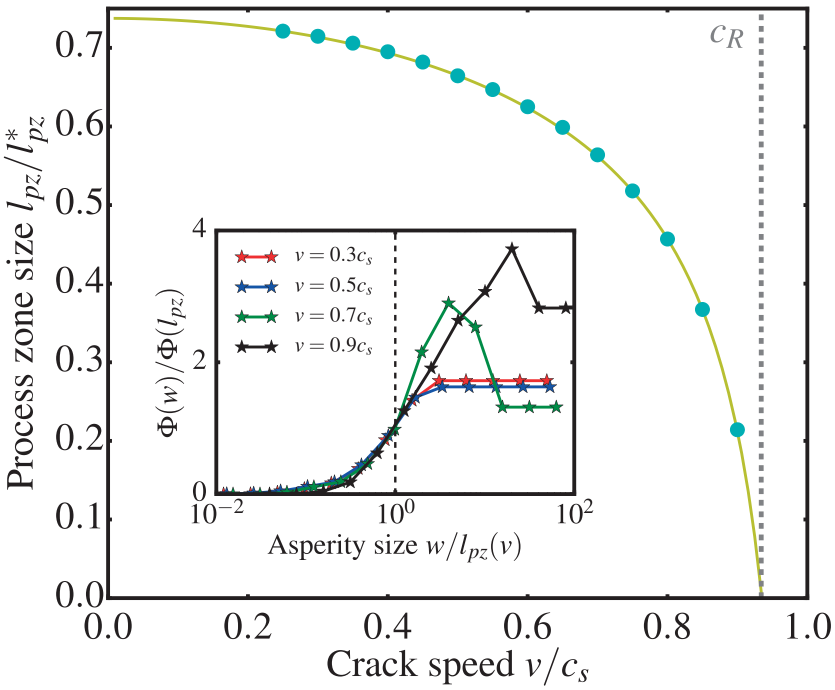

Figure 5.5 – Faster crack fronts interact with smaller heterogeneities. The main plot details how the process zone size contracts as the crack accelerates toward c_R. Cyan dots show simulation data compared with the theoretical prediction in yellow (details are provided in Section 5.7). The inset shows the increase of slip velocity as function of asperity size for $G_c^{\text{strong}}/G_c^{\text{weak}} = 3.5$ and different crack speeds using $l_{pz}(v)$ for normalization to collapse data.

5.6 Discussion

Taking advantage of the fine discretization allowed by the boundary integral formulation [17], we investigate numerically the interplay of a dynamic crack front with heterogeneities. A planar straight crack under plane strain conditions interplays with an idealized microstructure made of equi-spaced stripes of weaker and stronger areas. We reveal a complex mechanism where the nucleation and coalescence of crack fronts within the heterogeneous microstructure radiates elastic waves helping the rupture of neighboring asperities. This collective process occurring at the scale of the heterogeneous microstructure directly changes the macroscopic dynamics and facilitates the supershear transition. We present then how the size of the process zone is the length scale characterizing the perturbation of a dynamic front by material heterogeneities. This observation was confirmed with different sub-Rayleigh front speeds and heterogeneous microstructures. Moreover, the process zone size decreases with the crack velocity, shrinking to zero as v approaches c_R. As the rupture front accelerates toward c_R, it interacts therefore with smaller material heterogeneities (asperities, defects). We suggest that this process zone contraction amplifies thereby the dynamic instabilities and roughens the fracture surface of an accelerating crack front. This study shines a new light on the interplay between a dynamic rupture front and the material-heterogeneity length scales. The observations and conclusions drawn in this manuscript have direct implications in the understanding of earthquake dynamics [74, 170, 171] (supershear rupture) as well as the evolution observed in the fracture behavior of materials with increasing rupture speed [51, 166, 169] (interaction of crack with defects/microstructures, dynamic instabilities).

5.7 Supplemental material

5.7.1 Material properties

Elastic material properties of Homalite have been chosen for the simulations reported in this chapter; Young's modulus $E = 5.3$ [GPa], Poisson's ratio $\nu = 0.35$ and shear wave speed $c_s = 1263$ [m/s]. In the homogeneous segment, the interface fracture energy $G_c^H = 90$ [J/m^2] is defined by $\tau_c^H = 9$ [MPa] and $\delta_c = 0.02$ [mm].

5.7.2 Effect of heterogeneous microstructure

As a complement to Figure 5.2, the two rupture events are also presented in Figure 5.6 using the same color code as in Figures 5.4b-d to highlight the heterogeneous microstructure as well as the position of the rupture front. The growing pulse radiated in front of an accelerating shear crack [6, 9] is also clearly visible in Figure 5.6 as it causes early microcracks nucleation in the weaker areas.

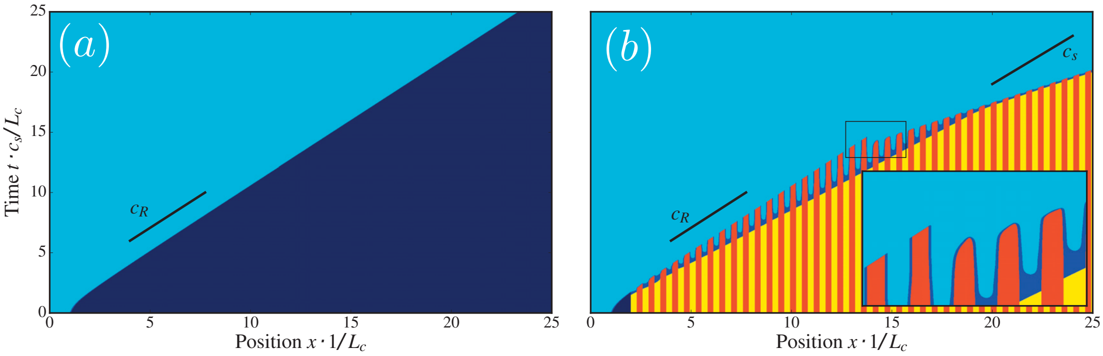

Figure 5.6 – Space-time diagrams of the two macroscopically equivalent dynamic fracture events described in Figures 5.2a-b. The color code is the same as in Figures 5.4b-d.

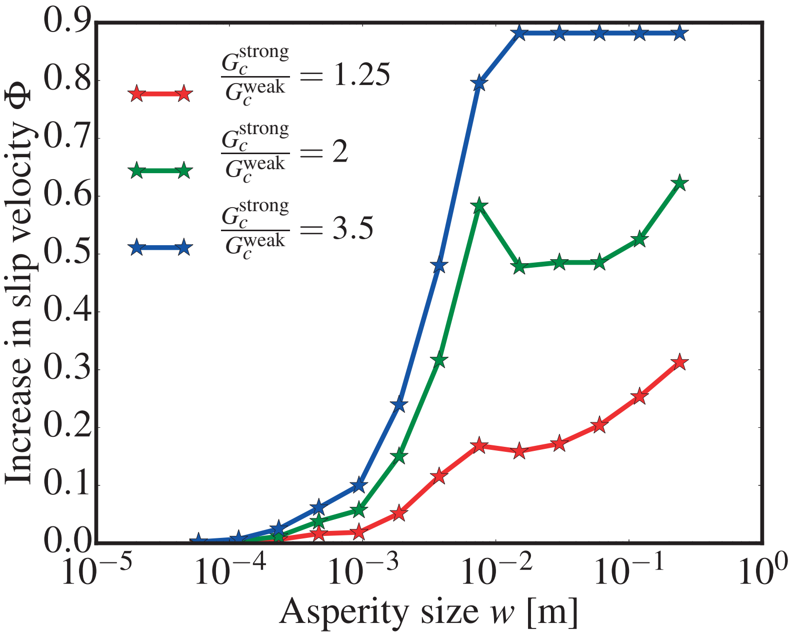

Figure 5.7 – Increase in slip velocity associated with the interaction of a dynamic crack growing at $v = 0.5c_s$ with a heterogeneous microstructure of a given asperity size and fracture energy ratio. Figure 5.4a presents the same data after normalization by the process zone size.

5.7.3 Transition from homogeneous to heterogeneous fracture

Figure 5.7 presents the data of Figure 5.4a before normalization. The increase in slip velocity Φ (cf. Equation 5.4) is used to quantify the interplay of the dynamic front with heterogeneities. Intuitively, the crack front perturbations associated with the heterogeneous microstructure increase with the asperity size w and/or the fracture energy contrast. The normalization by the characteristic length scale l_{pz} (see Figure 5.4a) collapses this data and explains the non-monotonic behavior observed as w changes.

5.7.4 Process zone size in dynamic fracture

When l_{pz} becomes small compared to other characteristic dimension of the system, the rupture dynamics predicted by cohesive models is expected to meet the prediction of the singular LEFM theory based on the dynamic energy release rate expressed as

$$G = \frac{1-\nu^2}{E} A_{II}(v) K_{II}^2, \tag{5.7}$$

where $A_{II}(v)$ is a universal function defined by

$$A_{II}(v) = \frac{\alpha_s v^2}{(1-\nu) D c_s^2}, \tag{5.8}$$

where $\alpha_{s,d}^2 = 1 - v^2/c_{s,d}^2$, and $D = 4\alpha_d \alpha_s - (1+\alpha_s^2)^2$. As shown in [42], A_{II} equals one when $v = 0$ and grows to infinity as the crack speed approaches the Rayleigh wave speed c_R. Rice [173] showed that the size of the process zone for dynamic mode II crack moving at a speed v is expected to follow

$$l_{pz}(v) = l_{pz}(v=0)/A_{II}(v). \tag{5.9}$$

Equation (5.9) thus predicts a process zone contraction with increasing crack speed, as also captured in our simulations (see Figure 5.5).

6 Supershear bursts in the propagation of tensile crack

This chapter presents dynamic effects arising when a crack front is distorted by the presence of heterogeneities along the rupture plane. The perturbation of an initially planar rupture front meeting a tougher circular asperity became an archetype problem of heterogeneous fracture, which has been extensively studied in the framework of first-order perturbation analysis. This chapter extends the investigations to strongly distorted crack fronts. For the first time, this work uncovers the existence of supershear episodes in the tensile (mode I) rupture of linearly elastic materials beyond the maximum allowable (sub-Rayleigh) speed predicted by the classical theory of dynamic fracture. While the admissible rupture speeds predicted by LEFM are verified for smooth crack fronts, we present numerically how a supershear burst can emerge from a discontinuity in crack front curvature and how these short-lived bursts create shock waves persisting far from the discontinuity site. This study shines new light on the dynamic fracture of materials characterized by the roughening of crack fronts where the rupture dynamics significantly diverges from LEFM predictions.

This chapter is a modified version of a scientific article currently under review:

F. Barras, R. Carpaij, P. H. Geubelle, and J.-F. Molinari, “Supershear bursts in the propagation of tensile crack in linear elastic material,” *Under review*, 2018

Further aspects of the 3D dynamics resulting from the distortion of a propagating crack front by a tougher asperity are studied and reported in two associated publications currently in preparation. The first one systematically compares the predictions of first-order models (quasi-static and dynamic) with the full elastodynamic responses computed by the boundary integral method:

K. Alidoost, F. Barras, A. Dubois, R. Carpaij, D. Bonamy, P. H. Geubelle, and J.-F. Molinari, “Crack front distorted by heterogeneities: Benchmarking the first-order perturbation models,” *In preparation*, 2018

The second work studies the propagation of front waves existing after the perturbation of dynamic crack fronts under shear and mixed mode loading conditions:

F.-E. Fekak, F. Barras, A. Dubois, D. Spielmann, D. Bonamy, P. H. Geubelle, and J.-F. Molinari, "Study of front waves: 3D dynamic response to a local perturbation of tensile and shear cracks," *In preparation*, 2018

6.1 Introduction

How fast cracks can propagate in linearly elastic solids is a long-standing question that has challenged scientists and engineers for many decades. The classical theory of LEFM [42, 43] predicts that the Rayleigh wave speed c_R of the surrounding bulk material is the limiting propagation speed of tensile (mode I) cracks, while intersonic crack speeds (i.e., between the shear wave speed c_s and the dilatational wave speed c_d) are allowed for in-plane shear (mode II) cracks. Using non-singular cohesive-like description of fracture, Burridge [46] and Andrews [47] proposed a mechanism enabling shear cracks to transition between the subsonic and intersonic regimes.

Due to crack kinking or branching, experimentally measured crack speeds are substantially lower, rarely exceeding 0.65 c_R [49, 56, 57]. However, constraining crack growth along a weaker plane allowed for the experimental confirmation of limiting velocities for both tensile [72] and shear [73] cracks. The latter study, which demonstrated the existence of supershear crack fronts in linear elastic materials, found direct relevance in the understanding of crustal earthquakes where slip fronts have been measured to propagate faster than c_s along some portion of the fault [74, 75].

Similarly to supersonic aircraft, elastic waves radiated from supershear cracks gather to form shock-wave fronts, also referred to as *Mach Cone*, leading to particularly violent earthquakes [9, 76–79]. Despite the relative rarity of supershear earthquakes reported in nature, recent experiments [171] suggest that short-lived supershear events may frequently occur at smaller scale of crustal fault, out of the resolution of seismic inversion, yet significantly impacting the rupture dynamics. Several studies described indeed how local variation in toughness or elastic properties can precisely favor the supershear transition of mode II cracks [80–83, 85, 125, 148] .

In this work, we describe how supershear propagation bursts triggered by the presence of a tougher heterogeneity distorting the front of a dynamically propagating planar crack can also exist in the tensile case, beyond the range of crack speeds predicted by the classical LEFM theory. This new result finds direct relevance in the fast tensile rupture of materials characterized by significant crack front roughening through the interaction with heterogeneities associated with the microstructure [51, 55, 169] or with microbranching instabilities [166, 178].

6.2 Set-up

We study the in-plane crack front propagation along a weak plane located along $y = 0$ in an infinite linearly elastic solid initially at rest under a uniform tensile stress τ^0. At time $t = 0$, a straight crack front parallel to the z-axis starts to grow dynamically in the positive x-direction before encountering a row of asperities. This 3D fracture problem is solved using a boundary integral formulation of the elastodynamic equations [16, 17] relating the normal displacement jump (or crack opening displacement) $\delta_n(x, z, t)$ and the normal traction stress $\tau_n(x, z, t)$ acting on the fracture plane. For the mode I fracture problem of interest, the spectral

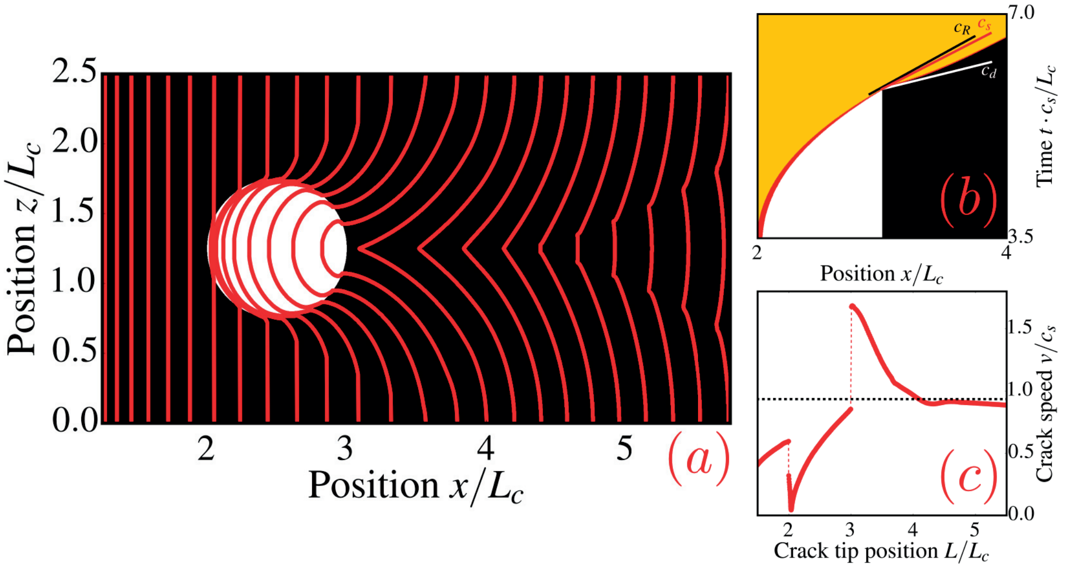

Figure 6.1 – A supershear burst occurs at the cusp located at the center of the crack front line $z = 1.25L_c$. a) Evolution of the crack front line (in red) captured at regular time interval. b) Space-time diagram of the rupture event along $z = 1.25L_c$. Colors divide broken surface (yellow), cohesive zone (red) and intact interface which is either black (homogeneous properties) or white (tougher asperity). c) Evolution of crack front velocity along $z = 1.25L_c$. The dashed black line depicts the Rayleigh wave speed.

formulation (Equation 3.17) is, once more, completed by interface conditions which imply the continuity of tractions and displacements along the interface as long as the normal traction τ_y is lower than the interface strength τ^{str}. Otherwise, the fracture process breaks the continuity of displacements and the velocity $\partial u_j^{\pm}/\partial t$ of the crack faces are computed such that $\tau_y^+ = \tau_y^- = \tau^{\text{str}}$, while the value of the interface strength is related to the opening displacement jump $\delta_n = u_y^+ - u_y^-$ through the following linear cohesive failure model:

$$\tau^{\text{str}}(x,z,t) = \tau_c(x,z)\,\{1 - \delta_n(x,z,t)/\delta_c(x,z)\}\,. \tag{6.1}$$

In Equation 6.1, τ_c and δ_c respectively denote the spatially varying failure strength and critical crack opening displacement of the weak plane, and $\{\xi\} = \xi$ if $\xi > 0$ and 0 otherwise. The nonlinear dissipative processes associated with the dynamic failure event are thus confined to the crack plane, with the fracture energy given by $G_c(x,z) = \frac{1}{2}\tau_c(x,z)\delta_c(x,z)$.

The characteristic length scale for this problem is chosen as the largest stable crack size L_c given by [31, 125]

$$L_c = \frac{2G_c^H}{\pi\left(\tau^0\right)^2}\frac{E}{(1-\nu^2)}, \tag{6.2}$$

where E and ν respectively denote the Young's modulus and Poisson's ratio of the elastic solid, and G_c^H is the fracture energy of the homogeneous portion of the fracture plane. In the initial phase of the failure event, the crack accelerates with a straight front through a homogeneous region stretching from $x = L_c$ to $x = 2L_c$, at which point it encounters a tougher circular asperity of diameter $\o = L_c$ and fracture energy $G_c^{\mathrm{asp}} = \zeta\, G_c^H$, with $\tau_c^{\mathrm{asp}}/\tau_c^H = \delta_c^{\mathrm{asp}}/\delta_c^H = \sqrt{\zeta}$. Due to the spectral nature of the numerical scheme, which is based on a Fourier series representation of the spatial variation of the interface quantities, the domain of interest is periodic, with a period chosen as $X = 10L_c$ and $Z = 2.5L_c$. The simulated fracture event thus involves the dynamic interaction of an initially straight mode I crack with a row of circular asperities. The rupture planes studied in this manuscript are typically discretized with 4096 x 1024 points in the x- and z-directions, respectively, providing more than four million sampling points along the fracture plane. The results discussed hereafter are non-dimensionalized but the material and failure properties used in the simulations are given hereafter.

6.3 Material properties

Material properties of Homalite have been chosen for the simulations reported in this chapter; Young's modulus $E = 5.3$ [GPa], Poisson's ratio $\nu = 0.35$, and shear wave speed $c_s = 1263$ [m/s]. The interface fracture energy $G_c^H = 50$ [J/m^2] is defined by the two parameters entering the cohesive failure model (Equation 1) $\tau_c^H = 5$ [MPa] and $\delta_c^H = 0.02$ [mm].

6.4 Methodology

A seed crack whose tips are initially parallel to the z-axis is artificially grown in the positive x-direction from $x = 0$, while the propagation of the left tip is prevented. In an infinite solid under uniform tension τ^0, the rate of energy released by growing a static through crack of size L is given by

$$G(v = 0, L) = \frac{(1-\nu^2)}{E}(\tau^0)^2\pi\frac{L}{2}. \tag{6.3}$$

At $t = 0$, the crack reaches the critical size L_c (cf. Equation 6.2) where $G(v = 0, L = L_c)$ exactly equates the fracture energy G_c^H and starts to propagate dynamically at a speed $v > 0$. In an infinite homogeneous solid, Freund [42] showed that the energy release rate evolves with propagation speed as $G(v, L) = g(v)G(v = 0, L)$, with $g(v)$ denoting a function which is unity for $v = 0$ and zero for $v = c_R$. Considering Equation 6.2 together with Equation 6.3, the dynamic energy balance can be expressed as

$$G(v, L) = G_c^H \Leftrightarrow \frac{L}{L_c} = \frac{1}{g(v)}. \tag{6.4}$$

In this framework, Figure 6.2 reports the crack dynamics obtained along a perfectly homogeneous interface ($\zeta = 1$) compared to Freund's approximation for a semi-infinite crack $g(v) \approx (1 - v/c_R)$ [42]. This approximation as well as the assumption of a semi-infinite crack explain the slight difference between predicted and simulated dynamics. For the reference case presented in Figure 6.1, the initially straight crack front starts interacting with the tougher asperity when $L = 2L_c$, which corresponds to an incident front speed $v = 0.6c_s$. Different incident crack front speeds can therefore be investigated by changing the asperity position according to Figure 6.2.

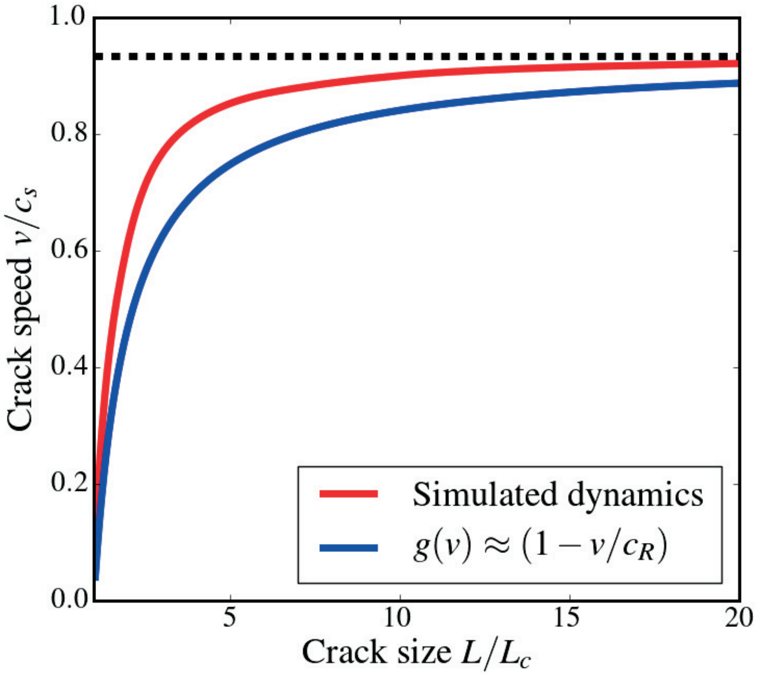

Figure 6.2 – Typical crack tip dynamics observed along a homogeneous fracture plane. The dashed line highlights the Rayleigh wave speed.

6.5 Supershear bursts

Rice [2] described how the distortion of a crack front interacting with an asperity may locally increase the stress intensity factor to a value sufficiently large to rupture the asperity. Following his first-order perturbation analysis, the interaction of quasi-static [60] and dynamic [15] crack front with heterogeneities can be precisely described as long as the perturbation to the crack front is small. Our numerical work thereby aims at widening the investigation toward larger toughness contrasts where higher-order effects cannot be neglected. In this context, our study uncovers the existence of short-lived supershear bursts emerging from large front distortions as presented in Figure 6.1 for $\zeta = 3$. At the center of the domain (along the line $z = Z/2 = 1.25L_c$), Figure 6.1c presents the evolution of crack front speed, which is always in the x-direction due to symmetry. Right after rupturing the heterogeneity, the crack speed temporarily exceeds c_s, which is visually confirmed in Figure 6.1b. This supershear burst

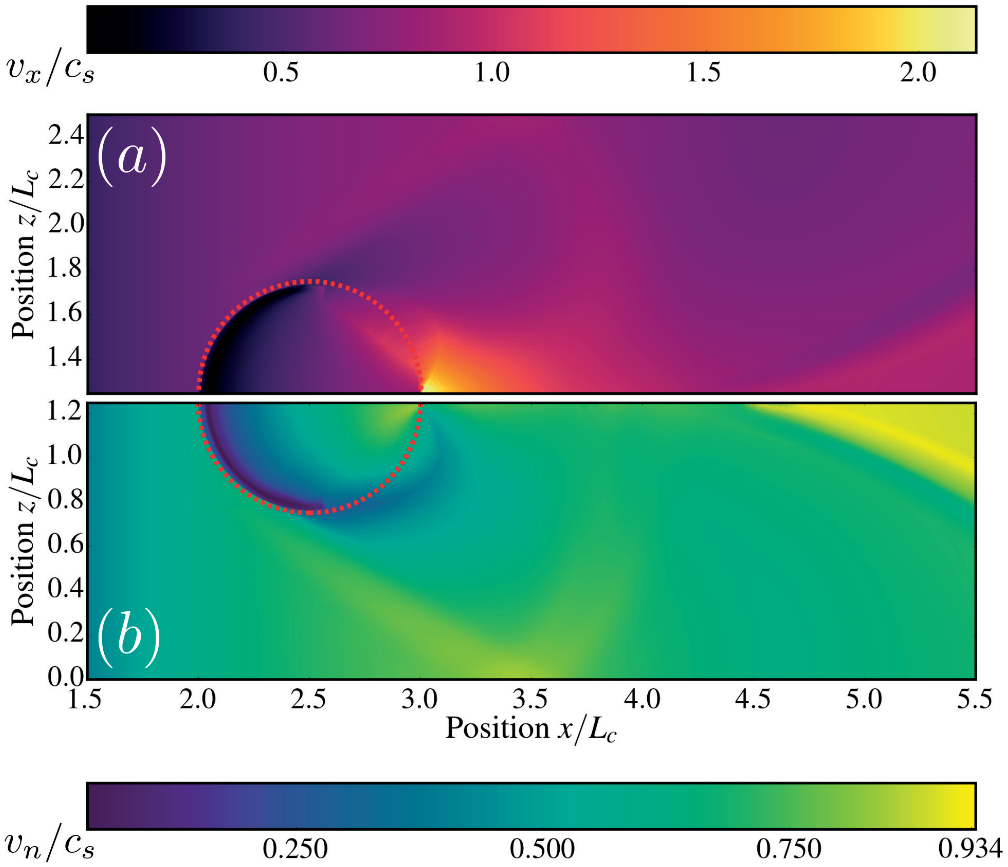

Figure 6.3 – The supershear burst arises exclusively at the cusp emerging along the front at $z = Z/2$. Evolution of the crack front velocity v_x/c_s in the x-direction (a) and in the direction normal to the crack front v_n/c_s (b) computed along the interface for $z < Z/2$ and $z > Z/2$. The color map is scaled between the minimum and maximum values verifying the supershear range of the apparent forward velocity v_x and the sub-Rayleigh range of the normal crack speed v_n ($c_R \cong 0.934 c_s$) predicted by LEFM for smooth crack front.

extends beyond the center line, as illustrated in Figure 6.3a, which presents the distribution of apparent crack velocity (i.e., the crack velocity v_x in the x-direction) over the entire crack plane. A related study conducted in mode II [82] has shown that asperities can be triggering sites for supershear propagation of shear cracks. However, unlike its mode II counterpart, super-Rayleigh propagation of tensile (mode I) cracks in a linear elastic material is energetically impossible. This fundamental result of the dynamic theory of LEFM is indeed verified in Figure 6.3b, which presents the spatial distribution of the crack speed v_n computed normal to the front. As apparent there, the crack speed remains sub-Rayleigh as long as the crack front curvature is continuous. The evolution of the crack front shape presented in Figure 6.1a reveals how the emergence of a cusp along the front line coincides with the episode of supershear propagation. This can be rationalized with geometric arguments presented in the next section.

6.6 Geometrical model

Next, we introduce a geometrical model that explains and predicts how a sub-Rayleigh crack velocity in the normal direction of the front can yield supershear velocity on the projected forward direction, when a geometrical cusp is formed.

Let $a(z,t)$ denotes the amplitude of the front distortion, i.e., the advance of the crack front at location z and time t relative to the front location at the kink ($z = Z/2$) (Figure 6.4). Let us assume that the crack front propagates at uniform subsonic speed κc_R (with $\kappa < 1$) in the direction of the local normal $\boldsymbol{n}$ to the front. Geometrical arguments readily lead to the following approximate expression of the forward velocity v_x of the front:

$$\frac{v_x(z,t)}{c_R} \approx \kappa\sqrt{1+\left(\frac{\partial a(z,t)}{\partial z}\right)^2}. \tag{6.5}$$

Based on the observed shape of the front immediately past the asperity (see Figure 6.1), let us

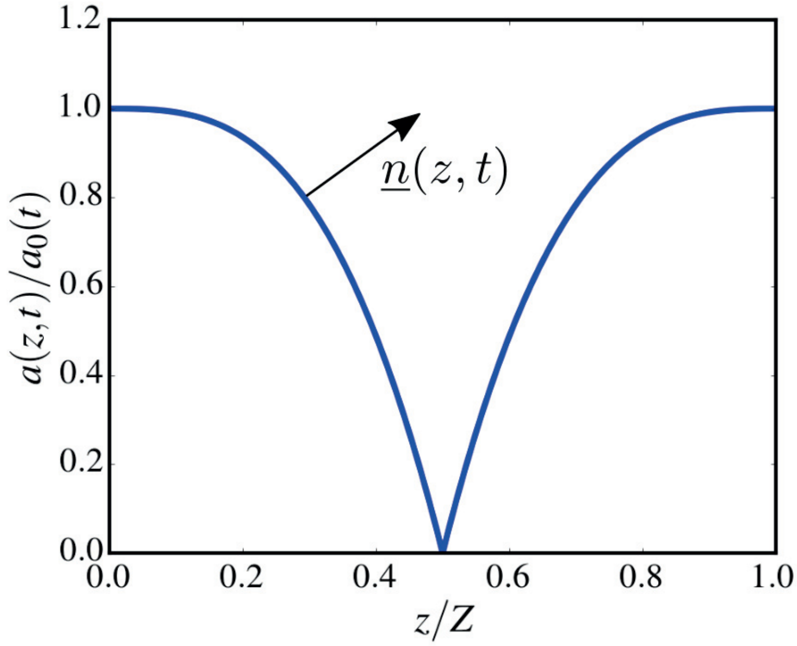

Figure 6.4 – Schematic representation of a kinked crack front, with $\boldsymbol{n}$ denoting the unit normal at (z,t).

adopt the following expression for the shape of the front between $0 \le z \le Z/2$:

$$a(z,t) = a_0(t)\Big(-8(z/Z)^3 + 1\Big), \tag{6.6}$$

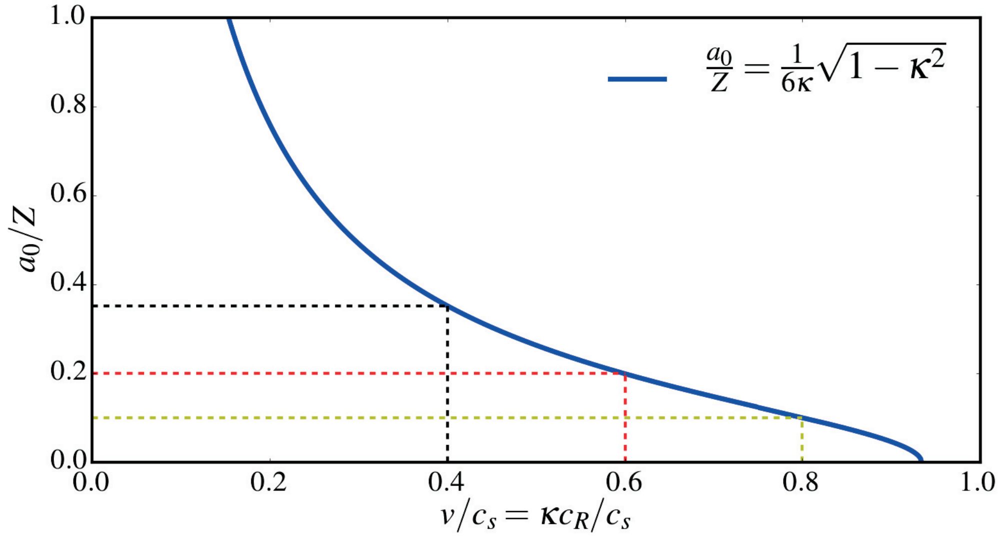

Figure 6.5 – Amplitude of the front perturbation required to observe $v_x > c_R$ at the center point as function of the incident crack speed v. The dashed lines highlight the required amplitude for each of the three different crack speeds considered in the parametric study presented in Figure 6.6.

where $a_0(t) = a(0,t) = a(Z,t)$. Equation 6.6 corresponds to the lowest order polynomial satisfying $a(0,t) = a_0(t)$, $a(Z/2,t) = 0$ as well as the continuity of tangents and curvatures across the periodic boundaries, i.e., $\frac{\partial a}{\partial z}(0,t) = \frac{\partial^2 a}{\partial z^2}(0,t) = 0$. Combining Equation 6.5 and 6.6, we obtain the values of the front perturbation at which the center point ($z = Z/2$) is predicted to propagate faster than c_R:

$$\frac{a_0}{Z} = \frac{1}{6\kappa}\sqrt{1-\kappa^2}. \tag{6.7}$$

This relation is presented in Figure 6.5. As expected, the amplitude of the front perturbation a_0 at which supershear crack motion appears decreases with increasing normal crack speed (i.e. with increasing value of κ).

For a given amplitude of the perturbation a_0/Z, we can also compute the section of the crack front defined as $z^* \le z \le (Z - z^*)$ that has a forward motion faster than the Rayleigh wave speed.

$$\frac{z^*}{Z} = \left(\frac{\sqrt{1-\kappa^2}}{24\kappa(a_0/Z)}\right)^{\frac{1}{2}}. \tag{6.8}$$

This relation is shown in Figure 6.7 for different values of the normal crack front speed. For the reference case of the manuscript ($v = 0.6c_s$), Equation 6.8 predicts therefore that the crack front, just after being released from the asperity, has an apparent forward velocity $v_x > c_R$ along a portion corresponding to $0.37 \le z/Z \le 0.63$ (or equivalently $0.925 \le z/L_c \le 1.575$) in agreement with the velocity profile presented in Figure 6.3.

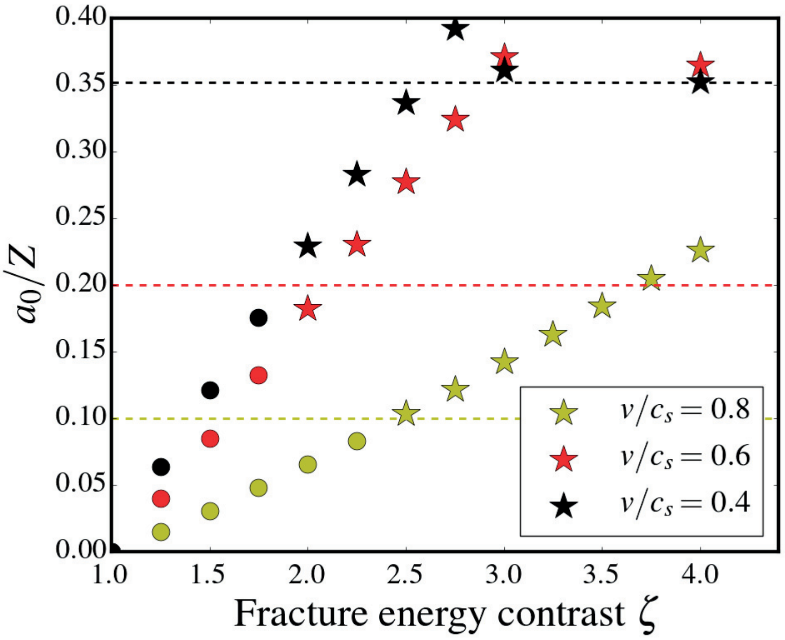

Figure 6.6 – Maximum crack front deflection a_0 observed for various asperity toughnesses and three different values of the incident crack speed v/c_s. The deflection of the crack front interacting with the tougher asperity either creates a supershear burst (star symbols) or not (round symbols). From the geometrical model (cf. Equation 6.7 and Figure 6.5), this observed transition is predicted to occur at a given crack front deflection, which depends on the incident crack speed and is depicted by the horizontal dashed lines.

6.7 Parametric study

The supershear bursts studied in this chapter for $v = 0.6c_s$ and $\zeta = 3.0$ are also observed with different incident crack speeds or asperity toughnesses as reported in Figure 6.6. The dashed lines correspond to the predicted minimum front perturbation required to observe a supershear burst at the center of the domain according to Equation 6.7. The proposed model gives therefore a quantitatively good prediction with fast crack front speeds. At slower crack velocity, the front perturbation becomes larger and stops complying with the model hypothesis of an uniform speed in the normal direction. This inverse relationship between the incident rupture speed and the front deflection is obvious in Figure 6.6 and can be understood from Freund's crack tip equation of motion [42]:

$$G_c = G = \frac{(1-\nu^2)}{E} A_I(v) K_I^2. \tag{6.9}$$

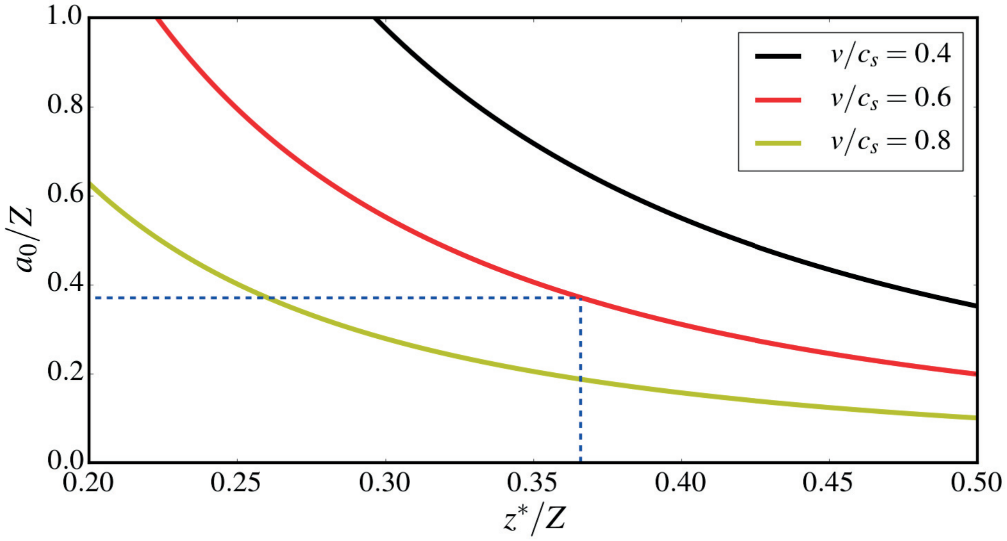

Figure 6.7 – Portion of the crack front moving with a forward velocity $v_x > c_R$. The dashed blue line emphasizes the expected portion for the reference case presented in Figure 6.3, while the value $a_0/Z = 0.371$ is read from Figure 6.6 ($v = 0.6c_s$ and $\zeta = 3$).

In Equation 6.9, K_I and $A_I(v)$ are respectively the mode I stress intensity factor and universal function defined by

$$A_I(v) = \frac{\alpha_d v^2}{(1-\nu)Dc_s^2}, \tag{6.10}$$

where $\alpha_{s,d}^2 = 1 - v^2/c_{s,d}^2$, and $D = 4\alpha_d\alpha_s - (1+\alpha_s^2)^2$. Front perturbation analyses presented in [2, 15, 60] describe how the crack front deflection created by the presence of the asperity leads to an increase of the stress intensity factor ΔK_I at the edge of a tougher heterogeneity to compensate its associated increase in interface fracture energy ΔG_c. In a first-order approximation, this change in energy release rate can be written as:

$$G_c + \Delta G_c = \frac{(1-\nu^2)}{E} A_I(v)(K_I + \Delta K_I)^2. \tag{6.11}$$

The velocity-dependent coefficient $A_I(v)$ monotonically increases with v, which implies that, the interaction of a faster crack speed with a given heterogeneity characterized by ΔG_c leads to a lower ΔK_I, i.e., to a smaller deflection of the crack front. For a more detailed description of the link between the perturbation amplitude for a dynamically propagating crack front and the associated effect on the local value of the stress intensity factor, please see [15].

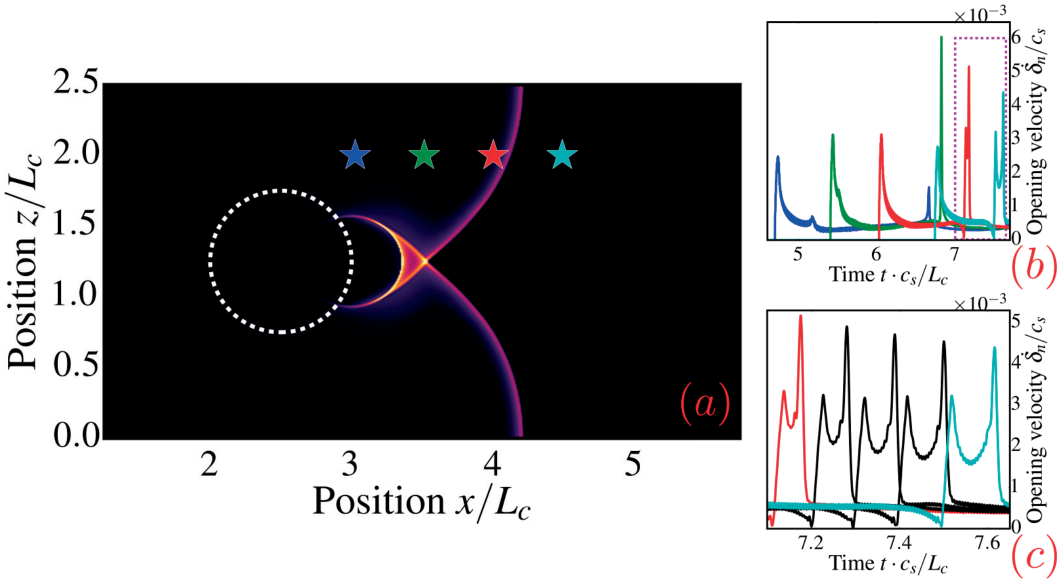

Figure 6.8 – The supershear burst creates shock waves driving energy far from the asperity site. a) Snapshot of crack opening velocity field $\dot{\delta}_n$ following the failure of the asperity whose position is highlighted by the white dashed circle. The colored stars denote the positions at which the time-evolution of $\dot{\delta}_n$ is computed and presented in (b) and (c). b) Evolution of $\dot{\delta}_n$ observed at the different positions highlighted in (a). The strong surface waves caused by the rupture of the asperity are visible after the initial peak characteristic of the rupture front. c) Zoom in $\dot{\delta}_n$ history (dotted rectangle in (b)) emphasizing first the trace leaved by the persistent “triangular” shock wave, sharply followed by the decaying “circular” front. The black curves correspond to additional sampling points located between the red and cyan positions.

6.8 Shock waves

Our study demonstrates how supershear propagation can also exist in the tensile failure of linear elastic materials. However, supershear events emerge exclusively where the crack front curvature is discontinuous and occur thereby in the form of localized burst along the crack front. Nevertheless, these short-lived bursts can have a significant impact on the overall rupture dynamics through the creation of shock waves associated with these supershear propagation events. Figure 6.8a presents the profile of the normal opening velocity field $\dot{\delta}_n$ just after the rupture of the heterogeneity. Two surface wave fronts can be identified: a circular front released by the failure of the asperity and growing radially at the Rayleigh wave speed along the fracture surface, and a triangular front characteristic of the shock wave generated by the supershear motion of the crack. For several locations along the fracture plane, Figure 6.8b shows how the amplitudes of these wave fronts are comparable to the opening velocities observed during the rupture. Moreover, as the circular wave front progressively decays as it expands along the fracture surface, the triangular shock wave front propagates along the fracture surface with a persistent amplitude [79], as highlighted in Figure 6.8c.

6.9 Conclusion

Taking advantage of the fine discretization allowed by the numerical scheme based on a spectral boundary integral formulation of the 3D elastodynamic equations, we study the large distortion of an initially straight dynamically propagating crack front as it interacts with a circular asperity. Our study uncovers the existence of supershear bursts emerging during the tensile failure of a linearly elastic material, beyond the range of crack propagation speeds allowed by the classical theory of dynamic LEFM. The crack front speeds computed in a direction normal to the propagating front remain sub-Rayleigh as long as the front curvature is continuous, and the supershear bursts are associated with the emergence of a cusp in the crack front caused by the heterogeneity. These supershear episodes create shock waves persisting along the fracture surfaces far from the asperity site. Several experimental studies [51, 56, 57] reported how fast tensile ruptures (between a few tenths of c_s and the branching velocity) diverge from LEFM predictions. These events are characterized by significant crack front distortions caused by microscopic heterogeneities [55, 169] and/or the nucleation of microbranches able to form cusps along the crack front line [178]. In this context, the resulting discontinuities are favorable site to trigger these short-lived “sonic booms” capable of significantly impacting the overall rupture dynamics.

7 Onset of sliding across scales

Along a frictional interface bounding two nominally flat solids, sliding initiates as the propagation of slip fronts bringing the interface from a sticking to a sliding state. This macroscopic rupture dynamics can be successfully mapped on the elastodynamics of a moving shear crack. However, this analogy does not apply to the nucleation process, which mostly develops at the scale of the microcontacts. In this context, this chapter studies the onset of rupture along a heterogeneous plane whose shear strength is sparsely distributed at some discrete spots along the interface. It hence bridges the heterogeneous fracture problem discussed in the previous chapters to the dynamics of frictional interfaces. This study first presents how a cohesive approach can be conveniently used to capture the two main failure mechanisms of the microcontact junctions (cf. Figure 2.14). Taking advantage of a scalable parallel implementation of the cohesive element method, this work explores how these different mechanisms arising at the microscale of frictional interfaces impact the nucleation and propagation of slip fronts observed macroscopically. These outstanding simulations (70M degrees of freedom) reveal how the "brittle-to-ductile" transition at the scale of the microcontacts can significantly reduce the apparent frictional strength of the interface, without any visible change in the macroscopic fracture energy measured during the slip front propagations. These results are then discussed and proposed as an explanation of the "slippery but tough" transition experimentally observed after the lubrication of frictional interfaces.

This chapter is currently being adapted into a scientific publication:

F. Barras, R. Aghababaei, and J.-F. Molinari, "Onset of sliding across scales: How the microcontacts impact frictional strength," *In preparation*, 2018

7.1 Introduction

The onset of sliding along frictional interfaces is driven by a similar dynamics than the one observed during the rupture of brittle materials. The frictional strength is unevenly distributed along the contacting plane, shear stresses concentrate at the edges of inherent flaws and eventually lead to the nucleation of rupture fronts propagating along the contact plane. Just like a propagating shear crack, the shear stress drops and sliding starts in the wake of a slip front that is moving along the interface. This analogy particularly suits the observed behaviors of frictional interfaces at a macroscopic scale and explains that earthquake dynamics has been studied for many decades as the propagation of shear cracks along crustal faults [43, 180].

In this framework, pioneer cohesive approaches have been developed to study numerically the propagation of slip fronts, for which the resistance to sliding is modeled as progressively dropping with interface slip (often referred to as *slip-weakening* models) [6, 40, 47, 110]. Using high-speed camera and photo-elasticity, slip fronts were later observed experimentally along interfaces bounding two blocks of PMMA. These "laboratory-earthquakes" confirmed the dynamics predicted by the early cohesive models [73, 76, 77].

Recent experiments [126] quantitatively showed how the LEFM theory perfectly describes the evolution of strains measured at a short distance from the interface during the propagation of slip fronts. From this fit, a unique parameter emerges, the equivalent fracture energy G_c of the frictional interface, which was later used to rationalize the observed arrest of slip fronts in light of the energy balance criterion [128, 129]. The same framework was also successfully applied to describe the failure of interfaces after lubrication [127]. Despite a reduction in the force required to initiate sliding, the equivalent fracture energy measured after lubrication was surprisingly higher than for the dry configuration [24]. This apparent paradox in the framework of linear elastic fracture mechanics is expected to arise during the nucleation phase, which is controlled by the microscopic nature of friction and contact. At the microscale, surfaces are rough and contact only occurs between the surface peaks, resulting in a very heterogeneous distribution of the sliding resistance [91, 181].

In this context, the objective of this work is to investigate numerically the role of this heterogeneous microscopic strength profile at the onset of sliding driven macroscopically. Using a cohesive approach implemented in a high performance finite-element library, we simulate the onset of sliding across two scales. At the macroscopic level, we study the dynamic stress fields and the energy balance at the onset of the rupture, while at the microscopic scale, we observe how the fracture process zone interplays with the heterogeneous strength profile. This study reveals how tiny differences in the length of the process zone, only visible at the scale of the microcontacts, can magnify the heterogeneous microstructure and have a direct impact on the nucleation phase.

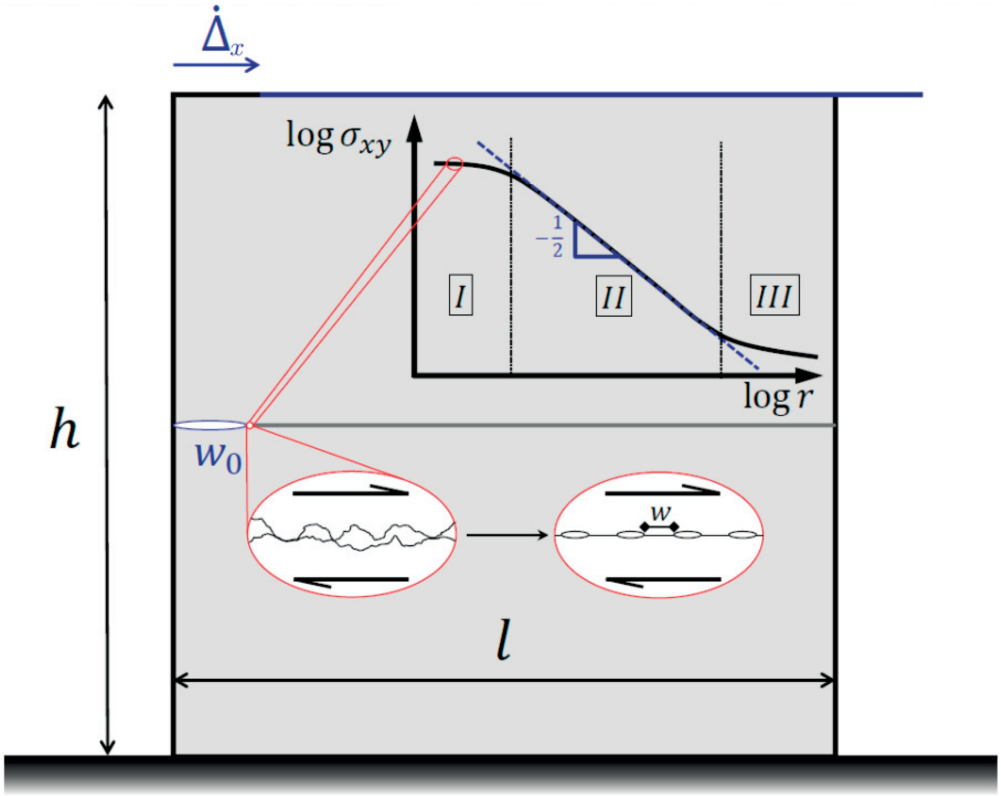

Figure 7.1 – Geometry of the studied problem. The inset presents the schematic shear stress σ_{xy} profile predicted by LEFM at a distance r from the crack tip. Dissipative zone (I) at the immediate vicinity of the tip. Far from the dissipative zone (II), σ_{xy} is dominated by the square root singularity. Further away from the tip (III), the non-singular contributions dominate the profile of σ_{xy} which converges toward the far-field stress conditions. Our work aims at describing how tiny perturbations only visible at the scale of (I) have a direct impact on the onset of rupture fronts.

7.2 Problem description

We consider two linearly elastic blocks of height $h/2$ brought into contact along their longitudinal face of length l. As presented in Figure 7.1, the two blocks are progressively sheared by displacing the top surface at a constant speed $\dot{\Delta}_x$, while the bottom surface is clamped. In a Cartesian system of coordinates, whose origin stands at the left edge of the contacting plane, the boundary conditions of this elastodynamic problem correspond to

$$\begin{cases} \boldsymbol{u}(x,-h/2,t) = 0 \\ \dot{u}_x(x,h/2,t) = \dot{\Delta}_x \\ u_y(0,y,t) = u_y(l,y,t) = 0 \end{cases} \tag{7.1}$$

and lead to a state of simple shear, for which the only non-zero components of the Cauchy stress tensor are $\sigma_{xy} = \sigma_{yx} = \tau$. The elastodynamic solution obtained from the conditions (7.1) in presence of a perfectly intact interface is given in Figure 7.2. At time $t = 0$, the two continua initially at rest start being progressively loaded with a shear wave whose amplitude corresponds to $\Delta\tau = \mu/c_s\,\dot{\Delta}_x$, with μ the elastic shear modulus and c_s the shear wave speed.

The assumption of an intact interface only holds during an initial stage until the displacement field across the contacting plane becomes discontinuous $\boldsymbol{\delta}(x,t) = \boldsymbol{u}(x,0^+,t) - \boldsymbol{u}(x,0^-,t)$. The sliding resistance emerges from a little-understood combination of phenomena developing at different length scales. In this work, the latter and associated dissipative processes are assumed to be constrained at the interface and entirely described by a slip-dependent cohesive law deriving from a thermodynamic potential $\Phi(\delta_x)$. As discussed later, the shape of this potential is chosen to reproduce the mechanical response of the microcontact junctions computed from atomistic simulations [105, 106, 182].

The real contact area between two deformable solids exists along a restricted fraction of the total surface area, leading to a very heterogeneous distribution of the sliding resistance, which highly depends on material and surface properties. The normal pressure and shear stress concentrate at the contacting peaks of the rough surfaces, while valleys remain free of stress. The primary objective of this study consists in understanding the effect of this very heterogeneous microscopic profile on the nucleation process of slip fronts. Nevertheless, the model could add residual friction at the valleys or in the trail of the fronts with no loss of generality. From this complex topography, the sliding motion initiates at the edges of a critical non-contacting region, which is assumed to exist at the very left of our model interface with a size w_0. Moreover, the rough contact distribution sketched in Figure 7.1 is approximated as a regular pattern of resisting and broken patches characterized by a unique critical length $w < w_0$.

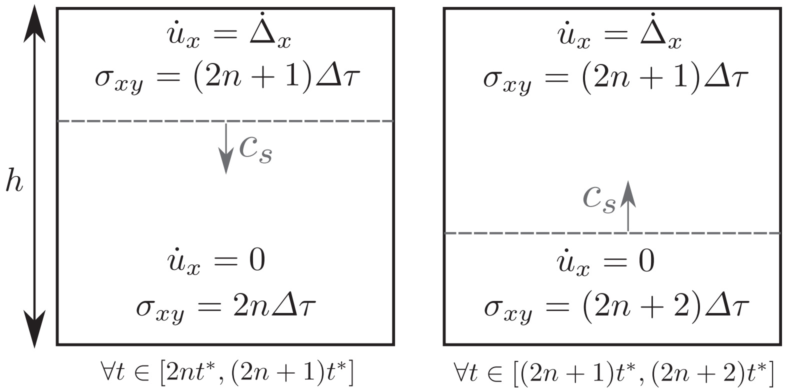
$\dot{u}_x = \dot{\Delta}_x$
$\sigma_{xy} = (2n+1)\Delta\tau$
c_s
h
$\dot{u}_x = 0$
$\sigma_{xy} = 2n\Delta\tau$
$\forall t \in [2nt^*, (2n+1)t^*]$
$\dot{u}_x = \dot{\Delta}_x$
$\sigma_{xy} = (2n+1)\Delta\tau$
c_s
$\dot{u}_x = 0$
$\sigma_{xy} = (2n+2)\Delta\tau$
$\forall t \in [(2n+1)t^*, (2n+2)t^*]$

Figure 7.2 – Elastodynamic solution under intact interface conditions. The dynamic fields are mediated by the vertical propagation of a shear wave front. $t^* = h/c_s$ is the time needed by the front to travel between the top and bottom surfaces and $n \in \mathbb{N}$ is the total number of reflections observed at the top boundary.

7.2.1 Numerical method

The elastodynamic equation is solved with a finite-element approach using a lumped mass matrix coupled to an explicit time integration scheme based on a Newmark-β method [140] according to the presentation given in Section 3.2. The stable time step is defined as function of the dilatational wave speed c_d and the spatial discretization Δs as

$$\Delta t = 0.7\frac{\Delta s}{c_d}, \tag{7.2}$$

with Δs being typically set to $\frac{l}{1000}$ in this work. The virtual work contribution (cf. Equation 3.33) of the frictional plane is written as

$$\hat{W}(t) = \int_0^l \tau(x,t)\hat{\delta}_x(x,t)dx, \tag{7.3}$$

with $\hat{\delta}_x$ being the virtual interface slip and τ the shear traction acting at the interface, which is derived from the thermodynamic potential and expressed as

$$\tau = \frac{\partial \Phi}{\partial \delta_x} = \frac{\delta_x}{\delta_c}\tau_c e^{1-\frac{\delta_x}{\delta_c}}, \tag{7.4}$$

for Φ being an exponential Rose-Ferrante-Smith universal potential [8]. In Equation 7.4, τ_c and δ_c are respectively the maximum strength and critical slip of the interface characterizing the exponential law sketched in Figure 7.3, for which the equivalent fracture energy corresponds to

$$G_c = \int_0^\infty \tau d\delta_x = e\tau_c\delta_c. \tag{7.5}$$

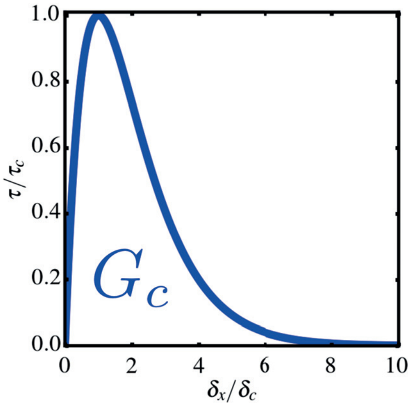

Figure 7.3 – Exponential cohesive law given in Equation 7.4 and derived from a Rose-Ferrante-Smith [8] type of universal binding potential.

This formulation has the interest of being equivalent to the cohesive slip-weakening law used in the macroscopic modeling of frictional interfaces [6,9] and, at the same time, representative of the micromechanical behavior observed during the progressive shearing of microcontact junctions [105, 106, 183]. Indeed, Aghababaei *et al.* [105, 106, 182] studied the shear failure of two interlocking asperities using atomistic simulations and reported how the profile of the tangential force versus sliding distance follows a similar evolution than the exponential cohesive law (see for example Fig. 1 of [106]). In this context, the chosen cohesive formulation can be interpreted as a coarse-grained representation of the underlying microcontact junctions.

More details about the finite-element formulation [18, 19, 184] and the implementation of cohesive element models [144, 145] can be found in the reference papers. Capturing the multi-scale nature of the problem requires an efficient and scalable parallel implementation, capable of handling several millions of degrees of freedom on high performance computing clusters. To this aim, we use our homemade open-source finite-element software, whose implementation is detailed in [146, 147] and whose sources can be freely accessed from the *c4science* platform [1].

7.2.2 Material properties

The results are presented hereafter with adimensional scales but the material properties of Homalite used in the simulations are given to the reader for the sake of reproducibility: Young's modulus $E = 5.3$ [GPa], Poisson's ratio $\nu = 0.35$, shear wave speed $c_s = 1263$ [m/s], and typical interface fracture energy $\langle G_c \rangle = 23$ [J/m^2].

---

[1] https://c4science.ch/project/view/34/

7.3 A characteristic length scale controlling the brittle-to-ductile transition

In this first part, we study the onset of sliding from a single uniform and homogeneous resisting junction of fracture energy G_c and size $(l - w_0)$. Figure 7.4a presents the evolution of energies observed during a typical rupture event, i.e, the applied external work W_Δ, the elastic strain energy E_{el}, the fracture energy E_{frac}, and the kinetic energy E_{kin}. During an initial phase, the elastic strain energy builds up in the system following the dynamics described in Figure 7.2 and depicted by the dashed lines in the energy plots of Figure 7.4a-b. After several back and forth reflections of the shear wave, a slip front nucleates at $x = w_0$, breaks the interface cohesion and releases $E^*_{\text{frac}} = G_c(l - w_0)$. The asterisk mark simply distinguishes the cumulative value of energy obtained after interface failure from its transient value, i.e. $E^* = E(t >> t^*)$. After the complete failure, an eventual excess of mechanical energy $(W^*_\Delta - E^*_{\text{frac}})$ remains in the system and takes the form of elastic vibrations in absence of any other dissipative process.

Figure 7.4b describes the evolution of energies observed during another rupture event, during which sliding initiates for a significantly lower applied external work, exactly balancing the interface energy $(W^*_\Delta = E^*_{\text{frac}})$. Perhaps surprisingly to the reader, these quantitatively different sliding events share identical elastic properties and fracture energy G_c. The different dynamics arise solely from the size of the process zone, which represents how sharp stresses concentrate or the damage diffuses at the vicinity of existing flaws. When the size of the process zone l_{pz} is comparable to the resisting junction size $(l - w_0)$, the sliding motion develops along a damage band spreading over the entire length of the interface with an energy balance similar to one observed in Figure 7.4b. Conversely, if $l_{pz} \ll (l - w_0)$, sliding initiates in the form of a crack front propagating from $x = w_0$ and leading to a more violent rupture as described in Figure 7.4a.

The limit of an infinitesimally small process zone corresponds therefore to a singular shear (mode II) crack, whose propagation initiates according to LEFM criterion $K_{II} > K_c$ [31]. K_c is the interface fracture toughness, which can be computed from the fracture energy as

$$K_c = \sqrt{G_c \frac{E}{(1-\nu^2)}}. \tag{7.6}$$

K_{II} is the stress intensity factor, which depends on the far-field shear stress σ^∞_{xy}, the crack size w_0 and a dimensionless factor χ accounting for the geometry:

$$K_{II} = \chi \sigma^\infty_{xy} \sqrt{\pi w_0}. \tag{7.7}$$

For the edge crack configuration of interest, χ can be approximated as 1.12, such that the rupture is expected to initiate when

$$\sigma^\infty_{xy} > \frac{1}{1.12}\sqrt{\frac{G_c}{\pi w_0}\frac{E}{(1-\nu^2)}}. \tag{7.8}$$

This Griffith-type [1, 10, 31] of criterion explains how the rupture nucleation is constrained by a thermodynamic criterion whose associated strain energy barrier can be estimated following Equation 7.8 as

$$E_{\mathrm{el}}^{\mathrm{lefm}} \approx \frac{1}{2\mu}\int_{\Omega}(\sigma_{xy}^{\infty})^2 d\Omega = \frac{G_c}{(1.12)^2}\frac{hl}{\pi w_0(1-\nu)}. \tag{7.9}$$

The resulting quadratic relationship between the far-field stress and the strain energy can be visualized from the initial build-up of strain energy (black dashed lines in the plots of Figure 7.4a and b).

Finally, linear elastic fracture mechanics predicts that the size of the process zone at the onset of the rupture scales according to the ratio K_c^2/σ_c^2. Using Equations 7.5 and 7.6, the process zone size at the onset of the rupture can therefore be estimated as

$$l_{pz} \approx e\frac{\delta_c}{\tau_c}\frac{E}{(1-\nu^2)} = \frac{G_c}{\tau_c^2}\frac{2\mu}{1-\nu}. \tag{7.10}$$

Along various interface properties and geometries, Figure 7.4c presents how the observed transition between sharp *crack-like* events (for $l_{pz}/(l-w_0) \ll 1$) and smoother *plastic-like* decohesions (for $l_{pz} \geqslant (l-w_0)$) can be rationalized using the size of the process zone. Note that the excellent alignment of data points observed in Figure 7.4c only exists between events triggered at a same loading rate $\mathit{\Delta\tau} = \mu/c_s\,\dot{\Delta}_x$, which dictates the dynamic overshoot visible along the vertical axis.

The evolution described in Figure 7.4c is equivalent to the transition from strength-control fracture ($F_\Delta^* \sim \tau_c\cdot(l-w_0)$) for large process zone toward toughness-control failure ($F_\Delta^* \sim \sigma_{xy}^{\infty}\cdot l$) with shorter process zone reported in the framework of tensile fracture [185]. F_Δ^* corresponds to the macroscopic force required to rupture the interface cohesion.

A similar brittle-to-ductile transition exists in the failure of the microcontact junctions (cf. middle and right plots of Figure 2.14). Aghababaei *et al.* [105] revealed how a characteristic junction size d^* mediates this transition from the brittle rupture of the apexes of junctions larger than d^* to the ductile smoothing of junctions smaller than

$$d^* = \lambda\frac{\Delta\gamma}{\sigma_j^2}\mu. \tag{7.11}$$

In the equation above, $\Delta\gamma$ corresponds to the energy associated to newly created surfaces (equivalent to G_c), while σ_j is the junction adhesive shear strength (equivalent to τ_c). λ is a dimensionless factor accounting for the geometry (typically in the range of unity) and, therefore, d^* (Equation 7.11) corresponds to a nano/microscopic physical interpretation of l_{pz} (Equation 7.10) used in the "coarse-grained" cohesive model. Remarkably, there is a direct analogy between the brittle-to-ductile transition (controlled by d^*) observed during the failure of microcontacts [105] and the "coarse-grained" dynamics (controlled by l_{pz}) presented in Figure 7.4c with the cohesive model. The latter represents therefore a powerful tool to probe

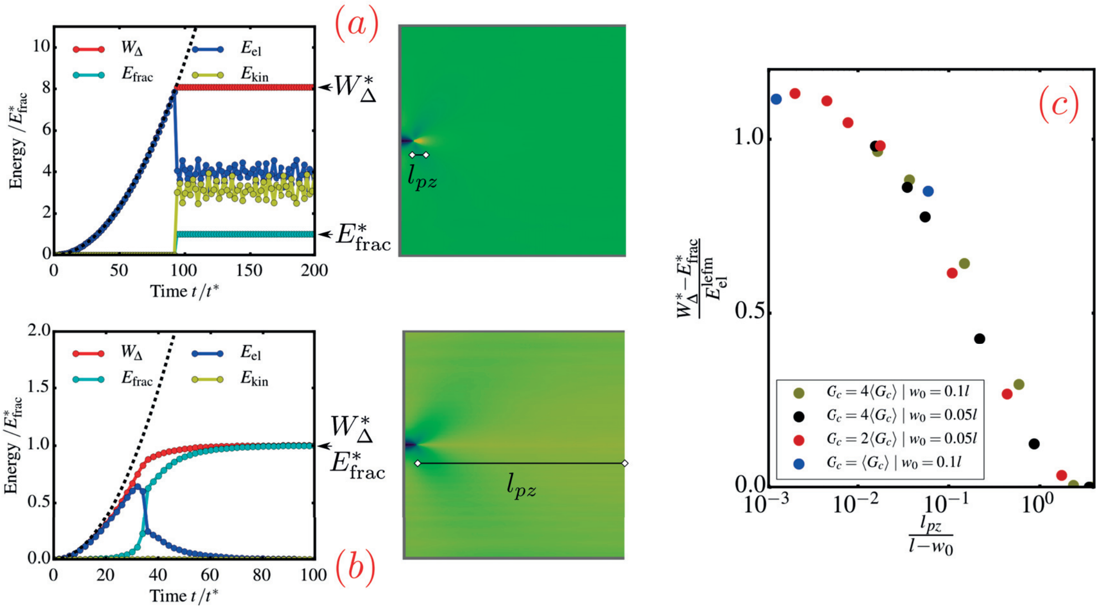

Figure 7.4 – The ratio of the process zone size to the length of the resisting junction mediates the work required to initiate sliding. (a) and (b) present two typical time evolutions of the energetic quantities prior to the rupture onsets, which occur, respectively, at $t = 92t^*$ and $t = 35t^*$. The two events shared the same elastic properties and $G_c = 4\langle G_c\rangle$, but their respective interface cohesive laws lead to $l_{pz}/(l - w_0) = 3.5 \cdot 10^{-2}$ and $l_{pz}/(l - w_0) = 3.5$. The latter are highlighted on the associated shear stress profiles presented for the two interfaces before the onset of sliding (the colors of each stress profile are scaled between zero and the respective values of τ_c). The dashed lines in (a) and (b) describe the theoretical build-up of elastic strain energy expected for intact interface conditions according to the dynamics presented in Figure 7.2. (c) Normalized external work required to initiate sliding between the two bodies as function of the ratio between the process zone size l_{pz} and the resisting junction size $(l - w_0)$ for different types of interface properties and geometries.

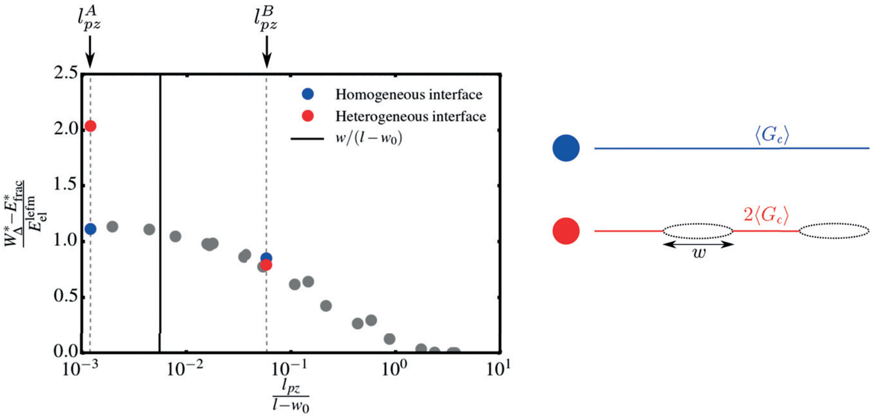

Figure 7.5 – Process zones smaller than w magnify the properties of the heterogeneous microcontacts, which are averaged in the case of larger process zone sizes. The colored circles present the results of two types of interfaces characterized by the same average rupture energy $\langle G_c \rangle$. Since $l_{pz}^{A,B} << l - w_0$, the two interfaces require a similar amount of work to start sliding when the strength is homogeneously distributed along the interface (blue circles). However, the two values of W^*_Δ significantly diverge in presence of heterogeneous microcontacts with a characteristic size w standing in between l_{pz}^A and l_{pz}^B (red circles). The grey circles recall the data presented in Figure 7.4c.

the impact of the microcontacts' physics on the macroscopic dynamics of frictional interfaces.

7.4 Effect of l_{pz} at the scale of the heterogeneous microcontacts

As illustrated in Figure 7.1, the contact between two solids occurs along a reduced portion of the interface, between the peaks of the microscopically rough surfaces. To understand the effect of this very heterogeneous strength profile, we idealized it as a regular array of intact and broken microscopic segments of characteristic size $w = 0.05 w_0 = 0.005 l$ and refine the spatial discretization to $\Delta s < \frac{l}{5000}$. The two orders of magnitude difference between the macro- and microscales lead to an outstanding computational cost (70M degrees of freedom).

Let us consider two interface cohesive properties leading both to an equal average rupture energy $\langle G_c \rangle$ and to two very small process zones ($l_{pz} << l - w_0$). We later refer to these two systems as *interface A* ($l_{pz}^A = 10^{-3}(l - w_0)$) and *interface B* ($l_{pz}^B = 5 \cdot 10^{-2}(l - w_0)$). For homogeneous and uniform interface properties, the ruptures of these two interfaces present very similar *crack-like* dynamics, in agreement with the results presented in the last section (see the blue circles in Figures 7.4 and 7.5). However when the calculations are repeated in presence of a heterogeneous microstructure, a significantly different amount of work is required to initiate sliding motion along the two interfaces (cf. red circles in Figure 7.5). This major change emerges from the introduction of a new length scale w in the systems, which exactly stands between the two process zone sizes l_{pz}^A and l_{pz}^B.

For $l_{pz}^B \cong 5w$, stress concentration at the edge of the largest flaw spans several valleys and

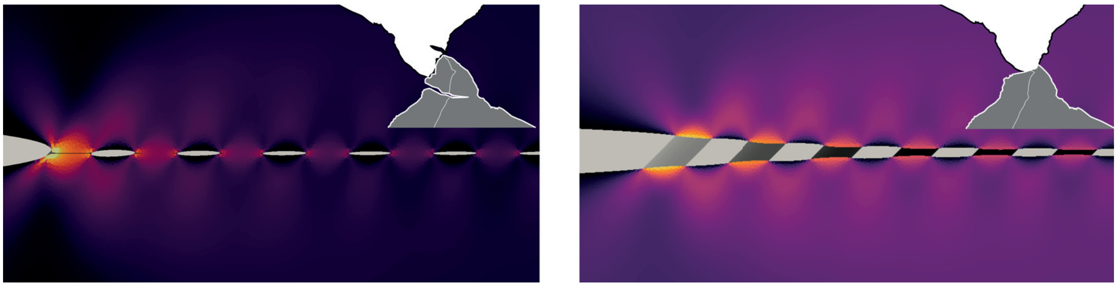

Figure 7.6 – Zooms at the tip of the critical junction ($x = w_0$) revealing the shear stress profile existing just before the onset of sliding for interfaces A and B. An artificial vertical displacement $\left(u_y(x,y) = u_x(x,y)\right)$ is applied to help visualizing the slip profile along the interface. The cohesive strength existing between the top and bottom surfaces is depicted with a gradation from black ($\tau^{\mathrm{str}} = \tau_c$) to white ($\tau^{\mathrm{str}} = 0$). (**Left**) For interface A, the shear stress and slip localize at the edge of the critical junction, magnifying its toughness. (**Right**) Along interface B, several microcontact junctions start slipping and damaging within the larger process zone. The sketches located in the top right of the plots associate these two distinct situations to the typical failure behaviors of microcontact junctions discussed in Figure 2.14.

resisting junctions. Within the process zone, several microcontact junctions start slipping and damaging during the initial loading phase. Their shearing response is thereby homogenized within the larger process zone and results in a quasi-homogeneous response. Conversely, for $l_{pz}^{A} \ll w$, stresses sharply concentrate at the edge of the microcontact patches. Hence, Griffith criterion applies and predicts that the advance da of the rupture front should release approximately $da \cdot 2\langle G_c \rangle$ of available strain energy, which is theoretically twice larger than in the homogenized situation ($da \cdot \langle G_c \rangle$). Hence, this toughening mechanism is expected to be even stronger with higher interface energy contrasts between the toughness of the microcontacts and the average macroscopic toughness of the interface.

These different damage mechanisms occur during the rupture nucleation at the scale of the heterogeneous microcontact clusters, as presented in Figure 7.6. However, no notable difference exists macroscopically between the rupture dynamics of interface A and B. In Figure 7.7, the stress profiles are measured at a macroscopic distance ($\gg w$) from the contacting plane as it is the case during experiments [126,127,129]. In both situations, the stress profiles presents the K-dominance predicted by LEFM for dynamic shear cracks and the associated dynamic energy release rates always equate $\langle G_c \rangle$. Therefore, apart from the significant difference in the force/work required to initiate sliding, the two interfaces present a very similar macroscopic dynamics mediated by the propagation of a slip front along the interface.

Two tiny differences visible in Figure 7.7 between the macroscopic stress profiles of interfaces *A* and *B* should be discussed. First, the stress amplitudes are larger for interface *A*. It results from a slight difference in the rupture speed, which is faster along interface *A*, since a larger amount of elastic energy is stored in the continuum before the onset of sliding. Second, elastic waves are visible in the stress profile of interface *A*, while they do not appear along interface

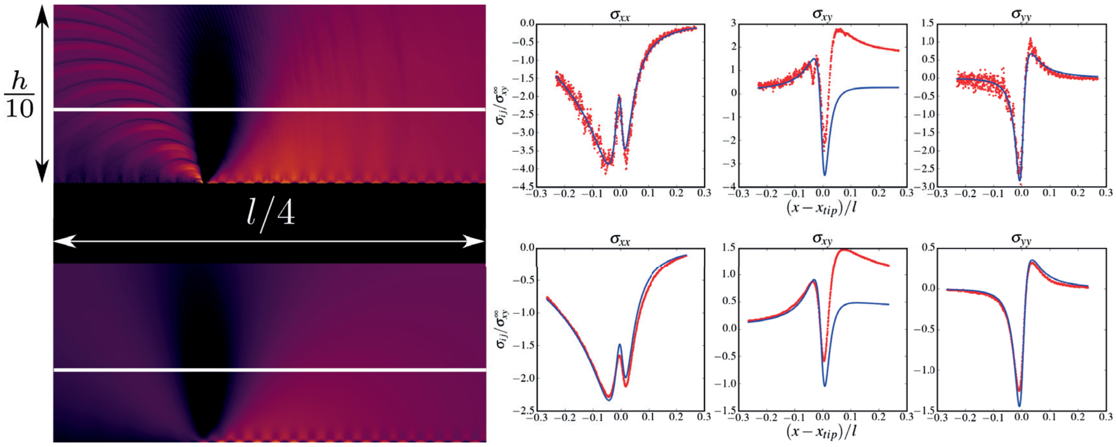

Figure 7.7 – At a distance from the interface the evolutions of the dynamic stress fields observed macroscopically during the rupture of the heterogeneous interfaces A (top) and B (bottom) comply with LEFM predictions for an interface fracture energy corresponding to $\langle G_c \rangle$. On the left panels, shear stress at the vicinity of the propagating slip front is mapped using the same color scale. To mimic the experimental measurements, the white lines highlight the position along which the components of the Cauchy stress tensor are presented on the right panels in red. LEFM stress fields, which are presented in Section 2.2, are plotted in blue for a fracture energy equal to $\langle G_c \rangle$. Note that the "bump" visible in the simulation profiles of σ_{xy} is expected and is caused by a shear wave propagating ahead of accelerating shear cracks. This phenomenon is discussed in details in [9].

B. These waves, which are studied in details in Chapter 5, arise only during the interplay of dynamic fronts with heterogeneities larger than l_{pz}. Furthermore, their amplitudes are expected to decay for microstructures smaller than the two orders of magnitude considered in these simulations and become out of the resolution of macroscopic experiments.

7.5 Discussion

Two elastic blocks brought into contact resist sliding motion across different scales. From a structural point of view, slip fronts nucleate at the critical portion of the interface and expend along the contacting plane, similar to the shear crack dynamics described in the linear elastic theory of fracture. At a smaller scale, surfaces have a rough profile, where the resistance to sliding is unevenly distributed between the peaks of the surface roughnesses. In this work, we demonstrate how this microscopic topography is critical in the nucleation phase of the rupture front, as it can bring two macroscopically identical interfaces to rupture at very different external work/force. To this aim, we study the onset of sliding across two scales using a scalable finite-element implementation coupled to an exponential cohesive law, which allows to have a closer look within the fracture dissipative zone, beyond the scope of singular fracture theory.

We first study how a single contact junction starts sliding under shear and show how the ratio of the junction length over the process zone size controls the rupture mechanism and the work required by the nucleation. A junction much larger than l_{pz} breaks through the propagation of a slip front similar to a shear crack [126, 127]. Along a junction of comparable size or smaller than the process zone, the sliding motion initiates along its entire length, similar to the plastic flowing of the contact junctions under shear stress pictured by Bowden and Tabor [5]. We further discuss how to connect this "coarse-grained" process zone size l_{pz} to the characteristic junction size d^* mediating the failure mechanisms of microcontact junctions.

Moreover, we present how these two rupture mechanisms can exist at the scale of the heterogeneous microcontacts even if the macroscopic rupture still follows the singular crack dynamics described by LEFM. When the process zone size is larger than the contact junctions, the response of several microcontacts and valleys is averaged. Conversely, for a process zone much smaller than the contact junctions, the sharp stress concentration magnifies the individual strength of the microcontacts leading to a stronger interface.

Therefore, a change in the size of the process zone visible only at the scale of the heterogeneous micostructure can significantly impact the apparent strength of the interface. Likewise, two interfaces with the same fracture energy and identical macroscopic behaviors can nevertheless required significantly different shear force/applied work to initiate sliding. This new description emerging from the multi-scale nature of the problem will bring fresh insights in our understanding of frictional interfaces, particularly during the nucleation phase of sliding events.

In this context, the brittle-to-ductile transition presented in this work brings an interesting explanation of the "slippery but tough" behavior of lubricated interfaces. Indeed, coating the surface with a lubricant reduces the adhesive junction shear strength σ_j (cf. Equation 7.11). Moreover, as reported by Bayart *et al.* [129], the lubricant also significantly increases the critical slip distance δ_c. These combined effects can therefore increase, simultaneously, l_{pz} (or equivalently d^*) at the scale of the microcontacts and the macroscopic fracture energy G_c. Physically, this means that the shear stresses and damage processes sharply concentrate at the edges of the microcontacts under dry conditions. After lubrication, they start spreading several microcontact junctions and leads to a more ductile failure of the junctions, resulting macroscopically into a more slippery but tougher interface.

Finally, the observations and conclusions presented in this manuscript also have implications for our understanding of the fracture of heterogeneous materials and particularly in the context of multi-scale and hierarchical materials [12, 13], for which the microstructure organization can be tuned to enhance the overall material properties.

8 The rupture dynamics of interfaces obeying laboratory-derived friction laws

The onset of sliding between two solids brought into contact offers us some useful insights on the earthquake dynamics and the seismic energy released and radiated in the ground. Historically, scientists described this problem with two distinct approaches. A first category of studies focused on the elastodynamic description of the surrounding solids and derived the energetics driving the propagation of the slipping event, inspired by dynamic fracture theory. A second class of studies focused on the interface and its complex frictional response. From laboratory experiments, empirical friction laws were proposed, inspired by the microcontact mechanics. This chapter aims at bridging these two important and complementary approaches. Using an elastodynamic boundary integral formulation, we simulate the propagation of slip fronts driving the onset of sliding using laboratory-derived *rate-and-state* friction laws. Taking advantage of the fine representation of the dynamic interface fields, the elastodynamic energy balance driving the slip front propagation is systematically computed. This study suggests then a new estimation of the *equivalent fracture energy* for rate-and-state interfaces and demonstrates the versatility of the proposed framework with different formulations. This work concludes by showing how the resulting fracture energy only represents a small fraction of the total breakdown energy associated to interface slip-weakening behavior, with direct implications in our understanding of the partition of earthquake energy budget.

The work detailed in this chapter will be disseminated as a scientific publication currently in preparation:

F. Barras, M. Aldam, E. A. Brener, E. Bouchbinder, and J.-F. Molinari, "On the rupture dynamics of interfaces obeying laboratory-derived friction laws," *In preparation*, 2018

Furthermore, the methodology presented in this work was applied to rationalized the nucleation of rupture fronts from quasi-quiescent frictional interface in light of Griffith's criterion. These results are detailed in a scientific publication currently under review:

E. A. Brener, M. Aldam, F. Barras, J.-F. Molinari, and E. Bouchbinder, "Unstable slip pulses and earthquake nucleation as a non-equilibrium first-order phase transition," *Under review*, 2018

8.1 Introduction

Two elastic solids come into contact at the scale of their surface roughnesses, leading to highly non-uniform distributions of pressure and stress, which concentrate at the peaks of the surface forming the *microcontacts* [91]. The frictional response of this heterogeneous topography mediates the onset of sliding and the rupture dynamics arising in many physical systems, including the earthquake cycle developing along crustal faults. The latter is typically characterized by silent periods followed by rapid seismic events [90]. In the literature, two distinct approaches exist to describe the frictional contact mechanics underlying this *stick-slip* behavior.

The first class of models is grounded on the elastodynamic equation governing the seismic energy budget. The propagation of slip front is described as a traveling shear crack and studied within the dynamic fracture framework [42, 43, 122]. To regularize the infinite shear stress predicted at the tip of singular cracks, pioneer cohesive models have been developed, for which the friction coefficient c_f is assumed to drop from a static to a dynamic value after the interface slips a characteristic distance [6, 110]. The so-called *slip-weakening* models have then been extensively used to study the rupture dynamics of seismic events including the speed of the front [47, 123, 124], the impact of fault heterogeneities [80, 82, 83, 85, 125] as well as the seismic energy budget [75, 134, 188]. By measuring the strain evolution during the onset of frictional slip, recent experiments quantitatively showed how dynamic fracture theory perfectly describes the slip front dynamics [126–129]. These experiments further highlight how the nucleation process still eludes the classical fracture mechanics models [24]. This discrepency is presumed to arise from the microscopic nature of contact.

The second type of approaches focuses on the frictional contact mechanics of rough multicontact interfaces (MCI). It emerges from the works of Dieterich [22] and Ruina [23], who proposed a frictional constitutive law describing the observed evolution of c_f with contact time and sliding velocity. In this laboratory-derived friction law, the friction coefficient is function of the sliding velocity and a “state” variable ϕ. The latter has a unit of time and is interpreted as the average age of the underlying microcontacts. Microcontact lifetime reduces with increasing sliding velocity, which causes a reduction of c_f. This *velocity-weakening* behavior is intrinsically unstable and received a significant attention in the literature as a potential mechanism explaining earthquake nucleation [23, 108, 115–117]. Several variations of the original *Dieterich-Ruina* formulation have been proposed in the literature [120], including the transition toward *velocity-strengthening* friction at much lower or larger sliding velocities [118, 119]. Recent “laboratory-earthquake” experiments [111] discussed how the evolution of the residual stress observed in the wake of the rupture front goes beyond the slip-weakening description but complies with the behavior emerging from rate-and-state formulations. However, the latter are essentially derived from empirical observations, whose upscaling to the dimensions of crustal faults is still debatable. Consequently, an increasing effort is given to propose quantitative physics-based interpretations of rate-and-state constitutive equations [118, 119, 121, 189].

In this context, our work aims to bridge these two complementary descriptions of frictional contact by applying the rigorous description of the rupture dynamics underlying the elastodynamic models of friction to the realistic frictional response existing in the laboratory-derived constitutive laws. Using a boundary integral formulation of the elastodynamic equation [16, 17], we study the dynamic propagation of slip fronts along a rate-and-state frictional interface. The very fine discretization of the contact plane enabled by the numerical scheme allows for mapping the asymptotic dynamic crack solution to the shear and velocity fields at the vicinity of slip fronts. In the first part of this chapter, we present the major concepts of dynamic fracture mechanics by studying the propagation of a shear crack simulated using a well-established cohesive approach, for which the fracture energy is a priori known. After this validation step, we apply the same framework to analyze the energy balance driving the propagation of slip fronts simulated with a rate-and-state friction law. We then propose a novel procedure enabling to integrate the equivalent fracture energy of rate-and-state friction laws by properly splitting the rapid rupturing of the microcontacts to the long term effects associated to the relaxation of the frictional interface. The suggested procedure, which is grounded on the physical interpretation of rate-and-state laws, is finally validated with various kinds of formulations. This work concludes by discussing the implication of this new framework on our current understanding of the earthquake dynamics and the partition of its energy budget.

8.2 Geometry and elastodynamic formulation

Let us consider two semi-infinite linearly elastic half-spaces in contact along the plane lying at $y = 0$ of a Cartesian system of coordinates. A z-invariant ($\frac{\partial \boldsymbol{u}}{\partial z} = \boldsymbol{u}_{,z} = 0$) out-of-plane displacement field ($\boldsymbol{u} = (0, 0, u_z)$) is assumed, such that the Lamé-Navier elastodynamic equation

$$(\lambda + \mu)\nabla(\nabla \cdot \boldsymbol{u}) + \mu \nabla^2 \boldsymbol{u} = \rho \frac{\partial^2 \boldsymbol{u}}{\partial t^2}, \tag{8.1}$$

becomes the following scalar wave equation:

$$c_s^2 (u_{z,xx} + u_{z,yy}) = u_{z,tt}. \tag{8.2}$$

In Equations 8.1 and 8.2, λ and μ are the Lamé elastic constants, while $c_s = \sqrt{\mu/\rho}$ is the shear wave speed computed as function of the density of the bulk material ρ and its shear modulus.

The two continua are initially sliding one on top of another, at a relative uniform steady-state velocity v^0 under a homogeneous initial shear pre-stress τ^0, such that the initial conditions correspond to

$$\begin{aligned} \dot{u}_z^+(x, y, z, t = 0) &= -\dot{u}_z^-(x, y, z, t = 0) = v^0/2 \\ \sigma_{yz}^+(x, y, z, t = 0) &= \sigma_{yz}^-(x, y, z, t = 0) = \tau^0. \end{aligned} \tag{8.3}$$

In the equations above, $\dot{u}_z$ and σ_{yz} are respectively the non-zero components of the velocity field and the Cauchy stress tensor, while the superscripts $+/-$ respectively denote the top $(y > 0)$ and bottom $(y < 0)$ half-spaces. At time $t = 0$, a perturbation is introduced along the interface and breaks the homogeneous steady-state sliding conditions. The precise nature of this initial perturbation is detailed later in the chapter.

8.3 Numerical method

The elastodynamic equation 8.2 is solved, once more, using a spectral boundary integral formulation relating the traction stresses acting along the interface located between two linearly elastic half-spaces and the resulting displacements. The derivation of this boundary integral method is presented in Chapter 3.1. In this chapter, an anti-plane independent formulation is adopted, for which the shear tractions at the interface τ_z are related to the displacements by

$$\tau_z^{\pm}(x,t) = \tau^0 - \frac{\mu}{c_s}\Big(\dot{u}_z^{\pm}(x,t) - v^0/2\Big) + f_z^{\pm}(x,t). \tag{8.4}$$

The first right-hand side (RHS) term τ^0 accounts for the pre-existing traction present along the interface in absence of any perturbation. The second RHS term represents the instantaneous response to a change in interface velocity $\dot{u}_z^{\pm}(x,t) - v^0/2$, while the last term, $f_z^{\pm}(x,t)$, accounts for the history of interface displacements. Both $f_z^{\pm}$ and $u_z^{\pm}$ are expressed in the spectral domain as convolution integrals

$$[f_z^{\pm}(x,t), u_z^{\pm}(x,t)] = e^{ikx}[F_z^{\pm}(k,t), U_z^{\pm}(k,t)], \tag{8.5}$$

with

$$F_z(k,t) = -\mu|k| \int_0^t H_{zz}\Big(|k|c_s(t-t')\Big) U_z(k,t')|k|c_s\,dt'. \tag{8.6}$$

The convolution kernel H_{zz} is computed from the Bessel function of the first kind J_1 as

$$H_{zz}(\gamma) = \frac{J_1(\gamma)}{\gamma}. \tag{8.7}$$

Four unknowns, $\tau_z^{\pm}$ and $\dot{u}_z^{\pm}$, exist for every (x,t) in Equation 8.4, which is therefore completed by interface conditions. Two distinct types of interface conditions are compared in this chapter, a fracture interface modeled with a cohesive approach, equivalent to slip-weakening models, and a frictional interface described by a rate-and-state formulation.

8.3.1 Cohesive formulation

In order to both introduce the main concepts of dynamic fracture and train our approach, we start by studying the dynamic propagation of a shear crack using a cohesive model of fracture, which directly prescribes the interface fracture energy. Along a fracture interface, the two continua are assumed to be initially at rest $v^0 = 0$ under a uniform shear stress smaller than interface strength $\tau^0 < \tau^{\text{str}}$. Hence, Equation 8.4 is completed by the continuity of tractions and displacements across the interface, as long as the shear traction τ_z is lower than τ^{str}. Otherwise, the fracture process breaks the continuity of u_z and the velocities $\dot{u}_z^{\pm}$ are computed such that $\tau_z^+ = \tau_z^- = \tau^{\text{str}}$. The value of interface strength is related to the resulting shear displacement jump $\delta_z = u_z^+ - u_z^-$ through the cohesive failure model:

$$\tau^{\text{str}}(x,t) = \tau_c\,\{1 - \delta_z(x,t)/\delta_c\}\,. \tag{8.8}$$

τ_c and δ_c respectively denote the failure strength and critical crack opening displacement of the rupture plane, and $\{\xi\} = \xi$ if $\xi > 0$ and 0 otherwise. The linear slip-weakening law described in Equation 8.8 leads to a prescribed value of the fracture energy

$$G_c = \int_0^{\delta_c} \tau_z d\delta_z = \frac{1}{2}\tau_c\delta_c. \tag{8.9}$$

In the context of frictional interfaces, the cohesive law (Equation 8.8) is equivalent to the slip-weakening approach [6, 110], for which the friction coefficient is assumed to drop from a static c_f^{stat} to a dynamic c_f^{dyn} value after the interface slips a critical distance δ_c.

8.3.2 Rate-and-state formulation

In the case of antisymmetric frictional sliding between two identical semi-infinite half-spaces in contact under a uniform pressure $\sigma^0 = -\sigma_{yy}(x, y = 0, t)$, the shear equation of motion becomes:

$$\tau_z(x,t) = c_f\Big(v(x,t), \phi(x,t)\Big)\sigma^0 = \tau^0 - \frac{\mu}{2c_s}\Big(v(x,t) - v^0\Big) + f_z(x,t), \tag{8.10}$$

with $v(x,t) = \dot{u}_z^+(x,t) - \dot{u}_z^-(x,t) = 2\dot{u}_z(x,t)$ being the relative sliding velocity between the top and bottom solids. In this chapter, v_c denotes the crack propagation speed in order to prevent any confusion with the rate variable $v(x,t)$. In rate-and-state formulations, the friction coefficient c_f depends both on $v(x,t)$ and a state variable $\phi(x,t)$. The latter can be understood as a macroscopic average lifetime of the microcontacts existing at smaller scales. During steady state sliding at velocity v^{ss}, the microcontacts lifetime is expected to stay constant, such that the state variable is expressed as

$$\phi^{\text{ss}} = \frac{D}{v^{\text{ss}}}, \tag{8.11}$$

with D being a characteristic length of the microstructure often in the range of μ-meter for the scale of laboratory experiments [91]. A large diversity of rate-and-state formulations emerged after the pioneer works of Dieterich [22] and Ruina [23]. These laws are typically characterized by a logarithmic dependence of the coefficient of friction on both v and θ. In this work, we rely on the recent formulation proposed in [190]:

$$c_f\Big(v(x,t),\phi(x,t)\Big) = c_f^0 + a\ln\Big(1+\frac{v(x,t)}{v^*}\Big) + bc_f^0\ln\Big(1+\frac{\phi(x,t)}{\phi^*}\Big), \tag{8.12}$$

even if, at the end of the chapter, we present how the results discussed in our work are independent from the choice of the rate-and-state formulation. c_f^0, a, b, v^* and ϕ^* are essentially empirical quantities measured during friction experiments. In addition to Equation 8.12, an ordinary differential equation describing the time evolution of ϕ should be defined. In this work, the original aging law proposed by Dieterich [22] is adopted:

$$\dot{\phi}(x,t) = 1 - \frac{v(x,t)\phi(x,t)}{D}. \tag{8.13}$$

Equations 8.10, 8.12 and 8.13 form a set of interface equations allowing to compute the time evolution of τ_z, v and ϕ.

Finally, the elastodynamic relations derived both for the cohesive and rate-and-state frameworks are integrated using an explicit time-stepping scheme

$$u_z^{\pm}(x,t+\Delta t) = u_z^{\pm}(x,t) + \dot{u}_z^{\pm}(x,t)\Delta t, \tag{8.14}$$

$$\phi(x,t+\Delta t) = \phi(x,t) + \dot{\phi}\Delta t. \tag{8.15}$$

In order to guarantee the stability and the convergence of the numerical scheme, Δt is defined as the time needed by a shear wave to travel a fraction $\beta = 0.2$ of one grid spacing: $\Delta t = \beta\Delta x/c_s$. In this chapter, the contact plane is typically discretized with 2^{15} points along the x-direction.

8.3.3 Bulk and interface properties

The material parameters of PMMA summarized in Table 8.1 have been chosen for the simulations reported in this chapter. As discussed in the last section, the message of this work is independent from the choice of the material parameters and interface formulations and the results are therefore presented to the largest extent with adimensional scales.

8.4 Crack tip equation of motion

Our modern understanding of fracture is often associated to the works of Griffith and Irwin, who respectively rationalized the balance of energy mediating crack growth [10] and derived the relation between the release of potential energy and the universal stress singularity existing at the vicinity of a crack tip in a linearly elastic material [1]. This well-established theory,

Parameter	Value	Unit
μ	3	[GPa]
ν	0.33	[-]
ρ	1200	[kg/m^3]
τ_c	5	[MPa]
δ_c	0.02	[mm]
G_c	50	[J/m^2]
D	0.5	[μm]
c_f^0	0.285	[-]
a	0.005	[-]
b	0.075	[-]
v^*	10^{-7}	[m/s]
ϕ^*	0.00033	[s]

Table 8.1 – Typical PMMA material parameters used in the simulations.

known as linear elastic fracture mechanics (LEFM) was extended to dynamic cracks whose propagation speed exceeds several tenths of the continuum shear wave speed c_s. The main concepts of this dynamic theory of fracture are briefly summarized hereafter and the interested readers are redirected to reference textbooks ([42, 43]) for a more detailed presentation.

Following the setup presented in the previous section, we study the propagation of a shear (mode III) crack computed using a cohesive slip-weakening law. This non-singular approach, which arose from the work of Dugdale [20] and Barrenblatt [21], became very popular in the numerical modeling of dynamic fracture ([125, 144, 145, 148]). The same approach can be adapted to model a frictional problem, for which the shear resistance is assumed to drop from a static to a dynamic value after sliding over a critical distance [6, 84, 85, 110, 191] .

The dynamic rupture is nucleated at the center of an interface initially at rest under a uniform shear stress $\tau_c > \tau_0 > 0$ by artificially growing an infinitesimal seed crack toward a size $L = L_c$, at which point it starts to grow spontaneously. L_c, often referred to as the *Griffith critical length*, represents the largest stable crack size, which corresponds for a mode-III shear crack in an infinite medium to

$$L_c = \frac{4\mu G_c}{\pi\tau_0^2}. \tag{8.16}$$

In this fracture example, no slip exists before rupture and hence $v^0 = 0$. Figure 8.1 presents the resulting dynamics where the initially stable crack progressively accelerates toward c_s, the maximum admissible rupture speed. During the failure, the instantaneous rate of dissipated

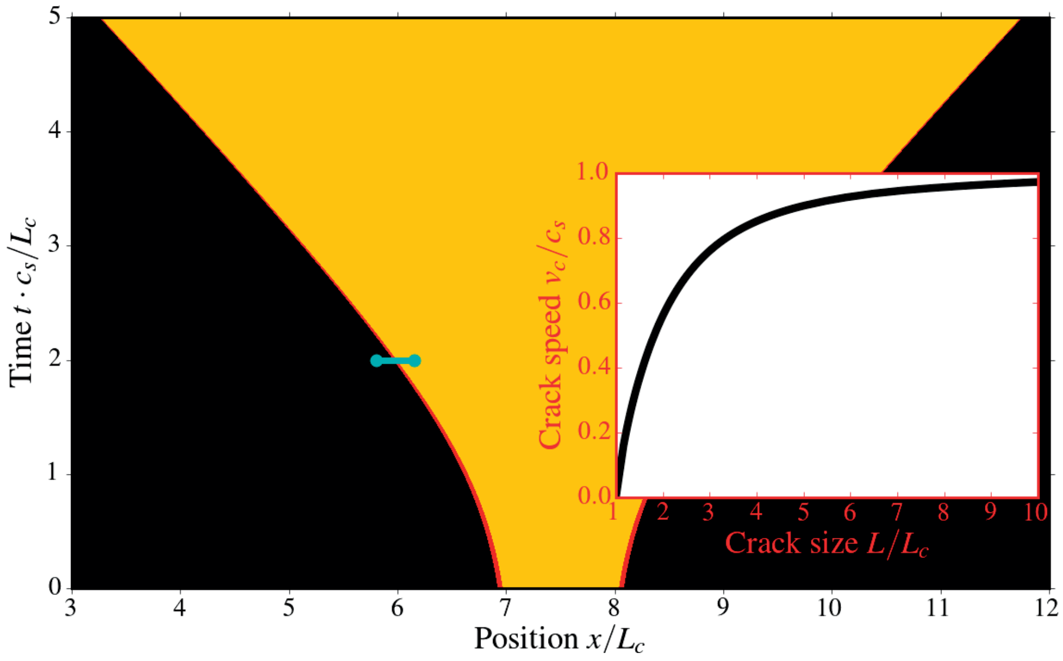

Figure 8.1 – Space-time diagram of the dynamic mode III rupture event whose colors divide broken surface (yellow), fracture process zone (red) and intact interface (black). The blue line highlights the instant at which snapshots of the stress and sliding velocity are presented in Figure 8.2. (**Inset**) Evolution of the rupture speed as function of the crack size.

energy by fracture can be integrated as [148]:

$$\frac{d}{dt}E_{\text{diss}}(t) = \int_{\text{process zone}} \tau_z(x,t)\,v(x,t)\,dx. \tag{8.17}$$

The right-hand-side integral is evaluated over the fracture process zone, which corresponds to the portion of the interface where both τ_z and v are non-zero. The fracture energy dissipated per unit crack advance dL is hence computed as

$$\frac{d}{dL}E_{\text{diss}}(t) = \frac{dE_{\text{diss}}}{dt}\frac{dt}{dL} = \frac{\dot{E}_{\text{diss}}(t)}{v_c(t)}. \tag{8.18}$$

$\frac{d}{dL}E_{\text{diss}}$ corresponds to the fracture energy and is therefore constant for the slip-weakening law of interest, which prescribed $\frac{d}{dL}E_{\text{diss}} = G_c$ (see the right plot of Figure 8.3).

Moreover LEFM predicts that the fracture energy exactly balances the potential energy released by unit crack advance in the bulk. The latter can be directly computed from the singular stress concentration near the crack tip, equivalently to the approach proposed by Irwin [1] and Williams [35] for a static crack. At the vicinity of a dynamic crack moving at speed v_c, the stress field is dominated by a universal square-root singular contribution of the form:

$$\sigma_{ij}(r,\theta,v_c) \sim \frac{K}{\sqrt{2\pi r}}\Sigma^{\sigma}_{ij}(\theta,v_c). \tag{8.19}$$

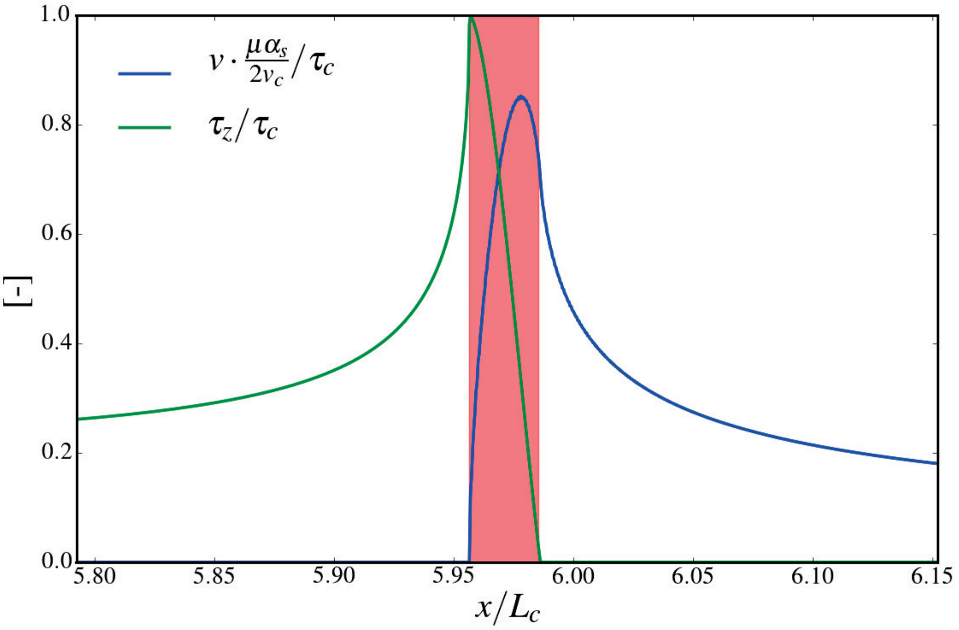

Figure 8.2 – Stress and velocity concentration observed in the neighborhood of the left-propagating crack tip at $t = 2c_s/L_c$ (corresponding to the cyan line in Figure 8.1). The red area highlights the fracture process zone.

Stresses are expressed in a polar system of coordinates r, θ whose origin stands at the tip of the propagating crack. K is the dynamic stress intensity factor and Σ^{σ}_{ij} are universal functions depending only on the angular coordinate θ and the crack speed. In the anti-plane shear configuration of interest, the mode III stress intensity factor K_{III} together with Σ^{σ}_{yz} are describing the stress field near the growing crack:

$$\sigma_{yz}(r,\theta,v_c) \sim \frac{K_{III}}{\sqrt{2\pi r}} \frac{\cos\frac{1}{2}\theta_s}{\sqrt{\gamma_s}}. \tag{8.20}$$

θ_s results from the system of coordinates, which is following the moving crack, such that $\tan\theta_s = \alpha_s \tan\theta$, with $\alpha_s^2 = 1 - v_c^2/c_s^2$ and $\gamma_s = \sqrt{1-(v_c \sin\theta/c_s)^2}$. Similarly, the asymptotic form of particle velocity at the vicinity of a dynamic mode III crack is expressed as

$$\dot{u}_z(r,\theta,v_c) \sim \frac{v_c K_{III}}{\mu\sqrt{2\pi r}} \Sigma^{v}_{ij}(\theta, v_c) = \frac{v_c K_{III}}{\mu\sqrt{2\pi r}} \frac{\sin\frac{1}{2}\theta_s}{\alpha_s\sqrt{\gamma_s}}. \tag{8.21}$$

Figure 8.2 presents the evolution of the interface fields $\tau_z = \sigma_{yz}$ and $v = 2\dot{u}_z$ in the neighborhood of the simulated crack. At the immediate vicinity of the crack, the cohesive description of fracture regularizes the singularity, smearing the tip of the crack over a finite distance, often named *fracture process zone*, which corresponds to the red areas in Figures 8.1 and 8.2. Hence, the latter complicates the definition of the exact crack tip location. However, no material is able to withstand the square-root singular stress field theoretically existing at the edge of cracks and a process zone, where nonlinear dissipations regularize the singularity, should indeed exist at the tip of any crack. Nevertheless, as long as the process zone size remains small compare to other length scales of the problem, the predictions of Equations 8.19 and 8.21 hold and the dynamic crack growth is driven by this singular contribution (K-controlled fracture). In this context, the mechanical energy released by unit crack advance, also named energy release rate, corresponds to

$$G(t) = \frac{1}{\alpha_s} \frac{K_{III}^2}{2\mu}. \tag{8.22}$$

The spectral formulation allows for a very-fine description of the interface quantities, such that the square-root singular contribution can be directly mapped on the evolution of τ_z and v in the direct neighborhood of the leftward propagating tip according to,

$$\tau_z = \sigma_{yz}(r = x_{\text{tip}}^{\tau} - x, \theta = 0, v_c) \sim \frac{K_{III}}{\sqrt{2\pi(x_{\text{tip}}^{\tau} - x)}}, \tag{8.23}$$

and

$$v = 2\dot{u}_z(r = x - x_{\text{tip}}^{v}, \theta = \pi, v_c) \sim \frac{K_{III}}{\sqrt{2\pi(x - x_{\text{tip}}^{v})}} \frac{2v_c}{\mu\alpha_s}. \tag{8.24}$$

x_{tip}^{τ} and x_{tip}^{v} are two extremely close, yet slightly different locations within the fracture process zone, corresponding to the positions of the theoretical singularities of, respectively, τ_z and v. Two unknowns exist for each of the Equations 8.23 and 8.24, namely the crack tip position and the dynamic stress intensity factor. Their values are obtained through a nonlinear least-squares regression [192–194] mapping the simulation data on the asymptotic solutions of Equations 8.23 and 8.24. The computed values of the stress intensity factor are then injected in Equation 8.22 to obtain the energy release rate G^{τ} and G^{v}, which are presented in Figure 8.3 and computed, respectively, from the dynamic evolution of τ_z and v. While it seems reasonable that two different singularity positions can exist for v and τ_z within the fracture process zone, the value of the energy release rate should be unique. In this context, both the rescaled velocity field $v \cdot \frac{\mu\alpha_s}{2v_c}$ and shear tractions τ_z are simultaneously fitted in order to find x_{tip}^{v} and x_{tip}^{τ}, plus a single value of K_{III}. The resulting unique value of G is also presented in Figure 8.3, where it exactly stands between G^{τ} and G^{v}. The observed variations between these three estimations of the energy release rate give useful information about the precision of the adopted fitting strategy. A fit enforcing a unique value of K_{III} and a unique position of the tip ($x_{\text{tip}}^{\tau} = x_{\text{tip}}^{v}$) has also been tested and yields very similar predictions of the energy release rate, standing in between G and G^{τ}. It has then been omitted in Figure 8.3 in order to not overload the plot.

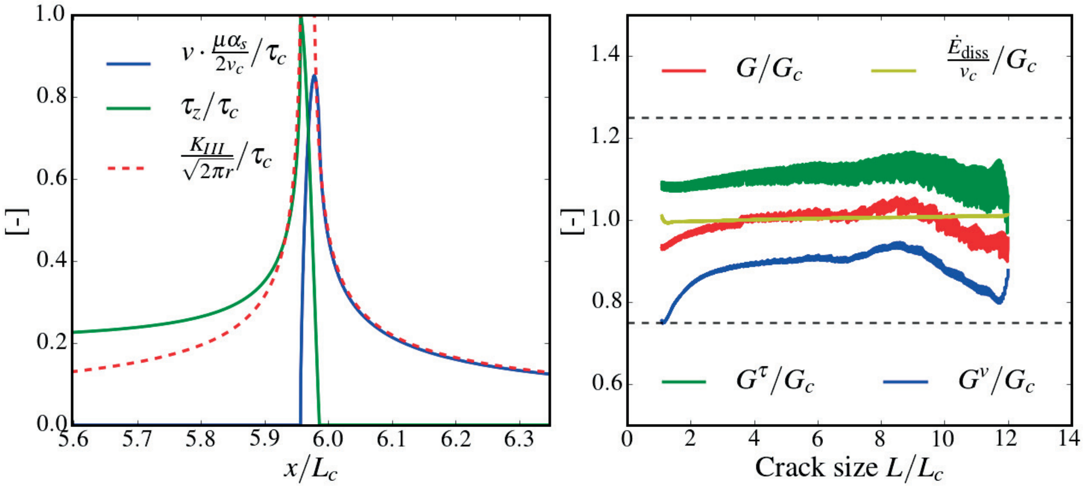

Figure 8.3 – (**Left**) Asymptotic contribution mapping the stress and velocity fields presented in Figure 8.2. (**Right**) Dynamic energy balance computed during crack propagation from the fracture energy $\dot{E}_{\text{diss}}/v_c$ (Equation 8.18), whose value G_c is prescribed in the slip-weakening model, and the energy release rate G (Equation 8.22). See the main text for an explanation of the differences between G, G^v and G^τ. The dashed gray lines are guide to the eyes highlighting the ±25% precision.

8.5 Rupture dynamics with rate-and-state friction laws

In the previous section, we precisely described the energy balance driving the propagation of a shear crack. In this section, we will repeat the same analysis for a frictional interface characterized by a rate-and-state formulation presented in Equation 8.12, for which no prescription of the interface strength or fracture energy exists. The rate-and-state formulation allows for a spontaneous nucleation of rupture fronts along an interface initially in steady-state equilibrium, instead of the artificial nucleation procedure (growth of a seed crack) described above with the slip-weakening law. The value of the friction coefficient observed during uniform steady-state sliding is obtained by combining Equations 8.11 and 8.12:

$$c_f(v^{\text{ss}}) = c_f^0 + a \ln\left(1 + \frac{v^{\text{ss}}}{v^*}\right) + b c_f^0 \ln\left(1 + \frac{D}{v^{\text{ss}} \phi^*}\right) \tag{8.25}$$

and is plotted in Figure 8.4 for the parameters described in Table 8.1.

Let us consider an interface initially at equilibrium under an initial pre-stress $\tau^0 = 0.36\sigma^0$. From Equation 8.25, two homogeneous steady-state sliding velocities exist to equilibrate the loading conditions $\tau^0/\sigma^0 = 0.36$. As illustrated in Figure 8.4, a slow sliding velocity v_w exists on the *velocity-weakening* branch ($d c_f^{\text{ss}} / d v^{\text{ss}} < 0$), while a fast sliding solution v_s exists on the *velocity-strengthening* branch ($d c_f^{\text{ss}} / d v^{\text{ss}} > 0$). v_w represents an unstable equilibrium state, as a slight increase (decrease) of the sliding velocity decreases (increases) the friction coefficient, which sustains even more the disequilibrium of the system. This work mainly focuses on

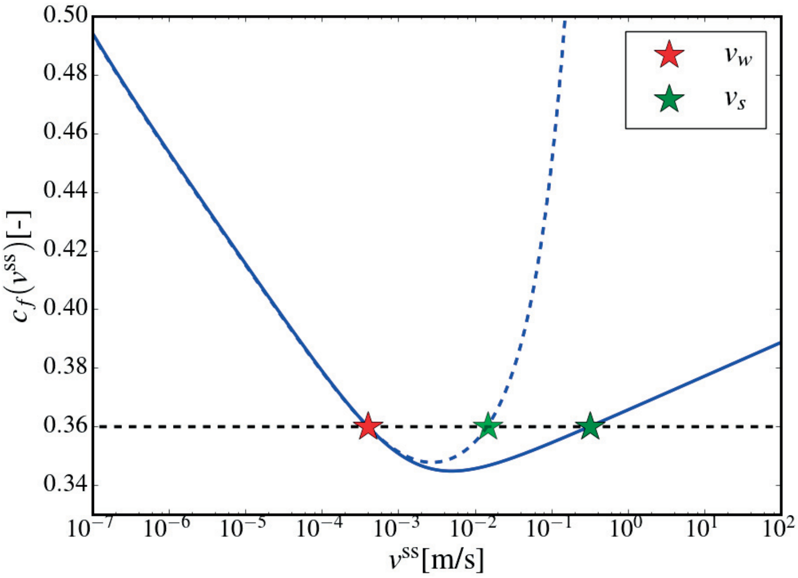

Figure 8.4 – Evolution of the friction coefficient observed under homogeneous steady-state sliding conditions. For a given loading ratio $\tau^0/\sigma^0 = 0.36$ (dashed black line), two equilibrium states exist, one at low slip rate on the velocity-weakening branch v_w and one at high slip rate on the velocity-strengthening branch v_s. The dashed blue line and its associated green star highlight the evolution of $c_f(v^{ss})$ accounting for inertial effects (see the main text for the detailed explanation).

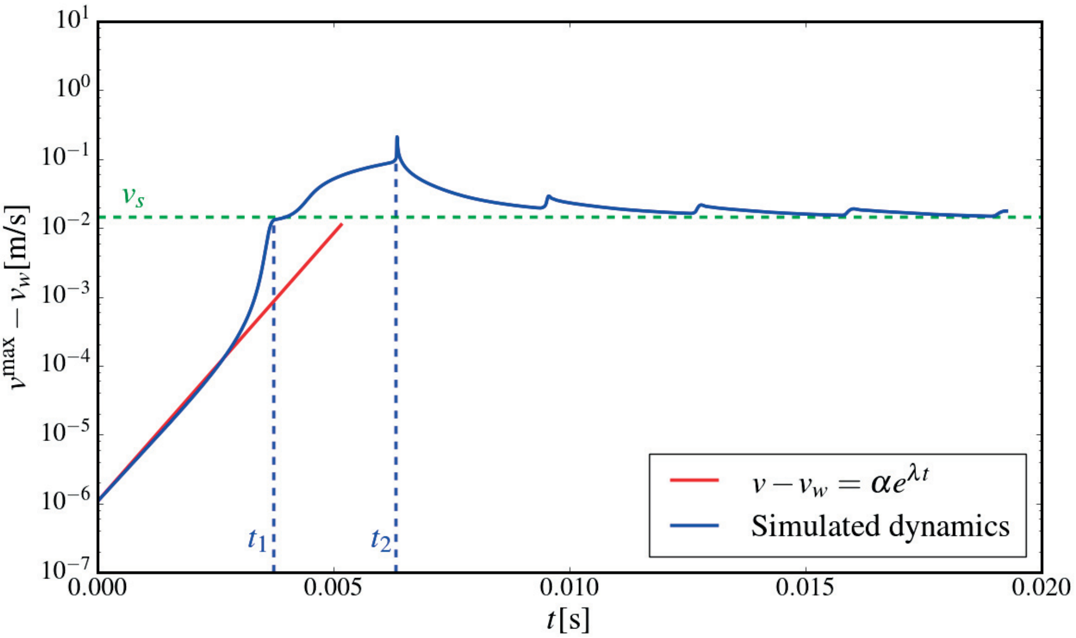

Figure 8.5 – Evolution of the maximum sliding velocity observed during the destabilization of an interface initially sliding uniformly at v_w. $t < t_1$: the perturbation grows following a linear instability regime (cf. Equation 8.28). $t_1 < t < t_2$: two rupture fronts are propagating along the contact plane. $t > t_2$: rupture fronts have broken the entire interface which progressively converges toward a new steady-state at v_s.

perturbations leading to a progressive slip acceleration and bringing the system to transition toward the stable equilibrium position on the strengthening branch (at $v = v_s$). It is important to note how within a semi-infinite half-space, inertia partially impedes the slip acceleration according to

$$c_f(v^{\mathrm{ss}}) = c_f(v_w) - \frac{\mu}{2c_s}\left(v^{\mathrm{ss}} - v_w\right), \tag{8.26}$$

which corresponds to the dashed blue line in Figure 8.4. Therefore, the actual steady state is reached for a sliding velocity slightly slower than v_s along an interface bounding two semi-infinite solids (or, by extension, along an interface for which this destabilization process occurs over time scales shorter than the time for waves reflection at the top/bottom boundaries). In this context, a tiny perturbation $\varepsilon = 10^{-6}$ of the state variable is introduced at $t = 0$ along the interface according to

$$\phi(x, t = 0) = \frac{D}{v_w} + \varepsilon \sin(kx), \tag{8.27}$$

with $k = 2\pi/X$, where we recall that X is the horizontal periodic scale, which is typically equal to $X = 10$[m]. Figure 8.5 details the progressive destabilization of the interface, which follows three distinct phases.

1. The initial stage of the perturbation growth can be studied through a linear stability analysis, which predicts an exponential evolution of the kind $\Delta v = v - v_w = \alpha e^{\lambda t}$. The growth rate λ can be approximated as [186]

$$\lambda \cong \frac{v_w}{4D\tilde{a}} \left(\sqrt{\left(2(c_f^0 \tilde{b} - \tilde{a}) - \frac{D\mu k}{\sigma^0}\right)^2 - 8\frac{D\mu k \tilde{a}}{\sigma^0}} + 2(c_f^0 \tilde{b} - \tilde{a}) - \frac{D\mu k}{\sigma^0} \right), \tag{8.28}$$

   which corresponds to the the largest positive eigenvalue with $\tilde{a} = \frac{a v_w}{v^* + v_w}$ and $\tilde{b} = \frac{bD}{D + v_w \phi^*}$. Figure 8.5 shows how this linear stability analysis remarkably describes the simulated dynamics. At the end of this initial stage, perturbation growth accelerates at the position of the largest slip rate, where it finally leads to the nucleation of two rupture fronts at a critical time t_1.

2. The second phase is characterized by the propagation of two slip fronts bringing the interface to slide at a faster slip rate in their wake. t_1 therefore corresponds to the time at which two rupture fronts start propagating. However, some extra time is required to develop a well-defined square-root singularity in the dynamic fields. In consequence, the analyses presented later in this chapter systematically commence slightly after t_1.

3. Finally, once the two rupture fronts have crossed the entire contact plane, a third stage starts, during which the interface progressively converges toward a new steady-state at v_s.

Figure 8.6 shows the typical profile of stress, velocity and state observed along the interface during these three-step transition at the onset of sliding.

While the first phase described above received a significant attention in the literature as a mechanism for earthquakes nucleation [23, 108, 115–117], the dynamics mediating the second phase is still overlooked, although paramount in the partition of earthquakes energy budget. Hence, the objective of this work is to systematically analyze the energy balance driving the propagation of the frictional fronts (during the second stage) in light of the dynamic fracture concepts presented in the previous section. First, the propagation of the stress and velocity peaks is tracked along the interface. As presented in Figure 8.7, these maxima of the stress and velocity fields have extremely close, yet distinct locations, where their respective evolutions are similar to the ones observed at the vicinity of a shear crack . Moreover, the propagation speed reported in Figure 8.7 is consistent with the admissible speed range predicted for dynamic mode III cracks (i.e. $0 < v_c < c_s$). Two notable differences should be addressed in order to draw a more quantitative picture.

First the shear stress only drops few percents of its magnitude in the wake of the front, whereas it completely vanishes along the free surfaces created by classical shear crack. Taking advantage of the linearity of the bulk constitutive equation, the residual shear stress τ_z^r observed far from the rupture front can be subtracted before mapping the singular shear crack solution

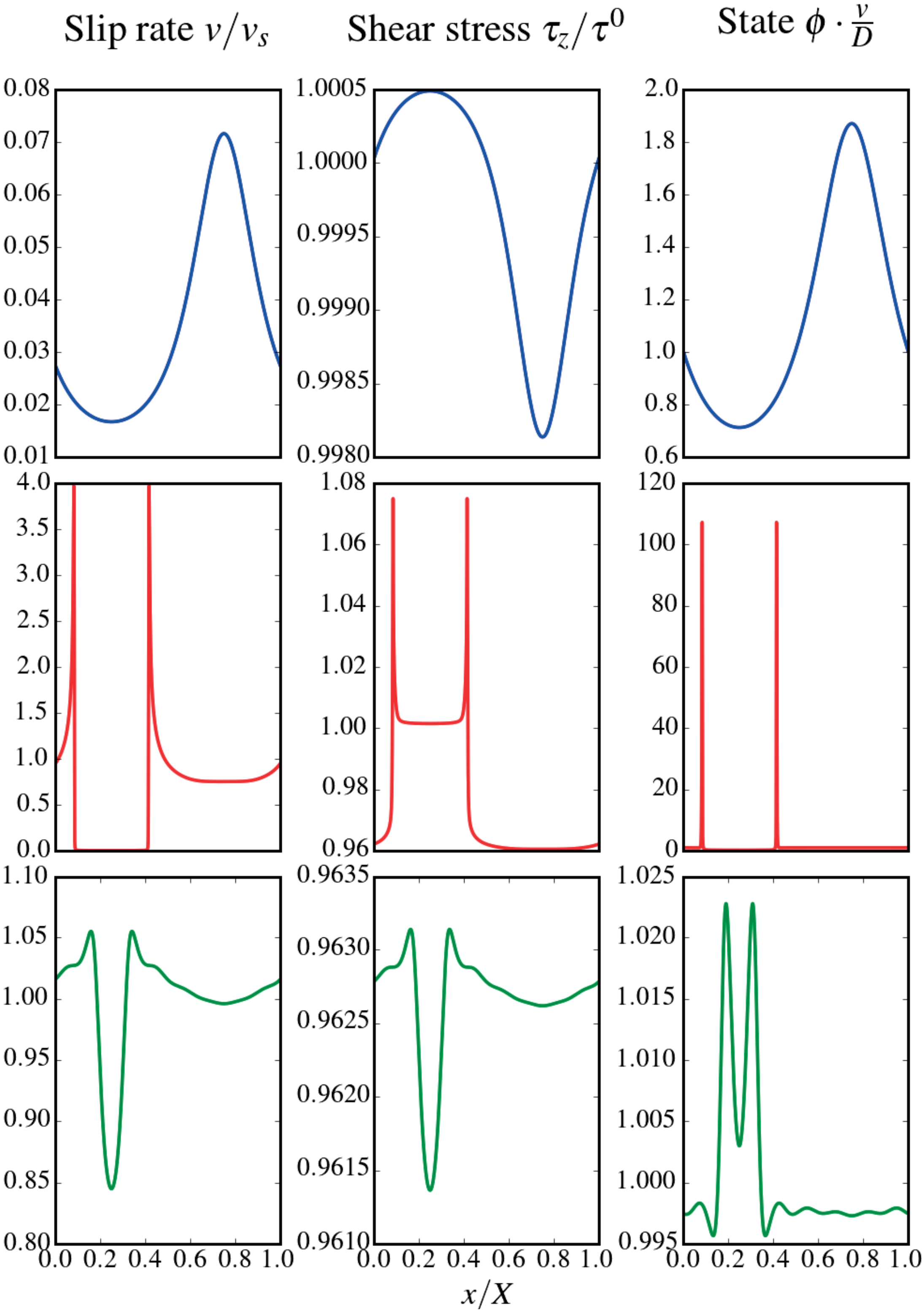

Figure 8.6 – Typical profiles of interface fields (v,τ_z,ϕ) observed during the three stages of the onset of sliding discussed in Figure 8.5, respectively in blue for $t < t_1$, in red for $t_1 < t < t_2$ and in green for $t > t_2$.

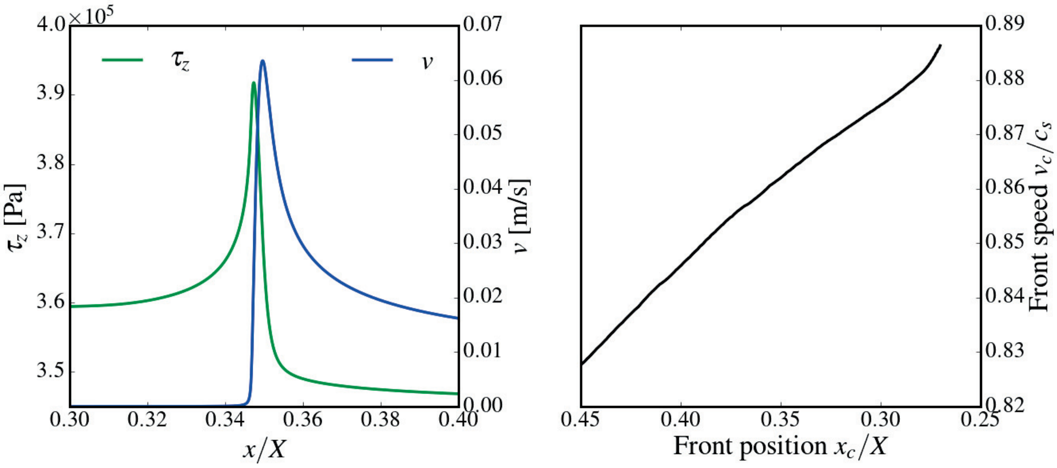

Figure 8.7 – (**Left**) Zoom into the stress and velocity profiles observed at the vicinity of the leftward propagating rupture front.(**Right**) Evolution of the propagation speed.

on a frictional problem [40, 126]. In this context, the shear stress field observed along the rate-and-state interface of interest can be decomposed as

$$\tau_z(t) = \Delta\tau_z(t) + \tau_z^r(t) = \frac{K_{III}(t)}{\sqrt{2\pi(x_{\text{tip}}^{\tau} - x)}} + \tau_z^r(t). \tag{8.29}$$

Following the derivation presented in the previous section (Equation 8.24), the velocity can be similarly expressed as

$$v(t) = \Delta v(t) + v^r(t) = \frac{K_{III}(t)}{\sqrt{2\pi(x - x_{\text{tip}}^{v})}}\frac{2v_c(t)}{\mu\alpha_s(t)} + v^r(t). \tag{8.30}$$

The far-field residual stress τ_z^r and velocity $v^r \cong 0$ are observed at different locations given by the form of the associated universal functions $\Sigma^{\sigma}(\theta, v_c)$ and $\Sigma^{v}(\theta, v_c)$, respectively in the wake and ahead of the propagating front.

Following the procedure discussed in the previous section, a unique value of $K_{III}(t)$ successfully emerges from the mapping of the square-root singular solution on Δv and $\Delta\tau_z$, which is presented in Figure 8.8 with the associated values of the energy release rate. The comparison of Figure 8.3 and 8.8 strongly supports that the propagation of the rupture fronts observed along a rate-and-state interface is driven by a similar release of potential energy than a dynamic shear crack.

The second major difference with the slip-weakening law used in the previous section is the fracture energy, which is not intrinsically prescribed in the rate-and-state friction law, but emerges from the rupture dynamics. Along a frictional interface, the equivalent fracture energy is not the sole dissipation mechanism entering the energy budget as a significant amount of frictional work is dissipated before, during and after the rupture event, essentially as heat. In

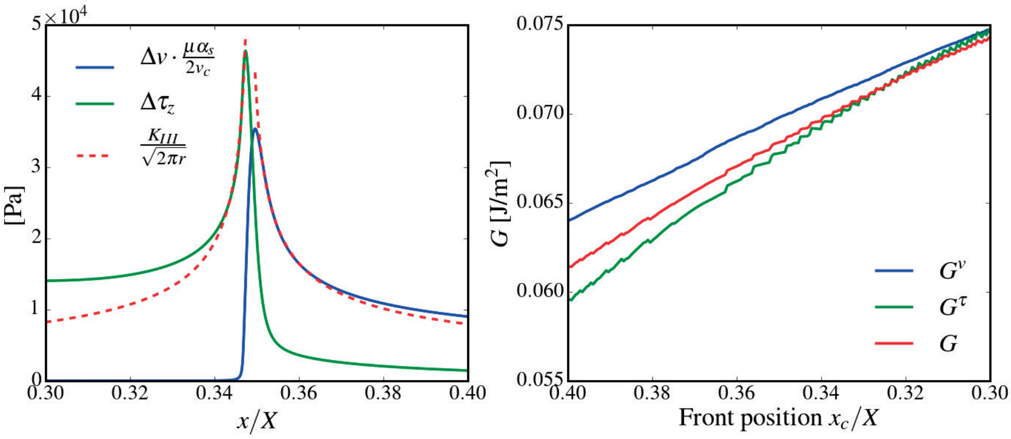

Figure 8.8 – (**Left**) Shear stress and velocity drops observed at the vicinity of a slip front are mapped by the asymptotic contribution described in Equations 8.29 and 8.30. (**Right**). The stress intensity factor emerging from this mapping is used to compute the elastic energy released rate, similarly as in Figure 8.3. However, the vertical axes are conversely displayed with units to emphasize that no intrinsic value of interface strength τ_c or energy G_c are prescribed with the rate-and-state formulation.

the context of slip-weakening models of friction, Ida [110] and Andrews [6] demonstrated how the equivalent fracture energy can be equivalently computed after subtracting the residual shear stress τ^r observed in the wake of slip front:

$$G_c = \int_0^{\delta_c} (\tau(\delta) - \tau^r)\, d\delta = \frac{1}{2}\sigma^0 (c_f^{\text{stat}} - c_f^{\text{dyn}})\delta_c. \tag{8.31}$$

The expression above can be understood in light of Equation 8.29, since, for slip-weakening friction law, no slip occur before the rupture and the residual shear stress takes a prescribed value of $\tau^r = \sigma^0 c_f^{\text{dyn}}$. In the rate-and-state formulation of interest, a significant amount of interface slip occurs before and after the rupture event and this “aseismic” motion should not enter the rupture energy budget. Moreover, the residual shear stress is not prescribed in the friction law. Combining these considerations with the formalism of Equations 8.31 and 8.17, the equivalent fracture energy can be written as

$$G_c(t) = \frac{\dot{E}_{\text{diss}}(t)}{v_c(t)} = \frac{1}{v_c(t)} \int_{\text{process zone}(t)} \Big(\tau_z(t) - \tau_z^r(t)\Big)\, v\, dx. \tag{8.32}$$

The above integral is hence evaluated over an equivalent process zone, which represents a sufficiently narrow region surrounding x_{tip}^{τ} and x_{tip}^{v}. In parallel to the asymptotic change in sliding velocity, the evolution of the state variable also has a direct impact on the rupture dynamics of rate-and-state interfaces [195]. Baumberger *et al.* [121] discussed how the evolution of the underlying real contact area A can be inferred from ϕ as

$$A(\phi) = A_0 \left[1 + b \ln\left(1 + \frac{\phi}{\phi^*}\right)\right], \tag{8.33}$$

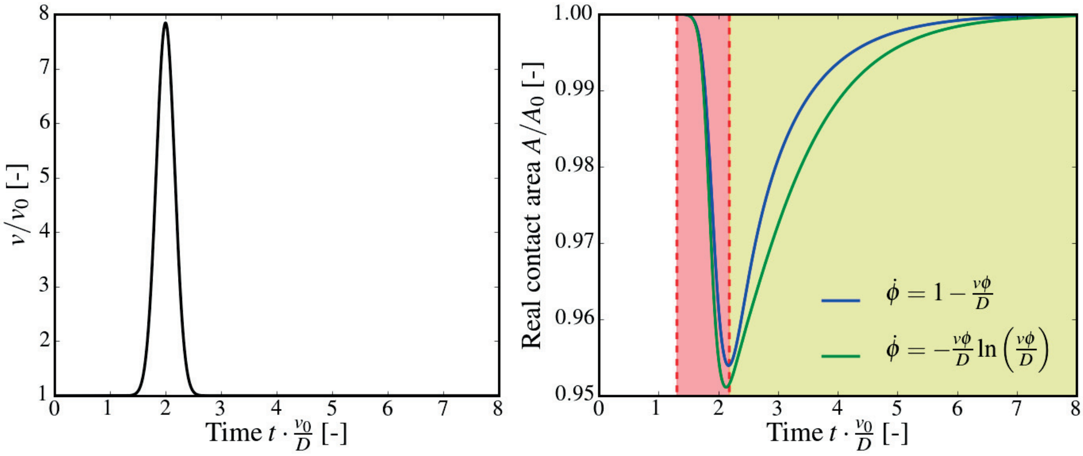

Figure 8.9 – (**Left**) Archetype evolution of the sliding velocity tailored to illustrate the frictional response of the rate-and-state interface at the vicinity of a rupture front. (**Right**) Evolution of the real contact area computed from Equation 8.33 with the evolution law described in Equations 8.13 and 8.38. The red area corresponds to the direct effect, during which the total contact area is reduced by the slip acceleration. At the end of this phase, the real contact area reaches a minimum value and starts to progressively rebuild over a longer time scale highlighted by the yellow area.

with A_0 a constant representing an initial area of contact. To illustrate the interplay between v and ϕ occurring at a given location during the rupture process, we tailor a slip acceleration with an archetype Gaussian shape and integrate the predicted evolution of the contact area given by Equations 8.13 and 8.33. Figure 8.9 presents the resulting response to this rapid change in sliding velocity, which occurs in two steps:

1. An instantaneous drop of the contact area responds to sliding acceleration. Microcontacts population is strongly rejuvenated during this initial phase, which is highlighted by the red area in the right plot of Figure 8.9.

2. After this direct response, a much slower increase of the real contact area starts and progressively brings the frictional interface toward a new steady-state equilibrium (identical to the initial state for this simplified example). This second phase, which can be physically interpreted as the progressive creep relaxation of the microcontacts [114], develops over much longer time scale than the one associated to the rupture process.

As discussed in the introduction, ϕ can be understood as the average lifetime of the underlying microcontacts population. When the interface slides at a steady velocity v^{ss}, the existing microcontacts are breaking at the same rate than new microcontacts are created. Hence, the macroscopic average lifetime reaches a constant value corresponding to $\phi_{ss} = D/v^{ss}$. The ratio $v\phi/D$ is therefore a dimensionless indicator of the interplay between v and ϕ on interface conditions.

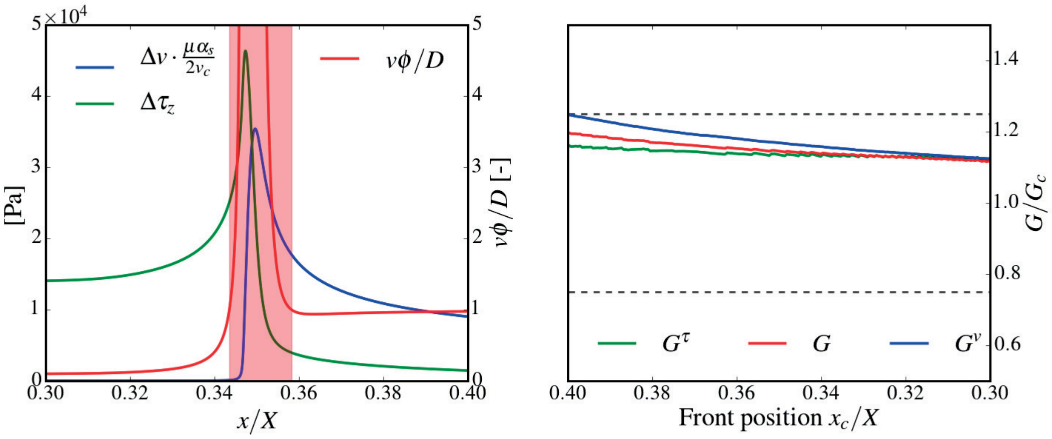

Figure 8.10 – (**Left**) The equivalent process zone described by the red area is outlined by the evolution of $v\phi/D$ which indicates the portion of the interface where the rupture is currently reducing the real contact area. (**Right**). Validation of the energy balance resulting from the mapping of the asymptotic fields presented in Figure 8.8 and the integration of the equivalent fracture energy from Equation 8.32.

In this context, we define the process zone as the region surrounding the rupture front over which $v\phi/D > 1$, i.e. the portion of the interface where the propagating rupture is currently breaking the microcontacts ($\dot{\phi} < 0$) and reducing the contact area (as in the red area of Figure 8.9). The resulting process zone is highlighted in Figure 8.10(**Left**) and directly used as the domain of integration for the evaluation of the fracture energy integral of Equation 8.32, which can be rewritten as

$$G_c(t) = \frac{\dot{E}_{\text{diss}}(t)}{v_c(t)} = \frac{1}{v_c(t)} \int_{v\phi/D>1} \left(\tau_z(t) - \tau_z^r(t)\right) v \, dx. \tag{8.34}$$

Figure 8.10(**Right**) presents the computed energy balance, which remarkably sustains our definition of the process zone and confirms the crack-like dynamics driving the rupture of rate-and-state interface. This definition of the equivalent fracture process zone is in agreement with the detailed study of the slip-weakening behavior of rate-and-state laws given in [195, 196]. Our simulations suggest however that a criterion on ϕ instead of τ_z is more robust to define the limits of the process zone, as the shear traction can experience further slip-weakening long after the rupture.

As presented in Figure 8.11, the suggested procedure is further validated by keeping the friction parameters constant but changing the bulk properties and far-field loading conditions. The latter includes in-plane (mode II) shearing, whose formulation is presented and discussed in the supplementary materials (Section 8.8). The measured energy budget suggests that the equivalent fracture energy is an intrinsic quantity emerging from the rate-and-state law, independent from the bulk properties but slightly varying with the front propagation speed. The effect of the rate-and-state parameters and formulations are investigated in the next section.

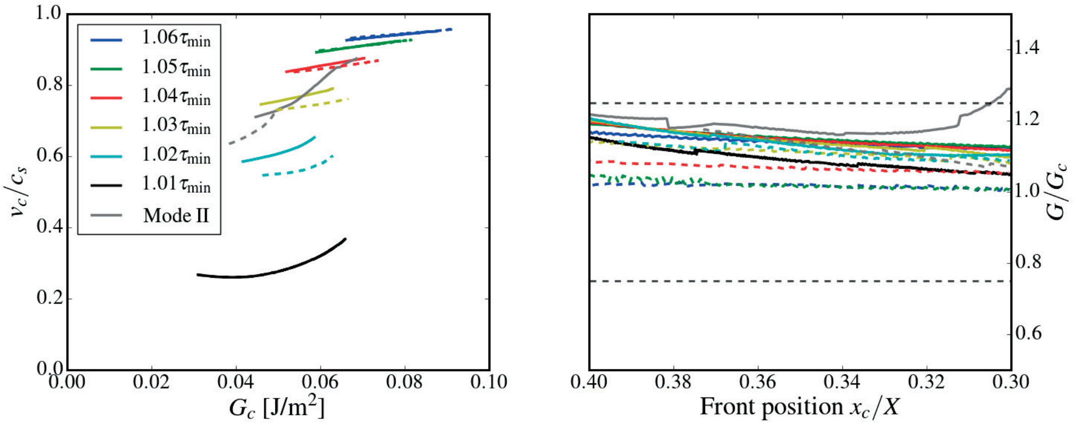

Figure 8.11 – (**Left**) Equivalent fracture energy measured for slip fronts moving under different interface conditions. The rate-and-state parameters are unchanged, while we investigate different bulk properties (dashed lines represent setups with μ being 10 times smaller), various far-field loadings (τ^0), including a mode II setup ($\tau^0 = 1.015\tau_{\min}$). $\tau_{\min}$ represents the minimum loading for which a steady-state sliding solution exists (i.e. the minimum of the steady-state curve of Figure 8.4.) (**Right**). Verification of the energy balance for the different setups presented in the left plot using the same color code.

8.6 Application to other rate-and-state formulations

In this section, we demonstrate how the proposed procedure to compute the equivalent fracture energy driving the propagation of slip front directly applies to the diverse rate-and-state formulations existing in the literature. For a detailed review of the different rate-and-state formulations and their history, the reader is redirected to [120]. Figure 8.12 presents three different forms of rate-and-state formulation considered in this chapter.

8.6.1 The original velocity-weakening formulation

The following formulation was proposed by Ruina [23] based on the observations reported by Dieterich [22]:

$$c_f\Big(v(x,t),\phi(x,t)\Big) = c_f^0 + a\ln\left(\frac{v(x,t)}{v^*}\right) + bc_f^0\ln\left(\frac{\phi(x,t)}{\phi^*}\right). \tag{8.35}$$

This original formulation, often referred to as the *Dieterich-Ruina* law, represents the class of rate-and-state formulation having a monotonic behavior in the steady-state regime (see the velocity-weakening green curve in Figure 8.12). Equation 8.35 was derived to describe the evolution of the frictional force with sliding velocities observed during frictional experiments. For the typical velocity range of these laboratory experiments, the frictional response is dominated by the aging contribution, for which sliding at a faster velocity reduces the average microcontacts age $\phi_{ss} = D/v_{ss}$ and leads to a velocity-weakening behavior.

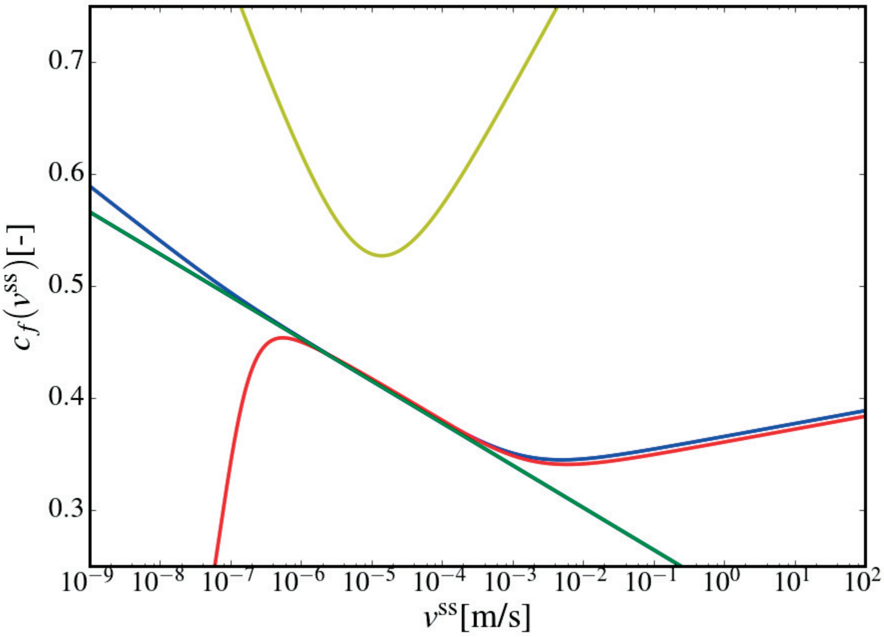

Figure 8.12 – Steady-state evolution of the friction coefficient observed for four different types of rate-and-state formulations. The blue curve represents the standard formulation used in this work (Equation 8.12). The same formulation is used with the parameters given in Table 8.2 (yellow curve). The green curve is the original Dieterich-Ruina formulation (Equation 8.35) and the red curve describes the “N-shaped” formulation given by Equation 8.37.

However, at much larger, or much smaller sliding velocities, rate-dependent effects prevail and the frictional response becomes velocity-strengthening. For a detailed mechanistic presentation of the rate-dependency of friction law, the reader is redirected to [118, 119].

8.6.2 Velocity-strengthening and slow earthquakes

The formulation used in this chapter (Equation 8.12) has the interest of regularizing the *Dieterich-Ruina* law at smaller sliding velocities ($v \to 0$) and contacting times ($\phi \to 0$). It received recent attention in the literature for its velocity-strengthening behavior, which also exists in frictional experiments at larger sliding velocities [114, 119]. Moreover, a large range of rupture speed can exist with this type of non-monotonic formulation, from inertial ruptures $v \sim c_s$ toward slow fronts $v/c_s \sim 10^{-3}$ [190], which can be observed in Figure 8.13 (in yellow) using the parameters of Table 8.2. The latter is particularly appealing in light of the recent observations of slow earthquakes, whose precise origins and mechanics are still mysterious [197–199].

Parameters	Value	Units
D	0.5	[μm]
c_f^0	0.1	[-]
a	0.05	[-]
b	1.2	[-]
v^*	10^{-8}	[m/s]
ϕ^*	0.05	[s]

Table 8.2 – Interface parameters leading to the steady-state behavior depicted by the yellow curve in Figure 8.12.

8.6.3 Nucleation from sticking conditions

Finally, a velocity-strengthening branch can arise at extremely small sliding velocities, mostly caused by the creep of the microcontacts. The resulting “N-shaped” frictional curve can be described by the following “regularized formulation”, proposed in [117]:

$$c_f\Big(v(x,t),\phi(x,t)\Big) = \Big(1 + b\ln(1+\frac{\phi(x,t)}{\phi^*})\Big)\Big(\frac{\theta}{\sqrt{1+(v_o/v(x,t))^2}} + \xi\ln(1+\frac{v(x,t)}{v_o})\Big) \tag{8.36}$$

associated to the evolution law

$$\dot{\phi}(x,t) = 1 - \frac{\phi(x,t)\sqrt{v(x,t)^2+v_o^2}}{D}. \tag{8.37}$$

The red curve in Figure 8.12 shows the constitutive law used in this chapter and obtained with the additional empirical variables $v_o = 10^{-7}$[m/s], $\theta = 0.28$[-] and $\xi = 0.005$[-]. As discussed in the introduction, the nucleation from a velocity-weakening branch arises through a linear instability [23, 108, 115–117]. Conversely, a *quasi-quiescent* steady-state exists at extremely small sliding velocities and represents a stable frictional state, from which the nucleation of rupture front is still overlooked. In a parallel work [187], we precisely describe how the nucleation of rupture fronts along an initially locked interface is driven by the propagation of slip pulses, which are intrinsically unstable, i.e. the pulse width either expands or decays, and serves as an equivalent "critical nuclei" of the sticking-to-sliding phase transition.

Following the procedure proposed in this chapter, we show how these unstable slip pulses are driven by a similar crack-like energy balance. The equivalent fracture energy of these pulses nucleating from a quiescent interface is presented in Figure 8.13 (in red) and takes a constant value almost independent of the slip pulse velocity or the shear pre-stress. From this constant value of the equivalent fracture energy, we construct a phase diagram rationalizing rupture nucleation along initially locked frictional interfaces [187].

8.6.4 Aging versus slip law

The ordinary differential equation governing the evolution of ϕ, referred to as *the evolution law*, exists with different forms in the literature. Aside from the *aging law* of Equation 8.13 (and its regularized form in Equation 8.37), Ruina [23] proposed the following *slip law*

$$\dot{\phi}(x,t) = -\frac{v(x,t)\phi(x,t)}{D}\ln\left(\frac{v(x,t)\phi(x,t)}{D}\right). \tag{8.38}$$

The two laws have a rather similar behavior (visible in Figure 8.9) characterized by the interplay of a direct effect followed by a long term relaxation. At the static limit, the friction coefficient stops evolving with the slip law, while the aging law accounts for the logarithmic strengthening of c_f with time. The equivalent fracture energies (cf. cyan curves in Figure 8.13) obtained with the procedure suggested in this chapter are however significantly lower for the slip law, in agreement with the behaviors reported in the literature [116, 196, 200].

8.6.5 Magnitudes of the equivalent fracture energy

Figure 8.13 presents the magnitudes of the equivalent fracture energy resulting for the different rate-and-state formulations previously described and presented in Figure 8.12. The slight variations from unity observed in Figures 8.10, 8.11 and 8.13 are expected to arise from the various uncertainties entering the estimations of both G_c (value of τ^r, definition of the equivalent process zone) and G (computation of v_c, fit of singular fields). Nevertheless, the observed variations are contained within the "admissible" precision range estimated with the cohesive approach (cf. Figure 8.3). The universality of the proposed procedure is hence verified and validated for several types of rate-and-state formulations found in the literature as well as rupture velocities scaling from the slow front dynamics at thousandth of c_s toward inertial rupture fronts moving at $v_c \sim c_s$.

Moreover, the resulting magnitudes of the equivalent fracture energy are in agreement with the analytical estimations proposed in the literature. For the aging law (Equation 8.13) and neglecting the "+1" terms within the logarithms of Equation 8.12, Bizzarri and Cocco [196] defined an equivalent critical slip distance for rate-and-state formulations:

$$\delta_c^{\mathrm{eq}} = D\ln(V/V_{bg}), \tag{8.39}$$

from which Ampuero and Rubin [116, 200] derived an estimation of the equivalent fracture energy under initial conditions near steady-state:

$$G_c = \frac{Dbc_f^0\sigma^0}{2}\ln^2(V/V_{bg}). \tag{8.40}$$

In the equations above, V_{bg} corresponds to the steady-state background velocity existing before the arrival of the rupture front, while V is the sliding velocity existing at the center of the nucleated crack. In light of the nucleation procedure followed in this chapter, one can reasonably set $V_{bg} = v_w$ and $V = v_s$. For the reference setup studied in this chapter, Equation 8.40 predicts therefore $G_c \cong 0.07[\mathrm{J/m^2}]$ in excellent agreement with the values reported in Figure 8.8(**Right**).

Similarly, we compute analytical predictions of G_c for the different configurations studied and reported in the inset of Figure 8.13(**Left**). The upside-down triangles indeed depict the analytical predictions, which are again in good agreement with the measured values. Nevertheless, few precisions should be given regarding those estimations:

- Equation 8.39 and 8.40 are not valid when a slip law (cf. cyan curves in Figure 8.13 and Equation 8.38) is used instead of the aging law. In this situation, Ampuero and Rubin [116] proposed the following estimation

  $$G_c = bc_f^0\sigma^0\int_0^\infty \ln(V/V_{bg})e^{-\delta/D}d\delta = Dbc_f^0\sigma^0\ln(V/V_{bg}). \tag{8.41}$$

  As the integration between 0 and ∞ leads to a slight overestimation of the equivalent fracture energy ($G_c \cong 0.023[\mathrm{J/m^2}]$), we choose to integrate between 0 and δ_c^{eq}. The later was estimated following the observation of Bizzarri and Cocco [196] that the equivalent critical slip distance with the slip law is three times smaller than with the aging law. We hence assume $\delta_c^{\mathrm{eq}} = D\ln(V/V_{bg})/3$, which leads, in combination with Equation 8.41, to the following estimation of the equivalent fracture energy for the slip law:

  $$G_c = Dbc_f^0\sigma^0\ln(V/V_{bg})\Big(1-(V_{bg}/V)^{\frac{1}{3}}\Big). \tag{8.42}$$

- The regularized rate-and-state law given in Equation 8.37 has a very similar behavior than the standard formulation (cf. comparison of the blue and red curves in Figure 8.12) for the sliding velocities observed during the rupture process ($v >> v_o$). Therefore, the estimated fracture energy is computed from Equation 8.40 using the parameters

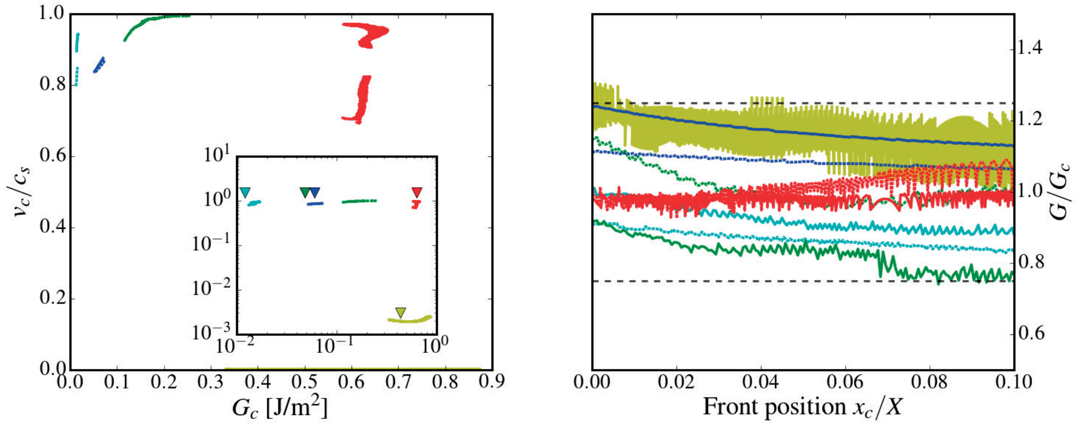

Figure 8.13 – Equivalent fracture energy versus rupture speed (**Left**) and energy balance (**Right**) computed for a large variety of slip fronts, emerging from different rate-and-state formulations, whose steady-state behaviors can be visualized in Figure 8.12. The standard formulation used in this manuscript is shown in blue for the aging evolution law and in cyan for the slip law. A slow rupture front (yellow) is simulated and studied using the set of parameters given in Table 8.2, while the behavior of interfaces following the original Dieterich-Ruina formulation is depicted in green. Unstable slip pulses nucleated from the N-shaped formulation of Equation 8.37 is plotted in red. The upside-down triangles in the inset of the right plot highlight the analytical predictions of G_c discussed in the main text. (Note that the vertical coordinate of these triangles is meaningless and arbitrarily chosen for the visualization.)

D and c_f^0 of the analogous standard formulation. Moreover, instead of v_w, an initial quasi-quiescent steady-state velocity is considered such that $V_{bg} \cong v_o$.

- The procedure described in this chapter to compute the equivalent fracture energy gives values in good agreement with the analytical predictions proposed in the literature. The applicability of the later is, however, limited to rupture fronts invading a region sliding under steady-state background conditions characterized by V_{bg}. We postulate that V_{bg} is equal to the initial steady-state sliding velocity, but the sine perturbation used to trigger the nucleation (cf. Equation 8.27) also causes slip deceleration in the left half of the domain before the arrival of the rupture front. If this deceleration brings the interface to a sliding regime significantly slower than the initial steady-state value $V_{bg} = v_w$, the analytical estimation underestimates then the value of G_c (which precisely explains the divergence observed for the green data points reported in Figure 8.13).

8.7 Conclusion

The rate-and-state friction laws, inherited from the works of Dieterich and Ruina, received an increasing interest for their ability to describe the subtle variations of frictional strength with sliding velocity, universally observed along various types of materials including papers, polymers and rocks [114]. However, a clear understanding of the physics underlying these laboratory-derived laws is still missing, and in particular, the energy budget behind the nucleation and propagation of rupture events.

In this work, we propose a framework to analyze the energy balance driving the propagation of slip fronts along frictional interfaces governed by a rate-and-state constitutive law. To this aim, we applied the concepts of the dynamic theory of fracture to study the propagation of slip fronts along a frictional interface between two semi-infinite linearly elastic half-spaces. Grounded on the physical interpretation of the state variable, we define a criteria to systematically integrate the equivalent fracture energy dissipated during the front advance and verify that the latter precisely balance the potential energy released by the rupture. We then successfully apply the proposed procedure to study the propagation of slip fronts with different forms (pulse-like versus crack-like), for a wide range of rupture speeds and using different rate-and-state formulations. We also demonstrate how the computed equivalent fracture energy is in excellent agreement with the existing analytical estimations.

The generic procedure proposed in this chapter to integrate the equivalent fracture energy (cf. Equation 8.34) is robust and suitable to study slip front dynamics under various kinds of initial conditions. This novel framework opens new prospects in the understanding of the equivalent fracture energy driving the onset of slip along along frictional interfaces. Unlike the standard slip-weakening formulation, the magnitude of G_c is not prescribed for the rate-and-state formulation. As presented in Figure 8.14, the equivalent fracture energy driving the rupture of the interface can hence represents only a small portion of the total *breakdown energy* measured during the onset of sliding. Moreover, the rupture process also arises over a short fraction ~ 5 [μm] of the total slip observed during the failure event. This critical slip distance is about one order of magnitude larger than the characteristic distance $D = 0.5$ [μm], in agreement with the observations of [195].

We underline that the equivalent fracture energy discussed in this work is not necessarily associated to cleavage or fracturing of the interface material. It does not bring information about the nature of the dissipation mechanisms but rather indicates which portion of the total energy dissipation is precisely involved in driving the rupture propagation (and controls its speed, its radiated energy, etc.) The new framework presented in this chapter will bring fresh insights in our understanding of the seismic energy budget and the large discrepancies existing between the estimation of the earthquake equivalent fracture energy and the values measured in laboratory experiments [131–134].

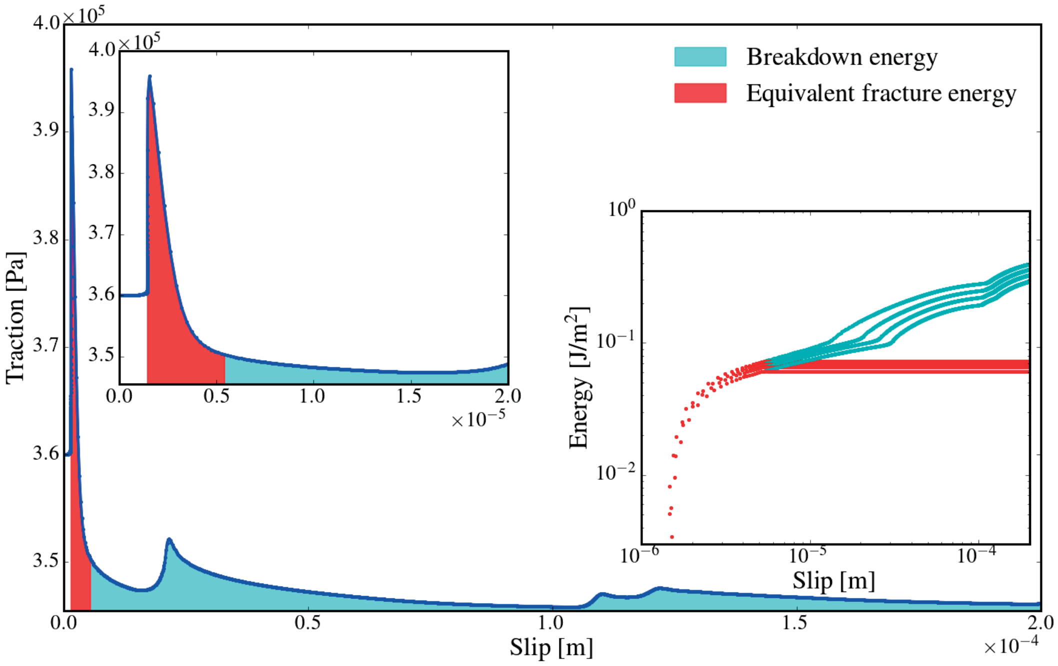

Figure 8.14 – Traction versus slip evolution observed along the interface at the position $x/X = 0.4$ during the rupture event detailed in Figure 8.6. The red area corresponds to the equivalent fracture energy driving the slip front propagation. (**Left inset**) Zoom in the traction versus slip evolution. (**Right inset**) Evolution of the breakdown and equivalent fracture energy computed at four different interface locations. The latter is dissipated during shorter time scales, concurrent to the arrival of the rupture front and, therefore, represents a small portion of the total breakdown energy.

8.8 Supplementary materials

The formalism presented above for the anti-plane shear setup can directly be applied to in-plane shearing. Unlike Equation 8.2, the elastodynamic equation is not scalar in this mode II fracture setup, which is governed by the following vectorial equation

$$c_d^2\nabla(\nabla\cdot\boldsymbol{u}) - c_s^2\nabla\times(\nabla\times\boldsymbol{u}) = \frac{\partial^2\boldsymbol{u}}{\partial t^2}, \tag{8.43}$$

involving also dilatation motion, which propagates at speed c_d. An equivalent boundary integral formulation can be used to solve the mode II elastodynamic. The formulation adopted in this work is similar to the one detailed in [125].

The asymptotic fields have a similar square-root singular form, such that the shear stress at the vicinity of a dynamic rupture front is written as [42]:

$$\sigma_{xy} = \frac{K_{II}}{\sqrt{2\pi r}}\frac{1}{D_\alpha}\Big\{4\alpha_d\alpha_s\frac{\cos\frac{1}{2}\theta_d}{\sqrt{\gamma_d}} - (1+\alpha_s^2)^2\frac{\cos\frac{1}{2}\theta_s}{\sqrt{\gamma_s}}\Big\}, \tag{8.44}$$

with $\gamma_{d,s} = \sqrt{1-(v_c\sin\theta/c_{d,s})^2}$, $\alpha_{d,s}^2 = 1 - v_c^2/c_{d,s}^2$ and $\tan\theta_{d,s} = \alpha_{d,s}\tan\theta$. $D_\alpha = 4\alpha_d\alpha_s - (1+\alpha_s^2)^2$ is a function of the crack speed, which is zero in the limits $v_c = 0$ and $v_c = c_R$. Similarly, the sliding velocity at the vicinity of a dynamic mode II crack is written as

$$\dot{u}_x = \frac{v_c\alpha_s K_{II}}{\mu D_\alpha\sqrt{2\pi r}}\Big\{2\frac{\sin\frac{1}{2}\theta_d}{\sqrt{\gamma_d}} - (1+\alpha_s^2)\frac{\sin\frac{1}{2}\theta_s}{\sqrt{\gamma_s}}\Big\}. \tag{8.45}$$

Along the frictional interface, these singular contributions can be mapped ahead of the rupture front

$$\tau_x = \sigma_{xy}(r = x_{\text{tip}}^\tau - x, \theta = 0, v_c) \sim \frac{K_{II}}{\sqrt{2\pi(x_{\text{tip}}^\tau - x)}}, \tag{8.46}$$

and behind it

$$v = 2\dot{u}_x(r = x - x_{\text{tip}}^v, \theta = \pi, v_c) \sim \frac{K_{II}}{\sqrt{2\pi(x - x_{\text{tip}}^v)}}\frac{2v_c\alpha_s}{\mu D_\alpha}\Big\{1-\alpha_s^2\Big\}. \tag{8.47}$$

A significant difference with the mode III setup is the ability of mode II fronts to propagate faster than the shear wave speed [6, 73]. Only sub-Rayleigh rupture fronts are discussed in the scope of this study. Figure 8.15 presents the mode II rupture dynamics observed along a cohesive interface. Ahead of an accelerating mode II crack, a shear wave advances at c_s and perturbs the mapping of the singular shear stress contribution. The effect of this wave, which was reported by Burridge [46] and Andrews [47] and extensively studied in [9], is visible in Figure 8.15 and leads to an overestimation of G and G^τ.

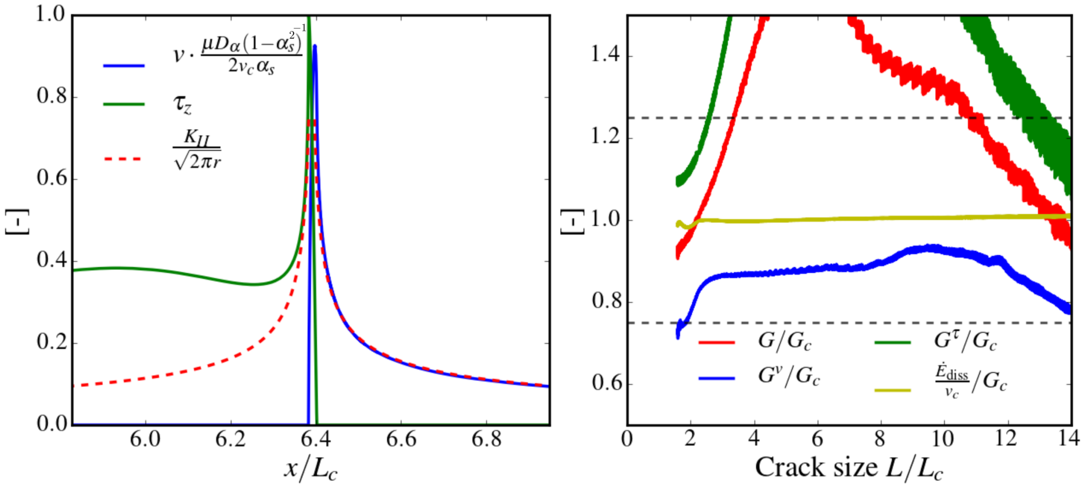

Figure 8.15 – A shear front traveling ahead of an accelerating mode II crack creates a “bump” in the shear stress profile, which slightly impacts the mapping of the stress intensity factors and, therefore, the value of G and G^τ. The plots are the mode II equivalent of Figure 8.10.

9 Conclusion

9.1 Summary

This thesis aimed at investigating the impact of heterogeneities on the propagation of dynamic rupture fronts within linearly elastic materials. Several types of heterogeneities were systematically studied.

The mismatch of elastic properties across the fracture plane represents a type of heterogeneous condition frequently encountered within geological layers as well as various engineering components since the advent of lightweight composite materials. These bimaterial conditions create specific surface perturbations arising in the form of large scale contact zones traveling in the wake of the rupture front, in spite of a tensile far-field loading. Their emergences are mainly governed by the crack front propagation speed. Hence, this thesis proposed a generalized description of the admissible rupture speeds depending on the direction of the rupture front relative to material point displacements. It showed how the combination of the admissible speeds existing for the top and bottom elastic solids predicts the onset of these surface instabilities, in agreement with the experimental observations.

The dynamic instabilities observed during the rapid failure of nominally homogeneous materials are rather emerging from microscopic heterogeneities in terms of fracture energy. Therefore, the homogeneous distribution of G_c along the fracture plane was replaced by an equivalent interface (in terms of the average fracture energy) represented by an idealized alternation of weaker and stronger regions. This comparison revealed how the rupture dynamics can be significantly impacted by the elastic waves radiated from heterogeneous interfaces, even in absence of any crack front distortion. Therefore, the amplitudes of these radiations were systematically studied as a function of the heterogeneous patterns (width of the heterogeneities, toughness contrast) and showed how the process zone is the characteristic size mediating the transition from quasi-homogeneous to heterogeneous fracture. Furthermore, the process zone size changes with the rupture speed and this work presented how its contraction as v_c approaches c_R brings the front to interact with smaller defects/heterogeneities existing along the interface. This relativistic contraction of the process zone was then proposed as a potential explanation of the increase of the surface mark density with the crack speed reported in the dynamic rupture of brittle materials [169].

This thesis also particularly emphasized the impact of heterogeneities on the regime of rupture for both tensile and shear cracks. This work demonstrated how the observed increase in elastic radiations along a heterogeneous interface significantly eases the supershear transition of mode II cracks. In particular, this study emphasized how supershear propagations can arise over much shorter distances and under a lower shear pre-stress than in the predictions of the homogeneous models. These results bring new insights into recent experimental measurements [171] suggesting that supershear events might frequently occur over shorter length scales and have a significant impact on the rupture energy budget.

For tensile cracks, the impact of supershear episodes is completely overlooked as rupture speeds above c_R are energetically forbidden by LEFM. For the first time, this work uncovered how supershear events can also occur for mode I ruptures, and how they are triggered by the presence of material heterogeneities. While c_R is the limiting propagation speed observed along the smooth portions of the crack front, supershear bursts can arise at the discontinuities created by large distortions of the front. Such local discontinuities may frequently occur along the rupture plane in presence of dynamic instabilities (triggered by the creation of a microbranch [178] or local heterogeneities). This study showed how the persistent shock waves created by these supershear bursts can significantly impact the rupture dynamics far from the discontinuity site.

This thesis concluded with two chapters investigating the propagation of slip fronts along frictional interfaces. The main challenge consisted in understanding the effect of the complex heterogeneous topography existing at the microscale of two rough surfaces in contact. These two chapters interestingly illustrated how the theoretical and numerical framework of this thesis can be applied to diverse types of physical systems driven by the propagation of rupture fronts.

The onset of sliding along a frictional interface was studied following two types of approaches. In the first one, the heterogeneous contact map was explicitly modeled as an idealized array of valleys and microcontact junctions, whose mechanical behaviors were described using an exponential cohesive law. An interesting connection was established between the coarse-grained process zone size l_{pz} and the critical junction size d^* controlling the failure of the microcontact junctions computed with atomistic simulations [105]. The latter typically arise via two distinct mechanisms: the brittle rupture of the junctions larger than d^* or the plastic smoothing of the junctions smaller than d^*. In this context, this thesis investigated the impacts of these two mechanisms occurring at the microscale of the interface on its macroscopic frictional strength. As a result, it showed how two macroscopically identical interfaces can have significantly different frictional strengths. This effect emerging from the heterogeneous microcontact topography was finally discussed and proposed as an explanation of the "slippery but tough" paradox observed with lubricated interfaces [24].

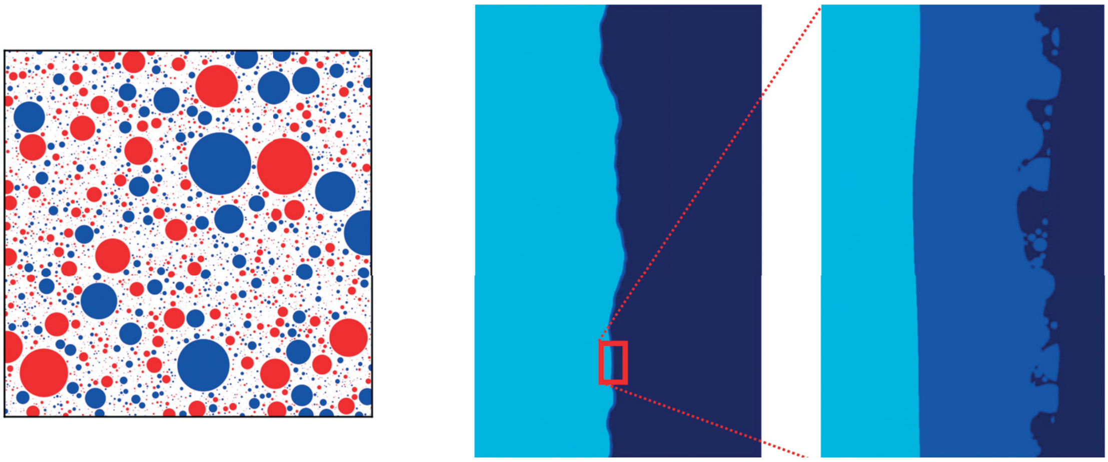

Figure 9.1 – Simulations snapshots of the propagation of a tensile crack along a heterogeneous rupture plane made of circular asperities of different radius (blue being weaker and red tougher heterogeneities). Two regimes exist as a function of the ratio of the asperity radius to the process zone size. (**Left**) Asperities much larger than the process zone distort the front line in agreement with the predictions of line tension models. (**Right**) At the scale of the fracture process zone, crack growth occurs through the nucleation and coalescence of microcracks from the locations of weaker asperities. The front is moving rightward, with colors dividing broken surface (cyan), cohesive zone (blue), and intact portion of the interface (dark blue).

Finally, the failure dynamics of frictional interfaces was studied in the framework of rate-and-state laws. In these formulations derived from laboratory experiments, the dynamics of the underlying microcontact junctions is implicitly incorporated within the friction constitutive law using a state variable, often interpreted as the average lifetime of the microcontacts. Grounded on the methodology developed to study the propagation of cohesive cracks, this thesis studied the energy release rate driving the propagation of slip fronts along rate-and-state interfaces. To this aim, the definition of an equivalent process zone was proposed and allowed to integrate an equivalent fracture energy of the interface balancing the energy release rate. The versatility of this procedure was then demonstrated with several rate-and-state formulations. This study demonstrated then how the equivalent fracture energy integrated along rate-and-state interfaces is significantly lower than the total breakdown energy. This new description of the equivalent fracture energy brings fresh insights on the energy budget of seismic events.

9.2 Outlook and perspectives

Taking advantage of the extremely fine discretization of the rupture plane enabled by a boundary integral formulation, the simulations reported in this manuscript brought several novel insights into the interplay between dynamic rupture fronts and heterogeneous interface conditions existing up to the scale of the process zone. This work opens many interesting prospects to push these analyses further. Three directions are highlighted below.

This work revealed how the size of the process zone and its contraction play a key role on the progressive roughening of the crack surfaces with rupture speed. In this context, extending the study to rupture planes containing a heterogeneous distribution of asperities and defects will enable to further study the impact of the process zone and its contraction on the three-dimensional crack dynamics. A proof of concept of such models is proposed in Figure 9.1, which presents the observed evolution of the crack front dynamics as the asperity radius approaches the process zone size. Remarkably the dynamics characterizing the crack advance at different scales (cf. Figure 2.12) are captured with a single cohesive model; At a scale larger than the fracture process zone, crack propagates as an elastic line distorted by the presence of heterogeneities, in agreement with the description of line tension models. Conversely, at the scale of the process zone, the front advances through the nucleation, growth and coalescence of microcracks located ahead of the main rupture front. Repeating the analysis with different rupture speeds and heterogeneous microstructures will shine a new light on the microcracking dynamics and the origin of the brittle to quasi-brittle transition reported in the literature [51].

This thesis showed how the finite size of the fracture process zone is paramount in the understanding of heterogeneous dynamic fracture. However, the finite width of the process zone was solely considered within the rupture plane. In absence of any preferential interface, the fracture process zone should similarly develop out of the rupture plane and becomes, thereby, a three-dimensional region evolving with the crack propagation speed. An illustration of its expected evolution was presented in Figure 2.9. The out-of-plane dimension of the process zone expands with crack propagation speed, while the in-plane process zone size is shrinking. The combined effects of these in-plane and out-of-plane evolutions of the fracture process zone on the rupture front and its interaction with pre-existing flaws is still overlooked. In this context, the variational phase-field model of fracture is a promising approach to describe out-of-plane dynamic instabilities [151, 201, 202]. Therefore, the ongoing coupling of the efficient boundary integral approach with a limited phase-field region (inserted in-between the top and bottom surfaces of the semi-infinite half-spaces) will enable unprecedented three-dimensional studies of the dynamic instabilities progressively emerging at the scale of the fracture process zone.

Finally, an estimation of the equivalent fracture energy for rate-and-state frictional laws was proposed, grounded on the energy balance of the propagating slip fronts. This new formulation will allow for a quantitative parametric study of the different rate-and-state formulations and their respective implications on the dynamics of frictional interfaces. Our study revealed how the equivalent fracture energy can represent only a small fraction of the total breakdown energy of frictional interfaces. Probing the framework proposed in this work with friction experiments should shine a new light on the equivalent fracture energy entering the energy budget of frictional interfaces and seismic events.

To conclude, the originality of this research work consisted in peeking into the Pandora's box of linear elastic fracture mechanics: the fracture process zone and its interplay with material heterogeneities. In order to avoid releasing the "evil" nonlinear dissipative processes it contains, a cohesive formulation was adopted to model their actions over a finite size, without losing the universality of LEFM. This work paved the way for further investigations on the permanent interactions existing between dynamic rupture fronts and the heterogeneous microstructure of materials and interfaces (flaws, inclusions, surface roughness), with potential implications ranging from earthquake science toward the design of micro-architected materials resilient to crack propagation.

Bibliography

[1] G. Irwin, “Analysis of Stresses and Strains Near the End of a Crack Traversing a Plate,” *J. Appl. Mech.*, vol. 24, pp. 361–364, 1957.

[2] J. R. Rice, “First-Order Variation in Elastic Fields Due to Variation in Location of a Planar Crack Front,” *Journal of Applied Mechanics*, vol. 52, no. 3, p. 571, 1985.

[3] P. Hemmer, A. Hansen, and S. Pradhan, “Rupture Processes in Fibre Bundle Models,” in *Modelling Critical and Catastrophic Phenomena in Geoscience*, vol. 705, pp. 27–55, Springer Berlin Heidelberg, 2006.

[4] J. D. Byerlee, “Theory of Friction Based on Brittle Fracture,” *Journal of Applied Physics*, vol. 38, no. 7, pp. 2928–2934, 1967.

[5] F. P. Bowden and D. Tabor, *The Friction and Lubrication of Solids*, vol. 1. Oxford university press, 2001.

[6] D. J. Andrews, “Rupture propagation with finite stress in antiplane strain,” *Journal of Geophysical Research*, vol. 81, no. 20, pp. 3575–3582, 1976.

[7] E. M. Dunham, “Conditions governing the occurrence of supershear ruptures under slip-weakening friction,” *Journal of Geophysical Research*, vol. 112, no. B7, 2007.

[8] J. H. Rose, J. Ferrante, and J. R. Smith, “Universal Binding Energy Curves for Metals and Bimetallic Interfaces,” *Physical Review Letters*, vol. 47, no. 9, p. 675, 1981.

[9] I. Svetlizky, D. Pino Munoz, M. Radiguet, D. S. Kammer, J.-F. Molinari, and J. Fineberg, “Properties of the shear stress peak radiated ahead of rapidly accelerating rupture fronts that mediate frictional slip,” *Proceedings of the National Academy of Sciences*, vol. 113, no. 3, pp. 542–547, 2016.

[10] A. A. Griffith, “The Phenomena of Rupture and Flow in Solids,” *Philosophical Transactions of the Royal Society A: Mathematical, Physical and Engineering Sciences*, vol. 221, no. 582-593, pp. 163–198, 1921.

[11] S. Xia, L. Ponson, G. Ravichandran, and K. Bhattacharya, “Toughening and Asymmetry in Peeling of Heterogeneous Adhesives,” *Physical Review Letters*, vol. 108, no. 19, 2012.

[12] M. Mirkhalaf, A. K. Dastjerdi, and F. Barthelat, “Overcoming the brittleness of glass through bio-inspiration and micro-architecture,” *Nature Communications*, vol. 5, p. 3166, 2014.

[13] E. Munch, M. E. Launey, D. H. Alsem, E. Saiz, A. P. Tomsia, and R. O. Ritchie, “Tough, Bio-Inspired Hybrid Materials,” *Science*, vol. 322, no. 5907, pp. 1516–1520, 2008.

[14] J. R. Raney, B. G. Compton, J. Mueller, T. J. Ober, K. Shea, and J. A. Lewis, “Rotational 3D printing of damage-tolerant composites with programmable mechanics,” *Proceedings of the National Academy of Sciences*, vol. 115, no. 6, pp. 1198–1203, 2018.

[15] J. R. Willis and A. B. Movchan, “Dynamic weight functions for a moving crack. I. Mode I loading,” *Journal of the Mechanics and Physics of Solids*, vol. 43, no. 3, pp. 319–341, 1995.

[16] P. H. Geubelle and J. R. Rice, “A spectral method for three-dimensional elastodynamic fracture problems,” *Journal of the Mechanics and Physics of Solids*, vol. 43, no. 11, pp. 1791–1824, 1995.

[17] M. S. Breitenfeld and P. H. Geubelle, “Numerical analysis of dynamic debonding under 2D in-plane and 3D loading,” *International Journal of Fracture*, vol. 93, no. 1/4, pp. 13–38, 1998.

[18] O. Zienkiewicz and R. Taylor, *The Finite Element Method for Solid and Structural Mechanics.* Elsevier, 2005.

[19] T. Belytschko, W. Liu, B. Moran, and K. Elkhodary, *Nonlinear Finite Elements for Continua and Structures.* John Wiley & Sons, 2nd ed., 2014.

[20] D. Dugdale, “Yielding of steel sheets containing slits,” *Journal of the Mechanics and Physics of Solids*, vol. 8, no. 2, pp. 100–104, 1960.

[21] G. Barenblatt, “The Mathematical Theory of Equilibrium Cracks in Brittle Fracture,” in *Advances in Applied Mechanics*, vol. 7, pp. 55–129, Elsevier, 1962.

[22] J. H. Dieterich, “Modeling of rock friction: 1. Experimental results and constitutive equations,” *Journal of Geophysical Research*, vol. 84, no. B5, p. 2161, 1979.

[23] A. Ruina, “Slip instability and state variable friction laws,” *Journal of Geophysical Research: Solid Earth*, vol. 88, no. B12, pp. 10359–10370, 1983.

[24] E. Bayart, I. Svetlizky, and J. Fineberg, “Slippery but Tough: The Rapid Fracture of Lubricated Frictional Interfaces,” *Physical Review Letters*, vol. 116, no. 19, p. 194301, 2016.

[25] M. J. Buehler, *Atomistic Modeling of Materials Failure.* Boston, MA: Springer US, 2008.

[26] J. D. Achenbach, *Wave Propagation in Elastic Solids*, vol. vol. 16, pr. 3 of *North-Holland series in applied mathematics and mechanics.* North-Holland, 3rd printing ed., 1980.

[27] W. M. Lai, D. Rubin, and E. Krempl, *Introduction to Continuum Mechanics.* Boston: Butterworth-Heinemann, fourth edition ed., 2010.

[28] A. F. Bower, *Applied Mechanics of Solids.* Boca Raton, FL: CRC Press, Taylor & Francis Group, 2010.

[29] L. Rayleigh, "On Waves Propagated along the Plane Surface of an Elastic Solid," *Proceedings of the London Mathematical Society*, vol. s1-17, no. 1, pp. 4–11, 1885.

[30] J. M. Barsom, *Fracture Mechanics Retrospective : Early Classic Papers (1913-1965)*, vol. 1 of *Retrospective publication series.* Philadelphia: ASTM, 1987.

[31] T. L. Anderson, *Fracture Mechanics: Fundamentals and Applications.* Boca Raton, FL: Taylor & Francis, 3rd ed. ed., 2005.

[32] C. E. Inglis, "Stresses in a plate due to the presence of cracks and sharp corners," *Transactions of the institute of naval architects*, vol. 55, no. 219-241, pp. 193–198, 1913.

[33] H. M. Westergaard, "Bearing pressures and cracks," *Journal of applied mechanics*, vol. 6, no. 2, pp. A49–A53, 1939.

[34] I. N. Sneddon, "The Distribution of Stress in the Neighbourhood of a Crack in an Elastic Solid," *Proceedings of the Royal Society A: Mathematical, Physical and Engineering Sciences*, vol. 187, no. 1009, pp. 229–260, 1946.

[35] M. L. Williams, "On the Stress Distribution at the Base of a Stationary Crack," *Journal of Applied Mechanics*, vol. 24, no. 1, pp. 109–114, 1957.

[36] M. L. Williams, "Stress singularities resulting from various boundary conditions in angular corners of plates in extension," *Journal of applied mechanics}*, vol. 19, no. 4, pp. 526–528, 1952.

[37] K. Ravi-Chandar, *Dynamic Fracture.* Amsterdam: Elsevier, 2004.

[38] J. R. Rice, "A Path Independent Integral and the Approximate Analysis of Strain Concentration by Notches and Cracks," *Journal of Applied Mechanics*, vol. 35, no. 2, p. 379, 1968.

[39] P. C. Paris, M. P. Gomez, and W. E. Anderson, "A rational analytic theory of fatigue," *The Trend in Engineering*, vol. 13, pp. 9–14, 1961.

[40] A. C. Palmer and J. R. Rice, "The growth of slip surfaces in the progressive failure of over-consolidated clay," *Proceedings of the Royal Society of London A: Mathematical and Physical Sciences*, vol. 332, no. doi:, pp. 527–548, 1973.

[41] D. M. McClung, "Fracture mechanical models of dry slab avalanche release," *Journal of Geophysical Research: Solid Earth*, vol. 86, no. B11, pp. 10783–10790, 1981.

[42] L. B. Freund, *Dynamic Fracture Mechanics.* Cambridge monographs on mechanics and applied mathematics, Cambridge: Cambridge University Press, 1990.

[43] B. V. Kostrov and S. Das, *Principles of Earthquake Source Mechanics.* Cambridge monographs on mechanics and applied mathematics, Cambridge: Cambridge University Press, 1988.

[44] A. Einstein, “Zur Elektrodynamik bewegter Körper,” *Annalen der Physik*, vol. 322, no. 10, pp. 891–921, 1905.

[45] L. B. Freund, “The mechanics of dynamic shear crack propagation,” *Journal of Geophysical Research*, vol. 84, no. B5, p. 2199, 1979.

[46] R. Burridge, “Admissible Speeds for Plane-Strain Self-Similar Shear Cracks with Friction but Lacking Cohesion,” *Geophysical Journal International*, vol. 35, no. 4, pp. 439–455, 1973.

[47] D. J. Andrews, “Rupture velocity of plane strain shear cracks,” *Journal of Geophysical Research*, vol. 81, no. 32, pp. 5679–5687, 1976.

[48] K. B. Broberg, “The near-tip field at high crack velocities,” *International Journal of Fracture*, vol. 39, no. 1-3, pp. 1–13, 1989.

[49] A. J. Rosakis, “Intersonic shear cracks and fault ruptures,” *Advances in Physics*, vol. 51, no. 4, pp. 1189–1257, 2002.

[50] K. Ravi-Chandar and W. G. Knauss, “An experimental investigation into dynamic fracture: I. Crack initiation and arrest,” *International Journal of Fracture*, vol. 25, no. 4, pp. 247–262, 1984.

[51] J. Scheibert, C. Guerra, F. Célarié, D. Dalmas, and D. Bonamy, “Brittle-Quasibrittle Transition in Dynamic Fracture: An Energetic Signature,” *Physical Review Letters*, vol. 104, no. 4, 2010.

[52] T. G. Boué, G. Cohen, and J. Fineberg, “Origin of the Microbranching Instability in Rapid Cracks,” *Physical Review Letters*, vol. 114, no. 5, 2015.

[53] J. A. Hauch, D. Holland, M. P. Marder, and H. L. Swinney, “Dynamic Fracture in Single Crystal Silicon,” *Physical Review Letters*, vol. 82, no. 19, pp. 3823–3826, 1999.

[54] T. Cramer, A. Wanner, and P. Gumbsch, “Energy Dissipation and Path Instabilities in Dynamic Fracture of Silicon Single Crystals,” *Physical Review Letters*, vol. 85, no. 4, pp. 788–791, 2000.

[55] K. Ravi-Chandar and W. G. Knauss, “An experimental investigation into dynamic fracture: III. On steady-state crack propagation and crack branching,” *International Journal of Fracture*, vol. 26, no. 2, pp. 141–154, 1984.

[56] K. Ravi-Chandar and W. G. Knauss, "An experimental investigation into dynamic fracture: II. Microstructural aspects," *International Journal of Fracture*, vol. 26, no. 1, pp. 65–80, 1984.

[57] J. Fineberg and M. Marder, "Instability in dynamic fracture," *Physics Reports*, vol. 313, no. 1-2, pp. 1–108, 1999.

[58] E. Bouchbinder, T. Goldman, and J. Fineberg, "The dynamics of rapid fracture: Instabilities, nonlinearities and length scales," *Reports on Progress in Physics*, vol. 77, no. 4, p. 046501, 2014.

[59] J. Fineberg and E. Bouchbinder, "Recent developments in dynamic fracture: Some perspectives," *International Journal of Fracture*, vol. 196, no. 1-2, pp. 33–57, 2015.

[60] H. Gao and J. R. Rice, "A First-Order Perturbation Analysis of Crack Trapping by Arrays of Obstacles," *Journal of Applied Mechanics*, vol. 56, no. 4, p. 828, 1989.

[61] S. Ramanathan, D. Ertaş, and D. S. Fisher, "Quasistatic Crack Propagation in Heterogeneous Media," *Physical Review Letters*, vol. 79, no. 5, pp. 873–876, 1997.

[62] J. Schmittbuhl and K. J. Måløy, "Direct Observation of a Self-Affine Crack Propagation," *Physical Review Letters*, vol. 78, no. 20, pp. 3888–3891, 1997.

[63] D. Bonamy, S. Santucci, and L. Ponson, "Crackling Dynamics in Material Failure as the Signature of a Self-Organized Dynamic Phase Transition," *Physical Review Letters*, vol. 101, no. 4, 2008.

[64] D. Bonamy, L. Ponson, S. Prades, E. Bouchaud, and C. Guillot, "Scaling Exponents for Fracture Surfaces in Homogeneous Glass and Glassy Ceramics," *Physical Review Letters*, vol. 97, no. 13, 2006.

[65] E. Katzav, M. Adda-Bedia, and B. Derrida, "Fracture surfaces of heterogeneous materials: A 2D solvable model," *Europhysics Letters (EPL)*, vol. 78, no. 4, p. 46006, 2007.

[66] J. Barés, L. Barbier, and D. Bonamy, "Crackling versus Continuumlike Dynamics in Brittle Failure," *Physical Review Letters*, vol. 111, no. 5, 2013.

[67] E. Bouchbinder, J. Mathiesen, and I. Procaccia, "Roughening of Fracture Surfaces: The Role of Plastic Deformation," *Physical Review Letters*, vol. 92, no. 24, 2004.

[68] S. Vernède, L. Ponson, and J.-P. Bouchaud, "Turbulent Fracture Surfaces: A Footprint of Damage Percolation?," *Physical Review Letters*, vol. 114, no. 21, 2015.

[69] D. Bonamy and E. Bouchaud, "Failure of heterogeneous materials: A dynamic phase transition?," *Physics Reports*, vol. 498, no. 1, pp. 1–44, 2011.

[70] L. Ponson, "Statistical aspects in crack growth phenomena: How the fluctuations reveal the failure mechanisms," *International Journal of Fracture*, vol. 201, no. 1, pp. 11–27, 2016.

[71] D. Coker, A. Rosakis, and A. Needleman, “Dynamic crack growth along a polymer composite–Homalite interface,” *Journal of the Mechanics and Physics of Solids*, vol. 51, no. 3, pp. 425–460, 2003.

[72] P. D. Washabaugh and W. G. Knauss, “A reconciliation of dynamic crack velocity and Rayleigh wave speed in isotropic brittle solids,” *International Journal of Fracture*, vol. 65, no. 2, pp. 97–114, 1994.

[73] A. J. Rosakis, O. Samudrala, and D. Coker, “Cracks Faster than the Shear Wave Speed,” *Science*, vol. 284, no. 5418, pp. 1337–1340, 1999.

[74] R. J. Archuleta, “A faulting model for the 1979 Imperial Valley earthquake,” *Journal of Geophysical Research: Solid Earth*, vol. 89, no. B6, pp. 4559–4585, 1984.

[75] K. B. Olsen, “Three-Dimensional Dynamic Simulation of the 1992 Landers Earthquake,” *Science*, vol. 278, no. 5339, pp. 834–838, 1997.

[76] K. Xia, A. J. Rosakis, and H. Kanamori, “Laboratory Earthquakes: The Sub-Rayleigh-to-Supershear Rupture Transition,” *Science*, vol. 303, no. 5665, pp. 1859–1861, 2004.

[77] K. Xia, A. J. Rosakis, H. Kanamori, and J. R. Rice, “Laboratory Earthquakes Along Inhomogeneous Faults: Directionality and Supershear,” *Science*, vol. 308, no. 5722, pp. 681–684, 2005.

[78] X. Lu, N. Lapusta, and A. J. Rosakis, “Pulse-like and crack-like ruptures in experiments mimicking crustal earthquakes,” *Proceedings of the National Academy of Sciences*, vol. 104, no. 48, pp. 18931–18936, 2007.

[79] E. M. Dunham and H. S. Bhat, “Attenuation of radiated ground motion and stresses from three-dimensional supershear ruptures,” *Journal of Geophysical Research: Solid Earth*, vol. 113, no. B8, 2008.

[80] Y. Liu and N. Lapusta, “Transition of mode II cracks from sub-Rayleigh to intersonic speeds in the presence of favorable heterogeneity,” *Journal of the Mechanics and Physics of Solids*, vol. 56, no. 1, pp. 25–50, 2008.

[81] E. Fukuyama and K. B. Olsen, “A Condition for Super-shear Rupture Propagation in a Heterogeneous Stress Field,” *Pure and Applied Geophysics*, vol. 159, no. 9, pp. 2047–2056, 2002.

[82] E. M. Dunham, P. Favreau, and J. M. Carlson, “A Supershear Transition Mechanism for Cracks,” *Science*, vol. 299, no. 5612, pp. 1557–1559, 2003.

[83] X. Ma and A. Elbanna, “Effect of off-fault low-velocity elastic inclusions on supershear rupture dynamics,” *Geophysical Journal International*, vol. 203, no. 1, pp. 664–677, 2015.

[84] D. Kammer, D. Pino Munoz, and J. Molinari, "Length scale of interface heterogeneities selects propagation mechanism of frictional slip fronts," *Journal of the Mechanics and Physics of Solids*, vol. 88, pp. 23–34, 2016.

[85] G. Albertini and D. S. Kammer, "Off-fault heterogeneities promote supershear transition of dynamic mode II cracks," *Journal of Geophysical Research: Solid Earth*, 2017.

[86] R. P. Singh, J. Lambros, A. Shukla, and A. J. Rosakis, "Investigation of the mechanics of intersonic crack propagation along a bimaterial interface using coherent gradient sensing and photoelasticity," *Proceedings of the Royal Society of London. Series A: Mathematical, Physical and Engineering Sciences*, vol. 453, no. 1967, pp. 2649–2667, 1997.

[87] A. J. Rosakis, O. Samudrala, R. P. Singh, and A. Shukla, "Intersonic crack propagation in bimaterial systems," *Journal of the Mechanics and Physics of Solids*, vol. 46, no. 10, pp. 1789–1813, 1998.

[88] O. Samudrala and A. J. Rosakis, "Effect of loading and geometry on the subsonic/intersonic transition of a bimaterial interface crack," *Engineering Fracture Mechanics*, vol. 70, no. 2, pp. 309–337, 2003.

[89] W. F. Brace and J. D. Byerlee, "Stick-Slip as a Mechanism for Earthquakes," *Science*, vol. 153, no. 3739, pp. 990–992, 1966.

[90] C. H. Scholz, *The Mechanics of Earthquakes and Faulting*. Cambridge: Cambridge University Press, 2nd ed., 6th print. ed., 2010.

[91] J. H. Dieterich and B. D. Kilgore, "Direct observation of frictional contacts: New insights for state-dependent properties," *Pure and Applied Geophysics*, vol. 143, no. 1-3, pp. 283–302, 1994.

[92] B. Weber, T. Suhina, T. Junge, L. Pastewka, A. M. Brouwer, and D. Bonn, "Molecular probes reveal deviations from Amontons' law in multi-asperity frictional contacts," *Nature Communications*, vol. 9, no. 1, 2018.

[93] S. M. Rubinstein, G. Cohen, and J. Fineberg, "Detachment fronts and the onset of dynamic friction," *Nature*, vol. 430, no. 7003, pp. 1005–1009, 2004.

[94] I. M. Hutchings, "Leonardo da Vinci's studies of friction," *Wear*, vol. 360-361, pp. 51–66, 2016.

[95] A. Fall, B. Weber, M. Pakpour, N. Lenoir, N. Shahidzadeh, J. Fiscina, C. Wagner, and D. Bonn, "Sliding Friction on Wet and Dry Sand," *Physical Review Letters*, vol. 112, no. 17, 2014.

[96] D. Dowson, *History of Tribology*. Addison-Wesley Longman Limited, 1979.

[97] G. Amontons, "De la résistance causée dans les machines," *Mémoires de l'Académie Royale A*, pp. 257–282, 1699.

[98] C. A. Coulomb, *Théorie Des Machines Simples.* Paris: Bachelier, 1821.

[99] V. L. Popov, *Contact Mechanics and Friction.* Berlin, Heidelberg: Springer Berlin Heidelberg, 2010.

[100] E. Popova and V. L. Popov, “The research works of Coulomb and Amontons and generalized laws of friction,” *Friction*, vol. 3, no. 2, pp. 183–190, 2015.

[101] F. P. Bowden and D. Tabor, “The Area of Contact between Stationary and between Moving Surfaces,” *Proceedings of the Royal Society A: Mathematical, Physical and Engineering Sciences*, vol. 169, no. 938, pp. 391–413, 1939.

[102] J. A. Greenwood and J. B. P. Williamson, “Contact of Nominally Flat Surfaces,” *Proceedings of the Royal Society A: Mathematical, Physical and Engineering Sciences*, vol. 295, no. 1442, pp. 300–319, 1966.

[103] B. B. Mandelbrot, *The Fractal Geometry of Nature*, vol. 173. WH freeman New York, 1983.

[104] S. Hyun, L. Pei, J.-F. Molinari, and M. O. Robbins, “Finite-element analysis of contact between elastic self-affine surfaces,” *Physical Review E*, vol. 70, no. 2, 2004.

[105] R. Aghababaei, D. H. Warner, and J.-F. Molinari, “Critical length scale controls adhesive wear mechanisms,” *Nature Communications*, vol. 7, p. 11816, 2016.

[106] R. Aghababaei, D. H. Warner, and J.-F. Molinari, “On the debris-level origins of adhesive wear,” *Proceedings of the National Academy of Sciences*, p. 201700904, 2017.

[107] L. Frérot, R. Aghababaei, and J.-F. Molinari, “A mechanistic understanding of the wear coefficient: From single to multiple asperities contact,” *Journal of the Mechanics and Physics of Solids*, vol. 114, pp. 172–184, 2018.

[108] J. R. Rice and A. L. Ruina, “Stability of Steady Frictional Slipping,” *Journal of Applied Mechanics*, vol. 50, no. 2, p. 343, 1983.

[109] E. Rabinowicz, “The Nature of the Static and Kinetic Coefficients of Friction,” *Journal of Applied Physics*, vol. 22, no. 11, pp. 1373–1379, 1951.

[110] Y. Ida, “Cohesive force across the tip of a longitudinal-shear crack and Griffith’s specific surface energy,” *Journal of Geophysical Research*, vol. 77, no. 20, pp. 3796–3805, 1972.

[111] V. Rubino, A. J. Rosakis, and N. Lapusta, “Understanding dynamic friction through spontaneously evolving laboratory earthquakes,” *Nature Communications*, vol. 8, p. 15991, 2017.

[112] T. L. Johnson and C. H. Scholz, “Dynamic properties of stick-slip friction of rock,” *Journal of Geophysical Research*, vol. 81, no. 5, pp. 881–888, 1976.

[113] J. H. Dieterich, “Time-dependent friction in rocks,” *Journal of Geophysical Research*, vol. 77, no. 20, pp. 3690–3697, 1972.

[114] T. Baumberger and C. Caroli, "Solid friction from stick–slip down to pinning and aging," *Advances in Physics*, vol. 55, no. 3-4, pp. 279–348, 2006.

[115] J. R. Rice, N. Lapusta, and K. Ranjith, "Rate and state dependent friction and the stability of sliding between elastically deformable solids," *Journal of the Mechanics and Physics of Solids*, vol. 49, no. 9, pp. 1865–1898, 2001.

[116] J.-P. Ampuero and A. M. Rubin, "Earthquake nucleation on rate and state faults – Aging and slip laws," *Journal of Geophysical Research*, vol. 113, no. B1, 2008.

[117] M. Aldam, M. Weikamp, R. Spatschek, E. A. Brener, and E. Bouchbinder, "Critical Nucleation Length for Accelerating Frictional Slip," *Geophysical Research Letters*, vol. 44, no. 22, pp. 11,390–11,398, 2017.

[118] Y. Estrin and Y. Bréchet, "On a model of frictional sliding," *Pure and Applied Geophysics*, vol. 147, no. 4, pp. 745–762, 1996.

[119] Y. Bar-Sinai, R. Spatschek, E. A. Brener, and E. Bouchbinder, "On the velocity-strengthening behavior of dry friction," *Journal of Geophysical Research: Solid Earth*, vol. 119, no. 3, pp. 1738–1748, 2014.

[120] C. Marone, "Laboratory-derived friction laws and their application to seismic faulting," *Annual Review of Earth and Planetary Sciences*, vol. 26, no. 1, pp. 643–696, 1998.

[121] T. Baumberger, P. Berthoud, and C. Caroli, "Physical analysis of the state- and rate-dependent friction law. II. Dynamic friction," *Physical Review B*, vol. 60, no. 6, pp. 3928–3939, 1999.

[122] K. Aki and Paul G. Richards, *Quantitative Seismology*. Sausalito, CA: University Science Books, 2nd edition ed., 2002.

[123] A. Needleman, "The effect of bond strength and loading rate on the conditions governing the attainment of intersonic crack growth along interfaces," *Journal of the Mechanics and Physics of Solids*, vol. 47, no. 12, pp. 2411–2449, 1999.

[124] A. Needleman, "An Analysis of Intersonic Crack Growth Under Shear Loading," *Journal of Applied Mechanics*, vol. 66, no. 4, p. 847, 1999.

[125] F. Barras, P. H. Geubelle, and J.-F. Molinari, "Interplay between Process Zone and Material Heterogeneities for Dynamic Cracks," *Physical Review Letters*, vol. 119, no. 14, 2017.

[126] I. Svetlizky and J. Fineberg, "Classical shear cracks drive the onset of dry frictional motion," *Nature*, vol. 509, no. 7499, p. 205, 2014.

[127] I. Svetlizky, D. S. Kammer, E. Bayart, G. Cohen, and J. Fineberg, "Brittle Fracture Theory Predicts the Equation of Motion of Frictional Rupture Fronts," *Physical Review Letters*, vol. 118, no. 12, p. 125501, 2017.

[128] D. S. Kammer, M. Radiguet, J.-P. Ampuero, and J.-F. Molinari, “Linear Elastic Fracture Mechanics Predicts the Propagation Distance of Frictional Slip,” *Tribology Letters*, vol. 57, no. 3, p. 23, 2015.

[129] E. Bayart, I. Svetlizky, and J. Fineberg, “Fracture mechanics determine the lengths of interface ruptures that mediate frictional motion,” *Nature Physics*, vol. 12, no. 2, p. 166, 2016.

[130] R. E. Abercrombie and J. R. Rice, “Can observations of earthquake scaling constrain slip weakening?,” *Geophysical Journal International*, vol. 162, no. 2, pp. 406–424, 2005.

[131] S. Nielsen, E. Spagnuolo, S. A. F. Smith, M. Violay, G. Di Toro, and A. Bistacchi, “Scaling in natural and laboratory earthquakes,” *Geophysical Research Letters*, vol. 43, no. 4, pp. 1504–1510, 2016.

[132] J. S. Chester, F. M. Chester, and A. K. Kronenberg, “Fracture surface energy of the Punchbowl fault, San Andreas system,” *Nature*, vol. 437, no. 7055, pp. 133–136, 2005.

[133] E. Tinti, P. Spudich, and M. Cocco, “Earthquake fracture energy inferred from kinematic rupture models on extended faults,” *Journal of Geophysical Research*, vol. 110, no. B12, 2005.

[134] S. Das, “Dynamic fracture mechanics in the study of the earthquake rupturing process: Theory and observation,” *Journal of the Mechanics and Physics of Solids*, vol. 51, no. 11-12, pp. 1939–1955, 2003.

[135] J. W. Morrissey and P. H. Geubelle, “A numerical scheme for mode III fracture problems,” *International Journal for Numerical Methods in Engineering*, vol. 40, no. 7, pp. 1181–1196, 1997.

[136] R. Courant, K. Friedrichs, and H. Lewy, “Über die partiellen Differenzengleichungen der mathematischen Physik,” *Mathematische annalen*, vol. 100, no. 1, pp. 32–74, 1928.

[137] M. S. Breitenfeld and P. H. Geubelle, “Parallel Implementation of a Spectral Scheme for Simulations of 3-D Dynamic Fracture Events,” *The International Journal of High Performance Computing Applications*, vol. 14, no. 1, pp. 26–38, 2000.

[138] W. Ritz, “Über eine neue Methode zur Lösung gewisser Variationsprobleme der mathematischen Physik.,” *Journal für die reine und angewandte Mathematik*, vol. 135, pp. 1–61, 1909.

[139] B. G. Galerkin, “Series solution of some problems of elastic equilibrium of rods and plates,” *Vestn. Inzh. Tekh*, vol. 19, pp. 897–908, 1915.

[140] N. M. Newmark, “A Method of Computation for Structural Dynamics,” *Journal of the Engineering Mechanics Division*, vol. 85, no. 3, pp. 67–94, 1959.

[141] G. Francfort and J.-J. Marigo, "Revisiting brittle fracture as an energy minimization problem," *Journal of the Mechanics and Physics of Solids*, vol. 46, no. 8, pp. 1319–1342, 1998.

[142] A. Karma, D. A. Kessler, and H. Levine, "Phase-Field Model of Mode III Dynamic Fracture," *Physical Review Letters*, vol. 87, no. 4, 2001.

[143] N. Moës, J. Dolbow, and T. Belytschko, "A finite element method for crack growth without remeshing," *International Journal for Numerical Methods in Engineering*, vol. 46, no. 1, pp. 131–150, 1999.

[144] X.-P. Xu and A. Needleman, "Void nucleation by inclusion debonding in a crystal matrix," *Modelling and Simulation in Materials Science and Engineering*, vol. 1, no. 2, p. 111, 1993.

[145] M. Ortiz and A. Pandolfi, "Finite-deformation irreversible cohesive elements for three-dimensional crack-propagation analysis," *International Journal for Numerical Methods in Engineering*, vol. 44, no. 9, pp. 1267–1282, 1999.

[146] N. Richart and J.-F. Molinari, "Implementation of a parallel finite-element library: Test case on a non-local continuum damage model," *Finite Elements in Analysis &amp; Design*, vol. 100, pp. 41–46, 2015.

[147] M. Vocialta, N. Richart, and J.-F. Molinari, "3D dynamic fragmentation with parallel dynamic insertion of cohesive elements," *International Journal for Numerical Methods in Engineering*, vol. 109, no. 12, pp. 1655–1678, 2017.

[148] F. Barras, D. S. Kammer, P. H. Geubelle, and J.-F. Molinari, "A study of frictional contact in dynamic fracture along bimaterial interfaces," *International Journal of Fracture*, vol. 189, no. 2, pp. 149–162, 2014.

[149] A. Livne, O. Ben-David, and J. Fineberg, "Oscillations in Rapid Fracture," *Physical Review Letters*, vol. 98, no. 12, 2007.

[150] T. Goldman, R. Harpaz, E. Bouchbinder, and J. Fineberg, "Intrinsic Nonlinear Scale Governs Oscillations in Rapid Fracture," *Physical Review Letters*, vol. 108, no. 10, 2012.

[151] J. Bleyer and J.-F. Molinari, "Microbranching instability in phase-field modelling of dynamic brittle fracture," *Applied Physics Letters*, vol. 110, no. 15, p. 151903, 2017.

[152] D. Coker and A. J. Rosakis, "Experimental observations of intersonic crack growth in asymmetrically loaded unidirectional composite plates," *Philosophical Magazine A*, vol. 81, no. 3, pp. 571–595, 2001.

[153] D. V. Kubair, P. H. Geubelle, and Y. Y. Huang, "Intersonic crack propagation in homogeneous media under shear-dominated loading: Theoretical analysis," *Journal of the Mechanics and Physics of Solids*, vol. 50, no. 8, pp. 1547–1564, 2002.

[154] J. Lambros and A. J. Rosakis, “Shear dominated transonic interfacial crack growth in a bimaterial-I. Experimental observations,” *Journal of the Mechanics and Physics of Solids*, vol. 43, no. 2, pp. 169–188, 1995.

[155] C. Liu, Y. Huang, and A. J. Rosakis, “Shear dominated transonic interfacial crack growth in a bimaterial-II. Asymptotic fields and favorable velocity regimes,” *Journal of the Mechanics and Physics of Solids*, vol. 43, no. 2, pp. 189–206, 1995.

[156] Y. Huang, W. Wang, C. Liu, and A. J. Rosakis, “Intersonic crack growth in bimaterial interfaces : An investigation of crack face contact,” *Journal of the Mechanics and Physics of Solids*, vol. 46, no. 11, pp. 2233–2259, 1998.

[157] X. P. Xu and A. Needleman, “Numerical simulations of dynamic crack growth along an interface,” *International Journal of Fracture*, vol. 74, no. 4, pp. 289–324, 1996.

[158] S. Hao, W. K. Liu, P. A. Klein, and A. J. Rosakis, “Modeling and simulation of intersonic crack growth,” *International Journal of Solids and Structures*, vol. 41, no. 7, pp. 1773–1799, 2004.

[159] D. S. Kammer, V. Yastrebov, P. Spijker, and J.-F. Molinari, “On the Propagation of Slip Fronts at Frictional Interfaces,” *Tribology Letters*, vol. 48, no. 1, pp. 27–32, 2012.

[160] V. Prakash, “Frictional response of sliding interfaces subjected to time varying normal pressures,” *Journal of Tribology*, vol. 120, no. 1, pp. 97–102, 1998.

[161] A. M. Rubin and J.-P. Ampuero, “Aftershock asymmetry on a bimaterial interface,” *Journal of Geophysical Research: Solid Earth*, vol. 112, no. B5, p. B05307, 2007.

[162] D. S. Kammer, V. A. Yastrebov, G. Anciaux, and J. F. Molinari, “The existence of a critical length scale in regularised friction,” *Journal of the Mechanics and Physics of Solids*, vol. 63, no. 0, pp. 40–50, 2014.

[163] K. W. Xia, C. E. Rousseau, and A. J. Rosakis, “Experimental investigations of spontaneous bimaterial interfacial fractures,” *Journal of Mechanics of Materials and Structures*, vol. 3, no. 1, pp. 173–184, 2008.

[164] R. P. Singh and A. Shukla, “Subsonic and intersonic crack growth along a bimaterial interface,” *Journal of Applied Mechanics*, vol. 63, no. 4, pp. 919–924, 1996.

[165] P. H. Geubelle and D. V. Kubair, “Intersonic crack propagation in homogeneous media under shear-dominated loading: Numerical analysis,” *Journal of the Mechanics and Physics of Solids*, vol. 49, no. 3, pp. 571–587, 2001.

[166] E. Sharon, S. P. Gross, and J. Fineberg, “Energy Dissipation in Dynamic Fracture,” *Physical Review Letters*, vol. 76, no. 12, pp. 2117–2120, 1996.

[167] K. Ravi-Chandar and B. Yang, “On the role of microcracks in the dynamic fracture of brittle materials,” *Journal of the Mechanics and Physics of Solids*, vol. 45, no. 4, pp. 535–563, 1997.

[168] A. Rabinovitch, G. Belizovsky, and D. Bahat, “Origin of mist and hackle patterns in brittle fracture,” *Physical Review B*, vol. 61, no. 22, pp. 14968–14974, 2000.

[169] C. Guerra, J. Scheibert, D. Bonamy, and D. Dalmas, “Understanding fast macroscale fracture from microcrack post mortem patterns,” *Proceedings of the National Academy of Sciences*, vol. 109, no. 2, pp. 390–394, 2012.

[170] M. Mello, H. S. Bhat, and A. J. Rosakis, “Spatiotemporal properties of Sub-Rayleigh and supershear rupture velocity fields: Theory and experiments,” *Journal of the Mechanics and Physics of Solids*, vol. 93, pp. 153–181, 2016.

[171] F. X. Passelegue, A. Schubnel, S. Nielsen, H. S. Bhat, and R. Madariaga, “From Sub-Rayleigh to Supershear Ruptures During Stick-Slip Experiments on Crustal Rocks,” *Science*, vol. 340, no. 6137, pp. 1208–1211, 2013.

[172] S. G. Psakhie, E. V. Shilko, M. V. Popov, and V. L. Popov, “Key role of elastic vortices in the initiation of intersonic shear cracks,” *Physical Review E*, vol. 91, no. 6, 2015.

[173] J. R. Rice, “The Mechanics of Earthquake Rupture.,” in *Physics of the Earth’s Interior*, pp. 555–649, Italian Physical Society and North Holland, 1980.

[174] J. W. Morrissey and J. R. Rice, “Crack front waves,” *J. Mech. Phys. Solids*, vol. 46, pp. 467–487, 1998.

[175] F. Barras, R. Carpaij, P. H. Geubelle, and J.-F. Molinari, “Supershear bursts in the propagation of tensile crack in linear elastic material,” *Under review*, 2018.

[176] K. Alidoost, F. Barras, A. Dubois, R. Carpaij, D. Bonamy, P. H. Geubelle, and J.-F. Molinari, “Crack front distorted by heterogeneities: Benchmarking the first-order perturbation models,” *In preparation*, 2018.

[177] F.-E. Fekak, F. Barras, A. Dubois, D. Spielmann, D. Bonamy, P. H. Geubelle, and J.-F. Molinari, “Study of front waves: 3D dynamic response to a local perturbation of tensile and shear cracks,” *In preparation*, 2018.

[178] I. Kolvin, G. Cohen, and J. Fineberg, “Crack Front Dynamics: The Interplay of Singular Geometry and Crack Instabilities,” *Physical Review Letters*, vol. 114, no. 17, 2015.

[179] F. Barras, R. Aghababaei, and J.-F. Molinari, “Onset of sliding across scales: How the microcontacts impact frictional strength,” *In preparation*, 2018.

[180] P. G. Richards, “Dynamic motions near an earthquake fault a three-dimensional solution,” *Bulletin of the Seismological Society of America*, vol. 66, no. 1, pp. 1–32, 1976.

[181] V. A. Yastrebov, G. Anciaux, and J.-F. Molinari, "From infinitesimal to full contact between rough surfaces: Evolution of the contact area," *International Journal Of Solids And Structures*, vol. 52, pp. 83–102, 2015.

[182] R. Aghababaei, T. Brink, and J.-F. Molinari, "Asperity-Level Origins of Transition from Mild to Severe Wear," *Physical Review Letters*, vol. 120, no. 18, 2018.

[183] P. Spijker, G. Anciaux, and J.-F. Molinari, "Relations between roughness, temperature and dry sliding friction at the atomic scale," *Tribology International*, vol. 59, pp. 222–229, 2013.

[184] T. Hughes, *The Finite Element Method: Linear Static and Dynamic Finite Element Analysis.* Dover Publications, 2000.

[185] Z. P. Bažant, "Scaling of quasibrittle fracture: Asymptotic analysis," *International Journal of Fracture*, vol. 83, no. 1, p. 19, 1997.

[186] F. Barras, M. Aldam, E. A. Brener, E. Bouchbinder, and J.-F. Molinari, "On the rupture dynamics of interfaces obeying laboratory-derived friction laws," *In preparation*, 2018.

[187] E. A. Brener, M. Aldam, F. Barras, J.-F. Molinari, and E. Bouchbinder, "Unstable slip pulses and earthquake nucleation as a non-equilibrium first-order phase transition," *Under review*, 2018.

[188] E. Fukuyama, "Radiation energy measured at earthquake source," *Geophysical Research Letters*, vol. 32, no. 13, 2005.

[189] E. Aharonov and C. H. Scholz, "A Physics-Based Rock Friction Constitutive Law: Steady State Friction," *Journal of Geophysical Research: Solid Earth*, vol. 123, no. 2, pp. 1591–1614, 2018.

[190] Y. Bar Sinai, E. A. Brener, and E. Bouchbinder, "Slow rupture of frictional interfaces," *Geophysical Research Letters*, vol. 39, no. 3, 2012.

[191] J.-P. Ampuero, J.-P. Vilotte, and F. J. Sánchez-Sesma, "Nucleation of rupture under slip dependent friction law: Simple models of fault zone," *Journal of Geophysical Research: Solid Earth*, vol. 107, no. B12, pp. ESE 2–1–ESE 2–19, 2002.

[192] E. Jones, T. Oliphant, P. Peterson, and others, "SciPy: Open source scientific tools for Python," 2001.

[193] J. J. Moré, "The Levenberg-Marquardt algorithm: Implementation and theory," in *Numerical Analysis* (G. A. Watson, ed.), vol. 630, pp. 105–116, Berlin, Heidelberg: Springer Berlin Heidelberg, 1978.

[194] M. A. Branch, T. F. Coleman, and Y. Li, "A Subspace, Interior, and Conjugate Gradient Method for Large-Scale Bound-Constrained Minimization Problems," *SIAM Journal on Scientific Computing*, vol. 21, no. 1, pp. 1–23, 1999.

[195] M. Cocco and A. Bizzarri, “On the slip-weakening behavior of rate- and state dependent constitutive laws,” *Geophysical Research Letters*, vol. 29, no. 11, 2002.

[196] A. Bizzarri and M. Cocco, “Slip-weakening behavior during the propagation of dynamic ruptures obeying rate- and state-dependent friction laws,” *Journal of Geophysical Research*, vol. 108, no. B8, 2003.

[197] K. Obara, “Nonvolcanic Deep Tremor Associated with Subduction in Southwest Japan,” *Science*, vol. 296, no. 5573, pp. 1679–1681, 2002.

[198] S. Ide, G. C. Beroza, D. R. Shelly, and T. Uchide, “A scaling law for slow earthquakes,” *Nature*, vol. 447, no. 7140, pp. 76–79, 2007.

[199] Z. Peng and J. Gomberg, “An integrated perspective of the continuum between earthquakes and slow-slip phenomena,” *Nature Geoscience*, vol. 3, no. 9, pp. 599–607, 2010.

[200] A. M. Rubin and J.-P. Ampuero, “Earthquake nucleation on (aging) rate and state faults,” *Journal of Geophysical Research: Solid Earth*, vol. 110, no. B11, 2005.

[201] J. Bleyer, C. Roux-Langlois, and J.-F. Molinari, “Dynamic crack propagation with a variational phase-field model: Limiting speed, crack branching and velocity-toughening mechanisms,” *International Journal of Fracture*, vol. 204, no. 1, pp. 79–100, 2017.

[202] C.-H. Chen, E. Bouchbinder, and A. Karma, “Instability in dynamic fracture and the failure of the classical theory of cracks,” *Nature Physics*, vol. 13, no. 12, pp. 1186–1190, 2017.

Fabian Barras

Contact information

Address
Computational Solid Mechanics Laboratory
School of Architecture, Civil and Environmental Engineering
École Polytechnique Fédérale de Lausanne
CH - 1015 Lausanne, Switzerland

Email fabian.barras@alumni.epfl.ch

ORCID 0000-0003-1109-0200

Research interests

Dynamic failure of materials and structures

- Physics of fast and sudden ruptures
- Dynamic fracture and fragmentation, crustal earthquakes, snow avalanches
- Bridging the microscopic aspects of failure to the long-range dynamics
- Toughening aspects of an heterogeneous microstructure

Computational modeling

- Probing beyond the assumptions of standard solutions
- Exploring large-scale computations and data using recent high performance computing capacities
- Actively developing and contributing to free softwares as a *sine qua non* of reproducible science
- Maintaining direct interactions with theoretical and experimental groups

Education

2018 **Doctor of Philosophy (Ph.D.)**, *École Polytechnique Fédérale de Lausanne*, Switzerland

- Doctoral program of civil and environmental engineering
- Thesis: "*When dynamic cracks meet disorder: A journey along the fracture process zone*"
- Advisor: Prof. Jean-François Molinari

2013 **Master ès Science (M.Sc.)**, *École Polytechnique Fédérale de Lausanne*, Switzerland

- Civil engineering
- Prize *Union patronale des ingénieurs et architectes vaudois*: best diploma in civil engineering

2011 **Bachelor ès Science (B.Sc.)**, *École Polytechnique Fédérale de Lausanne*, Switzerland

- Civil engineering

2008 **Maturité gymnasiale (high-school degree)**, *Lycée-Collège de la Planta*, Sion, Switzerland

- Physics and applied mathematics
- Prize *Société valaisanne de physique*: best degree in physics and applied mathematics

Research experiences

2013-2018 **Doctoral Assistant**, *École Polytechnique Fédérale de Lausanne*, Switzerland

- Computational Solid Mechanics Laboratory (LSMS)
- Active developer of two high performance scientific libraries; *Akantu* (finite-element method) and *cRacklet* (boundary integral formulation)
- Uncovering new dynamics arising from the interplay between a propagating crack front and material heterogeneities
- Participation in the preparation and supervision of several courses
- Supervision of ten semester projects and two master theses

2013-2018 **Scientific collaboration project**, *University of Illinois at Urbana-Champaign*, United States of America

- Prof. Philippe H. Geubelle (numerical group)
- Visiting scholar during the spring 2013
- Implementation of a boundary integral formulation of elastodynamics
- Dynamic fracture of interfaces in presence of tougher asperities or dissimilar elastic properties
- Co-supervision of two master theses on the dynamic fracture of heterogeneous interfaces

2017-2018 **Scientific collaboration project**, *Weizmann Institute of Science*, Rehovot, Israel

- Prof. Eran Bouchbinder and Michael Aldam (theoretical group)
- Onset of frictional slip and earthquake nucleation
- Understanding the rupture dynamics of interfaces described by laboratory-derived friction law

2017-2018 **Scientific collaboration project**, *Commissariat à l'énergie atomique et aux énergies alternatives (CEA)*, Paris-Saclay, France

- Prof. Daniel Bonamy and Alizée Dubois (experimental group)
- Dynamic failure of heterogeneous brittle materials
- Benchmarking the first-order models of heterogeneous fracture

Journal publications

[1] Fabian Barras, David S. Kammer, Philippe H. Geubelle, and Jean-François Molinari. A study of frictional contact in dynamic fracture along bimaterial interfaces. *International Journal of Fracture*, 189(2):149–162, October 2014.

[2] Fabian Barras, Philippe H. Geubelle, and Jean-François Molinari. Interplay between Process Zone and Material Heterogeneities for Dynamic Cracks. *Physical Review Letters*, 119(14), October 2017.

[3] Fabian Barras, René Carpaij, Philippe H. Geubelle, and Jean-François Molinari. Supershear bursts in the propagation of tensile crack in linear elastic material. *Under review*, 2018.

[4] Fabian Barras, Ramin Aghababaei, and Jean-François Molinari. Onset of sliding across scales: How the microcontacts impact frictional strength. *In preparation*, 2018.

[5] Fabian Barras, Michael Aldam, Efim A. Brener, Eran Bouchbinder, and Jean-François Molinari. On the rupture dynamics of interfaces obeying laboratory-derived friction laws. *In preparation*, 2018.

[6] Efim A. Brener, Michael Aldam, Fabian Barras, Jean-François Molinari, and Eran Bouchbinder. Unstable slip pulses and earthquake nucleation as a non-equilibrium first-order phase transition. *Under review*, 2018.

[7] Fatima-Ezzahra Fekak, Fabian Barras, Alizée Dubois, Damien Spielmann, D. Bonamy, Philippe H. Geubelle, and Jean-François Molinari. Study of front waves: 3D dynamic response to a local perturbation of tensile and shear cracks. *In preparation*, 2018.

[8] Kazem Alidoost, Fabian Barras, Alizée Dubois, René Carpaij, D. Bonamy, Philippe H. Geubelle, and Jean-François Molinari. Crack front distorted by heterogeneities: Benchmarking the first-order perturbation models. *In preparation*, 2018.

Conferences and workshops

2018 **13th World Congress in Computational Mechanics (WCCM XIII)**, *Shock waves produced by the interaction of dynamic crack with heterogeneities*, F. Barras, P.H. Geubelle, J.-F. Molinari, New York, New York, USA

2017 **5th International Conference on Computational Modeling of Fracture and Failure of Materials and Structures (CFRAC)**, *On the dynamic perturbation of crack front by microscale material heterogeneities*, F. Barras, P.H. Geubelle, J.-F. Molinari, Nantes,France

2016 **European Conference on Fracture (ECF 21)**, *The dynamic rupture of interfaces made of heterogeneous fracture properties*, F. Barras, P.H. Geubelle, J.-F. Molinari, Catania, Italy

2015 **Society of Engineering Science (SES), 52nd Annual Technical Meeting**, *The role of elastic waves during dynamic rupture of heterogeneous interfaces*, F. Barras, P.H. Geubelle, J.-F. Molinari, College Station, Texas, USA

2015 **Colloque national MECAMAT (Groupe Français de Mécanique des Matériaux)**, *Dynamic fracture along bimaterial and heterogeneous interfaces*, F. Barras, D.S. Kammer, P.H. Geubelle, J.-F. Molinari, Aussois, France

2014 **11th World Congress in Computational Mechanics (WCCM XI)**, *A study of friction in dynamic fracture along bimaterial interfaces*, F. Barras, D.S. Kammer, P.H. Geubelle, J.-F. Molinari, Barcelona, Spain

Invited seminars

2018 **SPHYNX laboratory, CEA, Paris-Saclay, France**, *Onset of slip along frictional interfaces: From microcontacts rejuvenation to earthquake dynamics*

Teaching experiences

Fall 2016 **Selected Topics in Mechanics of Solids and Structures**, *by Prof. Jean-François Molinari*
- Advanced class of fracture mechanics and elastodynamics
- 14 weeks. In charge of 1 hour/week exercise sessions, 20 students

Spring 2016 **Numerical modeling of solids and structures**, *by Prof. Jean-François Molinari*
- Introductory class of finite-element modeling
- 14 weeks. In charge of 2 hours/week exercise sessions, 30 students

Fall 2015 **Scientific programming for Engineers**, *by Dr. Guillaume Anciaux*
- Doctoral class about scientific programming
- 14 weeks. In charge of 2 hours/week exercise sessions plus mini-projects supervision, 20 students

Spring 2015 **Numerical modeling of solids and structures**, *by Prof. Jean-François Molinari*
- Introductory class of finite-element modeling
- 14 weeks. In charge of 2 hours/week exercise sessions, 30 students

Fall 2014 **General chemistry**, *by Prof. Christos Comninellis*
- Introductory class of chemistry
- 14 weeks. In charge of 2 hours/week exercise sessions, 50 students

Spring 2014 **Geometry**, *by Prof. Jürgpeter Buser*

- Introductory class of geometry
- 14 weeks. In charge of 2 hours/week exercise sessions, 50 students

Advised master theses (with Prof. P.H. Geubelle and Prof. J.-F. Molinari)

2016-2017 **René Carpaij**

- In-plane fracture in presence of a tougher heterogeneity: Comparison between a quasi-static and fully dynamic crack propagation method

2014-2015 **Damien Spielmann**

- Crack front waves under mode-II and mixed-mode loading

Advised semester projects and internships (with Prof. J.-F. Molinari)

Spring 2017 **Ismail Honsali**

- Crack propagation through heterogeneous media

Spring 2016 **Luis Carlos Muñoz Heinen**

- Study and calibration of 2D cohesive laws

Fall 2015 **Mohamed Ladeb**

- On the parallel implementation of the spectral method to simulate 3D dynamic fracture of materials

Fall 2015 **Gabrielle Muller**

- Simulation of Double Cantilever Beam fracture experiments

Fall 2015 **Erika Lopez**, *with Mauro Corrado*

- Contact between rough surfaces

Fall 2015 **Ollie Stephenson**

- Dynamic shear rupture front interacting with a circular asperity

Spring 2015 **Gabrielle Muller and Gabriele Albertini**

- A probabilistic approach to design civil engineering structures

Fall 2014 **Grosdidier Guillaume and Grand Charly**, *with Aurelia Cuba Ramos*

- Implementation of Mohr-Coulomb plasticity in a finite-element code

Spring 2014 **Damien Spielmann**

- Structural shell elements within Akantu

Spring 2014 **Sébastien Hartmann**

- Implementation of the undamped dynamics of Bernoulli Beam elements within Akantu

Community work

2017-2018 **Doctoral school of civil and environmental engineering**

- Elected Ph.D. student representative
- Mission: Participation in several school commissions elaborating the regulations of the doctoral studies (About one meeting per month)

2017-2018 **Teaching commission of civil engineering**

- Member
- Mission: Elaboration and validation of the study plan for the bachelor/master program in civil engineering (Quarterly meetings)

2017-2018 **Computational Solid Mechanics Laboratory**

- Lab sport coach
- Mission: Promote and maintain a healthy working environment